nagra.

Technical Report 17-12

Diffusion of selected cations and anions in compacted montmorillonite and bentonite

November 2017

M.A. Glaus, S. Frick, L.R. Van Loon

Paul Scherrer Institut, Villigen PSI

nagra.

Technical Report 17-12

Diffusion of selected cations and anions in compacted montmorillonite and bentonite

November 2017

M.A. Glaus, S. Frick, L.R. Van Loon

Paul Scherrer Institut, Villigen PSI

Preface

The Laboratory for Waste Management of the Nuclear Energy and Safety Research Department at the Paul Scherrer Institute is performing work to develop and test models as well as to acquire specific data relevant to performance assessments of planned Swiss nuclear waste repositories. These investigations are undertaken in close co-operation with, and with the partial financial support of, the National Cooperative for the Disposal of Radioactive Waste (Nagra).

Abstract

The present report gives a summary of the experimental results obtained from various diffusion experiments with positively and negatively charged radiotracers, including HTO as a neutral reference species, in compacted homoionic Na-montmorillonite and a natural bentonite. The purpose of the report is to document the results, the experimental methods and modes of data evaluation and further to test these data for internal consistency and propose simplified ways for their application in the safety analysis of a deep geological repository for radioactive waste.

The diffusion experiments comprised HTO, $^{22}Na^+$, $^{85}Sr^{2+}$, $^{134}Cs^+$, $^{36}Cl^-$, $^{35}SO_4^{2-}$ and $^{75}SeO_4^{2-}$ as the radiotracers and were carried out at bulk dry densities between 1300 and 1900 kg m^{-3} and using background electrolyte concentrations between 0.1 and 1.0 M for the contacting liquid phases. Through-diffusion was the basic method applied to all test systems. In order to verify the results obtained thereby and to obtain additional information on the role of the confining filters, through-diffusion was followed either by out-diffusion or tracer profile analysis. Depending on the diffusivities in the clay specimens, diffusion cells equipped with a flushed filter system were used in order to avoid potential difficulties in the data evaluation related to the formation of concentration gradients in the confining filters. In all cases where the latter gradients were clearly less than the respective gradients in the clay samples during the steady-state flux phase, diffusion cells with static filter systems were used. Best-fit parameter values were evaluated by various methods, comprising approximate analytical solutions of the diffusion equation and inverse modelling techniques involving numerical solver procedures. In many experiments the diffusion of the charged tracer ion was simultaneously measured with the diffusion of the uncharged HTO tracer in order to increase the comparability of the break-through curves.

The results are in good agreement with our observations for bulk-dry densities of 1900 kg m^{-3} published earlier. The diffusive fluxes of cationic tracers were larger than expected for a simple proportionality of the effective diffusion coefficients of the HTO tracer with the respective diffusion coefficients in bulk water. The diffusivities increased with decreasing concentration of the background electrolyte exhibiting the already observed dependency on cation charge. It can be concluded that the overall observed diffusive fluxes of cationic species are predominantly controlled by the entirety of mobile surface species, not only at the highest bulk-dry densities, but also at bulk-dry densities relevant for a realistic compaction of bentonite in the buffer and backfill materials foreseen in the disposal concept for high-level radioactive wastes. This behaviour applied basically for Na$^+$ and Sr^{2+}, for which surface species in the cation exchange sites (planar sites) are assumed to be the only surface species. For Cs$^+$, for which the existence of more than a single surface species is indicated in the sorption isotherms, this behaviour was more complex. The data suggest that the different Cs$^+$ surface species exhibit different surface mobilities.

For anionic radiotracers an inverse behaviour in diffusion was observed. The effective diffusion coefficients were lower than those predicted simply based on bulk water diffusion coefficients and decreased with decreasing concentration of the background electrolyte. This behaviour can be explained by different approaches regarding the distribution ratios of anions in bulk water and anions in the vicinity of negatively charged surfaces ("anion exclusion"). No attempts were undertaken in the present work to discriminate between the various models proposed in the literature.

The retardation of cationic species observed in the experiments with compacted clay samples were largely in agreement with predictions based on the selectivities for cation exchange obtained from measurements in dilute suspensions. No observations were made which would favour the view of reduced accessibility of sorption sites in compacted samples of clay minerals. It has rather to be assumed that the entire cation exchange capacity is available for exchange reactions. How-

ever, significant discrepancies in the sorption distribution coefficients could be observed in the case of Cs^+, with a trend of increasing Cs-selectivity with increasing bulk-dry density. It was proposed already in previous work related to studies on bentonite that this phenomenon can rather be explained by the different hydration properties of this alkali cation compared to Na^+. In the present work the dependencies observed for Na-montmorillonite were similar to the behaviour for bentonites, both in the transient phase of diffusion experiments and in sorption experiments with compacted clay samples. For Sr^{2+} a slightly decreasing Sr-selectivity with increasing bulk-dry density was observed in the experiments with compacted Na-montmorillonite. In view of the larger hydration sphere of Sr^{2+} compared to Na^+, this observation is thus in agreement with the behaviour of Cs^+, for which hydration provides less energy than for Na^+.

The present work clearly shows that the migration of charged radionuclides in charged argillaceous media needs to be related to the particular chemical conditions of the equilibrium solution. The simple pore diffusion model devoid of a surface diffusion component was found to be inadequate to describe the observed behaviour. A simple model based on the "Gimmi – Kosakowski" scheme for relating the effective diffusion coefficients with sorption distribution values and the extended Archie relation used to take into account geometrical effects, is proposed here for application in safety analysis. Such applications are, however, restricted to the type of cations investigated in the present work (alkali and alkaline-earth cations). It was shown in different work from our laboratory that surface diffusion plays also an important role in the diffusion of transition elements. However, in such cases only part of the surface species is mobile and needs to be taken into account for the evaluation of effective diffusion coefficients.

Zusammenfassung

Der vorliegende Bericht fasst die experimentellen Resultate zusammen, welche in Diffusions-experimenten mit unterschiedlich geladenen Tracerionen – einschliesslich HTO als ungeladenem Referenzsystem – in kompaktiertem homoionischen Na-Montmorillonit und natürlichem Bentonit gewonnen wurden. Der Zweck des Berichts besteht einerseits in der Dokumentation der experimentellen Vorgehensweisen, Resultate und der Auswertungsmethoden und andererseits in der Prüfung der Daten auf interne Konsistenz und einem Vorschlag zur vereinfachten Anwendung in der Sicherheitsanalyse für ein geologisches Tiefenlager für radioaktive Abfälle.

Die Diffusionsexperimente mit HTO, $^{22}Na^+$, $^{85}Sr^{2+}$, $^{134}Cs^+$, $^{36}Cl^-$, $^{35}SO_4^{2-}$ und $^{75}SeO_4^{2-}$ wurden bei Rohdichten zwischen 1300 und 1900 kg m^{-3} und Konzentrationen des Hintergrundelektrolyten zwischen 0.1 und 1.0 M durchgeführt. Grundsätzlich wurde in allen Experimenten die Durch-diffusionstechnik angewendet. Als zusätzliche Verifikation der hierbei erhaltenen Resultate und zum Zweck einer besseren Eingrenzung der Diffusivitäten in den begrenzenden Filtern wurden die Durchdiffusionsexperimente durch Out-diffusion oder durch eine Messung des Tracerprofils ergänzt. Abhängig von den Diffusivitäten in den Tonkörpern wurden Diffusionszellen mit gespül-ten Filtern verwendet, um allfällige Probleme mit dominanten Tracergradienten in den Filtern bei der Datenauswertung zu vermeiden. Wenn diese signifikant kleiner als jene in den Tonkörpern während der stationären Phase der Experimente waren, kamen Diffusionszellen mit statischen Filtern zum Einsatz. 'Best-fit'-Parameterwerte wurden mit unterschiedlichen Methoden, teils mit semi-analytischen Näherungsverfahren oder mit numerischen Lösungsprozeduren, ermittelt. In diversen Experimenten wurde die Diffusion der geladenen Testionen parallel mit der Diffusion von HTO gemessen, um eine bessere Vergleichbarkeit zu erzielen.

Die hier gewonnenen Resultate stimmen gut mit publizierten früheren Messungen bei Rohdichten von 1900 kg m^{-3} überein. Die diffusiven Kationenflüsse waren signifikant höher als die Erwar-tungswerte, welche auf einer simplen Proportionalität zwischen dem effektiven Diffusionskoeffi-zienten des ungeladenen HTO-Tracers und den entsprechenden Diffusionskoeffizienten in freiem Wasser beruhen. Die effektiven Diffusionskoeffizienten für kationische Spezies stiegen mit sin-kender Konzentration des Hintergrundelektrolyten an und wiesen die bereits früher festgestellte typische Abhängigkeit von der Kationenladung auf. Daraus lässt sich schliessen, dass der Gesamt-fluss kationischer Spezies vorwiegend durch mobile Oberflächenspezies kontrolliert wird und deren Gesamtheit zur Oberflächendiffusionskomponente beiträgt. Diese Schlussfolgerung gilt nicht nur für die höchsten hier eingesetzten Rohdichten, sondern auch für Rohdichten in den Bentonitverfüllungen und -ummantelungen, wie sie im Konzept zur Tiefenlagerung hochaktiver Materialien vorgesehen sind. Dieses Verhalten konnte grundsätzlich im Fall von Na$^+$ und Sr^{2+} beobachtet werden, bei welchen davon ausgegangen werden kann, dass die Kationenaustausch-spezies an den planaren Tonoberflächen die einzigen Oberflächenspezies sind. Das Verhalten von Cs$^+$, bei welchem die Sorptionsisothermen auf die Existenz von mehreren Oberflächenspezies hinweisen, war hingegen komplexer. Man kann davon ausgehen, dass die Oberflächenspezies von Cs$^+$ unterschiedliche Oberflächenmobilitäten aufweisen können.

Für anionische Spezies wurde ein gegenteiliges Verhalten beobachtet. Die effektiven Diffusions-koeffizienten waren tiefer als aufgrund der Diffusionskoeffizienten in freiem Wasser vorher-gesagt und nahmen mit sinkenden Konzentrationen des Hintergrundelektrolyten ab. Dieses Ver-halten lässt sich mit unterschiedlichen konzeptionellen Ansätzen zur Verteilung der Anionen im freien Wasser und den durch die negativ geladenen Oberflächen beeinflussten Wasserbezirken in den Tonporen ("Anionenausschluss") erklären. Es wurde in der vorliegenden Arbeit nicht ver-sucht, zwischen diesen unterschiedlichen Ansätzen in der Literatur zu unterscheiden.

Die in den Experimenten beobachtete Retardierung kationischer Spezies lag weitgehend im Bereich der Erwartungen aufgrund der aus Experimenten mit verdünnten Suspensionen gewonnenen Selektivitäten für den Kationenaustausch. Es konnten keine Hinweise auf eine allfällig reduzierte Kapazität des Tons, welche aufgrund der starken Kompaktierung hervorgerufen würde, gefunden werden. Es muss vielmehr davon ausgegangen werden, dass die gesamte Kationenaustauschkapazität des Tons zur Verfügung steht. Deutliche Unterschiede zwischen kompaktierten und dispergierten Tonsystemen wurden einzig im Fall von Cs^+ gefunden. Wie schon früher bei Experimenten mit Bentonit beobachtet, stieg die Selektivität von Cs^+ gegenüber derjenigen von Na^+ mit zunehmender Kompaktierung des Tons an. Dies kann mit der schwächeren Hydratisierung des Cs^+-Ions gegenüber Na^+ erklärt werden. Die früheren Beobachtungen an Bentonit wurden in den vorliegenden Experimenten mit Na-Montmorillonit bestätigt, sowohl für die transiente Phase eines Diffusionsexperiments, als auch in der stationären Phase eines Sorptionsexperiments an kompaktierten Tonkörpern. Im Fall von Sr^{2+} konnte eine ganz leichte Abnahme der Selektivität mit zunehmender Kompaktierung von Na-Montmorillonit nachgewiesen werden. Dies wäre angesichts der Tatsache, dass das Sr^{2+}-Ion stärker hydratisiert ist als Na^+, mit der obigen Hypothese zur ansteigenden Selektivität von Cs^+ gut vereinbar.

Die vorliegende Arbeit zeigt klar auf, dass die diffusive Ausbreitung von geladenen Spezies in geladenen Tonmaterialien stark von der chemischen Zusammensetzung des im Gleichgewicht stehenden Tonporenwassers abhängt. Ein einfaches Porendiffusionsmodell, in welchem eine Oberflächendiffusionskomponente fehlt, ist zur Beschreibung des beobachteten Verhaltens kationischer Spezies ungenügend. Der verfeinerte "Gimmi – Kosakowski" Ansatz zur Berücksichtigung der Abhängigkeit des effektiven Diffusionskoeffizienten vom Sorptions-Verteilungskoeffizienten sowie die erweiterte Archie-Beziehung zum Einbezug geometrischer Effekte werden hier als einfachste Alternative zur Anwendung in der Sicherheitsanalyse vorgeschlagen. Eine solche Anwendung ist allerdings auf die hier untersuchten Typen von Kationen einzuschränken (Alkali- und Erdalkalikationen). Es wurde in anderen Arbeiten aus unserem Labor gezeigt, dass die Oberflächendiffusion auch bei Übergangsmetallen von Bedeutung sein kann. In solchen Fällen ist allerdings nur ein Teil der sorbierten Oberflächenspezies zur Berechnung der Oberflächendiffusionskomponente zu berücksichtigen.

Résumé

Ce rapport présente la synthèse des résultats obtenus lors de diverses expériences de diffusion avec des radiotraceurs chargés positivement et négativement, y compris HTO en tant qu'espèce neutre de référence, dans une Na-montmorillonite mono-ionique compactée et dans une bentonite naturelle. L'objectif de ce rapport est de documenter les résultats, les méthodes expérimentales et les processus d'évaluation des données obtenues, pour ensuite tester la validité de ces données et proposer un protocole simplifié qui permettra de les utiliser pour les analyses de sureté effectuées dans le cadre du stockage des déchets nucléaires en couches géologiques profondes.

Les expériences de diffusion utilisant les radiotraceurs HTO, $^{22}Na^+$, $^{85}Sr^{2+}$, $^{134}Cs^+$, $^{36}Cl^-$, $^{35}SO_4^{2-}$ et $^{75}SeO_4^{2-}$ ont été menées à des densités d'argile (déshydratée) comprises entre 1300 et 1900 kg m^{-3} et en utilisant des concentrations d'électrolyte comprises 0.1 et 1.0 M. La méthode de base de "through-diffusion" a été appliquée à tous les systèmes expérimentaux. Afin de vérifier les résultats obtenus et d'obtenir des informations supplémentaires sur le rôle des filtres confinés, la "through-diffusion" a été suivie soit par la "out-diffusion", soit par l'analyse de profil des traceurs. En fonction de la diffusivité dans les échantillons d'argile, des cellules de diffusion équipées de filtres de flux ont été utilisées afin d'éviter, lors de l'interprétation des données, des difficultés qui seraient dues à la formation de gradients dans les filtres confinés. Quand les gradients mesurés durant la phase stationnaire des expériences dans les filtres étaient clairement inférieurs à ceux dans les échantillons d'argile, des cellules de diffusion équipées de filtres statiques ont été utilisées. Les valeurs de paramètres permettant d'obtenir le meilleur ajustement ont été évaluées en utilisant diverses méthodes, incluant les solutions analytiques approximées des équations de diffusion et des techniques de modélisation inverse utilisant des procédures de résolution numériques. Pour de nombreuses expériences, afin d'améliorer la comparabilité des données, la diffusion de l'ion traceur chargé et celle du traceur non chargé HTO ont été mesurées simultanément.

Les résultats obtenus concordent généralement avec nos observations précédentes impliquant des densités d'argile déshydratée de 1900 kg m^{-3}. Les flux diffusifs des traceurs cationiques ont été supérieurs aux prévisions, en considérant une proportionnalité simple entre le coefficient de diffusion effectif du traceur HTO et les coefficients respectifs dans l'eau. Les diffusivités augmentent avec la diminution des concentrations de l'électrolyte de base, mettant en évidence la relation avec la charge du cation qui a déjà été observée. On peut conclure que dans l'ensemble, les flux diffusifs observés pour les espèces cationiques sont principalement contrôlés par la totalité des espèces mobiles de surface, non seulement aux densités d'argile les plus élevées, mais aussi à celles qui correspondent à des taux de compaction réalistes pour la bentonite utilisée comme matériau de comblement, selon le concept de stockage des déchets radioactifs de haute activité. Ce comportement a pu être observé d'une façon générale pour Na$^+$ et Sr$^+$, pour lesquels on suppose que les espèces présentes dans les sites d'échange cationique de l'argile (sites planaires) sont les seules espèces de surface. Dans le cas de Cs$^+$, où les isothermes de sorption indiquent la présence de plusieurs espèces de surface, le comportement est plus complexe. Les données obtenues suggèrent que les différentes espèces de surface de Cs$^+$ ont des mobilités de surface différentes.

Pour les traceurs anioniques, un comportement inverse lors de la diffusion a été observé. Les coefficients de diffusion effectifs étaient moins élevés que ceux prédits en se basant simplement sur les coefficients de diffusion dans l'eau ; ils diminuaient en même temps que la concentration de l'électrolyte de base. Ce comportement peut être expliqué par les différentes méthodes relatives aux rapports de répartition des anions dans l'eau, et par la présence d'anions aux alentours des surfaces chargées négativement (exclusion anionique). Dans cette étude, aucune comparaison entre les divers modèles proposés dans la littérature n'a été effectuée.

La retardation des espèces cationiques durant les expériences effectuées avec des argiles compactées correspond largement aux prédictions basées sur les sélectivités des échanges cationiques, obtenues à partir de mesures dans des suspensions diluées. Aucune observation n'a pu étayer l'hypothèse d'une accessibilité réduite des sites de sorption dans les échantillons d'argile compactée. Au contraire, il semble bien que la totalité de la capacité d'échange cationique soit disponible pour les réactions d'échange. Toutefois, des incohérences significatives dans les coefficients de distribution de sorption ont pu être observés dans le cas de Cs^+, avec une tendance à l'augmentation de la sélectivité du Cs avec l'augmentation de la densité d'argile. Dans de précédents travaux liés à l'étude des bentonites, il a déjà été postulé que ce phénomène pourrait être expliqué par les différentes propriétés d'hydratation de ce cation alcalin, comparé à Na^+. Dans la présente étude, les corrélations observées pour la Na-montmorillonite mono-ionique sont identiques à celles observées pour les bentonites, aussi bien dans la phase transitive des expériences de diffusion que dans les expériences de sorption utilisant des argiles compactées. Pour Sr^{2+}, une légère baisse de la sélectivité en rapport avec l'augmentation de la densité de l'argile a été observée dans les expériences avec la Na-montmorillonite compactée. En considérant que la sphère d'hydratation de Sr^{2+} est plus grande que celle de Na^+, cette observation est donc en accord avec le comportement du Cs^+, pour lequel l'hydratation fournit moins d'énergie que pour Na^+.

Cette étude montre clairement que la migration des radionucléides chargés dans les milieux argileux chargés doit être mise en relation avec les conditions chimiques particulières de la solution d'équilibre. Il a été mis en évidence que le modèle simplifié de diffusion poreux, dépourvu d'une composante de diffusion de surface, n'est pas capable de reproduire les observations. Pour une application dans le cadre des analyses de sûreté, on propose ici un modèle simplifié, basé sur le schéma de "Gimmi – Kosakowski", qui relie les coefficients de diffusion effectifs aux valeurs de distribution de sorption et à une loi d'Archie étendue pour prendre en compte les effets géométriques. De telles applications sont toutefois restreintes aux familles de cations étudiées dans ce travail (cations alcalins et alcalino-terreux). On a par ailleurs montré dans notre laboratoire que la diffusion de surface joue aussi un rôle fondamental dans la diffusion des éléments de transition. Toutefois, dans de tels cas, seule une partie des espèces de surface est mobile et doit être prise en compte pour l'estimation des coefficients de diffusion effectifs.

Table of Contents

List of Tables

List of Figures

List of Symbols and Abbreviations used in the present Report

The following list comprises those abbreviations and symbols only which are used repeatedly in the present report. All other definitions are given in the text.

Abbreviation	Meaning
BPW	Synthetic bentonite pore water
CEC	Cation exchange capacity
dsb	Downstream boundary
FFDC	Flushed-filter diffusion cell
HPAEC / HPCEC	High performance anion / cation exchange chromatography
mom	Montmorillonite
SFDC	Static-filter diffusion cell
usb	Upstream boundary
Symbol	**Meaning** [1]
α	Rock capacity factor [–]
a	Activity [–]
c	Volumetric concentration [$n\,l^{-3}$]
C_{usb}	Volumetric concentration [$n\,l^{-3}$] at the upstream boundary
C_{tot_clay}	Volumetric concentration [$n\,l^{-3}$] in the clay (per total volume)
D_a	Apparent diffusion coefficient [$l^2\,t^{-1}$]
D_e	Effective diffusion coefficient [$l^2\,t^{-1}$]
D_{erw}	Normalised effective diffusion coefficient [–], see Gimmi & Kosakowski (2011)
D_f	Effective diffusion coefficient for confining filters [$l^2\,t^{-1}$]
D_p	Pore diffusion coefficient [$l^2\,t^{-1}$]
D_w	Diffusion coefficient in bulk aqueous phase [$l^2\,t^{-1}$]
∇c	Concentration gradient [$n\,l^{-4}$]
δ	Constrictivity [–]
ε	Porosity [–]
J	Flux [$n\,l^{-2}\,t^{-1}$], general and specifically measured in through-diffusion
J'	Flux [$n\,l^{-2}\,t^{-1}$], measured in out-diffusion
J_{dsb}	Flux [$n\,l^{-2}\,t^{-1}$], measured at the downstream boundary
f_w	Conversion factor for volumetric units
f_j^i	Counting efficiency for the measurement of isotope j in window i
κ	Sorption distribution capacity [–], see Gimmi & Kosakowski (2011)
K_c	Selectivity coefficient [units depending on stoichiometry]
K_p	Phase distribution coefficient [–]
μ_s	Relative surface mobility [–], see Gimmi & Kosakowski (2011)
ρ_{bd}	Bulk-dry density [$m\,l^{-3}$]
ρ_{mm}	Partial montmorillonite density in bentonite [$m\,l^{-3}$]
ρ_s	Solid density [$m\,l^{-3}$]
R_d	Sorption distribution coefficient [$m\,l^{-3}$]
τ^2	Tortuosity squared [–]

[1]   Base physical quantities are given in brackets (*l*: length, *m*: mass, *t*: time, *n*: amount of substance).

1   Introduction

1.1   Scope and aims of the report

In compacted smectite clays, such as bentonites, the hydraulic conductivity is extremely low which means that aqueous species are transported predominantly by molecular diffusion. The diffusive mass transfer of cationic species is retarded by sorption on the surface of the negatively charged clay particles. Owing to such unique properties (swelling, favourable retardation of many ionic aqueous species), bentonites are considered as ideal buffer and backfill materials in high-level radioactive waste repositories world-wide. After decades of research, the detailed processes behind the diffusive mass transport of charged species in charged compacted clays are still a subject of controversy in the literature (Bourg et al. 2003, Conca et al. 1993, Miller & Wang 2012). A process-based understanding implies that effective diffusion coefficients for the diffusion in compacted bentonites can be derived from diffusion coefficients in bulk water, which are well known for most elements. Before discussing the various difficulties behind such a procedure, a closer look has to be taken at the definition of the effective diffusion coefficient (D_e, m^2 s^{-1}). According to Fick's first law (Eq. 1.1), D_e is defined as a proportionality factor relating the diffusive flux (J, mol m^{-2} s^{-1}) to its driving force, for which the concentration gradient (∇c, mol m^{-4}) in the aqueous phase is usually assumed to be the relevant quantity:

$$J = -D_e \nabla c \tag{1.1}$$

Eq. (1.1) implicitly assumes that other driving forces such as temperature gradients, gradients in electrical potential, etc. are absent.

According to the classical pore diffusion model (Boving & Grathwohl 2001, van Brakel & Heertjes 1974), D_e is related to the diffusion coefficient in bulk water (D_w, m^2 s^{-1}) by:

$$D_e = \varepsilon \frac{\delta}{\tau^2} D_w \tag{1.2}$$

where ε is the accessible porosity, δ the constrictivity and τ^2 the tortuosity squared, all three quantities being geometric properties of the porous medium. While ε is a directly measurable quantity for many diffusing species, δ and τ^2 can only be derived as a lumped factor from experimental data using Eq. (1.2).

For the evaluation of D_e values of an unknown species it appears straightforward to measure δ/τ^2 for an appropriate selection of reference species and derive the unknown D_e of the species under consideration from its D_w value. However, each of these steps involves not only open questions of applicability, such as whether the factors ε and δ/τ^2 are universally applicable to all species. Also, the validity of Eq. (1.1) should not be taken indiscriminately. For the diffusion along uncharged pore surfaces the classical pore diffusion model appears to be applicable (Aldaba et al. 2014). In the case of the diffusive transport of charged species in charged porous media the limitations of this model are rather obvious. We showed recently that the species concentration in the aqueous phase may play only a subordinate role as the driving force for the diffusion of ^{22}Na$^+$ in clay minerals (Glaus et al. 2013). Instead the gradients in total amount of tracer sorbed to the clay determined the direction and the magnitude of the diffusive flux. Similar conclusions were also drawn recently for the diffusion of representatives of the transition metal series in charged clay minerals (Glaus et al. 2015a).

The generic aim of our activities related to the diffusion of radionuclides in argillaceous porous media is to identify the particular circumstances for the applicability of Eq. (1.2) and propose alternative formalisms for those cases in which it is not applicable. From these activities selected results were or are being published (Glaus et al. 2015a and b, Glaus et al. 2007, Glaus et al. 2013, Glaus et al. 2010, Van Loon et al. 2007, Yaroshchuk et al. 2007). Summarising these publications, the following main statements regarding the diffusive transport of charged species in charged clays can be put forward:

- The transport of cations in charged argillaceous porous media can be properly described using Fickian diffusion, provided that the contribution of mobile surface species is adequately taken into account for the calculation of the relevant concentration gradients.

- The transport of anions in charged argillaceous porous media can be properly described using Fickian diffusion, provided that the depletion of anionic species from the charged porosity is adequately taken into account for the calculation of the relevant concentration gradients.

Without discussing in more detail these statements – the reader is referred to the introductory sections in those works, to the relevant chapters in a state-of-the-art report (Jakob et al. *in prep.*) and to the Discussion section in the present report (*cf.* section 6) – one may note that their validity was corroborated so far in those works for the diffusion in compacted montmorillonite and illite of cations binding by cation exchange and, to some reduced degree, for the diffusion of bi-valent transition metals and of simple anions such as choride.

One of the main purposes of the present report is to summarise existing complementary experimental material relevant in the context of the mentioned statements and to test the entire data for internal consistency. The discussion of these data aims rather at their integration into the existing theories and hypotheses than at developing new theories.

A second aim of the work is to compare the sorption properties derived from the diffusion experiments using highly compacted clay samples with the sorption measurements performed in dilute dispersed systems. Sorption distribution ratios (R_d, m^3 kg^{-1}) are derived from the rock capacity factor (α, –) using the following relation:

$$\alpha = \varepsilon + R_d \rho_{bd}$$

(1.3)

where ε (–) is the total porosity and ρ_{bd} (kg m^{-3}) the bulk-dry density of the clay sample. Several reasons have been mentioned repeatedly in the open literature explaining potential discrepancies between sorption measurements on compacted and disperse systems. One of these reasons, rather related to clay rocks than clay minerals, is the accessibility of sorption sites, which may be reduced in compacted samples. Other reasons may be found in the changes of thermodynamic equilibria in the nanopores of the clay. It is well known that water near clay surfaces has different structural and dynamic properties than bulk water (Churakov & Gimmi 2011, González Sánchez et al. 2008b). If this surface water is present in predominant amounts, the impact on chemical equilibria such as protonation, complexation and formation of surface complexes is an open issue. No formal treatment is available from the open literature, which would allow for such effects to be taken quantitatively into account in speciation calculations. Other effects caused by the altered water activity may be seen in the hydration of cations. An example is the change in the selectivity for the exchange of Na^+ for Cs^+ in compacted bentonites under different conditions of clay compaction. It has been demonstrated experimentally that this selectivity increases with increasing bulk-dry density of bentonite (Van Loon & Glaus 2008). This has been interpreted as the result of the different hydration enthalpies of these two cations.

The present work, which focuses on experiments with montmorillonite and bentonite, is part of a broader project carried out at the Laboratory for Waste Management comprising experiments with other clay minerals, viz. illite and kaolinite. The intrinsic chemical and structural differences (e.g. cation exchange and hydration properties) between these clay minerals lead to different diffusive behaviour of charged radiotracers. Such differences help to identify the driving forces and diffusion paths in the different clay minerals. For simplicity the results obtained with kaolinite and illite are not discussed in the present report. They were published elsewhere (Aldaba et al. 2017, Glaus et al. 2007, Glaus et al. 2010, González Sánchez et al. 2008b). Two other publications (Glaus et al. 2015a and b) summarise the results obtained for the diffusion of more strongly sorbing cationic radiotracers carried out in the framework of the Euratom 7th Framework Catclay project. While the focus of that project was on the diffusion of transition metal cations in compacted illite, the scope of the present work, regarding cationic species, is restricted to cations interacting with negatively charged clay surfaces by a cation exchange mechanism.

In the course of our activities to measure the diffusion of charged species in smectite clays we realised step by step that the available experimental techniques suffered from a series of inadequacies relevant for the particular circumstances met in our experiments. For this reason, we continuously aimed at an optimisation of the methods applied and mathematical procedures for the evaluation of the results (Glaus et al. 2011). Because the present report summarises experiments from completely different stages of this research period, the reader may spot some methodic differences. It would not be an impossible task to completely homogenise the material by a re-iteration of the execution and evaluation of the experiments. The benefit would, however, not justify the immense effort in terms of additional experiments and computation time. The nuances gained thereby are of rather insignificant nature with regards to the main conclusions drawn. Otherwise such negligence would be less tolerable.

The scope of experimental systems tested here includes cationic radionuclides, such as ^{22}Na$^+$, ^{85}Sr^{2+}, ^{134}Cs$^+$ and anionic species such as ^{36}Cl$^-$, ^{35}SO$_4^{2-}$ and ^{75}SeO$_4^{2-}$. Most of these experiments were accompanied by diffusion measurements of an uncharged water tracer (HTO) as a reference. The diffusion of the test ions was investigated for montmorillonite and bentonite compacted to bulk-dry densities between 1300 and 1900 kg m^{-3}. This range covers the target bulk-dry density of a bentonite backfill or buffer foreseen in the design of a deep geological repository for high-level radioactive waste (Nagra 2002). The effect of phase distribution of the species on mass transfer rates (more information on the motivation for this issue will be given in the following paragraph and in section 1.2) was mainly accomplished by a variation of the concentration of the background electrolyte (NaClO$_4$) in the case of the experiments with montmorillonite. In the case of the experiments with bentonite, equilibrium pore waters were used to change the chemical composition of the bentonite as less as possible. The use of an electrolyte present at different concentrations would lead to a re-equilibration of the cations in the cation exchange sites.

The use of cationic radionuclides at trace concentrations compared to other constituents of the aqueous phase has conceptual implications. Its transport is not only governed by the own concentration gradient, but also by those of other species required to fulfil the conditions of electroneutrality. In case of diffusion in an argillaceous medium exhibiting cation exchange properties, these species can either be anions migrating together with the cations or other cations migrating in the counter-direction (Malusis et al. 2012). For the present case of smectite clay minerals the diffusive rates of trace anions and cations differ strongly under most of conditions with much lower rates for anions (Glaus et al. 2010). It can thus be reasonably assumed that the transport of trace cations is mostly accompanied by counter-diffusion of other cations in the clay. While these are Na$^+$ ions in the case of Na-montmorillonite, they may be Na$^+$, Ca^{2+} or Mg^{2+} in the case of bentonite. These circumstances may lead to intrinsic differences between montmorillonite and bentonite. For the experiments with radionuclides used at trace levels, an identification of the

coupling to other ions is impossible owing to the limitations of analytical accuracy. This question remains thus open in the frame of the present work. Note that a simple variation of the type of exchange cations on the clay surface cannot give direct information on the coupling effects, because such variations also cause differences in the geometric properties of the diffusion paths fundamentally changing the diffusive behaviour of all species.

1.2 Summary of the transport of charged species in charged argillaceous media focussing on smectite clay minerals

The following outline of the diffusive transport of charged species in charged argillaceous media is far from being comprehensive. It lacks a detailed description of the structural properties of the layered clay structure and the presence of isomorphic substitutions leading to the presence of fixed charges. All these properties are important key features determining the hydration and transport properties of a specific clay mineral. Valuable information can be found in books (Bergaya et al. 2006) or in relevant review articles (Altmann et al. 2012, Miller et al. 2010, Shackelford & Moore 2013). The literature cited in the present report is limited to approximately elder than 2015. Further, the following paragraphs are rather related to smectite clay minerals, such as montmorillonite.

According to Eq. (1.2) D_e values depend on the geometric properties of the porous medium and on the molecular properties of the diffusant in bulk water. One would thus expect that the diffusive fluxes of a sequence of different species in a given porous medium only depend on their D_w values. For the comparison of two different species (characterised in the following by the superscripts $'$ and ^{0}), a proportionality between the tracer fluxes and the diffusion coefficients in bulk water holds for a given tracer concentration gradient:

$$\frac{J'}{J^0} = \frac{D_w'}{D_w^0} \tag{1.4}$$

This simple relationship is not fulfilled in the comparison of the diffusion of charged with uncharged species in charged clay minerals (Glaus et al. 2010, Jensen & Radke 1988, Molera & Eriksen 2002, Muurinen et al. 1986, van Schaik et al. 1966) and clay rocks containing charged clay minerals (Appelo et al. 2010, Gimmi et al. 2014, Melkior et al. 2007).

The reason for such a discrepancy is not *a priori* clear. An obvious explanation can be found in inadequate assumptions regarding the geometric parameters. As an example, it may be the case that the diffusion paths for two different species in the narrow pore network are not the same. Consequently, the constrictivity or the tortuosity factors would not be equal. Inappropriate assumptions regarding the relevant tracer concentration gradients can be viewed as another explanation. The classical pore diffusion model assumes that the pore fluid has similar physico-chemical properties as bulk water and that concentration continuity exists at the interface between the external bulk water and the clay pore water. This assumption may be incorrect for the narrow pores of compacted clays on nanometre scales. The energetic state of most water and solutes may be influenced by different types of chemical interactions with the huge area of clay surfaces, such as Van der Waal's or dipole-dipole interactions (e.g. hydrogen bridges). This may lead to a discontinuity of the species activity at the interface between external bulk water and the clay.

In the absence of an exact knowledge of the chemical processes leading to such discontinuities, they can simply be described using a phase distribution coefficient (K_p), comparable to an octanol-water distribution coefficient, for example:

$$K_p = \frac{a_{cpw}}{a_{bw}}$$

(1.5)

a_{cpw} is the species activity in the clay phase and a_{bw} the activity in the solution phase (viz. the external bulk water). Such a phase equilibrium does not specify the chemical form of the species in the clay. It may be bound to the surface, or it may be present as a hydrated species in water attributable to the clay phase.

An equilibration according to Eq. (1.5) is feasible for all types of chemical species from a fundamental point of contemplation. It is particularly relevant for charged species. For negatively charged clays (such as smectites), an enrichment of positively charged solution species and a depletion of negatively charged species in the clay can be expected based on electrostatic interactions. If tracer diffusion across a porous clay sample sandwiched between two solutions only differing in the tracer concentration is regarded, the K_p values at both interfaces between clay and external solution are identical. Fig. 1.1 depicts such a situation for a dynamic distribution of a cationic species between clay and solution in a steady-state phase situation, in which the tracer fluxes in all locations of the clay sample are identical. The relevant activity (or concentration) difference for tracer diffusion in the clay, Δa_{cpw} is given as:

$$\Delta a_{cpw} = K_p \Delta a_{bw}$$

(1.6)

The activity difference based on a_{cpw} is larger than the respective difference for a_{bw} because K_p in this example is larger than 1. Assuming that the tracer in the clay phase is mobile, the respective tracer fluxes for the cationic species will be larger than for a species with $K_p = 1$. An important prerequisite for the validity of Eq. (1.6) is that the equilibration of the phase distribution equilibrium is much faster than the diffusive process.
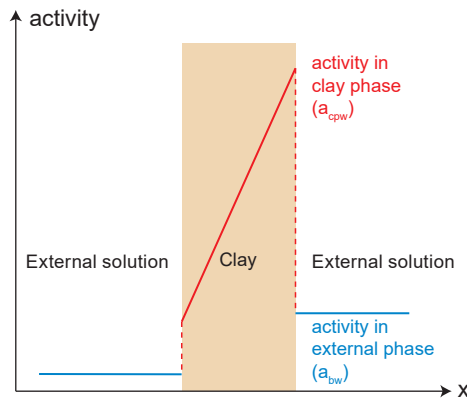
Fig. 1.1: Schematic representation of tracer discontinuities for a phase distribution equilibrium of a cationic species ($K_p > 1$) between the external solution and the clay phase.

The same situation is shown in Fig. 1.2 for the distribution of an anionic species, for which K_p is typically less than one owing to the electrostatic repelling of anions from the negatively charged clay surface. This effect is frequently denoted to as anion exclusion in the literature. The expected tracer fluxes of anionic species are thus lower than for a species with $K_p = 1$.
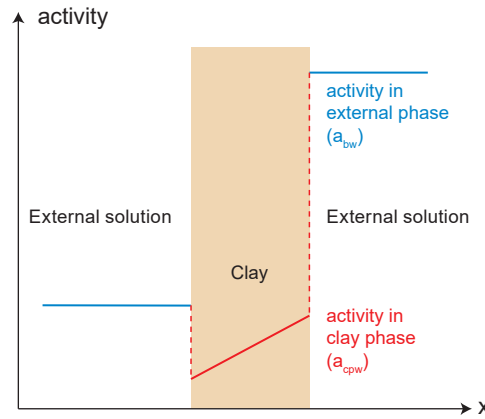
Fig. 1.2:   Schematic representation of tracer activities for a phase distribution equilibrium of anionic species ($K_p < 1$) between external solution and clay pore solution.

D_e values are traditionally rather related to tracer concentration gradients in the external aqueous phase. In such cases the definition of D_e may be extended in Fick's first law according to:

$$J = -D_e^{int}\nabla a_{cpw} = -D_e^{int}\nabla a_{bw}K_p = -D_e\nabla a_{bw} \tag{1.7}$$

where D_e^{int} is an ("intrinsic") effective diffusion coefficient for the diffusion of tracer species in the clay phase and D_e the effective diffusion coefficient for the diffusion of tracer species in the external aqueous phase. These diffusion coefficients are thus related by:

$$D_e = D_e^{int}K_p \tag{1.8}$$

This definition of an effective diffusion coefficient comprises thus not only the dynamic molecular properties of the tracer species together with the geometric properties of the clay pores, but also the chemical equilibration of the species activities between the clay and the aqueous phase. It is out of doubt that this definition entails various difficulties in the application for transport calculation. As an example, such D_e values may be time- and space-dependent quantities, which does not make sense from physical intuition.

In order to avoid such obscurities, Birgersson & Karnland (2009) used "intrinsic diffusion coefficients" combined with activity discontinuities at the clay-solution interfaces for the description of the diffusion of Na$^+$ and Cl$^-$ in smectites. They assumed the entire pore space to be built from a single type of pore water, viz. the interlayer water in montmorillonite[1]. While they used cation exchange to describe the enrichment of Na$^+$ in the clay phase, a Donnan equilibrium distribution was applied to take into account for the depleting of anions from the clay phase. The authors were able to model a variety of literature data for Na$^+$ (Glaus et al. 2007) and Cl$^-$ (Van Loon et al. 2007) using a consistent ion equilibrium condition for both cations and anions.

Glaus et al. (2007) used ion selectivity coefficients for the calculation of D_e values defined according to Eq. (1.8) for primary data evaluation. These D_e values were thus dependent on the chemical parameters influencing the phase distribution of the tracer ion, such as the concentration

---

[1]   The Swedish authors themselves term their approach frequently as the "interlayer-approach". While further experiments from the present authorship has demonstrated that such a model may also be applicable to clays in which the interlayers are not accessible, such as in compacted illites, this terminology may become obsolete. "Local-gradient approach" may possibly be more meaningful than "interlayer-approach".

of the background electrolyte concentration. The authors renormalised their D_e values for the respective sorption distribution coefficients for cation exchange as a second step, also ending with an "intrinsic" coefficient for the diffusion of $^{22}Na^+$ and $^{85}Sr^{2+}$ in the interlayer (a so-called D_{IL} value). Both approaches are thus fully equivalent if correctly applied. The "intrinsic" diffusion coefficients for cations are independent of the chemical composition of the external medium and do not exceed the values of an uncharged HTO tracer.

A validation of the "interlayer approach" for a rather broad variety of experimental conditions has been demonstrated recently in a concerted investigation from the Swedish and the PSI-LES research group (Glaus et al. 2013). In contrast to the traditional diffusion setup depicted in Fig. 1.1 and 1.2, diffusion was started with equal tracer concentrations, but different concentration of the background electrolyte on both sides of the clay sample. According to the principles of isotopic dilution, the solution concentration of the radioactive isotope will be lower in the low salt-concentration reservoir upon equilibration compared to the reservoir with high salt concentration. The opposite holds for the amount of the radioactive isotope in the clay phase: The concentration of the radioactive $^{22}Na^+$ isotope is larger in the clay phase near the solution with lower salt concentration. Fig. 1.3 shows schematically the concentration distribution of the stable $^{23}Na^+$ isotope and the radioactive $^{22}Na^+$ isotope for a steady-state flux situation in a homoionic Na-montmorillonite. The almost exclusive presence of $^{23}Na^+$ in the planar cation exchange sites leads to a large and evenly distributed concentration of the stable isotope in the clay, which does not depend on time and its concentration in solution. In contrast the distribution of the radioactive $^{22}Na^+$ isotope in the clay is determined by the evolution with time of the concentration (or activity) of $^{22}Na^+$ in the solution phase.
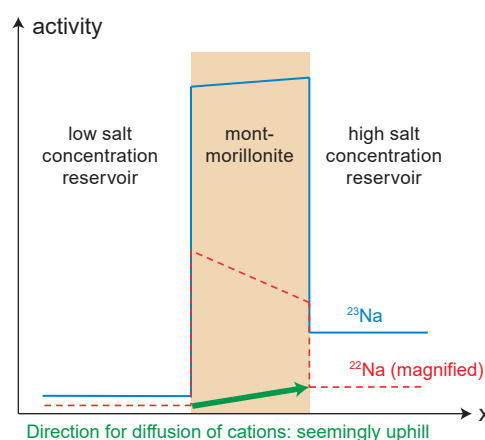
Fig. 1.3:   Schematic representation of tracer activities (concentrations) for a phase distribution equilibrium between external solution and clay phase in the "uphill" diffusion experiment, in which different concentrations of the background electrolyte were applied to both sides of the clay sample.

The flux of the $^{22}Na^+$ isotope observed in the "uphill experiment" was directed towards the high salt concentration reservoir (*cf.* the green arrow). The direction of the flux (directed towards higher concentration) occurs "uphill" only from the perspective of the differences in the aqueous phase concentrations. From the perspective of the differences of the concentration in the clay phase, the flux is "downhill" and thus in agreement with Fickian diffusion. The experiments demonstrated thus that the concentration (or activity) gradient in the clay phase is actually the driving force for diffusion under the conditions of these experiments and not the concentration gradient in the external bulk aqueous phase.

For a valuable prediction of tracer fluxes across compacted clay minerals, the tracer concentration gradient in the clay phase has to be combined with appropriate molecular diffusion coefficients. These diffusion coefficients can be viewed as analogues of D_w values relevant for diffusion in the clay phase. Experimental information is available merely for the water molecule only, using e.g. quasi-elastic neutron scattering techniques (González Sánchez et al. 2008a, Malikova et al. 2010). It was shown in these works that the molecular diffusion coefficients in the clay pore water of compacted montmorillonite were lower by a factor between 2 or 3 compared to the respective D_w values. Almost no such information is available for other species, with the exception of a recent publication in which a combined approach using impedance spectroscopy and water adsorption measurements was applied for the determination of molecular diffusion coefficients of cationic species in the interlayer of MX-80 bentonite (Salles et al. 2015). In view of the different types of displacements occurring at molecular scales in the diffusion of different species, it is clear that the same factor cannot be applied to all kind of diffusing species. It has been shown by atomistic simulations that the ratio of the molecular diffusion coefficients of Na^+ and Cs^+ in montmorillonite may differ depending on the degree of hydration of the clay phase (Kosakowski et al. 2008).

The complexity of the model approaches depicted so far may additionally be increased by the assumption of different pore types exhibiting different properties with respect to diffusion and uptake properties. Conflicting information from the literature regarding the thickness of hydrated interlayer pores in montmorillonite lead to different distributions of pore types with potentially different properties regarding the physicochemical state of the pore water (Holmboe et al. 2012, Kozaki et al. 1998, Norrish 1954). Bourg et al. (2003) proposed a diffusion model (the "macro/nanopore model") for bentonite comprising parallel fluxes across porosities with interlayer and free pore water properties. They (Bourg et al. 2006) modelled literature data for the diffusion of tritiated water using a porosity distribution based on the X-ray diffraction data of Kozaki et al. (1998). Similarly, the model was applied to literature data for the diffusion of Na^+ in bentonites (Bourg et al. 2007) favouring the macro/nanopore approach. The discrimination from a surface diffusion approach was, however, not so clear with respect to the uncertainties of the experimental data. The validity of a parallel flux approach for cation diffusion has also been demonstrated for a broad variety of soils, clays and clay rocks through a normalisation analysis of relevant literature data (Gimmi & Kosakowski 2011). This approach will be discussed in more detail in section 6.1. Furthermore, such models are readily applicable for the diffusion of anions. Commonly it is assumed that a smaller fraction of the clay porosity exhibits almost bulk water properties in which anions can diffuse without electrostatic restrictions. Depending on the model, anions may be completely excluded from other porosities like the interlayer porosity, or their activity may be strongly decreased according to the principle of Donnan exclusion of anions. Further their concentration may also be reduced near the charged particle surfaces. Depending on the structural properties of the clays, the electropotential at such surfaces may be different than in the interlayers, where an overlapping of the negative potential is commonly assumed. It is still an open question, which of these basic approaches is best.

Different model concepts may also be applied for the interaction between positively charged solutes and the negatively charged clay surface. Although these issues are not directly related to the molecular diffusion process, they will affect the overall mass transport in clay because the species distribution between different aqueous phase types influences the relevant concentration gradients. An average Donnan equilibrium distribution has been frequently applied for such purposes (Birgersson & Karnland 2009, Jougnot et al. 2009, Tournassat & Appelo 2011) owing to its simple parameterisation. Similarly, can be stated for the description of cation exchange processes using a selectivity approach (Glaus et al. 2007). Whether it is necessary to use a more realistic description of the spatial cation concentration distribution near the charged clay surfaces, such as implemented in a Poisson-Boltzmann approach (Hedstrom & Karnland 2012, Ochs et al. 2001, Tachi & Yotsuji 2014) is not clear from a pragmatic point of view.

Summarising it may be stated that the experimental data available from the literature is not fully suited for a clear discrimination of the various feasible model approaches. The parameter variations (e.g. type of radionuclide, chemical conditions in the equilibrium aqueous phase, type of charge-compensating cations, etc.) are not systematic enough for an unequivocal interpretation. The reason may partly be found in diverging experimental strategies among the various research groups. Also important is the general underestimation of the limits of the validity of the experimental techniques. It is extremely important to undertake appropriate efforts to extend these limits (Glaus et al. 2015b, Glaus et al. 2011, Glaus et al. 2008). It may also be stated that a variety of interpretations applied in earlier years to experimental data were based on secondary evidences such as apparent diffusion coefficients calculated from sorption distribution coefficients obtained from disperse clay suspensions, or virtual tracer fluxes of unknown species in free pore water directly derived from diffusion coefficients for water tracers. Owing to the inappropriate character of such assumptions, conflicting conclusions were drawn for certain parameter variations, such as the variation of clay compaction. This has typically lead to ambiguities e.g. regarding the validity of the surface diffusion approach in the earlier literature (Conca et al. 1993). In recent years the validity of this concept has been demonstrated for a variety of conditions (clay compaction, salinity of the external solution) not only for cations from the alkaline and earth-alkaline series (Glaus et al. 2007, Glaus et al. 2013, Jensen & Radke 1988), but also for representatives of the transition elements (Glaus et al. 2015a).

It does not require advanced capabilities in foreseeing the future to say that different models for the description of the diffusion of charged species in charged argillaceous media will exist in parallel with similar justification. The single pore approach may be rather suited for application in densely compacted clay minerals. Its limits for application for cation diffusion in compacted Na-montmorillonite has recently been shown for rather low compactions of ~ 1000 kg m^{-3} (Bestel et al. *in prep.*). A parallel flux model including an aqueous phase exhibiting bulk water properties will probably be more suited for application in clay rock owing to the larger pore sizes in these media. Its applicability to a broad series of radionuclides has been demonstrated for a unique set of fitting parameters (Appelo et al. 2010). Obviously, such models can be readily converted to a single-porosity model by making one of the flux contributions negligible, while the opposite direction is less feasible.

1.3   Report structure

Based on the, rather unusual scope of the report (a "late emergence" of unpublished material – aged up to 10 years and related to material published over a time period of ~ 5 years) the structure had to be adapted in several respects in order to present the main lines in a coherent context without breaking it by possibly important, but rather subordinate observations and discussions. The close linkage between existing literature and the experiments described here is the main reason for the apparently excessive citing of own publications in the present report and shall in no way be interpreted as a narcissistic attitude of the authors. The most important features of the present report can be characterised as follows.

The results chapter summarises in tabular form the scope and the most important experimental conditions of the diffusion tests and provides the best fit parameter values (typically the effective diffusion coefficients (D_e), rock capacity factors (α) and, partly, the derived sorption distribution ratios (R_d) in the same tables). All experimental data, if not immediately significant for the discussion, are shown graphically in Appendix sections. As described in more detail in sections 2.4 and 2.5, the best-fit parameter values were obtained by numerical fitting. The comparison between the experimental data with the fits to the data including ranges of uncertainty of the best-fit parameter values are also shown in the plots of the Appendix sections. Experiment-specific information regarding procedures applied in the execution and evaluation are given as key words in the

footnote of the results tables. Only the very generic aspects of these issues are described in a separate method chapter. Consequently, the full information on experimental procedures and procedures applied in the data evaluation is distributed over different chapters.

Similarly, the data evaluation is distributed over two chapters because it has to be carried out on two different levels. The first level of data evaluation is the fitting procedure, by which the best-fit parameter values are obtained. The basis for this fitting is given by Fick's first and second law; it is therefore a mainly mathematical issue. The second level of data evaluation is the integration of the best-fit parameter values in existing diffusion models. This is a more open issue which is not only based on diffusion models, but also takes into account the specific aspects given by the clay, such as pore structure and the impact of the surface charges in the clays. The evaluation of the data is thus not a purely mathematical topic, but also influenced by mineralogical, chemical and physicochemical aspects.

The experimental test systems are subdivided in two main chapters referring to experiments with montmorillonite (Chapter 3) and bentonite (Chapter 4). Experiments with the former clay mineral are mostly focused on bulk-dry densities 1300 and 1600 kg m^{-3}, while most of the results obtained for 1900 kg m^{-3} were already published in the mentioned journal articles (*cf.* section 1.1). The various experiments at the lower bulk-dry densities are primarily subdivided according the various radionuclides tested, but also to groups of different concentrations of the background electrolyte. The reason for this subdivision can be seen in the different experimental procedures applied for different electrolyte concentration ranges, which was necessary for obtaining optimal results. As outlined above such variations were less frequently applied in the case of the experiments with bentonite. The preservation of the original distribution of the various cations on the bentonite surface was the main motivation for using equilibrium pore waters in that case. For this reason, the subsections of the bentonite chapter are purely structured according to the various radionuclides. An additional chapter (Chapter 5) summarises accessory information (other than from diffusion experiments) relevant for the interpretation of the diffusion data. Chapter 6 is a synthesis of the results given in this report and our previous articles in the open literature. Besides the overall discussion of the results obtained for the diffusion of cationic and anionic species in view of existing models for diffusion near the surfaces of charged clays, it also provides a tentative procedure of their application in the safety assessment of argillaceous materials used as natural or technical barriers to prevent the migration of radionuclides from a deep-geological repository for radioactive waste to the biosphere.

2   Materials and Methods

Most of the techniques applied have been published in the open literature (Glaus et al. 2007, Glaus et al. 2010, Shackelford 1991, Van Loon & Jakob 2005, Van Loon et al. 2003a). The following sections briefly summarise the most important aspects. The use of diffusion cells with advectively flushed filters has been described recently (Glaus et al. 2015b). In contrast to traditional diffusion cells, where the liquid in the porous filters is stagnant, no concentration gradients (or only small gradients caused by inhomogeneities in the flow field) are established in the advectively flushed filters. This helps to reduce the overall uncertainties in the results owing to uncertainties stemming from the filter properties (Glaus et al. 2008). More details are provided in section 2.2. Also, the conceptual issues for data evaluation and the estimation of experimental uncertainties are based on existing literature work (Van Loon & Soler 2003).

2.1   Reagents, samples and analytical procedures

High purity reagents were obtained from Fluka (Buchs, Switzerland) or Merck (Dietikon, Switzerland). De-ionised water was used throughout (Milli-Q® water) for the preparation of the solutions. Radioisotopically pure HTO, ^{22}Na$^+$, ^{85}Sr^{2+}, ^{134}Cs$^+$, ^{36}Cl$^-$, ^{35}SO$_4^{2-}$ and ^{75}SeO$_3^{2-}$ were obtained from Isotope Products Europe (Blaseg, Germany) or Eckert & Ziegler (Valencia, CA, USA). Most of these radioisotope preparations contained defined amounts of the respective stable isotope elements. ^{75}SeO$_3^{2-}$ was converted to ^{75}SeO$_4^{2-}$ by oxidation with NaOCl and subsequently isolated as a pure selenate species by semi-preparative fractionation using high-performance anion chromatography.

The montmorillonite was obtained from Milos (Greece) and used after conditioning to the homo-ionic Na$^+$-form. The procedures for preparation and the mineralogic characterisation of the raw and the conditioned material have been described in Glaus et al. (2010). The structural composition based on elemental analysis is $[Si_4O_{20}(OH)_4]$ $(Al_{1.54}Fe^{III}_{0.05}Fe^{II}_{0.04}Mg_{0.36}Ti_{0.01})$ $(Na_{0.37}K_{0.02})$. Further information can also be found in González Sánchez et al. (2008b), where the same conditioning procedures on the same material were applied.

The bentonite used in this study was Volclay KWK (Südchemie, Germany), which is a commercial successor product of MX-80 having a similar mineral composition, but slightly changed grain size. The smectite fraction in Volclay KWK is ~ 70 %. Further properties can be found in Van Loon et al. (2007). For a comparison of experimental results, note the metal loading being mixed Na$^+$, Ca^{2+}, Mg^{2+} in Volclay KWK, while it is purely Na$^+$ in conditioned montmorillonite.

Radiochemical assays of ^{22}Na$^+$, ^{85}Sr^{2+}, ^{134}Cs$^+$ and ^{75}SeO$_4^{2-}$ were carried out with a γ-counter (Minaxi-γ, Autogamma 5000 series, Canberra-Packard), those of HTO, ^{36}Cl$^-$, and ^{35}SO$_4^{2-}$ by liquid scintillation counting (Tri-carb 2250 CA, Canberra-Packard) using Ultima Gold XR (Canberra-Packard) as the scintillation cocktail at a ratio of 15 cm^3 of cocktail to 5 cm^3 of sample.

2.2   Diffusion experiments

Most of the experiments were carried out at bulk-dry densities between 1300 and 1900 kg m^{-3}. The bulk-dry density is defined as the total mass of solid per total volume of the solid including the volume of porosity. It is related to the solid (or grain) density (ρ_s, kg m^{-3}) and porosity (ε) according to the following relation:

$$\rho_{bd} = \rho_s(1-\varepsilon)$$

(2.1)

The situation is more complicated in the case of bentonite, which is a mixture of montmorillonite and different accessory minerals (mainly quartz and feldspar, *cf.* section 2.1), which are commonly assumed to have no significant porosity. It is therefore useful for some purposes to define a 'partial montmorillonite density' for bentonite (ρ_{mm}, kg m^{-3}). ρ_{mm} characterises the mass of montmorillonite per volume of montmorillonite plus volume of pores and is calculated (Sato & Suzuki 2003) as:

$$\rho_{mm} = \frac{f_{mm}\,\rho_{bd}}{1 - \dfrac{(1-f_{mm})\rho_{bd}}{\rho_{s,acc}}}$$

(2.2)

where f_{mm} is the fractional mass content of montmorillonite in bentonite and $\rho_{s,acc}$ is the solid density of accessory minerals.

The experimental setup uses a peristaltic circulation system in which a solution is continuously transported from a liquid reservoir along the confined cylindrical clay sample and recycled back to the reservoir (Van Loon et al. 2003a). Diffusion occurs perpendicular to the circular cylinder surfaces. Two types of diffusion cells were used, one of these being the classical diffusion cell in which the liquid is pumped alongside the filters (Glaus et al. 2007, Van Loon et al. 2003a) and the other being equipped with a sealing system by which the flow of the liquid is forced to pass through the filters. The filter system of the former diffusion cell is denoted as "stagnant" (cell type abbreviated to *SFDC*), the one of the latter as "flushed" (cell type abbreviated to *FFDC*). Fig. 2.1 shows a schematic layout of the *FFDC*. The clay sample (brown) has cylindrical geometry and is directly compacted in the sample holder (1) using adapters with the same diameter as the clay sample. After compaction the cell is assembled by adding filters (blue), sealing (red) and two end-pieces (2). The arrows indicate the position of the circular channels from which the fluid can enter the filter pores. The liquid is guided from the injection channel to pass through the filter and leave the cell via the extraction channel. The liquid in the filter porosity is homogenised thereby to a large extent, preventing thus the formation of concentration gradients in the filters. Further details were described in Glaus et al. (2015b).
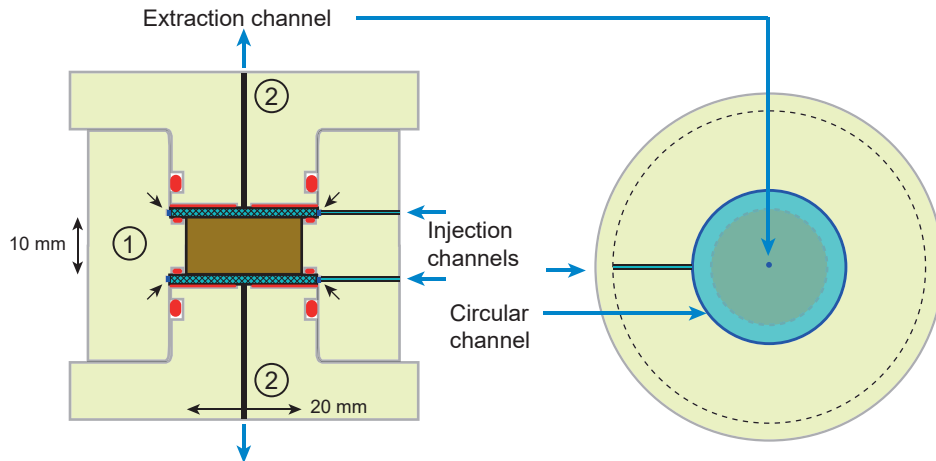
Fig. 2.1:   Side view (left) and top view (right) of a diffusion cell with advectively flushed filters (*FFDC*).

Most of the diffusion experiments were carried out in duplicate. Through-diffusion was carried out only after saturation of the clay with the appropriate electrolyte solution, which lasted at least 4 weeks. For the saturation, one reservoir was connected to one side of the diffusion cell, while the other side was left open to enable displaced air to escape from the cell. After 1 week, a second reservoir was connected to the other side of the cell, and saturation proceeded from both sides. The diffusion was started by exchanging one of the solutions against a fresh solution containing the desired amount of the radioactive tracer ("the upstream reservoir"), while the volume of the other reservoir ("the downstream reservoir") was lowered to a minimum size in order to measure the diffusive transfer of the radiotracer with the highest possible sensitivity. The amount of radiotracer lost from the upstream reservoir to the clay sample and the downstream reservoir was not replenished leading thus to a variable boundary condition at the upstream side. Depending on the dynamics of the evolution of the tracer concentration in both reservoirs, small samples (100 – 200 μdm^3) were taken from the upstream reservoir at regular time intervals in order to measure the evolution of the tracer concentration as a function of time.

The analysis of the water contents in the clay samples performed after diffusion by cutting the clay samples into segments in direction of diffusion, revealed that the bulk-dry density in the clay sample was lower at the boundary zones near the confining filters, throughout all experiments in which compacted samples of montmorillonite or bentonite were used. Details are reported here in section 5.1; the phenomenon has also been described in Glaus et al. (2011). These inhomogeneities persisted and appeared to remain stable along the entire duration of the diffusion experiments. No obvious hydro-mechanical explanation is available from the literature for these inhomogeneities. Simple expansion of the compacted sample by loss of clay particles into the filters can be excluded (*cf.* section 5.2).

The solution in the downstream reservoir was exchanged against a tracer free solution at regular time intervals in order to maintain a low tracer concentration on the average. Note that the solution in the circulation loop and in the filter system of the diffusion cell was not exchanged thereby. The amount of radiotracer remaining from the previous sample was therefore subtracted from the total amount of tracer in the reservoir solution in order to calculate the amount of diffused radiotracer (Van Loon et al. 2003b). Also note that the maximum radiotracer concentration in the downstream reservoir reached high values in single cases, for which the classical assumption of a zero-boundary concentration condition was no longer applicable. This behaviour is inherently associated to the use of many cationic elements under conditions for which the diffusive flux is strongly augmented by surface diffusion effects. As shown recently (Glaus et al. 2015b) different models may be applied for the evaluation of such cases which lead to an appropriate evaluation of best-fit parameter values. These models were also applied in the present work. The assumption of a zero-concentration boundary condition, however, leads to a systematic underestimation of D_e values. Despite the existence of appropriate mathematical models to circumvent such issues, it would have been advisable to choose more elaborate methods to maintain a true zero-concentration downstream boundary for such cases. The so-called draining method (Glaus et al. 2015b), in which the solution at the downstream side is not recycled but drained from the cell with subsequent accumulation of the radiotracer in a trap column, offers a solution to such cases.

As discussed in Glaus et al. (2008) and Glaus et al. (2015b) large tracer fluxes lead to situations where the diffusive properties of the confining filters must be taken into account in the evaluation of best-fit parameter values. In such cases the concentration differences between the up- and the downstream reservoir are not only located on the clay sample, but distributed between filter and clay, or even predominantly located on the filters. Diffusion through the filters is thus the rate determining process for the latter case. Fig. 2.2 shows the steady-state concentration gradients in a clay sample obtained after through-diffusion may differ for various ratios of effective diffusivities of the tracer in the filter and the clays. A quantitative description of these phenomena was given in Glaus et al. (2008).
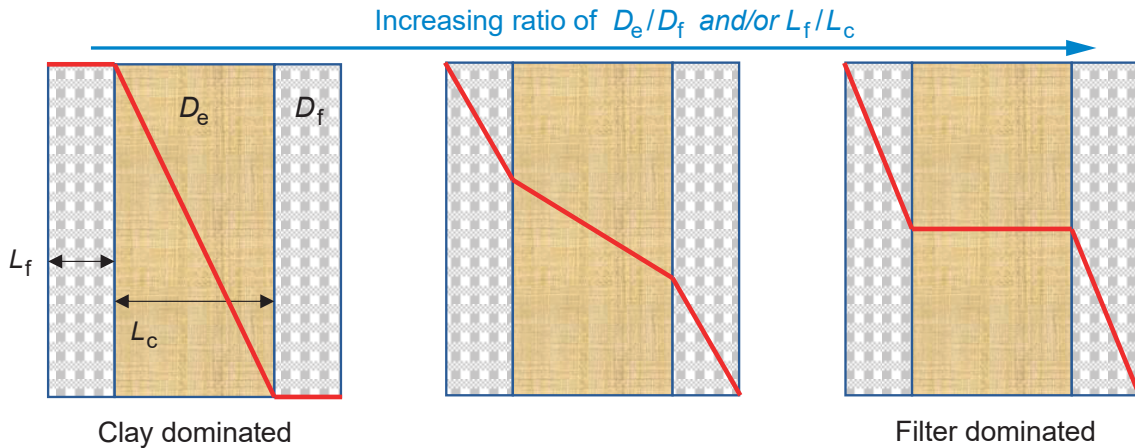
Fig. 2.2:   Schematic representation of the steady-state concentration gradient (red) in the clay sample (ochre) and the confining filters (grey) for different cases regarding the ratio of effective diffusivities and thicknesses of the clay sample and the confining filters.

In all such cases the use of inappropriate values for the diffusion coefficients in the filters may also lead to biased results, whereby the true D_e values are commonly underestimated. It was demonstrated that the diffusive properties of the confining filters change upon exposition to strongly swelling clays leading to generally lower effective diffusion coefficients for the filters compared to the fresh state after production (Glaus et al. 2008). During the time of that publication we favoured the use of experience values gained from independent measurements of filter diffusion coefficients using the filters previously present in the clay diffusion experiments. It turned out, however, that single filters exhibited diffusion properties significantly deviating from such experience values. On the one hand, significant differences regarding the effective diffusivities were noted for different production lots and on the other hand, the clogging of filter pores with clay particles may lead to changes in capacity factors of the filters in the case of sorbing radionuclides.

A viable solution to identify such cases is the evaluation of the filter diffusion properties from the initial decrease of radiotracer concentration in the upstream reservoir. Such a procedure is applicable in situations with moderate or strong sorption of the radiotracer to the clay. In such cases the dominant tracer concentration gradients are almost entirely located on the filters. More details for this procedure can be found in Glaus et al. (2015b). Note that, for such cases, it is crucial to choose an appropriate ratio of the amount of radiotracer in the upstream reservoir compared to the uptake capacity of the clay, which is given by the mass of clay and its cation exchange capacity for the cations investigated in the present context. This choice cannot always be readily taken in advance without knowing the relevant properties of the clay. If the amount of radiotracer in the upstream reservoir is too large, the rate of concentration decrease is not significant enough. If it is too low, almost the entire amount of radiotracer will disappear from the upstream reservoir also leading to situations where the evaluation of the best-fit parameter values may be accompanied by uncertainties, which are insignificant in "normal" situations.

Most of these through-diffusion experiments did not reach a true steady-state flux situation owing to the significant decrease of tracer concentration in the upstream reservoir. However, using appropriate mathematical models, a reliable evaluation of best-fit parameter values from these experiments was also possible.

In most cases through-diffusion was followed by measuring the tracer profile after slicing the clay sample or by out-diffusion. The methods applied follow the description in Glaus et al. (2007) and Van Loon & Jakob (2005), respectively. Both out-diffusion and sample profiling can be viewed as a verification and substantiation of the results obtained in through-diffusion. The results obtained by out-diffusion or from the tracer profiles can be used as a blind prediction test case for the best-fit parameter values obtained from through-diffusion. Further they may reveal additional information on the specific features of a given experimental situation.

In out-diffusion, the initial tracer fluxes at the previous upstream and the previous downstream side differ according to the concentration gradients reached after through-diffusion. The ratio of the initial fluxes at the two sides of a diffusion cell in out-diffusion gives thus direct evidence on the diffusive properties of the confining filters in relation to those of the clay sample. A comparison of the assignment of the diffusive filter properties based on the results of out-diffusion with the method of initial decrease of tracer concentration in the source reservoir in through-diffusion is thus a valuable test for the consistency of the assumptions taken for the confining filters.

Whether the results of through- and out-diffusion (or profile analysis, respectively) are evaluated separately, or whether the two sets of information are pooled together, has to be decided individually. If fundamental differences between the two data sets exist, a separate evaluation is preferable. The separate evaluation of the out-diffusion (or the concentration profile, respectively) may give additional evidence for the underlying processes. If the differences are tolerable, the evaluation of the pooled data has the advantage that the calculated uncertainties better represent the real uncertainties than in a separate evaluation. However, certain discrepancies between the blind predictions and the experimental data can be expected for the initial phase of out-diffusion, in which the tracer distribution in the filters can be disturbed during the early flushing of the tubings with tracer-free solution. Further discrepancies are expected in the last stage of out-diffusion. During that phase of the experiment the assumption of a zero-tracer concentration in the liquid reservoirs may clearly not be justified. A significant bias in the calculated tracer gradients and tracer fluxes may arise. Consequently, such points have been commonly omitted from the evaluation.

2.3 Signal discrimination in multi-tracer experiments

The diffusion of the various radioactive tracers was measured in sequence; each new tracer run was started after the out-diffusion of the previous tracer had been completed. In some experiments, the HTO and ^{36}Cl or HTO and ^{22}Na tracers were monitored simultaneously in a single run.

2.3.1 Combination of γ- and β-emitters

A typical example is the determination of the individual activities of tritium and ^{85}Sr in samples containing the two isotopes. This can be achieved by a γ-measurement and a separate liquid scintillation measurement. The activity of ^{85}Sr can be determined independently from the γ-measurement, because tritium is a pure β-emitter. Knowing the ^{85}Sr activity from the γ-measurement, the activity of tritium can be calculated in the liquid scintillation measurement by subtracting the counting rate of ^{85}Sr according to its calculated activity in the test sample. As these measurements are usually shifted in time, it is necessary to take into account the decay of the ^{85}Sr isotope between the two measurements. The following relations are used for these purposes with the definitions:

N^{γ}: Net counting rate [s^{-1}] of ^{85}Sr in the sample for the γ-measurement

N^{lsc}: Net overall counting rate [s^{-1}] of tritium and ^{85}Sr^{2+} in the sample for liquid scintillation counting

A_j^i :   Activity of isotope j (tritium or ^{85}Sr) in the test sample for measurement i (γ-measurement and liquid scintillation counting, respectively)

f_j^i :   Counting efficiency for the measurement of isotope j (tritium or ^{85}Sr) in the test sample for measurement i (γ-measurement and liquid scintillation counting, respectively)

m^i: Mass of the test samples for measurement i (γ-measurement and liquid scintillation counting, respectively)

t^i: Date and time of the measurement i (γ-measurement and liquid scintillation counting, respectively)

$$N^{\gamma} = A_{Sr}^{\gamma} \cdot f_{Sr}^{\gamma} \tag{2.3}$$

$$N_{tot}^{lsc} = A_{Sr}^{lsc} \cdot f_{Sr}^{lsc} + A_{HTO}^{lsc} \cdot f_{HTO}^{lsc} \tag{2.4}$$

The activity of the ^{85}Sr^{2+} isotope in the liquid scintillation counting sample is calculated from the counting rate in the γ-measurement as follows:

$$A_{Sr}^{lsc} = \frac{N^{\gamma}}{f_{Sr}^{\gamma}} \cdot \frac{m^{lsc}}{m^{\gamma}} \cdot 2^{-\frac{t^{lsc} - t^{\gamma}}{t_{1/2}(Sr)}} \tag{2.5}$$

This quantity is used as a correction term for the calculation of the activity of HTO:

$$A_{HTO}^{lsc} = \frac{N_{tot}^{lsc} - A_{Sr}^{lsc} f_{Sr}^{lsc}}{f_{HTO}^{lsc}} \tag{2.6}$$

The overall uncertainties on the calculated activities are readily obtained from error propagation of the uncertainties resulting from counting statistics.

2.3.2   β/β discrimination

β/β discrimination was applied for example to simultaneously measure the diffusion of HTO and ^{36}Cl$^-$ in liquid scintillation counting. Owing to the narrow window of measurement of the HTO signal (0 – 10 keV), the signals above this energy range can be entirely attributed to ^{36}Cl$^-$, for which the energy range goes up to ~ 800 keV. The signals were therefore measured in a lower energy window between 0 and 10 keV and a higher energy window between 10 and 800 keV. Using similar definitions as in the preceding section (with the indices 1 denoting the lower energy window and 2 denoting the upper energy window), the relations between the counting rates and the tracer activities can be given as follows:

$$N^{\beta 1} = A_{HTO} \cdot f_{HTO}^{\beta 1} + A_{Cl} \cdot f_{Cl}^{\beta 1} \tag{2.7}$$

$$N^{\beta 2} = A_{Cl} \cdot f_{Cl}^{\beta 2} \tag{2.8}$$

The activity of ^{36}Cl$^-$ can thus be directly obtained from Eq. (2.8):

$$A_{Cl} = \frac{N^{\beta 2}}{f_{Cl}^{\beta 2}} \tag{2.9}$$

and the activity of HTO is obtained from combination of Eq. (2.7) with Eq. (2.9):

$$A_{HTO} = \left(N^{\beta 1} - \frac{N^{\beta 2} f_{Cl}^{\beta 1}}{f_{Cl}^{\beta 2}} \right) \left(f_{HTO}^{\beta 1} \right)^{-1}$$

(2.10)

The overall uncertainties on the calculated activities are readily obtained from error propagation of the uncertainties resulting from counting statistics.

2.4   Models for numerical simulations

While the experimental data were evaluated largely using several approximations of a pseudo steady-state flux situation for a variable concentration boundary (Yaroshchuk et al. 2008) in the beginning of the project phase, this method was continuously replaced by numerical procedures provided by the software package Comsol Multiphysics® (Comsol, Switzerland). The present report only contains results obtained using the latter procedures.

Briefly the Comsol Multiphysics® model consisted of three geometric domains representing the sequential filter–clay–filter sandwich in 1-D or axisymmetric 2-D along the direction of diffusion. The 'transport of dilute species' interface allows assigning the effective diffusion coefficients and reaction terms (R) for each of domains:

$$R = (1-\alpha)\frac{\partial c}{\partial t}$$

(2.11)

The transport equation has the form:

$$\frac{\partial c}{\partial t} + \nabla \cdot (-D_e \nabla c) = R$$

(2.12)

Note that this equation can readily be converted to Fick's second law by combining Eq. (2.11) and Eq. (2.12) to give:

$$\frac{\partial c}{\partial t} + \nabla \cdot (-D_e \nabla c) = \frac{\partial c}{\partial t} - \alpha \frac{\partial c}{\partial t}$$

(2.13)

which is equivalent to:

$$\alpha \frac{\partial c}{\partial t} = \nabla \cdot (D_e \nabla c)$$

(2.14)

corresponding to Fick's second law with $D_a = D_e/\alpha$.

The α factor is mostly assumed to be constant for a given composition of the aqueous phase, which may e.g. not be applicable for the case of non-linear sorption. However, no indications of such behaviour have been encountered in the present experiments. In the case of Cs^+, however, a notable dependence of α on the bulk-dry density has been observed (*cf.* sections 3.2.5 and 4.4; more background information is given in section 5.5). This dependence in not only related to inhomogeneities of the clay samples (Glaus et al. 2011), but also to the particular differences in the hydration properties of the Cs^+ and Na^+ ions (Van Loon & Glaus 2008). Empiric functions were used in these cases to define a position-dependent function for α (*cf.* sections 3.2.5 and 4.4).

Instead of using physical domains for the reservoir solutions, their concentrations were simulated using calculational variable boundary conditions at the interface between the filter and the reservoir. From the initial conditions at $t = 0$ with $m_{usb}{}^0 = c_{usb}{}^0 \cdot V_{usb}$ and $m_{dsb}{}^0 = 0$, where m denotes mass [kg] and c volumetric concentration [mol m^{-3}], the subscripts usb and dsb the upstream and the downstream boundary and the superscript 0 zero time, the following mass balances are used to calculate the up- and the downstream boundary conditions $c_{usb}(t)$ and $c_{dsb}(t)$:

$$c_{usb}(t) = \frac{\left(m_{usb}^0 - m_{dif}(t)\right)}{V_{usb}} step_{usb}$$

(2.15)

$$c_{dsb}(t) = \frac{m_{dsb}(t)}{V_{dsb}}$$

(2.16)

$m_{dif}(t)$ is the mass lost from the upstream reservoir at time t, and $step_{usb}$ is a time-step function evolving sigmoidally from 0 to 1 within the first second of calculation. It is used to avoid numerical issues for concentration discontinuities between solution and clay. $m_{dif}(t)$ and $m_{dsb}(t)$ are evaluated from the solution of ordinary differential equations:

$$\frac{\partial\left(m_{dif}(t)\right)}{\partial t} - A_{cs} J_{usb} = 0$$

(2.17)

and

$$\frac{\partial\left(m_{dsb}(t)\right)}{\partial t} - A_{cs} J_{dsb} = 0$$

(2.18)

for the downstream boundary. A_{cs} is the cross-section area which is constant for the geometry used in the experiments (diffusion perpendicular to the front sides of a cylindrical clay samples). In many cases it was appropriate to assume a zero-concentration for the latter boundary. In those cases where this did not apply, a continuous function based on measured average values were used. Details for this procedure can be found in Glaus et al. (2015b).

2.5   Evaluation of best-fit parameter values and their uncertainties

Best-fit parameter values were obtained from a parameter optimisation routine (related to the 'resnorm' function in Matlab®), in which the Comsol Multiphysics® model was used as a Matlab® script. The *lsqnonlin* algorithm was used to find the best-fit parameter values by solving nonlinear least-squares curve fitting of the form:

$$\min_x \|f(x)\|_2^2 = \min_x \left(f_1(x)^2 + f_2(x)^2 + ... + f_n(x)^2\right)$$

(2.19)

Uncertainties specified in this procedure define confidence intervals at the 95 % level. Depending on the experiment and the model, the combined experimental data (upstream reservoir concentration, downstream radiotracer flux, profile of total tracer concentration in the clay – or out-diffusion data) were used as the data source. In most cases the adjustable parameters were D_e and α. As aforementioned the effective diffusion coefficient of the confining filters (D_f, m^2 s^{-1}) was also used as an adjustable parameter in some cases. Its capacity was assumed as equal to the measured total filter porosity implying no interaction between the radiotracer and the filters taking place.

In those cases, in which D_f was used as a fixed value for the parameter optimisation, the uncertainties related to D_f had to be taken properly into account. A relative uncertainty of $\pm\,25\,\%$ was assumed for D_f in those cases, and two optimisation routines were performed, one using the lower limit of D_f and the other using its upper limit. The best-fit parameter values for D_e and α were calculated as the arithmetic mean of these two bounding cases.

A comparison between the uncertainties of the best-fit parameter values with the experimental uncertainties of the experimental data allows addressing the validity of the solutions found in the numerical calculations. For that purpose, worst-case combinations of the best-fit parameter values (typically D_e, α and D_f) were used to calculate upper and lower reasonable limits of the best solutions. This has been done in a heuristic manner in the present report. The upper limit was based on a combination of the largest D_f, the largest D_e and the lowest α value, while the lower limit was based on a combination of lowest D_f, lowest D_e and largest α value. This gives the true worst cases in the flux data at the downstream boundary, indeed. However, for the worst cases at the upstream boundary, different parameter combinations would be required. In view of the fact that the parameter sensitivity is much larger in the flux data at the downstream boundary compared to the upstream reservoir concentration data, we only rely on the former parameter sensitivity. The comparison of the best-fit case (based on the best-fit parameter values) with the bounding cases for the combined parameter uncertainties is shown in the figures in the Appendices as solid and dashed lines, respectively. A relatively good internal consistency of the experimental data and the parameter evaluation is indicated in those cases where the area covered by the bounding cases is similar to the uncertainties of the individual data points. It may also be given in those cases in which the latter quantities are smaller. In those cases, a certain underestimation of the uncertainties of the diffusive properties of the filters may be indicated. The converse situation, the area of bounding cases being smaller than data uncertainties, would have to be interpreted in the sense that the uncertainties of the best-fit parameter values may have been severely underestimated.

It is not straightforward to discuss the impact of the individual parameter uncertainties on the overall uncertainty of the best-fit solution for the out-diffusion experiments and through-diffusion experiments stopped during the transient phase – where the evaluation was based on tracer profile analysis. In all these cases it is not possible to define a fixed set of parameter values leading to bounding worst-case situations during the entire time interval of the experiment. Statistic approaches, viz. the Latin Hypercube sampling procedure were applied, in which a defined number of assessments was carried out after a random selection of appropriate parameter combinations. It is simply stated here that these assessments did not change significantly the interpretation of the experiments and the quantification of parameter uncertainties. It is therefore abstained in this report to discuss the results of these statistical approaches. However, they helped to substantiate the reliability in the results.

In single cases the uncertainties of the best-fit parameter values were unreasonably large. This was particularly the case where the parameters exhibited correlation. In such cases the only way-out was to use common sense and tentative sensitivity analysis to characterise the parameter uncertainties. Specific details to the individual procedures applied can be found in the tables where the best-fit parameter values are summarised.

3   Results for Diffusion in compacted Montmorillonite

3.1   Diffusion of HTO

Results for HTO were obtained in most cases by through- and out-diffusion. In single cases tracer profiles were measured after through-diffusion. The present section summarises experiments carried out at ρ_{bd} of 1300 and 1600 kg m^{-3}, in which the concentration of NaClO$_4$ in the external solution was varied. The results of similar experiments at ρ_{bd} of 1900 kg m^{-3} were published previously (Glaus et al. 2007). The experimental data are given in Appendix A1. Tab. 3.1 gives an overview of the best-fit parameter values obtained. In agreement with earlier observations (Glaus et al. 2007, Glaus et al. 2010), no significant dependence of D_e and α on the concentration of the background electrolyte could be observed. D_e values clearly decreased with increasing bulk-dry density. The difference between the porosity (calculated from water loss upon heating to 105° C) and α was not significant for the 1300 kg m^{-3} samples. A slight bias can be observed for the 1600 kg m^{-3} samples, for which the reason is unknown. However, no substantial uptake of the tracer by the clay (e.g. by isotopic exchange of HTO) could be substantiated within the range of the uncertainties.

Tab. 3.1:   Results of through-diffusion experiments with HTO in compacted Na-*mom* [a].

Label	ρ_{bd} [kg m^{-3}]	ε [–]	NaClO$_4$ [M]	D_e [b] [m^2 s^{-1}]	α [b] [–]
1064_13A	1297	0.54	0.01	$(1.1 \pm 0.2) \times 10^{-10}$	0.53 ± 0.10
1064_13B	1301	0.52	0.10	$(1.1 \pm 0.2) \times 10^{-10}$	0.59 ± 0.10
1064_13C	1299	0.57	1.0	$(1.2 \pm 0.3) \times 10^{-10}$	0.57 ± 0.11
1064_16A	1608	0.43	0.01	$(5.2 \pm 0.9) \times 10^{-11}$	0.52 ± 0.09
1064_16B	1602	0.43	0.10	$(5.5 \pm 0.8) \times 10^{-11}$	0.52 ± 0.08
1064_16C	1605	0.43	1.0	$(5.4 \pm 0.8) \times 10^{-11}$	0.52 ± 0.08

[a]   Experimental details: Single-tracer experiment; SFDC (0.5 µm filter pore size); sample geometry (diameter × thickness): 25.6 mm × 10.4 mm; volume of source reservoir: 100 ml; volume of target reservoirs: 50 – 100 ml; observation time: ~ 45 d.

[b]   Best-fit parameter values were evaluated using $c_{usb}(t)$ and $J_{dsb}(t)$ as the fitted data. The Comsol Multiphysics® model uses non-stationary boundary conditions with given initial reservoir concentration; D_f was set to 7.0×10^{-11} m^2 s^{-1} (generic value).

3.2   Diffusion of cations: Bulk-dry densities of 1300 and 1600 kg m^{-3}

3.2.1 ^{22}Na$^+$ through- and out-diffusion (combined with HTO): 0.5 and 1.0 M NaClO$_4$

The combined diffusion of ^{22}Na$^+$ and HTO was measured by through- and out-diffusion at bulk-dry densities of 1300 and 1600 kg m^{-3}. The results measured at a bulk-dry density of ~ 1900 kg m^{-3} were published previously (Glaus et al. 2007). The majority of data was measured in combination with HTO using *SFDC's*. A few experiments were carried out under identical conditions as system test experiments using *FFDC's*. The results for the through-diffusion experiments are given in Tab. 3.2, those of the out-diffusion experiments in Tab. 3.3. The experimental data are given in Appendix A2 and A3.

Tab. 3.2:   Results of through-diffusion experiments with ^{22}Na$^+$ (and simultaneously measured HTO) in compacted Na-*mom* [a].

Label	ρ_{bd} [kg m^{-3}]	ε [–]	NaClO$_4$ [M]	Tracer	D_e [b] [m^2 s^{-1}]	α [b] [–]
1055_1A	1295	0.54	0.5	^{22}Na$^+$ HTO	$(1.6 \pm 0.4) \times 10^{-10}$ $(8.8 \pm 1.5) \times 10^{-11}$	2.6 ± 0.4 0.55 ± 0.14
1055_1B	1305	0.53	0.5	^{22}Na$^+$ HTO	$(1.1 \pm 0.2) \times 10^{-10}$ $(8.4 \pm 0.6) \times 10^{-11}$	2.30 ± 0.41 0.55 ± 0.14
1055_2A	1293	0.54	1.0	^{22}Na$^+$ HTO	$(5.9 \pm 1.1) \times 10^{-11}$ [c] $(7.8 \pm 1.3) \times 10^{-11}$	1.8 ± 0.3 [c] 0.55 ± 0.13
1055_2B	1287	0.54	1.0	^{22}Na$^+$ HTO	$(6.4 \pm 1.3) \times 10^{-11}$ [c] $(7.8 \pm 1.3) \times 10^{-11}$	1.4 ± 0.2 [c] 0.55 ± 0.13
1055_3A	1558	0.44	0.5	^{22}Na$^+$ HTO	$(1.0 \pm 0.2) \times 10^{-10}$ $(3.9 \pm 0.7) \times 10^{-11}$	2.6 ± 0.4 0.44 ± 0.09
1055_3B	1560	0.44	0.5	^{22}Na$^+$ HTO	$(8.9 \pm 1.4) \times 10^{-11}$ $(4.2 \pm 0.7) \times 10^{-11}$	3.0 ± 0.4 0.44 ± 0.09
1055_4A	1565	0.44	1.0	^{22}Na$^+$ HTO	$(4.3 \pm 0.6) \times 10^{-11}$ [c] $(3.8 \pm 0.7) \times 10^{-11}$	1.8 ± 0.3 [c] 0.44 ± 0.09
1055_4B	1562	0.44	1.0	^{22}Na$^+$ HTO	$(4.4 \pm 0.6) \times 10^{-11}$ [c] $(3.8 \pm 0.7) \times 10^{-11}$	1.8 ± 0.2 [c] 0.44 ± 0.09

[a]   Experimental details: Combined-tracer experiment; *SFDC* (10 μm filter pore size); sample geometry (diameter × thickness): 25.6 mm × 10.4 mm; volume of source reservoir: 100 ml; volume of target reservoirs: 50 – 100 ml; observation time: ~ 78 d.

[b]   Best-fit parameter values were evaluated using c_{usb} (t) and J_{dsb} (t) as the fitted data. The Comsol Multiphysics® model uses non-stationary boundary conditions with given initial reservoir concentration; D_f was set to 9.0×10^{-11} m^2 s^{-1} for ^{22}Na$^+$ and 1.2×10^{-10} m^2 s^{-1} for HTO (generic values).

[c]   Highly unreliable results because of disturbances in the flux; the results of the subsequent out-diffusion tests were clearly more reliable.

A series of observations merit a closer discussion for the evaluation of the best-fit parameter values:

- By some unknown reasons the flux of ^{22}Na$^+$ was disturbed for a longer period in the experiments with 1.0 M NaClO$_4$. The evaluation of best-fit parameter values was severely impeded in those cases. However, similar experiments were run earlier without simultaneous HTO diffusion. These experiments did not show the disturbance in flux and resulted in comparable best-fit parameters values. Further, the results of the out-diffusion experiments were clearly more reliable. They were used for further data processing.

- The range of uncertainty in the flux curves induced by the parameter uncertainties of D_e and α (*cf.* the dotted lines in the figures in Appendix A2) is larger than the uncertainties of the individual data points in the experiments with ^{22}Na$^+$. This is an indication that the systematic uncertainties in the filter diffusion properties (not comprised by the error bars of the data) are dominating the overall uncertainties.

- The D_e values for HTO are lower than those shown in Tab. 3.1. The deviation is clearly out-side the experimental uncertainty; however, it is in general less than 25 %. This shows that the sample-to-sample uncertainty may be larger than the overall uncertainty of a single measurement of D_e. Whether such deviations may be related to the use of different batches of Na-*mom* (same preparation method) could not clearly be demonstrated by the experiments but would be a rather obvious presumption.

- The agreement between the results of through-diffusion and out-diffusion is in general very good. The model curves shown in Appendix A3 are blind predictions from through-diffusion.

Tab. 3.3:   Results of the out-diffusion experiments with ^{22}Na$^+$ (and simultaneously measured HTO) in compacted Na-*mom* [a].

Best-fit parameter values deviating from those of the through-diffusion experiments are printed in Italics.

Label	ρ_{bd} [kg m^{-3}]	ε [–]	NaClO$_4$ [M]	Tracer	D_e [b] [m^2 s^{-1}]	α [b] [–]
1055_1A	1295	0.54	0.5	^{22}Na$^+$ HTO	$(1.6 \pm 0.4) \times 10^{-10}$ $(8.8 \pm 1.5) \times 10^{-11}$	2.6 ± 0.4 0.55 ± 0.14
1055_1B	1305	0.53	0.5	^{22}Na$^+$ HTO	$(1.1 \pm 0.2) \times 10^{-10}$ $(8.4 \pm 0.6) \times 10^{-11}$	*2.60 ± 0.41* 0.55 ± 0.14
1055_2A	1293	0.54	1.0	^{22}Na$^+$ HTO	$(5.9 \pm 1.1) \times 10^{-11}$ $(7.8 \pm 1.3) \times 10^{-11}$	*1.3 ± 0.3* 0.55 ± 0.13
1055_2B	1287	0.54	1.0	^{22}Na$^+$ HTO	$(6.4 \pm 1.3) \times 10^{-11}$ $(7.8 \pm 1.3) \times 10^{-11}$	1.4 ± 0.2 0.55 ± 0.13
1055_3A	1558	0.44	0.5	^{22}Na$^+$ HTO	$(1.0 \pm 2.0) \times 10^{-10}$ $(3.9 \pm 0.7) \times 10^{-11}$	2.6 ± 0.4 0.44 ± 0.09
1055_3B	1560	0.44	0.5	^{22}Na$^+$ HTO	$(8.9 \pm 1.4) \times 10^{-11}$ $(4.2 \pm 0.7) \times 10^{-11}$	3.0 ± 0.4 0.44 ± 0.09
1055_4A	1565	0.44	1.0	^{22}Na$^+$ HTO	$(4.3 \pm 0.6) \times 10^{-11}$ $(3.8 \pm 0.7) \times 10^{-11}$	1.8 ± 0.3 0.44 ± 0.09
1055_4B	1562	0.44	1.0	^{22}Na$^+$ HTO	$(4.4 \pm 0.6) \times 10^{-11}$ $(3.8 \pm 0.7) \times 10^{-11}$	1.8 ± 0.2 0.44 ± 0.09

[a]   Experimental details: Combined-tracer experiment; *SFDC* (10 μm filter pore size); sample geometry (diameter × thickness): 25.6 mm × 10.4 mm; volume on previous source side: 50 ml; volume on previous target side: 20 ml; observation time: ~ 45 d.

[b]   Best-fit parameter values were evaluated using J'_{usb}(t) and J'_{dsb}(t) as the fitted data. The Comsol Multiphysics® model uses a zero-concentration boundary condition at both sides of the diffusion cell; D_f was set to 9.0×10^{-11} m^2 s^{-1} for ^{22}Na$^+$ and 1.2×10^{-10} m^2 s^{-1} for HTO (generic values).

3.2.2 ^{22}Na$^+$ through- and out-diffusion: 0.1 M NaClO$_4$

Through-diffusion experiments using 0.1 M NaClO$_4$ as the background electrolyte were not conducted with the same experimental equipment as those for 0.5 and 1.0 M NaClO$_4$. The diffusive resistance of Na-*mom* is too low compared to the porous filters at such a low salinity. For this reason, the flushed-filter technique was applied. The results of these experiments are given in Tab. 3.4. The experimental data are given in Appendix A4. A time window restricted to the first 10 days was used for evaluation of the best-fit parameter values for HTO, because the steady-state flux phase is well represented in that short time. The deviations from the simulation observed later on can probably be explained with inconsistencies between the scintillation cocktail batches and the counter efficiencies measured in the calibration samples.

Tab. 3.4: Results of through-diffusion experiments with ^{22}Na$^+$ (and simultaneously measured HTO) in compacted Na-*mom*.

Label	ρ_{bd} [kg m^{-3}]	ε [–]	NaClO$_4$ [M]	Tracer	D_e [c] [m^2 s^{-1}]	α [c] [–]
1058_1A [a]	1297	0.537	0.1	^{22}Na$^+$	$(7.0 \pm 0.9) \times 10^{-10}$ [c]	13.0 ± 3.9 [c]
				^{22}Na$^+$	$(8.6 \pm 1.0) \times 10^{-10}$ [d]	11.5 ± 3.9 [d]
				HTO	$(1.3 \pm 0.4) \times 10^{-10}$ [c]	0.55 ± 0.20 [c]
1047#3_2 [b]	1597	0.430	0.1	^{22}Na$^+$	$(3.3 \pm 0.36) \times 10^{-10}$ [c]	16.0 ± 3.9 [c]
				HTO	n.d.	n.d.

[a] Experimental details: Combined-tracer experiment; *FFDC* (1 µm filter pore size); sample geometry (diameter × thickness): 20.0 mm × 10.0 mm; volume of source reservoir: 200 ml; volume of target reservoirs: 50 ml; observation time: ~ 43 d.

[b] Experimental details: Single-tracer experiment; *FFDC* (10 µm filter pore size); sample geometry (diameter × thickness): 20.0 mm × 10.0 mm; volume of source reservoir: 1000 ml; volume of target reservoirs: 20 – 100 ml; observation time: ~ 110 d.

[c] Best-fit parameter values were evaluated using $c_{usb}(t)$ and $J_{dsb}(t)$ as the fitted data. The Comsol Multiphysics® model uses non-stationary boundary conditions with given initial reservoir concentration; D_f was set to 10^{-5} m^2 s^{-1} for ^{22}Na$^+$ and HTO (assuming no diffusive resistance of the filters).

[d] As shown in Fig. 3.1 the assumption of $D_f = 10^{-9}$ m^2 s^{-1} is a more realistic assumption.

Experiment 1058_1A is an illustrative case, where a reduced performance of the flushed-filter system and its impact on the uncertainty of the results can be demonstrated. In many cases it was observed that the diffusive resistance of the flushed filter was not negligible compared to the diffusive resistance of the clay sample. A clear indication can be seen in the tracer profile, if the tracer activity at the down-stream boundary significantly differs from zero. This was observed in the case of the diffusion of ^{22}Na$^+$ in 1058_1A (*cf.* Fig. 3.1). It has to be assumed that local concentration gradients may have been formed to some degree owing to slight inhomogeneities in the flow field. In order to take into account the existence of partially stagnant zones in the filters for the evaluation of the best-fit parameter values, the filters are treated in the modelling as having homogeneous diffusive properties with a formal D_f[2] which is then also treated as an adjustable parameter. As a general experience from such considerations, $10^{-9} < D_f < 5 \times 10^{-9}$ m^2 s^{-1} is a reasonable range of these formal filter diffusivities.

---

[2] The formal character of D_f values is founded in the circumstance that purely one-dimensional diffusion properties in the filters are applied for simplicity to describe their three-dimensional advection-diffusion behaviour. For this reason, the numbers used for D_f are meaningless and should, under no circumstances, be compared to the diffusion coefficients in bulk water.
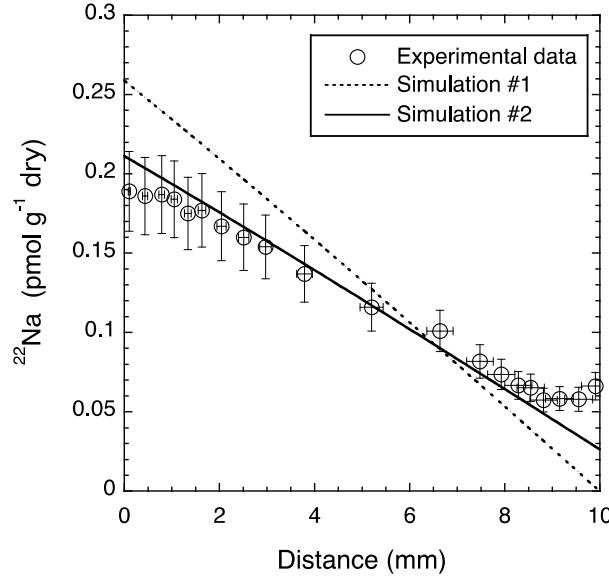
Fig. 3.1:   Profile of ^{22}Na$^+$ measured after through-diffusion (experiment 1058_1A).

Simulation #1 assumes no diffusive resistance of the filters (*cf.* parameter values from Tab. 3.4), while simulation #2 was obtained using $D_e = 8.5 \times 10^{-10}$ m^2 s^{-1}, $D_f = 1 \times 10^{-9}$ m^2 s^{-1} and $\alpha = 11.5$ as the best-fit values.

Another indication that the filter diffusivity has been overestimated in the best-fit parameter values of Tab. 3.4 is the relatively large value for α. For a homoionic clay, the latter value can be derived (Glaus et al. 2007) alternatively from the cation-exchange capacity (*CEC*, given in eq kg^{-1}) and the concentration of the inert electrolyte ([A], given as M) with f_w a volumetric conversion factor (10^{-3} m^3 dm^{-3}) according to:

$$\alpha = \varepsilon + \rho_{bd} R_d = \varepsilon + \rho_{bd} \frac{CEC}{[A]} \cdot f_w \qquad (3.1)$$

Using a *CEC* of 0.85 eq kg^{-1} results in $\alpha = 11.6$ under the conditions of the experiment. If D_f is set to 10^{-9} m^2 s^{-1} and α to 11.5, D_e remains the only adjustable parameter. A good agreement with the flux and reservoir concentration is obtained for $D_e = 8.5 \times 10^{-10}$ m^2 s^{-1} (*cf.* Fig. 3.2). As can be taken from Fig. 3.1, the resulting agreement of the tracer profile data with the simulation is much better than for assuming no diffusive resistance of the filters. The remaining discrepancies can be explained mainly by the inhomogeneous compaction of the clay (*cf.* section 5.1). The adapted parameter values are therefore preferred over those given in Tab. 3.4. Such a decision can, however, be only made if a reliable tracer profile is available. Out-diffusion measurements would also serve that purpose, provided that the values measured in the initial phase can be trusted, which has to be put into question in many cases.
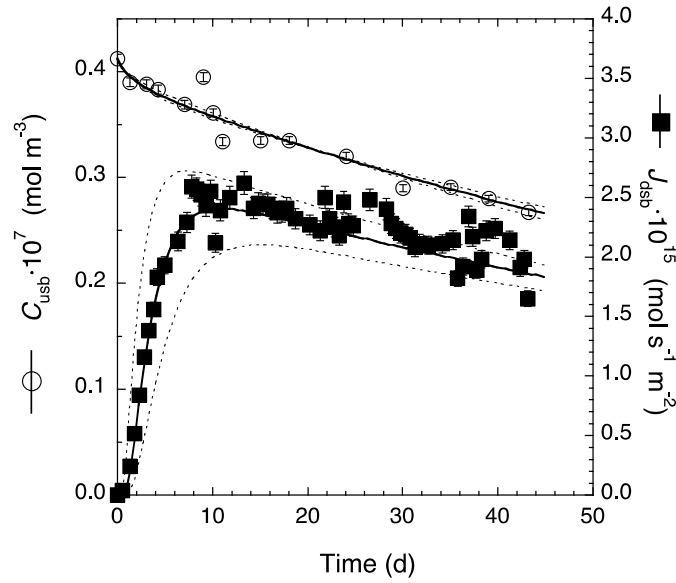
Fig. 3.2:   Flux at the zero-concentration boundary and reservoir concentration of ^{22}Na$^+$ diffu-
sion in Na-*mom* at ρ_{bd} = 1297 kg m^{-3} and 0.1 M NaClO$_4$ external salt concentration
(experiment 1058_1A, *cf.* Tab. 3.4).

The model curve was obtained using D_e = 8.5 × 10^{-10} m^2 s^{-1}, D_f = 1 × 10^{-9} m^2 s^{-1} and α = 11.5
as best-fit parameter values.

3.2.3 ^{85}Sr^{2+} through- and out-diffusion: 0.5 and 1.0 M NaClO$_4$

Measurements for ^{85}Sr^{2+} were done as single-tracer experiments by through-diffusion and, in a
few cases, by out-diffusion at bulk-dry densities of 1300 and 1600 kg m^{-3} using *SFDC's*. The
results for the through- and the out-diffusion experiments are given in Tab. 3.5. The experimental
data are shown in Appendix A5.

The results measured at a bulk-dry density of ~ 1900 kg m^{-3} and salinities between 0.5 and 1.0 M
were published previously (Glaus et al. 2007). Additional experiments at this bulk-dry density
extending the range of background electrolyte concentrations were also carried out and are
reported in section 3.4.1.

Tab. 3.5: Results of the through- and out-diffusion experiments with $^{85}Sr^{2+}$ in compacted Na-*mom* [a].

Label	ρ_{bd} [kg m^{-3}]	ε [–]	NaClO$_4$ [M]	Diffusion	D_e [b] [m^2 s^{-1}]	α [b] [–]
1055_1A	1295	0.54	0.5	through	$(3.6 \pm 1.9) \times 10^{-10}$	20.0 ± 4.1
				out	$(4.5 \pm 1.9) \times 10^{-10}$	19.0 ± 4.1
1055_1B	1305	0.53	0.5	through	$(3.6 \pm 2.2) \times 10^{-10}$	25.0 ± 5.6
				out	n.d.	n.d.
1055_2A	1293	0.54	1.0	through	$(1.1 \pm 0.2) \times 10^{-10}$	6.5 ± 1.1
				out	$(1.1 \pm 0.2) \times 10^{-10}$	7.5 ± 1.1
1055_2B	1287	0.54	1.0	through [c]	$(1.0 \pm 0.1) \times 10^{-10}$	6.3 ± 0.5
				out [c]	$(1.0 \pm 0.1) \times 10^{-10}$	6.3 ± 0.5
1055_3A	1558	0.44	0.5	through	$(1.6 \pm 0.5) \times 10^{-10}$	23.0 ± 4.0
				out	n.d.	n.d.
1055_3B	1560	0.44	0.5	through	$(1.8 \pm 0.5) \times 10^{-10}$	22.0 ± 3.0
				out	n.d.	n.d.
1055_4A	1565	0.44	1.0	through	$(5.3 \pm 0.70) \times 10^{-11}$	7.3 ± 1.0
				out	$(5.3 \pm 0.70) \times 10^{-11}$	8.5 ± 1.0
1055_4B	1562	0.44	1.0	through	$(5.5 \pm 0.70) \times 10^{-11}$	7.0 ± 1.0
				out	$(5.5 \pm 0.70) \times 10^{-11}$	7.5 ± 1.0

[a] Experimental details for through-diffusion: Single-tracer experiment; *SFDC* (10 μm filter pore size); sample geometry (diameter × thickness): 25.6 mm × 10.4 mm; volume of source reservoir: 200 ml; volume of target reservoir: 20 – 100 ml; observation time: 160 – 225 d (depending on salinity and clay compaction). Experimental details for out-diffusion: Same as for through-diffusion with volume on previous source side: 100 – 20 ml; volume on previous target side: 50 – 20 ml observation time: ~ 100 d (depending on salinity and clay compaction).

[b] Best-fit parameter values were evaluated using $c_{usb}(t)$ and $J_{dsb}(t)$ as the fitted data for through-diffusion and $J'_{usb}(t)$ and $J'_{dsb}(t)$ for out-diffusion. The Comsol Multiphysics® model uses non-stationary boundary conditions with given initial reservoir concentration for through-diffusion; D_f set to 8.5×10^{-11} m^2 s^{-1} (representing the average from two measurements on filters from the present experiment). For the out-diffusion a zero-concentration boundary condition was applied.

[c] Obtained from simultaneous fitting the through- and the out-diffusion data using D_f as an adjustable parameter, too (8.5×10^{-11} m^2 s^{-1} _2B).

3.2.4 $^{85}Sr^{2+}$ through- and out-diffusion: 0.1 NaClO$_4$

Measurements for $^{85}Sr^{2+}$ were done in combination with HTO by through-diffusion only at ρ_{bd} of 1300 and 1600 kg m^{-3} using the *FFDC's*. The flux measurements turned unstable after a period of ~ 50 days, a phenomenon most probably related to instabilities of the tracer concentration gradients near the downstream boundary (Glaus et al. 2015b). Owing to the uncertainties related to the initial tracer distribution in the clay, it was not possible to obtain useful information from out-diffusion. Although a pseudo-steady-state flux phase could not be reached in these experiments, the range of diffusion parameters could be restricted in a reasonable way, as will be shown in the following. Similarly to the experiments with $^{22}Na^+$, a formal diffusive resistance of the filters had to be taken into account. This can immediately be seen in the initial decrease of the reservoir concentration, which is less steep than would be expected for the case of ideal filter behaviour (no diffusive resistance). In order to better discriminate between valuable and erroneous measurements, the results of all experiments carried out under identical conditions were pooled together.

For the present measurements this means that each four experiments carried out at a bulk-dry density of $\sim$ 1300 and $\sim$ 1600 kg m^{-3} were taken together. The strategy to determine the best-fit parameter values and explore their ranges of uncertainty consisted in first narrowing the range of possible D_f values and then determining D_e for a given range of α values ($\alpha = 350 \pm 50$, which is in agreement with the measurements carried out at bulk-dry density of 1900 kg m^{-3}). Sensitivity analysis shows that the range of uncertainty of D_f is relatively narrow and that its distribution is highly asymmetrical: The impact of variations of D_f to the lower side of the optimum on D_e is very large, whereas it is almost insensitive to the higher side of D_f. For this reason, the classic approach of error propagation is unproductive for the present case. Instead a series of scenarios with variable D_f were tested, where optimal values for D_e and α were determined for the given D_f. α was only varied in the above specified range of values, because the general experience with cations like Na^+ and Sr^{2+} has shown a good agreement between sorption distribution ratios obtained by batch sorption experiments and diffusion experiments. It can thus be expected that α does not change significantly upon a change in the degree of compaction. However, α was adjusted within the above-specified range of uncertainty according to the experience that low values of D_f lead to an increased retardation of the tracer-breakthrough. The best-fit parameter values for α and D_e obtained for the various D_f values are shown in Tab. 3.6.

Tab. 3.6:   Sensitivity analysis in the determination of D_e and α for a series of given D_f values in the diffusion experiments with $^{85}Sr^{2+}$ at a bulk-dry density of $\sim$ 1300 kg m^{-3} and 0.1 M NaClO$_4$ (cells 1058_5A, 1058_5B, 1058_7A, 1058_7B) .

Scenario	D_f	D_e [m^2 s^{-1}]	α [–]
#1	1×10^{-8}	2.0×10^{-9}	300
#2	6×10^{-9}	2.0×10^{-9}	300
#3	4×10^{-9}	2.0×10^{-9}	300
#4	3×10^{-9}	2.3×10^{-9}	300
#5	2×10^{-9}	3.0×10^{-9}	350
#6	1×10^{-9}	7.0×10^{-9}	400
#7	5×10^{-10}	3.0×10^{-8}	400

A comparison between the experimental data and the fit-curves for the scenarios of Tab. 3.6 is shown in Figs. 3.3 and 3.4. Scenario #7 can clearly be ruled out, because it is only in agreement with a minority of the experimental data, while the other scenarios are all fairly well representing the experimental data, although there are nuances in the initial phase of the reservoir concentration data. In order to avoid an intricate discussion of asymmetrical distribution of uncertainties, the ranges of D_e and α in Tab. 3.6 for scenarios #1 to #6 are taken into account as possible values with their centre values being the best-fit parameter values (*cf.* Tab. 3.8 for a summary of the best-fit values and their uncertainties for both experiments at 1300 and 1600 kg m^{-3}).
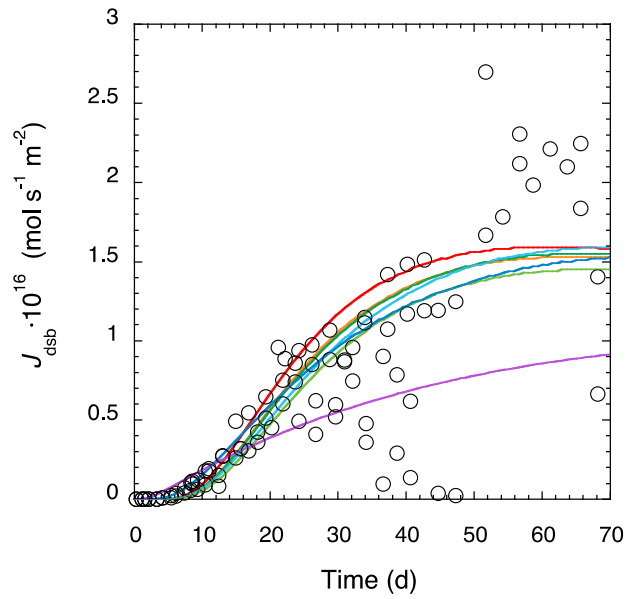
Fig. 3.3:   Flux of $^{85}Sr^{2+}$ at the zero-concentration boundary in through-diffusion in Na-*mom* at ρ_{bd} = 1299 kg m^{-3} and 0.1 M NaClO$_4$ external salt concentration (experiment 1058_5A,5B,7A,7B, pooled data).

The model curves are from scenarios #1 – 7 in Tab. 3.6, going from red to violet.
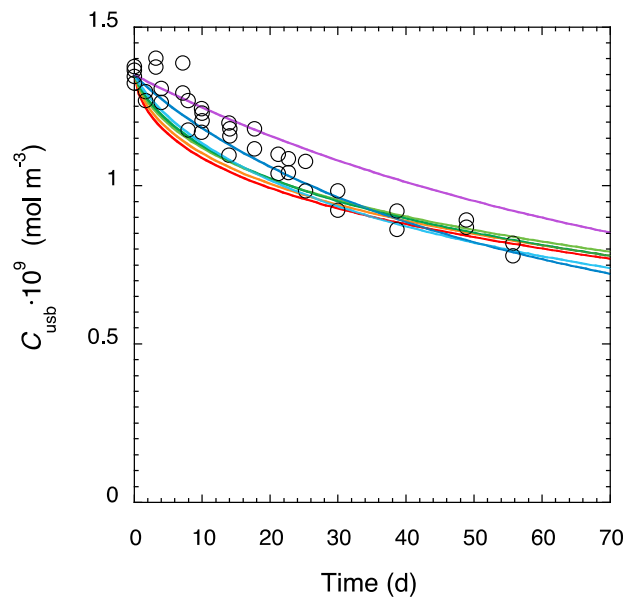
Fig. 3.4:   Reservoir concentration of $^{85}Sr^{2+}$ in through-diffusion in Na-*mom* at ρ_{bd} = 1299 kg m^{-3} and 0.1 M NaClO$_4$ external salt concentration (experiment 1058_5A, 5B,7A,7B, pooled data).

The model curves are from scenarios #1 – 7 in Tab. 3.6, going from red to violet.

A similar evaluation of the best-fit parameter values for the experiments carried out at ρ_{bd} of 1600 kg m^{-3} is shown in Tab. 3.7 for scenario analysis and Figs. 3.5 and 3.6 for the fit curves. For the evaluation of the best-fit parameters values, the flux data in the time window 0 – 40 d were taken into account only, because the majority of the following data were obviously erroneous. No parameter values can be found that would explain either the very high (4 – 8 mol s^{-1} m^{-2}) or the very low (< 1 mol s^{-1} m^{-2}) flux data in view of the reservoir concentration data. Unfortunately, no reason could be found for these anomalous results. The sensitivity analysis (Tab. 3.7) with the data measured in the first 40 d allows, however, for an estimate of the range of valuable values for D_e and α to be made.

Tab. 3.7: Sensitivity analysis in the determination of D_e and α for a series of given D_f values in the diffusion experiments with $^{85}Sr^{2+}$ at a bulk-dry density of ~ 1300 kg m^{-3} and 0.1 M NaClO$_4$ (cells 1058_5A, 1058_5B, 1058_7A, 1058_7B).

Scenario	D_f [m^2 s^{-1}]	D_e [m^2 s^{-1}]	α [–]
#1	5×10^{-9}	1.5×10^{-9}	200
#2	3×10^{-9}	2.0×10^{-9}	300
#3	2×10^{-9}	2.5×10^{-9}	350
#4	1×10^{-9}	4.0×10^{-9}	400
#5	8×10^{-10}	6.0×10^{-9}	450
#6	5×10^{-10}	5.0×10^{-8}	800

Tab. 3.8: Summary of the best-fit parameter values obtained from through-diffusion experiments of $^{85}Sr^{2+}$ in compacted Na-*mom* estimated from the range of possible values in a sensitivity analysis (*cf.* Tabs. 3.6 and 3.7).

ρ_{bd} [kg m^{-3}]	NaClO$_4$ [M]	D_e [m^2 s^{-1}]	α [–]
1299	0.1	$(4.5 \pm 2.5) \times 10^{-9}$	350 ± 50
1602	0.1	$(3.8 \pm 2.2) \times 10^{-9}$	330 ± 120
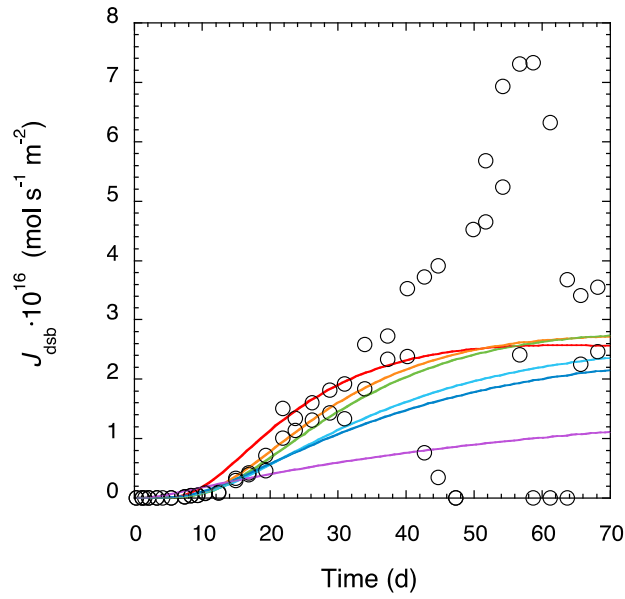
Fig. 3.5:   Flux of $^{85}Sr^{2+}$ at the zero-concentration boundary in through-diffusion in Na-*mom* at ρ_{bd} = 1602 kg m^{-3} and 0.1 M NaClO$_4$ external salt concentration (experiment 1058_6A and 6B, pooled data).

The model curves are from scenarios #1 – 6 in Tab. 3.7, going from red to violet.
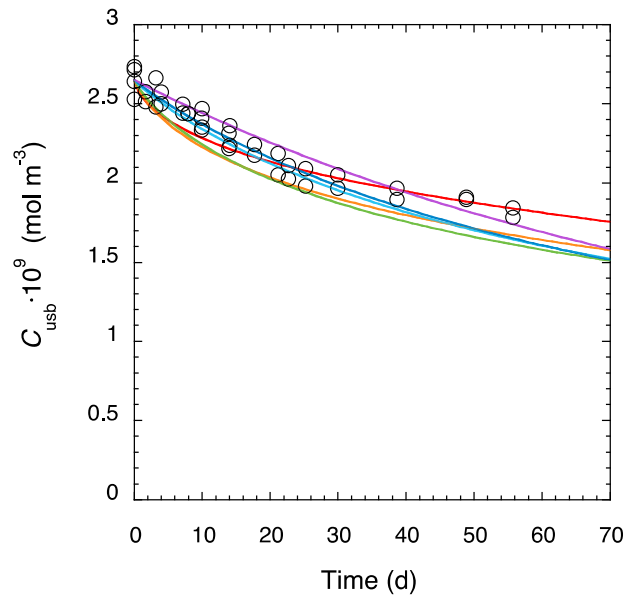
Fig. 3.6:   Reservoir concentration of $^{85}Sr^{2+}$ in through-diffusion in Na-*mom* at ρ_{bd} = 1602 kg m^{-3} and 0.1 M NaClO$_4$ external salt concentration (experiment 1058_6A and 6B, pooled data).

The model curves are from scenarios #1 – 6 in Tab. 3.7, going from red to violet.

3.2.5 $^{134}Cs^+$ in-diffusion, various conditions

3.2.5.1   Concept and experimental procedures

The experiments represent a spot-check investigation on the effect of a variable background concentration of stable Cs. The idea behind this variation is found in the intricate sorption isotherms measured for the uptake of Cs^+ by montmorillonite (B. Baeyens, personal communication, see Fig. 3.7). At low background concentrations of stable Cs^+, R_d increases, which has been tentatively explained by the presence of illite impurities in the montmorillonite. Illite possesses so-called frayed-edge sites, which have a higher affinity for Cs^+ than the planar cation-exchange sites on montmorillonite. It can be hypothesised that the 3-D spatial arrangement of oxide ligands of the solid in the frayed-edge sites would lead to a significant decrease of the mobility of bound Cs^+. It was thus interesting to measure the influence of the background electrolyte concentration on the diffusive behaviour of Cs^+ at different occupancies of the Cs sites. For this purpose, it was necessary to have the clay saturated with a defined amount of stable Cs^+.
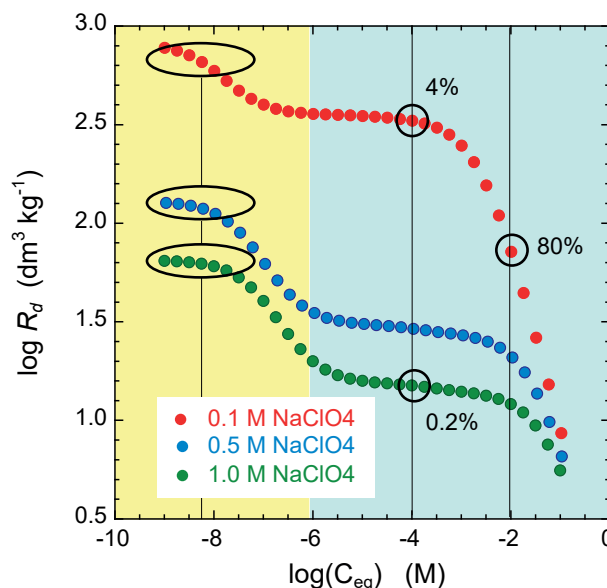
Fig. 3.7:   Sorption isotherms for the sorption of Cs^+ on Na-*mom* calculated for the salinities specified in the legend.

> The circles show the conditions, under which conditions the diffusion experiments were carried out. The yellow area indicates the predominance are of illite-type sites, the blue area the predominance of planar cation exchange sites. Depending on the equilibrium Cs^+ concentration, different degrees of saturation of the clay with Cs^+ are attained (indicated as % of fractional saturation of the planar sites).

In view of the extensive contact times required to saturate a compacted clay plug homogeneously with Cs, the material was pre-equilibrated with Cs^+ in a batch-type experiment, freeze-dried and then compacted to prepare clay plugs for the diffusion experiments. The amount of Cs^+ added to the clay was calculated such as to obtain equilibrium with the desired Cs^+ concentrations in the contacting liquid phase. At this point another difficulty comes into play: The respective reference sorption measurements were carried out at relatively low solid : liquid ratios, whereas in the diffusion experiment the clay is used in a highly compacted form. It is known from previous work (Van Loon & Glaus 2008) that the selectivity of smectite clays for Cs^+ increases with increasing

degree of clay compaction. The literature data were measured for bentonite; no similar measurements were available for pure montmorillonite. In view of this lack of knowledge, the amount of Cs^+ added was based on the measurements in dilute clay suspensions, and possible subsequent changes of sorption equilibria upon compaction were taken as acceptable. Fig. 3.7 shows the conditions at which the diffusion experiments were carried out.

As a further part of the experimental concept, the diffusion of HTO was measured prior to the experiments with $^{134}Cs^+$. The necessity for such measurements is given by the observation that the diffusive behaviour of smectites may vary with the type of cations present on the planar exchange sites. Melkior et al. (2009) showed that HTO diffusion in bentonite depended on the loading with Cs^+: At high loadings, HTO diffusion was increased compared to a purely Na^+-exchanged bentonite. This observation was attributed to changes in the microstructure of the clay. High-resolution transmission electron microscopy on such samples revealed an increase in crystalline structures instead of gel-like structures that were observed for a purely Na^+-exchanged bentonite. From this observation it was hypothesised that the ratio of crystalline to gel-like phases had an influence on the geometric factors for diffusion and therefore a direct influence on the diffusive fluxes of HTO.

The in-diffusion technique was combined with measuring the reservoir concentration of the $^{134}Cs^+$ tracer. Independent information on D_e and α can thereby be obtained similarly to the evaluation of a through-diffusion experiment. However, two aggravations have to be taken into account in the evaluation of the experiments: (i) If the diffusive resistance of the confining filters is significant, uncertainties arise with respect to the boundary conditions on the reservoir's side, and (ii) inhomogeneities of clay compaction (*cf.* section 5.1) lead to inhomogeneities in the expected tracer profile, because the measured total concentration of the tracer (C_s, defined as a volumetric concentration with respect to V_{tot}, the total clay volume) depends directly on the degree of compaction according to:

$$C_s = C_{pw} \cdot \alpha = C_{pw} \cdot (R_d \rho_{bd} + \varepsilon) \tag{3.2}$$

C_{pw} is the respective pore water concentration. In order to prevent as much as possible such artefacts, flushed-filter diffusion cells were used in order to keep the tracer concentration gradient in the confining filters at minimum, and sufficient time was allowed for the tracer to penetrate deeper into the clay than just the inhomogeneous boundary layer.

In the case of the experiments with $^{134}Cs^+$ tracer, the Cs profile was measured simply by γ-scintillation of the sectioned clay samples. In the case of the experiments with a stable Cs background, the latter cations were extracted by equilibrating the sectioned clay samples with a solution of RbCl. The amount of Rb^+ in these solutions was chosen to represent the 20-fold of the cation exchange sites present in the clay sample.

A mischance occurring during the preparation of the Cs-loaded clay samples is noteworthy. Depending on the concentration of $NaClO_4$ used to obtain the desired amount of Cs loading of the clay, substantial amounts of this salt remained in the samples subjected to freeze-drying. During the subsequent re-saturation of the compacted clay samples with the background electrolyte solution, these amounts $NaClO_4$ redissolved, which lead to bulk-dry densities in the clay samples lower than the target values.

3.2.5.2   Results: Diffusion of HTO

The transient phase of diffusion of HTO was not evaluated; therefore no α values are specified. D_e values were calculated from the tracer fluxes during the steady-state flux phase and the respective tracer concentrations in the reservoir solution. A summary is given in Tab. 3.9. These values have to be discussed in view of the effects of the loading of cation exchange sites with stable Cs^+, and of the effect of different clay compaction. The second aspect can be considered by recalculating all D_e values to an arbitrarily chosen reference bulk-dry density using Archie's law (Archie 1942):

$$D_e = A\varepsilon^m \tag{3.3}$$

with the parameters $A = 9.8 \times 10^{-11}$ m^2 s^{-1} and $m = 1.81$ (Glaus et al. 2010). The normalised values show a clear difference between the experiments carried out with and without stable Cs^+ added. As suggested by the measurements of Melkior et al. (2009), HTO diffusion measured under a significant level of stable Cs^+ is faster than under trace conditions.

Tab. 3.9:   Summary D_e values for HTO measured before in-diffusion of $^{134}Cs^+$.

Cell label	NaClO$_4$ [M]	ρ_{bd} [kg m^{-3}]	$^{133}Cs^+$ [mM]	D_e HTO [m^2 s^{-1}]	$D_{e,nor}$ HTO [c] [m^2 s^{-1}]
1061_16A	0.1	1550	– [a]	$(7.1 \pm 1.6) \times 10^{-11}$	$(7.1 \pm 1.6) \times 10^{-11}$
1061_16B	0.5	1540	– [a]	$(6.4 \pm 1.6) \times 10^{-11}$	$(6.3 \pm 1.6) \times 10^{-11}$
1061_16C	1.0	1590	– [a]	$(7.1 \pm 1.6) \times 10^{-11}$	$(7.5 \pm 1.7) \times 10^{-11}$
1061_1B	0.1	1360	0.1 [b]	$(12 \pm 3) \times 10^{-11}$	$(9 \pm 2) \times 10^{-11}$
1061_2B	0.1	1510	10 [b]	$(12 \pm 4) \times 10^{-11}$	$(11 \pm 4) \times 10^{-11}$
1061_1C	1.0	1050	0.1 [b]	$(23 \pm 7) \times 10^{-11}$	$(13 \pm 4) \times 10^{-11}$

[a]   No extra $^{133}Cs^+$ added. Measured values during HTO diffusion were $< 3 \times 10^{-8}$ M.

[b]   Target concentrations of the solutions added. Measured values deviated from these values, because the clay was not in equilibrium with these solutions (for more explanations, *cf.* text).

[c] D_e values normalised to a reference ρ_{bd} of 1550 kg m^{-3}.

3.2.5.3   Results: Diffusion of $^{134}Cs^+$

Fig. 3.8 shows the reservoir concentrations and the $^{134}Cs^+$ profiles measured after the in-diffusion phase for the experiments 1061_16A–C, in which no stable Cs^+ has been added. For a first qualitative interpretation of these results, it is noticeable that the reservoir concentrations reflect a clear dependence on the concentration of the background electrolyte, as can be expected for cation-exchange. With decreasing concentration of the background electrolyte, the $^{134}Cs^+$ concentration in the reservoir solution decreases faster owing to less competition for cation-exchange sites between $^{134}Cs^+$ and Na^+.

The penetration depth is, if one disregards the differences of contact time, the same for all external salinities. In other words, D_a values are similar irrespective of the concentration of the background electrolyte. This shows that the D_e values for the diffusion of $^{134}Cs^+$ are also depending on the concentration of the background electrolyte, as was already observed in the preceding sections for the diffusion of Na^+ and Sr^{2+}. The modelling strategy was similar to that applied in

section 3.2.4, in that D_f, D_e and α were treated as adjustable parameters, whereby a minimum degree of freedom could be attributed to D_f (in view of the flushed-filter technique) otherwise it was not possible to model in a reasonable way the exact decrease in reservoir concentration during the phase where the diffusive flux was almost completely depending on the filter properties.
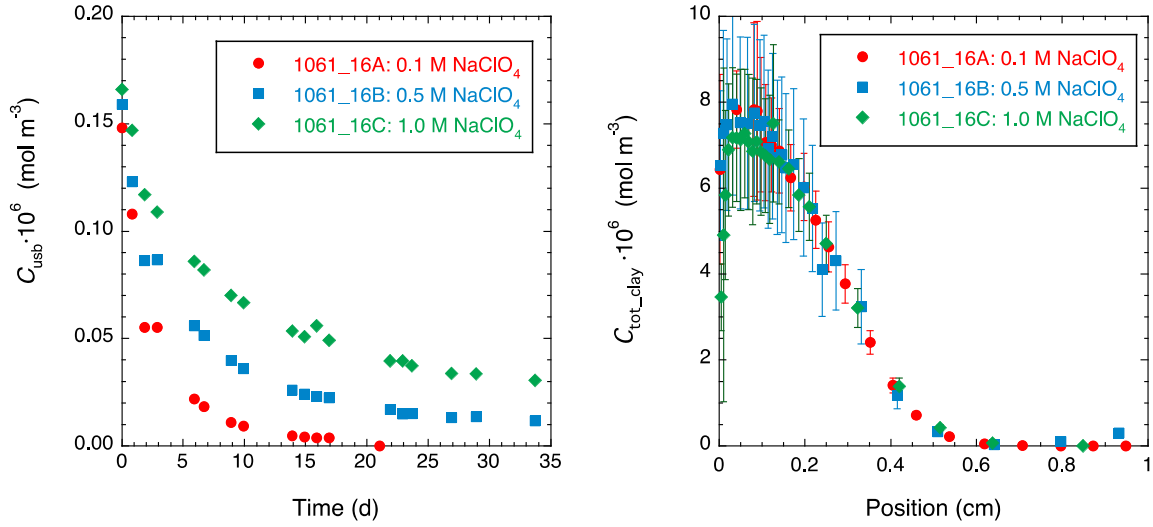
Fig. 3.8:   Evolution of the reservoir concentration (left hand plot) of $^{134}Cs^+$ in-diffusion into compacted Na-*mom* in the experiments where no stable Cs^+ was added; the right hand plot shows the tracer profiles measured at the end of the in-diffusion (21 d for 1061_16A, 34 d for 1061_16B and 16C).
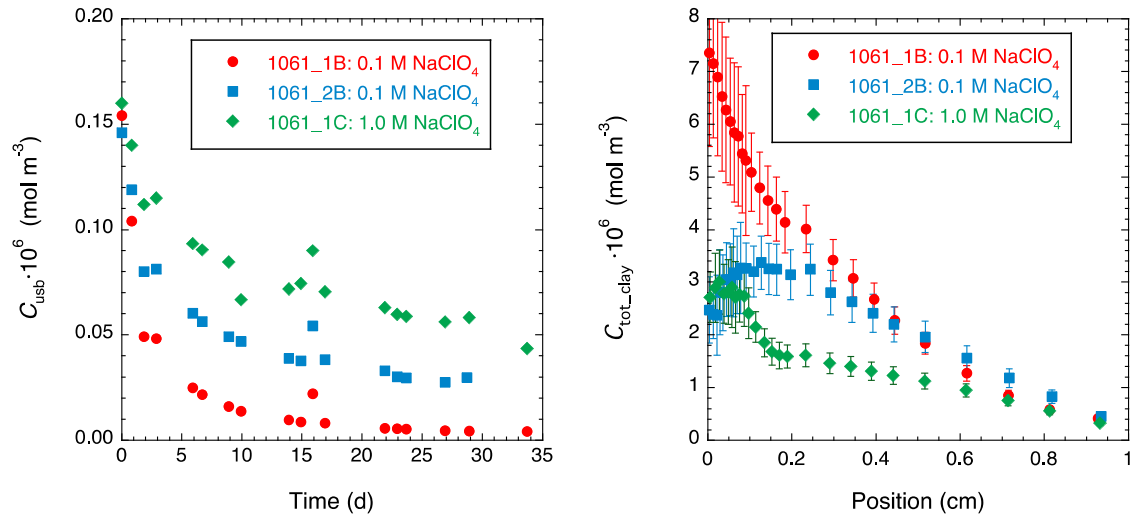
Fig. 3.9:   Evolution of the reservoir concentration (left hand plot) of $^{134}Cs^+$ in-diffusion into compacted Na-*mom* in the experiments with stable Cs^+ added; the right hand plot shows the tracer profiles measured at the end of in-diffusion (29 d for 1061_2B, 34 d for 1061_1B and 1C).

A clearly different picture was obtained in the experiments with stable Cs^+ added (*cf.* Fig. 3.9). While the reservoir concentrations exhibit a similar dependence on the concentration of the back-

ground electrolyte as in the experiments at trace concentration, the depth of the profiles is much larger, indicating that D_a values are larger. For a qualitative interpretation, it is at a first glance not clear, whether this effect shall be attributed to decreased R_d or increased D_e values. This question can be answered in the course of the determination of the best-fit parameter values, because there is a limited degree of freedom to determine α, once the range of possible D_f values is known.

Another striking feature in the profile data are the irregularities at the reservoir's side, particularly visible in the case of experiments 1061_1B and 1061_1C. From the distribution of stable Cs^+ (cf. Fig. 3.10) across the clay plugs also measured after the in-diffusion of $^{134}Cs^+$, the reason for the increased contents of $^{134}Cs^+$ near the reservoir's boundary can readily be understood. These data are recalculated in Fig. 3.10 to relative contents with respect to the CEC in order to make visible the differences between target and measured loadings of the clay with Cs^+.
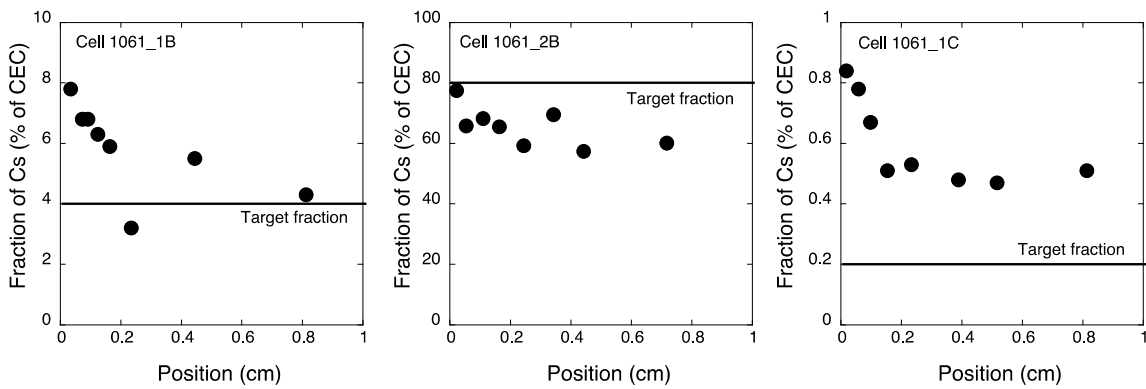
Fig. 3.10:   Distribution of stable $^{133}Cs^+$ across the clay samples measured after the in-diffusion of $^{134}Cs^+$.

The data are expressed in relation to the CEC using a value of 0.85 mmol g^{-1}.

Fig. 3.10 shows that the target values of $^{133}Cs^+$ loading are fairly well met, but also that the distribution is not homogeneous, but rather increased at the reservoir's boundary. In agreement with the observation of increased selectivity of bentonite for Cs with increasing bulk-dry density, such a dependency can also be postulated for the present case, where the clay is Na-*mom*. The distribution is inhomogeneous because the time given for equilibration of the clay with the external electrolyte solution (~ 60 d) is simply not enough to homogeneously saturate the sample with $^{133}Cs^+$. According to isotopic equilibrium between $^{134}Cs^+$ and $^{133}Cs^+$, the contents of the former isotope are also increased at the reservoir's boundary. In order to keep the modelling of the data at a reasonable level of complexity the profile data between 0 and 0.2 cm were, however, not taken into account for the modelling of the experiments where stable Cs was added.

As the only remaining irregularity the inhomogeneous distribution of the bulk-dry density was taken into account for modelling of the data. As an example, this distribution is shown in Fig. 3.11 for cell 1061_2B. In order to avoid numerical artefacts caused by the scatter of the data, the bulk-dry density profiles were approximated by an empiric exponential expression of the form:

$$\rho_{bd} = a\left(1 - e^{-bx-c}\right)e^{-dx}$$

(3.4)

where x is the position of the segment and a, b, c and d are adjustable parameters.
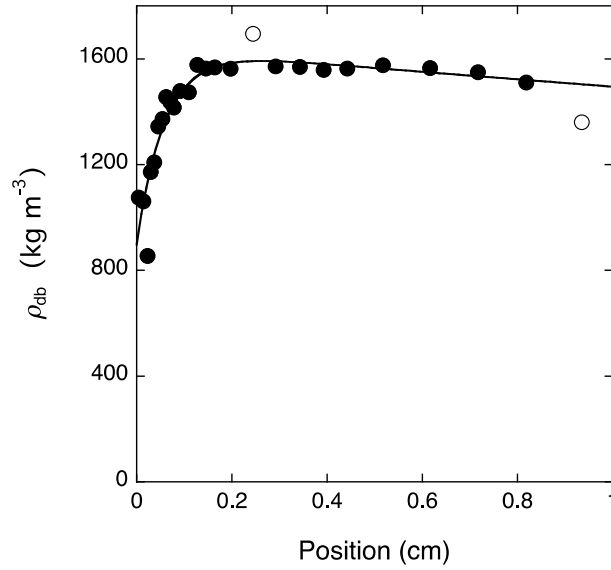
Fig. 3.11:   Measured bulk-dry density in sample 1061_2B and fitting the data (filled symbols considered, open symbols treated as outliers) by Eq. (3.2).

Using such empiric functional dependencies, a functional relationship between α and the position x can be devised:

$$\alpha_{(x)} = R_d \cdot \rho_{\text{bd}(x)} + \varepsilon \tag{3.5}$$

It would even be possible to take into account a dependence of R_d on the bulk-dry density according to the observation that the selectivity of bentonite for Cs increases with increasing bulk-dry density (Van Loon & Glaus 2008). However, this would lead to an excessive increase of degree of freedom. A few preliminary calculations showed that such a refinement of the modelling may lead to a slight, but rather insignificant improvement of the agreement between the data and the model. For this reason, position-independent values of R_d were assumed for the modelling of the experimental data. Figs. 3.12a and b show exemplarily a series of fit curves with variable D_e values for two fixed D_f values (10^{-9} and 3×10^{-9} m^2 s^{-1}, which can be taken approximately as the range of possible D_f values). From these two simulations it becomes evident that the reservoir concentration fits are sensitive only on variations of D_f, while the profiles almost don't change. The best fit of the data is obtained for $D_e = 9 \times 10^{-10}$ m^2 s^{-1} with an estimated relative uncertainty of $\sim 20\%$. The determination of the best-fit parameter values for the other experiments was carried out in a similar way. They are given in Tab. 3.10, and the best-fit curves are shown in Appendix A6.
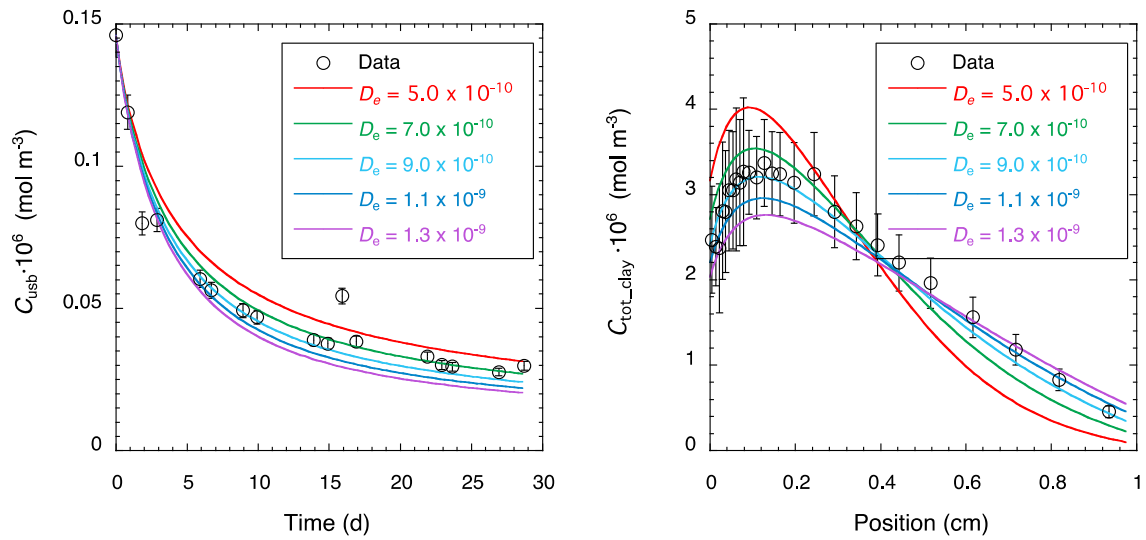
Fig. 3.12a: Fit of the reservoir concentration (left hand plot) and the tracer profile (right hand plot) in experiment cell 1061_2B using fixed values for D_f (10^{-9} m^2 s^{-1}) and R_d (0.10 m^3 kg^{-1}) and the dependence of the bulk-dry density shown in Fig. 3.11.

D_e (m^2 s^{-1}) was varied as indicated in the legend.
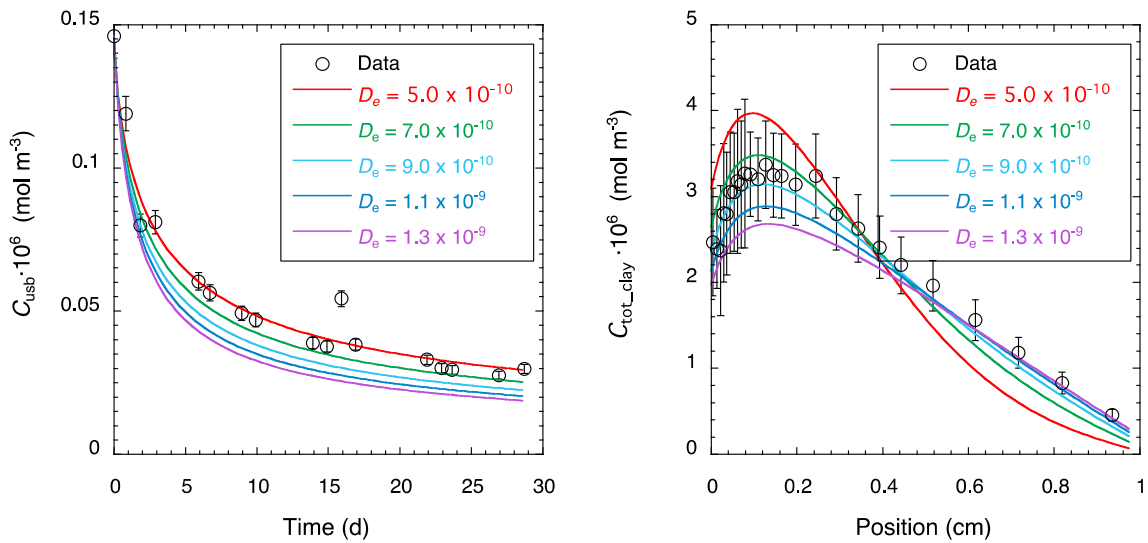
Fig. 3.12b: Fit of the reservoir concentration (left hand plot) and the tracer profile (right hand plot) in experiment cell 1061_2B using fixed values for D_f (3×10^{-9} m^2 s^{-1}) and R_d (0.10 m^3 kg^{-1}) and the dependence of the bulk-dry density shown in Fig. 3.11.

D_e (m^2 s^{-1}) was varied as indicated in the legend.

Tab. 3.10:   Summary D_e values for the in-diffusion of $^{134}Cs^+$.

Label	NaClO$_4$ [M]	ρ_{bd} [kg m^{-3}]	$^{133}Cs^+$ [mM]	D_e ^{134}Cs [m^2 s^{-1}]	R_d [m^3 kg^{-1}]
1061_16A	0.1	1550	– [a]	$(4.0 \pm 0.8) \times 10^{-9}$	1.65 ± 0.33
1061_16B	0.5	1540	– [a]	$(7.0 \pm 1.0) \times 10^{-10}$	0.42 ± 0.08
1061_16C	1.0	1590	– [a]	$(3.6 \pm 0.5) \times 10^{-10}$	0.21 ± 0.04
1061_1B	0.1	1360	0.1 [b]	$(3.2 \pm 0.6) \times 10^{-9}$	0.75 ± 0.11
1061_2B	0.1	1510	10 [b]	$(9.0 \pm 2.0) \times 10^{-10}$	0.10 ± 0.02
1061_1C	1.0	1050	0.1 [b]	$(4.5 \pm 0.5) \times 10^{-10}$	0.035 ± 0.005

[a]   No extra $^{133}Cs^+$ added. Measured values during HTO diffusion were $< 3 \times 10^{-8}$ M.

[b]   Target concentrations of the solutions added. Measured values deviated from these values, because the clay was
       not in equilibrium with these solutions (for more explanations, *cf.* the text).

3.3   Diffusion of $^{36}Cl^-$ (combined with HTO): Bulk-dry densities of 1300 and 1600 kg m^{-3}

The combined diffusion of HTO and $^{36}Cl^-$ was measured at bulk-dry densities of 1300 and 1600 kg m^{-3} and at background electrolyte concentrations (NaClO$_4$) of 0.5 and 1.0 M in a similar layout as for the combined diffusion of HTO and $^{22}Na^+$ (*cf.* section 3.2.1). Following the out-diffusion of these tracers (not monitored), through-diffusion of $^{22}Na^+$ and subsequently of $^{85}Sr^{2+}$ was measured separately. The tracer fluxes of the latter measurements gave a disordered picture, particularly for the flux data of $^{85}Sr^{2+}$. It was presumed that these effects might have been caused by the use of thinner confining filters (thicknesses of 1.0 mm instead of 1.6 mm). The shape of these thin filters had a more bevelled edge profile resulting in a worse confinement for the swelling clay compared to the situation with 1.6 mm filters. For all these uncertainties the results of the experiments of $^{22}Na^+$ and $^{85}Sr^{2+}$ were not used in the present report. However, no significant discrepancies could be noted for the results for HTO of the present experiment and those described in section 3.2.1. Because the experiments with $^{36}Cl^-$ were carried out simultaneously with HTO, these results can be used with similar reliability and are therefore reported in the following.

The results for the through-diffusion experiments of HTO and $^{36}Cl^-$ are given in Tab. 3.11, the experimental data in Appendix A7. In agreement with the findings of Van Loon et al. (2007), D_e values for $^{36}Cl^-$ are smaller than those of HTO throughout. A trend of increasing D_e and α values for $^{36}Cl^-$ with increasing concentration of the background electrolyte is visible, while no such dependence is observed for HTO. After the through-diffusion experiments the clay samples were cut into segments and the concentration profile of the ClO_4^- anion was measured by ion chromatography. The data showed a similar picture as the measurements shown in Fig. A7 and A8, exhibiting the typical features of increased total porosity and anion accessible porosity near the boundaries between clay and filters. For a very accurate determination of D_e and α such inhomogeneities would have to be taken into account according to the methods described in Glaus et al. (2011). A few test calculations showed that the systematic bias in the best-fit parameter values was less than 10 % and thus less than the experimental uncertainties given in Tab. 3.11. One may, however, note that the best-fit parameter values given in Tab. 3.11 may systematically underestimate the true values by $\sim 5 – 10$ %.

Tab. 3.11:   Results of the through-diffusion experiments with $^{36}Cl^-$ (and simultaneously measured HTO) in compacted Na-*mom* [a].

Cell label	ρ_{bd} [kg m^{-3}]	ε [–]	NaClO$_4$ [M]	Tracer	D_e [b] [m^2 s^{-1}]	α [b] [–]
1045_1A	1308	0.53	0.5	$^{36}Cl^-$	$(1.4 \pm 0.1) \times 10^{-11}$	0.20 ± 0.03
				HTO	$(7.6 \pm 1.1) \times 10^{-11}$	0.60 ± 0.15
1045_1B	1304	0.53	0.5	$^{36}Cl^-$	$(1.3 \pm 0.1) \times 10^{-11}$	0.22 ± 0.03
				HTO	$(7.7 \pm 1.1) \times 10^{-11}$	0.65 ± 0.15
1045_2A	1282	0.54	1.0	$^{36}Cl^-$	$(1.6 \pm 0.2) \times 10^{-11}$	0.35 ± 0.05
				HTO	$(7.9 \pm 1.2) \times 10^{-11}$	0.76 ± 0.17
1045_2B	1317	0.53	1.0	$^{36}Cl^-$	$(1.4 \pm 0.2) \times 10^{-11}$	0.35 ± 0.05
				HTO	$(7.6 \pm 1.1) \times 10^{-11}$	0.81 ± 0.17
1045_3A	1623	0.42	0.5	$^{36}Cl^-$	$(2.2 \pm 0.5) \times 10^{-12}$	0.09 ± 0.02
				HTO	$(3.5 \pm 0.5) \times 10^{-11}$	0.49 ± 0.09
1045_3B	1623	0.42	0.5	$^{36}Cl^-$	$(1.9 \pm 0.5) \times 10^{-12}$	0.09 ± 0.03
				HTO	$(3.2 \pm 0.5) \times 10^{-11}$	0.49 ± 0.09
1045_4A	1622	0.42	1.0	$^{36}Cl^-$	$(3.7 \pm 0.3) \times 10^{-12}$	0.12 ± 0.01
				HTO	$(3.5 \pm 0.6) \times 10^{-11}$	0.50 ± 0.10
1045_4B	1623	0.42	1.0	$^{36}Cl^-$	$(2.4 \pm 0.3) \times 10^{-12}$	0.13 ± 0.02
				HTO	$(3.1 \pm 0.5) \times 10^{-11}$	0.54 ± 0.10

[a]   Experimental details: Combined-tracer experiment; *SFDC* (10 μm filter pore size); sample geometry (diameter × thickness): 25.6 mm × 11.5 mm; volume at upstream side: 190 ml; volume at downstream side: 10 – 100 ml; observation time: ~ 50 d.

[b]   Evaluation of best-fit parameter values by calculation of numerical solutions in Comsol Multiphysics® assuming a homogeneous porosity distribution: Non-stationary boundary conditions with given initial reservoir concentration; D_f set to 1.2×10^{-10} m^2 s^{-1} for $^{36}Cl^-$ and 1.5×10^{-10} m^2 s^{-1} for HTO (measured at the end of the experiment).

3.4   Diffusion of cations: Bulk-dry density of 1900 kg m^{-3}

3.4.1   Diffusion of $^{85}Sr^{2+}$

Previous measurements for $^{22}Na^+$ and $^{85}Sr^{2+}$ at ρ_{bd} of 1900 kg m^{-3} are published in the open literature (Glaus et al. 2007, Glaus et al. 2010) with the exception of a few experiments with $^{85}Sr^{2+}$ described in the following.

The aim of experiment TON.1027 was to obtain more information on the possible reasons for the irregularities in the flux curves of $^{85}Sr^{2+}$ diffusion (*cf.* Fig. 3 in Glaus et al. 2007). Typically, two phases of diffusion with differing parameter characteristics can be distinguished. If the first part only of the data is used for the determination of D_e and α, the resulting modelled data underestimate the flux values measured in the second part of the experiment. If the latter group is chosen for determining D_e, the opposite is the case for the first group. The best-parameter values were therefore chosen to represent a compromise between those two phases of the experiment. One explanation could be a slow geometrical rearrangement of the clay particles leading to changes in the connectivities between the individual pore spaces and consequently to changes in the geometric factors. In the course of experiment TON.1027 this option was tested by several measure-

ments of HTO diffusion during a single diffusion measurement of $^{85}Sr^{2+}$. The combination of these two tracers can be handled by the same analytical procedures as the combination of $^{22}Na^+$ and HTO (*cf.* section 2.3.1), because the decay of HTO produces no response in γ-counting. The activity of $^{85}Sr^{2+}$ is therefore available directly from the latter measurement and can be used for correction of the mixed signal of both isotopes in the liquid scintillation counting. The diffusion experiments were started with a mixed reservoir solution of both isotopes and followed until the diffusive flux of HTO reached the steady-state phase. After that the reservoir solution was exchanged by a fresh solution with its concentration of $^{85}Sr^{2+}$ matching the previous one, but devoid of HTO. The latter solution was twice exchanged against a fresh $^{85}Sr^{2+}$ reservoir solution in a time lag of 1 week. Three exchanges in total were sufficient to bring down the activity of HTO to a negligible level so that a restart of HTO diffusion was in principle possible. No special care was taken to keep the volume of the tracer reservoir solutions constant. For this reason, the decrease of $^{85}Sr^{2+}$ concentration in the reservoir was not homogeneous with respect to time evolution. This special situation was taken into account in the modelling of the experiments by defining the time dependence of the up-stream boundary condition according to the measured tracer concentrations in the reservoir solution across the whole duration of the experiment. This is in contrast to the commonly applied procedure, where the initial concentration at time zero only was fixed and the further evolution of the reservoir concentration was calculated according to the modelled loss of tracer owing to diffusion and sorption in the clay and the filters.

The results of experiment TON.1027 are summarised in Tab. 3.12. The respective flux curves and the evolution of the reservoir concentrations are shown in Appendix A8. In agreement with previously published data on $^{85}Sr^{2+}$ diffusion, the flux curves obtained in the experiments with 10 mm thick clay plugs are in good agreement with the fit curves, while those of the experiments with 5.4 mm thick samples exhibit the previously observed bi-phasic characteristics. The increase of $^{85}Sr^{2+}$ fluxes in the final phase of the experiment can probably be explained by the decreased sampling intervals in that phase. Such effects are rather omitted from the present discussion; an in-depth explanation can be found in Glaus et al. (2015b). The HTO results show no discrepancies within the three repeat measurements, suggesting that the geometric properties of the clay plugs remain constant during the complete phase of $^{85}Sr^{2+}$ diffusion. To this end no satisfying explanation for this irregular behaviour of $^{85}Sr^{2+}$ diffusion could be found. One possible reason might be a very slow diffusion path that could be an explanation for the slight increase of the tracer flux in the near steady-state phase. In view of the fact that the sample is several millimetres thick and that the length of a representative element volume is on the micrometre scale, such a view appears to be rather implausible.

Tab. 3.12:   Results of combined through-diffusion experiments (labelled TON.1027) with $^{85}Sr^{2+}$ and HTO in compacted Na-*mom* in 1.0 M NaClO$_4$.

During the entire observation time of $^{85}Sr^{2+}$ diffusion, HTO diffusion was repeatedly measured (denoted to as HTO #1, HTO #2 and HTO #3). The detailed sequence of the experiments can be taken from Appendix A8.

Label	ρ_{bd} [kg m^{-3}]	ε [–]	d [mm]	Tracer	D_e [a] [m^2 s^{-1}]	α [a] [–]
1027_5A [b]	1956	0.30	5.28	$^{85}Sr^{2+}$	$(1.2 \pm 0.2) \times 10^{-11}$	5.0 ± 0.6
				HTO #1	$(1.5 \pm 0.2) \times 10^{-11}$	0.42 ± 0.05
				HTO #2	$(1.6 \pm 0.2) \times 10^{-11}$	0.40 ± 0.05
				HTO #3	$(1.6 \pm 0.2) \times 10^{-11}$	0.42 ± 0.06
1027_5B [b]	1950	0.30	5.26	$^{85}Sr^{2+}$	$(1.3 \pm 0.2) \times 10^{-11}$	5.0 ± 0.6
				HTO #1	$(1.7 \pm 0.3) \times 10^{-11}$	0.43 ± 0.15
				HTO #2	$(1.7 \pm 0.3) \times 10^{-11}$	0.43 ± 0.15
				HTO #3	$(1.7 \pm 0.4) \times 10^{-11}$	0.42 ± 0.15
1027_10C [c]	1962	0.30	10.34	$^{85}Sr^{2+}$	$(8.0 \pm 1.0) \times 10^{-12}$	3.0 ± 0.4
				HTO #1	$(1.5 \pm 0.2) \times 10^{-11}$	0.40 ± 0.05
				HTO #2	$(1.5 \pm 0.2) \times 10^{-11}$	0.40 ± 0.06
				HTO #3	$(1.5 \pm 0.2) \times 10^{-11}$	0.40 ± 0.06
1027_10D [c]	1958	0.30	10.31	$^{85}Sr^{2+}$	$(8.0 \pm 1.1) \times 10^{-12}$	3.0 ± 0.4
				HTO #1	$(1.4 \pm 0.2) \times 10^{-11}$	0.38 ± 0.05
				HTO #2	$(1.5 \pm 0.2) \times 10^{-11}$	0.38 ± 0.06
				HTO #3	$(1.5 \pm 0.2) \times 10^{-11}$	0.35 ± 0.06

[a]   Evaluation of best-fit parameter values by calculation of numerical solutions in Comsol Multiphysics®: Non-stationary boundary conditions with given reservoir concentration as a function of time according to the measured concentrations in the reservoir solution; D_f set to 6×10^{-11} m^2 s^{-1} for $^{85}Sr^{2+}$ and 1.1×10^{-10} m^2 s^{-1} for HTO (generic values).

[b]   Experimental details: Combined-tracer experiment; *SFDC* (10 µm filer pore size); sample geometry (diameter × thickness): 25.6 mm × 5.4 mm; volume of source reservoir: 190 ml; volume of target reservoirs: 10 – 50 ml; observation time for $^{85}Sr^{2+}$ diffusion: 204 d.

[c]   Experimental details: Combined-tracer experiment; *SFDC* (10 µm filter pore size); sample geometry (diameter × thickness): 25.6 mm × 10.4 mm; volume of source reservoir: 180 ml; volume of target reservoirs: 10 – 30 ml; observation time for $^{85}Sr^{2+}$ diffusion: 430 d.

Another unsolved question is the discrepancy between sorption distribution coefficients determined from measured tracer profiles and from break-through times. This issue is exemplarily shown using the data of cell 10C. A similar picture was obtained from the other experiments in series TON.1027. The measured tracer profile is shown in Fig. 3.13. Extrapolation of the amount of tracer to the up-stream boundary at the interface between clay and filter by linear regression yields 4.43×10^{-14} mol g^{-1} of dry clay.
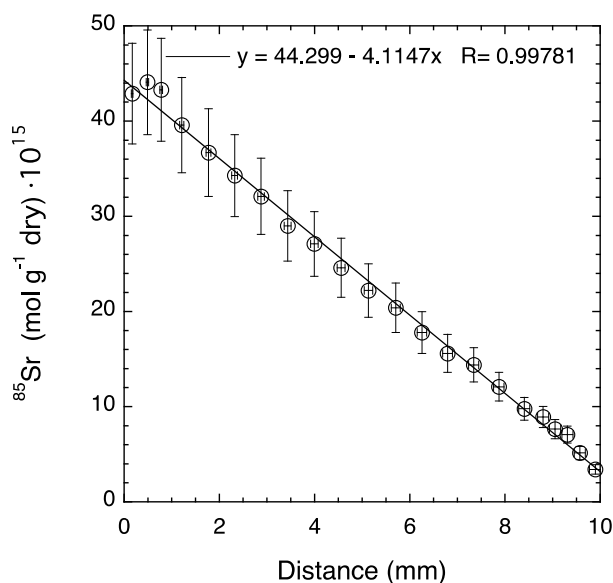
Fig. 3.13:   Profile of $^{85}Sr^{2+}$ measured after through-diffusion (experiment 1027_10C).

The tracer concentration in the reservoir solution at termination of the through-diffusion was 1.12×10^{-14} mol cm^{-3}. Owing to the relatively low diffusive tracer fluxes in the clay, the concentration gradients on the filters are almost insignificant and, despite some uncertainties with respect to the filter properties, the solution concentration at the interface between filter and clay can be predicted with rather high reliability to be 1.07×10^{-14} mol cm^{-3}. The R_d calculated as the ratio of solid concentration divided by solution concentration is thus of the order of 4.1×10^{-3} m^3 kg^{-1}, and $\alpha = 8.4$. This is much larger than the value given in Tab. 3.12 (3.0 ± 0.4) and far beyond all uncertainties involved. Again, no explanation for this inconsistency has so far been found. It has been observed in tracer profiles of $^{85}Sr^{2+}$ throughout (*cf.* the discrepancies between R_d values calculated from flux data and from tracer profiles in Glaus et al. 2007), whereas no such discrepancies are usually noted for $^{22}Na^+$ diffusion data. This issue has not yet found due attention in the literature. Note that HTO profiles were also measured after termination of the through-diffusion experiments. The extrapolated concentrations were in good agreement with the reservoir solution concentrations (data not shown).

Another experiment investigating the diffusion of $^{85}Sr^{2+}$ through *Na-mom* at bulk-dry densities of ~ 1900 kg m^{-3} is labelled as TON.1023. The aim of this experiment was to measure the diffusion of $^{85}Sr^{2+}$ at the lowest salinities practicable for the static filter cell technique in order to corroborate more broadly the quadratic dependence of D_e values of the bivalent Sr^{2+} on the concentration of the background electrolyte. The experiment is thus to be viewed as an extension of the parameter range to the already published results for 0.5 and 1.0 M NaClO$_4$ (Glaus et al. 2007). At the time when this experiment was carried out, the flushed-filter technique was not yet available. In view of the quadratic dependence of D_e values on the salinity for the bivalent Sr^{2+}, the scope of feasible salinities was rather limited. The experiments were carried out at concentrations of 0.2 and 0.3 M using 10 mm thick clay samples. Relatively long experimental durations for such experiments were thus foreseeable.

The results of experiment TON.1023 are summarised in Tab. 3.13. In contrast to some observations previously made with $^{85}Sr^{2+}$ tracers (*cf.* experiment TON.1027 for example), the agreement of the results obtained from the flux and tracer profile data is fairly good. In other words, R_d values calculated from tracer breakthrough and from mass balance considerations at the interface between solution and clay are identical within the range of uncertainty.

No valuable explanation is available for obtaining partially contradicting evidences from seemingly equal experiments (TON.1023 and TON.1027). The reason might be related to the porosity inhomogeneities of the clay samples near the clay boundaries and the observed dependency of R_d values on bulk-dry density (as will be discussed in section 5.4). Filter effects, which are more pronounced in the experiments carried out at low ionic strength, can rather be excluded. The consistency of the R_d values is rather good exactly in these experiments. In view of the rather similar duration of the experiments and the similar values of the D_a values involved, potential time scaling effects are difficult to evaluate. The variation of clay thickness in the experiments TON.1027 is probably not significant enough for an unambiguous discussion.

Tab. 3.13: Results of through-diffusion experiments (labelled TON.1023) with $^{85}Sr^{2+}$ in compacted Na-*mom* at low external salinities [a].

Label	ρ_{bd} [kg m^{-3}]	ε [–]	NaClO$_4$ [M]	Diffusion	D_e [b] [m^2 s^{-1}]	α [b] [–]
1023_10A	1910	0.32	0.2	through Profile	$(2.6 \pm 0.9) \times 10^{-10}$ $(1.8 \pm 0.5) \times 10^{-10}$	100 ± 22 87 ± 19
1023_10B	1956	0.30	0.2	through Profile	$(2.0 \pm 0.5) \times 10^{-10}$ $(1.5 \pm 0.4) \times 10^{-10}$	95 ± 22 92 ± 18
1023_10C	1895	0.32	0.3	through Profile	$(1.0 \pm 0.2) \times 10^{-10}$ $(0.90 \pm 0.2) \times 10^{-10}$	65 ± 13 61 ± 9
1023_10D	1952	0.30	0.3	through Profile	$(1.1 \pm 0.2) \times 10^{-10}$ $(6.5 \pm 1.7) \times 10^{-11}$	75 ± 15 65 ± 15

[a] Experimental details: Single-tracer experiment; *SFDC* (10 μm filter pore size); sample geometry (diameter × thickness): 25.6 mm × 10.4 mm; volume of source reservoir: ~ 1000 ml; volume of target reservoirs: 6 – 200 ml; observation time: ~ 420 d.

[b] Best-fit parameter values were evaluated using $c_{usb}(t)$ and $J_{dsb}(t)$ as the fitted data. The Comsol Multiphysics® model uses non-stationary boundary conditions with given reservoir concentration as a function of time according to the measured concentrations in the reservoir solution; evolution of concentration in the down-stream reservoir taken into account according to measured values; D_f was set to 6×10^{-11} m^2 s^{-1} (1023_10A and B) and 7×10^{-11} m^2 s^{-1} (1023_10C and D).

3.4.2 Through-diffusion of $^{134}Cs^+$

Through-diffusion measurements of $^{134}Cs^+$ at conditions, under which the majority of Cs surface species is bound to strong sorption sites (viz. at low Cs concentrations) cannot readily be done in highly compacted smectites within reasonable time. Nevertheless a few tests were carried out using Na-*mom* samples with thicknesses of ~ 1 mm, for which breakthrough times of a couple of months could be expected. These tests served rather for look-and-see purposes testing the validity of results obtained with thin clay samples. It had to be expected that the impact of the boundary issues observed for compacted Na-*mom* samples increases with decreasing sample thickness. In order to keep the sorption equilibrium of Cs at a manageable level, all experiments were carried out using 1.0 M NaClO$_4$ as the background electrolyte.

The results obtained reflected indeed the expected difficulties. The downstream fluxes exhibited a large scattering, and the tracer profiles measured at the end-of through-diffusion were almost completely flat. It is reasonable to assume that the scatter of the downstream flux data reflects the oscillations induced by the temporal changes in the local tracer distribution in the clay at the downstream boundary. It has been shown that such phenomena can be handled using appropriate

numerical models, which take into account the increase of tracer concentration in the downstream reservoir instead of assuming a zero-tracer concentration boundary (Glaus et al. 2015b). However, even the application of such models (using a time average of the downstream reservoir concentration) failed to exactly represent the experimental data. As can be seen from the Figures in Appendix A9, the fit curves exhibited some minor temporal instabilities, while the scatter of the experimental data was much larger. Some unknown phenomena appear to amplify the local gradient effects. Owing to the stochastic nature of this scattering and in view of the abundant set of data points, an evaluation of the experiments appears yet to be promising. Tab. 3.14 summarises the best-fit parameter values obtained. The most important feature in these data is the increase of R_d with increasing bulk-dry density. This phenomenon has already been observed for bentonite (Van Loon & Glaus 2008) and has been explained by the difference in the hydration enthalpies of Na^+ and Cs^+ resulting in the observed dependence of the selectivity for the exchange of these two cations on the hydration state of the interlayer porosity. Interestingly the values for D_e are almost invariant with bulk-dry density and the respective sorption values.

Tab. 3.14:   Results of through-diffusion of $^{134}Cs^+$ combined with tracer profile analysis in compacted Na-*mom* (experiment TON.1034) [a].

The contacting background electrolyte was 1 M NaClO$_4$.

Label	ρ_{bd} [kg m^{-3}]	ε [–]	D_e [b] [m^2 s^{-1}]	α [b] [–]	D_f [b] [m^2 s^{-1}]	R_d [c] [m^3 kg^{-1}]
1034_13C	1365	0.52	$(4.1 \pm 1.7) \times 10^{-10}$	186 ± 48	$(9.5 \pm 0.8) \times 10^{-11}$	0.14 ± 04
1034_13D	1355	0.52	$(3.1 \pm 1.6) \times 10^{-10}$	199 ± 51	$(7.5 \pm 0.8) \times 10^{-11}$	0.15 ± 0.04
1034_16A	1667	0.42	$(2.7 \pm 1.4) \times 10^{-10}$	473 ± 201	$(7.0 \pm 1.3) \times 10^{-11}$	0.28 ± 0.12
1034_16B	1657	0.42	$(1.9 \pm 1.0) \times 10^{-10}$	453 ± 156	$(9.8 \pm 1.6) \times 10^{-11}$	0.27 ± 0.09
1034_19A	1978	0.31	$(3.4 \pm 0.4) \times 10^{-10}$	3163 ± 352	$(4.8 \pm 0.3) \times 10^{-11}$	1.6 ± 0.18
1034_19B	1949	0.32	$(1.2 \pm 0.2) \times 10^{-10}$	2016 ± 291	$(4.3 \pm 0.3) \times 10^{-11}$	1.03 ± 0.15

[a]   Experimental details for through-diffusion: Single-tracer experiment; stagnant filters (10 µm pore size); sample geometry (diameter × thickness): 25.6 mm × 1 – 2 mm; volume of source reservoir: 200 – 1000 ml; volume of target reservoir: 10 – 100 ml; observation time: ~ 180 – 850 d.

[b]   Best-fit parameters values obtained from Matlab® script parameter optimisation using a 1-D-*chds* Comsol Multiphysics® model and c_{usb}(t), J_{dsb}(t) and C_{tot_clay}(x) as the fitted data. Non-stationary boundary conditions with given initial reservoir concentration for through-diffusion and a time average function C_{dsb}(t) was applied for all cases. A homogeneous distribution of bulk-dry density was assumed for simplicity and because no significant variability was observed in the measurements of dry weight of the clay segments.

[c]   Derived from best-fit parameter values.

3.5   Diffusion of anions: Bulk-dry density of 1900 kg m^{-3}

3.5.1   Through- and out-diffusion of $^{35}SO_4^{2-}$

The diffusion of $^{35}SO_4^{2-}$ was measured for the general interest in the inter-comparison between negatively charged species with different net charge. There is, however, the difficulty of finding negatively charged inorganic species with similar inertness as for the chloride anion for example. Sulfate was chosen for this purpose owing to the relatively good solubility of various salts with cations from the alkaline and earth-alkaline series.

The measurements were carried out at a single bulk-dry density (1900 kg m^{-3}) whereby the concentration of the background electrolyte was varied in order to assess the anion-exclusion effects. The results are summarised in Tab. 3.15 and in Appendix A10. The measurements were characterised by two unexpected issues: (i) an interaction between the $^{35}SO_4^{2-}$ tracer and Na-*mom* took place leading to large break-through times and thus to long experimental durations. (ii) Some sort of discontinuities in the source reservoir concentrations was measured, for which no good explanation was available. The measured concentration values were thus directly used as a boundary condition for the simulations shown in the Appendix. This is in contrast to the usual procedure, in which only the initial concentration has been used as a given input value and the decrease in tracer concentration was calculated from the modelled loss of mass in the reservoir. However, the question of which of these two options is preferred, turned out as of minor importance for the evaluation of the best-fit parameter values. No effects of inhomogeneous distribution of clay porosity near the boundaries to the confining filters were taken into account for the evaluation of the best-fit parameter values. For the lowest background electrolyte concentrations, out-diffusion was followed after through-diffusion. These tests served rather for qualitative purposes than for the evaluation of best-fit parameter values.

As can be expected for anion-exclusion phenomena, the data exhibit clear trends of increasing D_e values with increasing ionic strength. Also, the α values increased with increasing concentration of the background electrolyte. The values measured for 1.0 M NaClO$_4$ experiments clearly indicate some interaction between the $^{35}SO_4^{2-}$ tracer and Na-*mom*, because the α values were larger than the total porosity. It may be assumed that the interaction between $^{35}SO_4^{2-}$ and Na-*mom* is not a simple competition between $^{35}SO_4^{2-}$ and the ClO$_4^-$ anion, but rather the result of an isotopic exchange process. Indications for the presence of sulfate containing mineral phases in Na-*mom* were found in the anion extraction profiles (*cf.* Fig. A12 to A14 in Appendix A1), where significant amounts of SO$_4^{2-}$ were detected upon extraction of the clay segments with water. The observed SO$_4^{2-}$ profiles indicate the presence of a sparingly soluble SO$_4^{2-}$ phase, which gets solubilised only in a slow process compared to the duration of a diffusion experiment. The uptake of the $^{35}SO_4^{2-}$ tracer by the solid phase is most probably also the reason for the rather unusual behaviour of this element in out-diffusion. Gypsum can be excluded as a candidate for this SO$_4^{2-}$-bearing mineral phase owing to its relatively good solubility. During the many washing steps in the conditioning procedure of the preparation of Na-*mom*, gypsum is expected to have dissolved completely.

Tab. 3.15:   Results of through- and out-diffusion experiments using $^{35}SO_4^{2-}$ in compacted Na-*mom* (experiment TON.1032) [a].

Label	ρ_{bd} [kg m^{-3}]	ε [–]	NaClO$_4$ [M]	D_e [b] [m^2 s^{-1}]	α [b, c] [–]
1032_1A [d]	1942	0.32	0.1	$(4.8 \pm 1.4) \times 10^{-15}$	0.0060 ± 0.0019
1032_1B [d]	1954	0.31	0.1	$(7.2 \pm 1.7) \times 10^{-15}$	0.0075 ± 0.0022
1032_2A	1945	0.32	0.5	$(7.0 \pm 1.1) \times 10^{-14}$	0.40 ± 0.10
1032_2B	1951	0.32	0.5	$(6.3 \pm 1.0) \times 10^{-14}$	0.40 ± 0.10
1032_3A	1962	0.31	1.0	$(1.2 \pm 0.2) \times 10^{-13}$	0.60 ± 0.10
1032_3B	1950	0.32	1.0	$(1.2 \pm 0.2) \times 10^{-13}$	0.50 ± 0.10

[a]   Experimental details for through-diffusion: Single-tracer experiment; stagnant filters (10 μm pore size); sample geometry (diameter × thickness): 25.6 mm × 5.2 mm; volume of source reservoir: 100 ml; volume of target reservoir: 5 ml; observation time: 260 – 810 d. Experimental details for out-diffusion: Same as for through-diffusion with solution volumes 5 ml; observation time: ~ 180 d.

[b]   Best-fit parameters values were calculated from through-diffusion data only, using average values of c_{usb} (t) and J_{dsb} (t) in the quasi-stationary flux phase of the experiment as an input for the analytical solution approximating this situation (Glaus et al. 2008). The parameter uncertainties were assessed from error propagation of the analytical solution. Effective diffusion coefficients for the filters were set to $D_f = (5.0 \pm 1.25) \times 10^{-11}$ m^2 s^{-1}.

[c]   No R_d values were determined from α because it is not possible to assess the accessible porosity independently.

[d]   Out-diffusion was only measured in these experiments. The results were only used for qualitative comparison purposes in a blind-prediction scenario based on the best-fit parameters of through-diffusion.

3.5.2   Through- and out-diffusion of $^{75}SeO_4^{2-}$

The diffusion of $^{75}SeO_4^{2-}$ was measured for the general interest in the inter-comparison between negatively charged species with different net charge and for the particular interest in this element as a dose relevant radionuclide. The experiments were carried out under the same conditions as the experiments with $^{35}SO_4^{2-}$, whereby out-diffusion was measured in all cases. A particular feature of these experiments was the small source reservoir volumes of ~ 10 ml. These were caused by the small amounts of $^{75}SeO_4^{2-}$ tracer available for the experiments (*cf.* section 2.1). In view of the long duration of the through-diffusion phase, a significant loss of water through evaporation was noted in the source reservoirs. This circumstance was taken into account in the Comsol Multiphysics® model by introducing an evaporation rate of ~ 10 μl d^{-1} which lead to a noticeable increase of the tracer concentration in the source reservoir and concomitantly also in the tracer flux at the downstream boundary. Otherwise these experiments were clearly less influenced by irregularities as was the case for the experiments with $^{35}SO_4^{2-}$. As was the case for this latter tracer, the out-diffusion of $^{75}SeO_4^{2-}$ is also largely deviating from the expected behaviour. No attempt was therefore made to extract independent information on the diffusive properties from the out-diffusion data.

The results are summarised in Tab. 3.16; the experimental data are shown in Appendix A11. A trend of increasing D_e and α values with increasing salinity can be observed which is, however, less clear than in the case of $^{35}SO_4^{2-}$.

Tab. 3.16:   Results of through- and out-diffusion experiments using $^{75}SeO_4^{2-}$ in compacted Na-*mom* (experiment TON.1059) [a].

Label	ρ_{bd} [kg m^{-3}]	ε [–]	NaClO$_4$ [M]	D_e [b] [m^2 s^{-1}]	α [b, c] [–]
1059_1A	1994	0.30	0.1	$(2.4 \pm 0.3) \times 10^{-14}$	0.027 ± 0.007
1059_1B	1989	0.30	0.1	$(2.4 \pm 0.3) \times 10^{-14}$	0.030 ± 0.008
1059_2A	1945	0.32	0.5	$(3.7 \pm 0.6) \times 10^{-14}$	0.06 ± 0.01
1059_2B	1951	0.32	0.5	$(3.2 \pm 0.5) \times 10^{-14}$	0.05 ± 0.01
1059_3A	1962	0.31	1.0	$(5.3 \pm 0.7) \times 10^{-14}$	0.06 ± 0.01
1059_3B	1950	0.32	1.0	$(6.1 \pm 0.7) \times 10^{-14}$	0.06 ± 0.01

[a]   Experimental details for through-diffusion: Single-tracer experiment; stagnant filters (10 µm pore size); sample geometry (diameter × thickness): 25.6 mm × 3 – 5 mm; volume of source reservoir: 10 ml; volume of target reservoir: 10 ml; observation time: 250 – 310 d. Experimental details for out-diffusion: Same as for through-diffusion with solution volumes 8 ml; observation time: ~ 180 d.

[b]   Best-fit parameters values were calculated from through-diffusion data only, using average values of $c_{usb}(t)$ and $J_{dsb}(t)$ in the quasi-stationary flux phase of the experiment as an input for the analytical solution (Glaus et al. 2008) approximating this situation. The parameter uncertainties were assessed from error propagation of the analytical solution. Effective diffusion coefficients for the filters were set to $D_f = (5.0 \pm 1.25) \times 10^{-11}$ m^2 s^{-1}. The out-diffusion data were only used for qualitative comparison purposes in a blind-prediction scenario based on the best-fit parameters of through diffusion.

[c]   No R_d values were determined from α because it is not possible to assess the accessible porosity independently.

4   Results for Diffusion in compacted Bentonite

4.1   Diffusion of HTO

Results for HTO diffusion in Volclay KWK were obtained by through- and out-diffusion. The following section summarises an experiment, in which the bulk-dry density and the type and concentration of the background electrolyte solution were varied. The background electrolyte solutions were commonly synthetic equilibrium pore waters. For each of bulk dry densities, the composition of these pore waters (abbreviated to BPW1300, BPW1600, BPW1900) was calculated based on the mineral phases present in the bentonite, the loading of the exchangeable cations and the presence of anions in the clay. Their composition is given in Van Loon & Glaus (2008). For each of the bulk dry densities, measurements using a $NaClO_4$ solution (0.3 M) of similar ionic strength are additionally available. For the bulk dry density of 1600 kg m^{-3} the $NaClO_4$ concentrations were further extended to a range between 0.01 and 1.0 M.

Approximately 26 % (Van Loon & Glaus 2008) of the cation exchange capacity of the starting material are occupied by bi-valent cations (Ca^{2+} and Mg^{2+}). It can be expected that parts of this inventory will be exchanged against Na^+ to a variable extent depending on the concentration of the background electrolyte. For a 1 M $NaClO_4$ solution almost all cation exchange sites will be present in the Na^+-form, while the original loading will be preserved more or less for 0.01 M $NaClO_4$. The duration of the re-saturation phase is sufficient to allow for the cation exchange processes to occur almost quantitatively. The experiments carried out at different concentrations of $NaClO_4$ will, strictly taken, not be directly comparable because D_e values in a Na-exchanged montmorillonite are lower by a factor of ~ 2.5 compared to a Ca-exchanged montmorillonite (González Sánchez et al. 2008b).

Tab. 4.1 gives an overview of the results obtained; the experimental data are shown in Appendix B1. No significant dependence of D_e and α on the salinity in the external solutions can be observed in the data. D_e values clearly decrease with increasing bulk-dry density. The difference between calculated porosity values and α is not significant. Consequently, no uptake of the tracer by the clay can be substantiated within the range of the uncertainties.

Tab. 4.1:　　Results of through- and out-diffusion experiments of HTO in compacted Volclay [a].

Label	ρ_{bd} [kg m^{-3}]	ρ_{mm} [kg m^{-3}]	ε [–]	Background electrolyte	D_e [b] [m^2 s^{-1}]	α [b] [–]
13A HTO	1306	1117	0.53	BPW1300	$(1.4 \pm 0.2) \times 10^{-10}$	0.50 ± 0.07
13B HTO	1320	1131	0.53	0.3 M NaClO$_4$	$(1.6 \pm 0.2) \times 10^{-10}$	0.50 ± 0.05
16A HTO	1598	1411	0.43	BPW1600	$(8.2 \pm 0.5) \times 10^{-11}$	0.43 ± 0.03
16B HTO	1603	1416	0.43	0.01 M NaClO$_4$	$(8.6 \pm 2.6) \times 10^{-11}$ $(8.6 \pm 2.6) \times 10^{-11}$	0.83 ± 0.44 0.45 ± 0.15
16C HTO	1613	1427	0.42	0.3 M NaClO$_4$	$(7.9 \pm 0.6) \times 10^{-11}$	0.41 ± 0.04
16D HTO	1602	1415	0.43	1.0 M NaClO$_4$	$(9.0 \pm 0.9) \times 10^{-11}$	0.41 ± 0.05
19A HTO	1911	1748	0.32	BPW1900	$(3.3 \pm 0.2) \times 10^{-11}$	0.36 ± 0.03
19B HTO	1886	1721	0.33	0.3 M NaClO$_4$	$(3.4 \pm 0.1) \times 10^{-11}$	0.35 ± 0.03

[a]　Experimental details for through-diffusion: Single-tracer experiment; stagnant filters (10 μm pore size); sample geometry (diameter × thickness): 25.6 mm × 10.4 mm; volume of source reservoir: 200 ml; volume of target reservoir: 20 – 100 ml; observation time: 14 – 20 d. Experimental details for out-diffusion: Same as for through-diffusion with solution volumes of 20 ml; observation time: ~ 20 – 25 d (depending on clay compaction).

[b]　Best-fit parameters values obtained from Matlab® script parameter optimisation using a 1-D-*chds* Comsol Multiphysics® model using $c_{usb}(t)$ and $J_{dsb}(t)$ as the fitted data in through-diffusion and $J'_{usb}(t)$ and $J'_{dsb}(t)$ in out-diffusion. Non-stationary boundary conditions with given initial reservoir concentration for through-diffusion and given effective diffusion coefficients for the filters: D_f: $(2.0 \pm 0.5) \times 10^{-10}$ m^2 s^{-1}. The assumption of $C_{dsb} = 0$ was applied for all cases. The out-diffusion data were only used for qualitative comparison purposes in a blind-prediction scenario based on the best-fit parameters of through diffusion. Only in the case of experiment 16B HTO, significant discrepancies between through- and out-diffusion was observed. The results obtained from out-diffusion are given on a separate line.

4.2　　　　Diffusion of ^{22}Na$^+$

Results for ^{22}Na$^+$ diffusion in Volclay KWK were obtained from experiments in which three different bulk-dry densities (1300, 1600 and 1900 kg m^{-3}) were tested. The background electrolyte solutions were synthetic equilibrium pore waters (abbreviated to BPW1300, BPW1600, BPW1900). For each of the bulk dry densities, the composition of these pore waters was calculated based on the mineral phases present in the bentonite, the loading of the exchangeable cations and the presence of anions in the clay (Van Loon & Glaus 2008). For each of bulk dry densities duplicate through-diffusion experiments were carried out (labelled A and B). After reaching the steady-state flux phase, the tracer profile was measured in series A after profiling the clay sample, whereas the series B experiments were subjected to out-diffusion.

Tab. 4.2 gives an overview of the results obtained. Graphic representations of the time dependence of the tracer concentration in the source reservoir and the flux measured at the target reservoir boundary can be found in Appendix B2. The evaluation of the best-fit parameter values was done in two separate steps for the combined information of the concentration of the tracer in the source reservoir and tracer flux into the target reservoir on the one hand and the tracer profile measured after through-diffusion on the other hand. Only the former data sets were used as source data for the parameter optimisation. The tracer profiles were subsequently calculated as a blind prediction from the best-fit parameter values obtained. An excellent agreement with the measured tracer profiles was obtained in all cases (*cf.* the plots of series labelled A). Similarly, the out-diffusion data (series labelled B) were used as a blind prediction of the results obtained from

through-diffusion. Slight adaption of the model parameter values was necessary in a few cases. Whereas the unaltered D_e values could be used, α values had to be adapted. With one exception (experiment BEN.1004_19B), the changes were, however, almost within the experimental parameter uncertainty.

Tab. 4.2: Results of through-diffusion experiments combined with tracer profile analysis of $^{22}Na^+$ in compacted Volclay [a].

Label	ρ_{bd} [kg m^{-3}]	ρ_{mm} [kg m^{-3}]	ε [–]	D_e [b] [m^2 s^{-1}]	α [b] [–]	R_d [m^3 kg^{-1}] [c]
BEN1004_13A	1301	1112	0.54	$(4.1 \pm 1.5) \times 10^{-10}$ [d] $(4.1 \pm 1.5) \times 10^{-10}$ [e]	3.3 ± 0.5 [d] 3.3 ± 0.5 [e]	$(2.1 \pm 0.3) \times 10^{-3}$ $(2.1 \pm 0.3) \times 10^{-3}$
BEN1004_13B	1302	1113	0.54	$(3.5 \pm 0.9) \times 10^{-10}$ [d] $(3.5 \pm 0.9) \times 10^{-10}$ [f]	3.0 ± 1.3 [d] 3.7 ± 1.3 [f]	$(1.9 \pm 0.8) \times 10^{-3}$ $(2.4 \pm 0.9) \times 10^{-3}$
BEN1004_16A	1595	1408	0.43	$(2.4 \pm 0.3) \times 10^{-10}$ [d] $(2.4 \pm 0.3) \times 10^{-10}$ [e]	3.2 ± 0.3 [d] 3.2 ± 0.3 [e]	$(1.7 \pm 0.2) \times 10^{-3}$ $(1.7 \pm 0.2) \times 10^{-3}$
BEN1004_16B	1600	1413	0.43	$(2.3 \pm 0.3) \times 10^{-10}$ [d] $(2.3 \pm 0.3) \times 10^{-10}$ [f]	3.2 ± 1.0 [d] 3.7 ± 1.0 [f]	$(1.7 \pm 0.5) \times 10^{-3}$ $(2.0 \pm 0.6) \times 10^{-3}$
BEN1004_19A	1905	1742	0.32	$(1.3 \pm 0.2) \times 10^{-10}$ [d] $(1.3 \pm 0.2) \times 10^{-10}$ [e]	3.4 ± 0.6 [d] 3.4 ± 0.6 [e]	$(1.6 \pm 0.3) \times 10^{-3}$ $(1.6 \pm 0.3) \times 10^{-3}$
BEN1004_19B	1904	1741	0.32	$(8.5 \pm 1.1) \times 10^{-11}$ [d] $(8.6 \pm 1.1) \times 10^{-11}$ [f]	2.2 ± 0.5 [d] 4.0 ± 0.8 [f]	$(1.0 \pm 0.20) \times 10^{-3}$ $(1.9 \pm 0.4) \times 10^{-3}$

[a] Experimental details for through-diffusion: Single-tracer experiment; stagnant filters (10 µm pore size); sample geometry (diameter × thickness): 25.6 mm × 10.4 mm; volume of source reservoir: 200 ml; volume of target reservoir: 10 – 100 ml; observation time: 144 d. The electrolyte solutions were synthetic equilibrium bentonite pore waters appropriate for the respective bulk-dry densities (Van Loon & Glaus 2008). Experimental details for out-diffusion: Same as for through-diffusion with solution volumes 20 – 30 ml; observation time: ~ 30 – 100 d (depending on clay compaction).

[b] Best-fit parameters values obtained from Matlab® script parameter optimisation using a 1-D-*chds* Comsol Multiphysics® model using $c_{usb}(t)$ and $J_{dsb}(t)$ as the fitted data in through-diffusion and $J'_{usb}(t)$ and $J'_{dsb}(t)$ in out-diffusion. For the experiments that were terminated by tracer profile analysis, $c_{usb}(t)$, $J_{dsb}(t)$ and $c_{tot\_clay}(x)$ were used as the fitted data Non-stationary boundary conditions with given initial reservoir concentration for through-diffusion and given effective diffusion coefficients for the filters: D_f: 1.1×10^{-10} m^2 s^{-1}, 0.95×10^{-10} m^2 s^{-1} and 0.5×10^{-10} m^2 s^{-1} for the bulk dry densities of 1300, 1600 and 1900 kg m^{-3}, respectively. The assumption of C_{dsb} = 0 was applied for all cases.

[c] Derived from best-fit parameter values.

[d] Parameters obtained from through-diffusion.

[e] Parameters applied from through-diffusion as a blind-prediction scenario for out-diffusion.

[f] Parameters obtained from through-diffusion combined with tracer profile analysis.

4.3 Diffusion of $^{85}Sr^{2+}$

The setup and parameter variations in the diffusion experiments with $^{85}Sr^{2+}$ was analogous to those with $^{22}Na^+$. The only difference was that the clay plugs were thinner (~ 5 mm compared to ~ 10 mm in the experiments with $^{22}Na^+$). For the lowest bulk-dry densities, the evaluation of the experimental data revealed somewhat increased inconsistencies between the results of the through-diffusion phase and the tracer profiles and the results of out-diffusion, respectively.

Because no obvious reason could be identified for these inconsistencies, the entire sets of data (through- and out-diffusion on the one hand, through-diffusion and tracer profiles on the other hand) were used for the evaluation of the best-fit parameter values. The data inconsistencies are thus backed up in the parameter uncertainties. In all these experiments a clear influence of the static filter systems on the quasi steady-state tracer flux could be noted. The effective diffusion coefficients of the filters were also treated as an adjustable parameter in some appropriate cases. Besides all these rather minor issues an excellent data consistency can also be noted for the experiments with $^{85}Sr^{2+}$. Tab. 4.3 gives an overview of the results; the experimental data are shown in Appendix B3.

Tab. 4.3:   Results of through-diffusion experiments combined with tracer profile analysis or out-diffusion of $^{85}Sr^{2+}$ in compacted Volclay [a].

Label	ρ_{bd} [kg m^{-3}]	ρ_{mm} [kg m^{-3}]	ε [–]	D_e [b] [m^2 s^{-1}]	α [b] [–]	D_f [c] [m^2 s^{-1}]	R_d [d] [m^3 kg^{-1}]
13A Sr	1295	1106	0.54	$(3.1 \pm 0.4) \times 10^{-10}$ [e]	16.3 ± 0.9 [e]	$(1.3 \pm 0.2) \times 10^{-10}$ [e]	$(1.2 \pm 0.1) \times 10^{-2}$
13B Sr	1310	1121	0.53	$(4.8 \pm 0.8) \times 10^{-10}$ [f]	19.7 ± 1.1 [f]	$(8.8 \pm 0.7) \times 10^{-11}$ [f]	$(1.5 \pm 0.1) \times 10^{-2}$
16A Sr	1619	1433	0.42	$(2.9 \pm 1.3) \times 10^{-10}$ [g]	18.0 ± 2.9 [g]	$(7.5 \pm 1.9) \times 10^{-11}$	$(1.1 \pm 0.2) \times 10^{-2}$
16B Sr	1611	1425	0.42	$(3.3 \pm 1.6) \times 10^{-10}$ [h]	17.9 ± 2.9 [h]	$(7.5 \pm 1.9) \times 10^{-11}$	$(1.1 \pm 0.2) \times 10^{-2}$
19A Sr	1896	1732	0.32	$(1.0 \pm 0.3) \times 10^{-10}$ [g]	14.0 ± 2.1 [g]	$(6.0 \pm 1.5) \times 10^{-11}$	$(7.2 \pm 1.1) \times 10^{-3}$
19B Sr	1902	1738	0.32	$(9.0 \pm 2.4) \times 10^{-11}$ [h]	14.0 ± 2.1 [h]	$(6.0 \pm 1.5) \times 10^{-11}$	$(7.2 \pm 1.1) \times 10^{-3}$

[a]   Experimental details for through-diffusion: Single-tracer experiment; stagnant filters (10 µm pore size); sample geometry (diameter × thickness): 25.6 mm × 5.3 mm; volume of source reservoir: 200 ml; volume of target reservoir: 10 – 150 ml; observation time: 144 d. The electrolyte solutions were synthetic equilibrium bentonite pore waters appropriate for the respective bulk-dry densities (Van Loon & Glaus 2008). Experimental details for out-diffusion: Same as for through-diffusion with solution volumes 20 – 30 ml; observation time: ~ 100 d.

[b]   Best-fit parameters values obtained from Matlab® script parameter optimisation using a 1-D-*chds* Comsol Multi-physics® model: Non-stationary boundary conditions with given initial reservoir concentration for through-diffusion. The assumption of $C_{dsb} = 0$ was applied for all cases.

[c]   Treated as a fitting parameter in experiments 13A Sr and 13B Sr. In all other cases D_f was used as an input quantity for the parameter optimisation procedure.

[d]   Derived from best-fit parameter values

[e]   Parameters obtained from a simultaneous fit of the through-diffusion and the tracer profile data.

[f]   Parameters obtained from a simultaneous fit of the through- and out-diffusion data.

[g]   Parameters obtained from through-diffusion. These could be successfully used as a blind prediction of the tracer profile data.

[h]   Parameters obtained from through-diffusion. These could be successfully used as a blind prediction of the out-diffusion data.

4.4   Diffusion of $^{134}Cs^+$

Diffusion of $^{134}Cs^+$ in Volclay KWK was measured using the same samples as for the experiments with $^{85}Sr^{2+}$. Those samples used for the tracer profiles were no longer available; single measurements were thus performed for each of bulk-dry densities (1300, 1600 and 1900 kg m^{-3}) in the experiments with $^{134}Cs^+$. After reaching the steady-state flux in through-diffusion, the experiments were terminated by measuring the tracer profiles. Note that the rock capacity factors for the Volclay KWK samples were lower than in the case of pure montmorillonite (*cf.* section 3.2.5.3). For this reason, the evaluation of the through-diffusion experiments could be carried out successfully. However, a series of complicating factors, as outlined below, had also to be taken into account in the present case.

In contrast to all previous experiments with Volclay KWK the modelling of the data had to be adopted according to the specific sorption properties of the $^{134}Cs^+$ tracer. Although the through-diffusion experiments reached a quasi-steady-state phase, the tracer profiles were characterised by a non-linear behaviour, in which the amount of sorbed tracer at the boundaries between clay and filter decreased. This behaviour is in agreement with published data on sorption of $^{134}Cs^+$ on compacted samples of Volclay KWK (Van Loon & Glaus 2008), where an increase of R_d values with increasing bulk dry density was explained by the different hydration behaviour of the competing Na^+ and Cs^+ cations. Because the boundary regions between the filter and clay in the experiments with Volclay KWK were characterised by a decrease of bulk dry density, such effects are also effective in diffusion experiments with compacted samples of this clay. As a consequence, R_d values were treated as position depending quantities in the modelling. Owing to the lack of a detailed description of $R_{d(x)}$ as a function of bulk dry density, a linear relation was assumed for simplicity, which was calculated by interpolation from two known nodes ($\rho_{bd,1}/R_{d,1}$ and $\rho_{bd,2}/R_{d,2}$) according to:

$$R_{d(x)} = \frac{R_{d,2} - R_{d,1}}{\rho_{bd,2} - \rho_{bd,1}} \rho_{bd(x)} + \frac{\rho_{bd,2} R_{d,1} - \rho_{bd,1} R_{d,2}}{\rho_{bd,2} - \rho_{bd,1}}$$

(4.1)

The position -dependent values for the bulk dry density ($\rho_{bd(x)}$) was obtained from measuring the water content of the individual slices. The position-dependent rock capacity factor, $\alpha_{(x)}$, was finally obtained in analogy to Eq. (3.4) as follows:

$$\alpha_{(x)} = R_{d(x)} \cdot \rho_{bd(x)} + \varepsilon$$

(4.2)

Note that ε was assumed as invariable of position in these calculations, which is a reasonable simplification in view of the relatively small changes of ε compared to the large values of $\alpha_{(x)}$.

A parameter optimisation routine was subsequently run using simultaneously the reservoir concentration, flux at the downstream boundary and tracer profile data, treating D_e, $R_{d,1}$ and $R_{d,2}$ as adjustable parameters (for the pair of nodes $\rho_{bd,1} = 1300$ kg m^{-3} and $\rho_{bd,2} = 1600$ kg m^{-3} or $\rho_{bd,1} = 1600$ kg m^{-3} and $\rho_{bd,2} = 1900$ kg m^{-3}, respectively) and using D_f values fixed at lower and upper boundaries of 1.01×10^{-10} m^2 s^{-1} and 1.69×10^{-10} m^2 s^{-1}, respectively.

Tab. 4.4 gives an overview of the results obtained. Graphic representations of the time dependence of the tracer concentration in the source reservoir and the flux measured at the target reservoir boundary can be found in Appendix B4.

Tab. 4.4: Results of through-diffusion experiments combined with tracer profile analysis of $^{134}Cs^+$ in compacted Volclay KWK [a].

Label	ρ_{bd} [kg m^{-3}]	ρ_{mm} [kg m^{-3}]	ε [–]	D_e [b] [m^2 s^{-1}]	α [c] [–]	D_f [b] [m^2 s^{-1}]	R_d [b,d] [m^3 kg^{-1}]
13B Cs	1310	1121	0.53	$(1.0 \pm 0.2) \times 10^{-9}$	70 ± 10	$(1.4 \pm 0.1) \times 10^{-10}$	$(5.3 \pm 0.7) \times 10^{-2}$
16B Cs	1611	1425	0.42	$(1.2 \pm 0.1) \times 10^{-9}$	158 ± 13	$(1.4 \pm 0.1) \times 10^{-10}$	$(9.8 \pm 1.09) \times 10^{-2}$
19B Cs	1902	1738	0.32	$(1.3 \pm 0.1) \times 10^{-9}$	1352 ± 647	$(1.2 \pm 0.1) \times 10^{-10}$	$(7.1 \pm 1.09) \times 10^{-1}$

[a]   Experimental details for through-diffusion: Single-tracer experiment; stagnant filters (10 μm pore size); sample geometry (diameter × thickness): 25.6 mm × 5.3 mm; volume of source reservoir: 200 ml; volume of target reservoir: 5 – 100 ml; observation time: 130 – 254 d.

[b]   Best-fit parameters values obtained from Matlab® script parameter optimisation using a 1-D-*chds* Comsol Multiphysics® model: Non-stationary boundary conditions with given initial reservoir concentration for through-diffusion. A continuous function of C_{dsb} as a function of time based on measured concentrations of $^{134}Cs^+$ in the downstream reservoir was applied for all cases (*cf.* the text).

[c]   Quantities derived from best-fit parameter values.

[d] R_d is a function of ρ_{bd}. The specified value applies for the given value.

Sorption of $^{134}Cs^+$ on compacted samples of Volclay has been previously measured under the same conditions as in the diffusion experiments (Van Loon & Glaus 2008). In those experiments synthetic bentonite pore waters containing $^{134}Cs^+$ were in contact with Volclay samples compacted in diffusion cells (thicknesses between ~ 5 and 7 mm) until no significant change in the activity of the contacting solution could be observed. Sorption distribution coefficients were calculated from the loss of activity in these solutions. A comparison between the results of these experiments with those of the present diffusion experiments is shown in Fig. 4.1. The agreement between the two data sets is very good. This cannot simply be expected *a priori*, because the results of the diffusion experiments depend on the previously mentioned issues, such as appropriate assumptions regarding tracer concentration gradients on the confining filters and the inhomogeneities near the clay boundaries. The good data consistency increases thus the confidence in the methods applied in the evaluation of the diffusion experiments from an independent view.
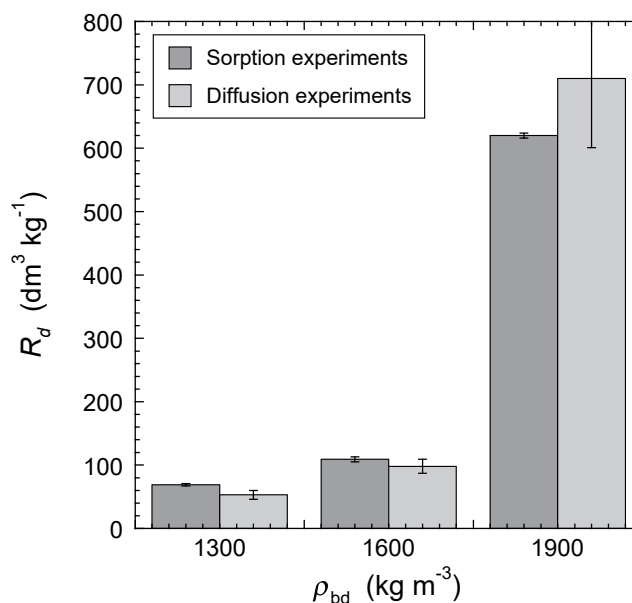
Fig. 4.1:   Comparison of R_d values for $^{134}Cs^+$ on Volclay obtained from sorption measurements on compacted samples with those obtained from the present diffusion experimens (*cf.* Tab. 4.4).

4.5   Diffusion of $^{36}Cl^-$

A comprehensive set of diffusion data for $^{36}Cl^-$ has been published previously (Van Loon et al. 2007) using NaCl solutions as the background electrolyte. In accordance with the experiments described in the previous sections, the present experiments were carried out in synthetic bentonite pore waters in order to test whether the solution composition or the type of cations in the cation exchange sites may have an influence on anion exclusion. Three different bulk-dry densities (1300, 1600 and 1900 kg m^{-3}) were tested in the present experiments. The respective synthetic pore waters had ionic strengths of 0.26, 0.29 and 0.33 M. The experiments were carried out as through-diffusion experiments followed by out-diffusion. Each of these phases was evaluated separately. The plots of the out-diffusion data (*cf.* Appendix B5) clearly show the signature of porosity inhomogeneities near the clay boundaries (Glaus et al. 2011): The tracer fluxes on the previous source reservoir side are larger than expected from the through-diffusion phase. This trend developed increasingly with increasing bulk-dry density. However, no adaptation in the modelling was carried out for the present data in order to maintain the comparability with the literature data (Van Loon et al. 2007). In agreement with those evaluations the present out-diffusion data were only fitted to the results obtained from the previous target side. The results given in Tab. 4.5 show a rather good consistency between the data measured during the through-diffusion and the out-diffusion phase. This was less the case for the published data (Van Loon et al. 2007) where discrepancies in the accessible porosity exceeding the experimental uncertainties were noted.

Tab. 4.5: Results of through- and out-diffusion experiments of $^{36}Cl^-$ in compacted Volclay KWK [a].

Label	ρ_{bd} [kg m^{-3}]	ρ_{mm} [kg m^{-3}]	ε [–]	Mode	D_e [b] [m^2 s^{-1}]	α [b,c] [–]
BEN1006_13B	1302	1113	0.54	through out	$(1.8 \pm 0.1) \times 10^{-11}$ $(1.8 \pm \text{n.a.}) \times 10^{-11}$	0.10 ± 0.02 $0.13 \pm \text{n.a.}$
BEN1006_16B	1600	1413	0.43	through out [d]	$(3.1 \pm 0.3) \times 10^{-12}$ $(3.1 \pm \text{n.a.}) \times 10^{-12}$	0.045 ± 0.015 $0.045 \pm 0. \text{ n.a.}$
BEN1006_19B	1904	1741	0.32	through out [d]	$(3.4 \pm 0.2) \times 10^{-13}$ $(3.4 \pm \text{n.a.}) \times 10^{-13}$	0.016 ± 0.002 $0.022 \pm \text{n.a.}$

[a] Experimental details for through-diffusion: Single-tracer experiment; stagnant filters (10 μm pore size); sample geometry (diameter × thickness): 25.6 mm × 10.4 mm; volume of source reservoir: 200 ml; volume of target reservoir: 20 ml; observation time: 35 – 50 d. Experimental details for out-diffusion: Same as for through-diffusion with solution volumes of 20 ml; observation time: ~ 10 – 30 d (depending on clay compaction).

[b] Best-fit parameters values obtained from Matlab® script parameter optimisation using a 1-D-*chds* Comsol Multiphysics® model: Non-stationary boundary conditions with given initial reservoir concentration for through-diffusion and given effective diffusion coefficients for the filters: D_f: $(2.5 \pm 0.5) \times 10^{-10}$ m^2 s^{-1}. The assumption of $C_{dsb} = 0$ was applied for all cases.

[c] No R_d values were derived because a possible positive or negative sorption could be demonstrated unambiguously.

[d] Flux data from the up-stream boundary were not used for data fitting because of boundary effects effective for anions (Glaus et al. 2011).

A comparison between those data and the present data is shown in Fig. 4.2. No significant differences between the experiments in pure electrolytes and those in synthetic pore waters can be spotted. It can thus be concluded that the nuances regarding the composition of the equilibrium solutions are of minor importance for the diffusive behaviour of negatively charged species.
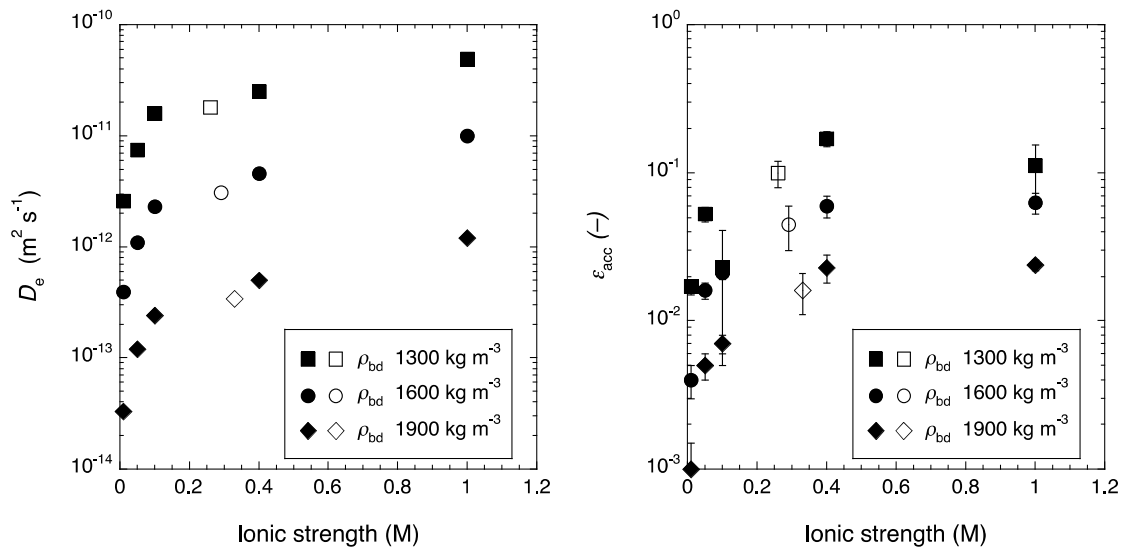

Fig. 4.2: Comparison of literature data (Van Loon et al. 2007) measured in NaCl electrolytes (full symbols) and the data given in Tab. 4.5 measured in synthetic pore waters (empty symbols).

The error bars of the left-hand plot are of the same order of magnitude as the symbols.

4.6   Diffusion of $^{35}SO_4^{2-}$

The diffusion of $^{35}SO_4^{2-}$ was measured for the general interest in the comparison between negatively charged species with different net charge. There is, however, the difficulty of finding negatively charged inorganic species with similar inertness of the chloride anion for example. Sulfate was chosen for this purpose knowing that bentonite contains sulfate minerals. It has thus to be expected that some isotopic exchange or surface interactions may occur as already observed in the case of Na-*mom* (*cf.* section 3.5.1). The measured α values may thus not be fully representative for the porosity accessible to sulfate.

Three different bulk-dry densities (1300, 1600 and 1900 kg m^{-3}) in combination with the appropriate synthetic bentonite pore waters were tested, using pairs of experiments for which the through-diffusion phase was a replicate measurement. Each one sample (labelled B) of these pairs was cut into segments in order to measure the tracer profile after through-diffusion, while the other (labelled A) was subjected to out-diffusion.

The parameter optimisation routine was run using concatenated data from through-diffusion/ tracer profile, and through-diffusion/out-diffusion, respectively. Possible discrepancies between the two data sources can thus less be recognised on the one hand. On the other hand, the parameter uncertainties obtained thereby better reflect intrinsic model uncertainties compared to parameter uncertainties obtained from a separate treatment. Further the Comsol Multiphysics® model used for numerical simulation of the through-diffusion/profile data was extended to use a position-dependent function for the capacity factor α.

$$\alpha_{(x)} = R_d \cdot \rho_{db(x)} + \varepsilon_{(x)}$$

(4.3)

The position-dependent function of ε ($\varepsilon_{(x)}$) was calculated from the loss of water in the segments upon drying (Van Loon et al. 2007) and the position-dependent function for ρ_{bd} was derived from $\rho_{bd} = \rho_s(1 - \varepsilon_{(x)})$, resulting in

$$\alpha_{(x)} = R_d \cdot \rho_s(1 - \varepsilon_{(x)}) + \varepsilon_{(x)}$$

(4.4)

Such inhomogeneities in the anion accessible porosity were identified as the reason for non-linear anion distribution in smectites (Glaus et al. 2011) which occurs even in a steady-state flux situation. Using the data of sample 13B it was tested whether significant differences in the best-fit parameter values would be obtained in a homogeneous (*cf.* Figs. 28a and 28b, Appendix B.6) versus an inhomogeneous scenario (*cf.* Figs. 28c and 28d, Appendix B.6) for the distribution of the anion accessible porosity. Also, was it tested whether significant differences arise for a position-dependent distribution of D_e values. The results of this comparison show that the differences in the best-fit parameter values are of similar order of magnitude as the parameter uncertainties themselves. Consequently, such nuances in model assumptions are of subordinate importance.

The data of the A series were evaluated from a model assuming a homogeneous distribution of the anion-accessible porosity for simplicity (no dry weight can be determined when carrying out out-diffusion). In out-diffusion the observed tracer fluxes at the previous source reservoir side were slightly larger than the predictions from a homogeneous pore distribution model. In the case of chloride diffusion, inhomogeneities near the clay/filter boundaries were successfully invoked to model the out-diffusion data for both the previous source and the previous target reservoir (Glaus et al. 2011). A trend of enhanced initial fluxes at the previous source reservoir side with decreasing concentration of the background electrolyte was observed in the case of chloride out-diffusion. This trend can be explained as being the result of an increasing anion-exclusion effect

with decreasing salinity. In the present case of $^{35}SO_4^{2-}$ out-diffusion the salinities were of the same order of magnitude for all synthetic pore waters applied which makes a discussion in the respect of ionic strength effects useless. However, there is a trend of increasing flux enhancement on the previous source reservoir side with increasing bulk-dry density. This makes sense in view of an effect of anion-accessible porosity because the fractional contribution of diffuse double layer porosity (*cf.* section 6.3) increases with increasing bulk-dry density (Van Loon et al. 2007). It may also be noted that the tracer fluxes on both sides conform to each other after sufficient time.

This is in contrast with the data measured for Milos montmorillonite (*cf.* section 3.5.1). It has also to be noted that the α values measured for Volclay were significantly smaller than those for montmorillonite. In the latter case it was hypothesised that an isotopic exchange reaction between $^{35}SO_4^{2-}$ and a sparingly soluble sulfate-bearing mineral phase was the reason for the large α values. It is somewhat surprising that such effects were not observed for Volclay, which is a more complex mineral mixture compared to the purified Na-*mom*. There is currently no good explanation for this seeming discrepancy.

The results are given in Tab. 4.6; the experimental data are shown in Appendix B.6. A comparison with the chloride data shows that the D_e values for sulfate are lower by factors of 3 to 5, while the α values tend to be even larger. This is a clear indication that the α values for sulfate are also slightly influenced by some non-identified sorption phenomena and do not fully represent the anion-accessible porosity.

Tab. 4.6:   Results of through-diffusion of $^{35}SO_4^{2-}$ combined with tracer profile analysis in compacted Volclay KWK [a].

Cell label	ρ_{bd} [kg m^{-3}]	ρ_{mm} [kg m^{-3}]	ε [–]	D_e [b] [m^2 s^{-1}]	α [b] [–]
BEN1009_13A	1312	1123	0.53	$(5.8 \pm 0.6) \times 10^{-12}$ [c]	0.13 ± 0.02 [c]
BEN1009_13B	1297	1108	0.54	$(6.2 \pm 0.5) \times 10^{-12}$ [d,e]	0.16 ± 0.01 [d,e]
BEN1009_13B	1297	1108	0.54	$(6.4 \pm 0.4) \times 10^{-12}$ [d,f]	0.13 ± 0.01 [d,f]
BEN1009_16A	1602	1415	0.43	$(8.7 \pm 0.8) \times 10^{-13}$ [c]	0.065 ± 0.003 [c]
BEN1009_16B	1605	1419	0.43	$(8.7 \pm 0.8) \times 10^{-13}$ [d]	0.094 ± 0.002 [d]
BEN1009_19A	1900	1736	0.32	$(7.6 \pm 0.5) \times 10^{-14}$ [c]	0.065 ± 0.005 [c]
BEN1009_19B	1897	1733	0.32	$(5.6 \pm 0.6) \times 10^{-14}$ [d]	0.026 ± 0.001 [d]

[a]   Experimental details for through-diffusion: Single-tracer experiment; stagnant filters (10 μm pore size); sample geometry (diameter × thickness): 25.6 mm × 5.3 mm; volume of source reservoir: 200 ml; volume of target reservoir: 10 – 150 ml; observation time: 144 d. Experimental details for out-diffusion: Same as for through-diffusion with solution volumes 20 – 30 ml; observation time: ~ 100 d.

[b]   Best-fit parameters values obtained from Matlab® script parameter optimisation using a 1-D-*chds* Comsol Multiphysics® model: Non-stationary boundary conditions with given initial reservoir concentration for through-diffusion. The assumption of $C_{dsb} = 0$ was applied for all cases. D_f was fixed at $(1.0 \pm 0.25) \times 10^{-10}$; the diffusive resistance of the filters could almost be ignored thus.

[c]   Best-fit parameter values obtained from simultaneously fitting the through- and out-diffusion data.

[d]   Best-fit parameter values obtained from simultaneously fitting the through-diffusion and the tracer profile data.

[e]   Model with constant α (assuming a homogeneous distribution of clay porosity).

[f]   Model with position-dependent α function (assuming an inhomogeneous distribution of clay porosity near the clay boundaries).

5   Accessory Information

5.1   Profiles of water and anion contents in compacted montmorillonite

After the through-diffusion phase in the experiments described in section 3.1 (Tab. 3.1), the clay samples were cut into segments for determination of the water content by drying. Subsequently the content of perchlorate in the segments was measured by HPAEC after aqueous extraction. From these data, the total water porosity and the anion accessible porosity were calculated as a function of the segment position. The results are shown in Figs. A7 and A8 in Appendix A.1. In agreement with earlier observations (Glaus et al. 2011), most of the profiles are characterised by an inhomogeneous distribution of the total and anion-accessible porosity near the planar cylindrical boundaries. Average values calculated from the homogeneous central part are given in Tab. 5.1. The values are in agreement with the generally observed trend of decreasing accessibility with decreasing concentration of the background electrolyte (Van Loon et al. 2007).

Tab. 5.1:   Average porosity values (± standard uncertainty) of Na-*mom* saturated with $NaClO_4$ calculated from profiling after through-diffusion.

Label	ρ_{bd} [kg m^{-3}]	ε [a] [–]	$NaClO_4$ [M]	Total water porosity	Anion accessible porosity
1064_13A	1297	0.54	0.01	0.54 ± 0.01	0.04 ± 0.03
1064_13B	1301	0.52	0.10	0.53 ± 0.01	0.09 ± 0.03
1064_13C	1299	0.57	1.0	0.52 ± 0.01	0.14 ± 0.05
1064_16A	1608	0.43	0.01	0.46 ± 0.01	0.03 ± 0.02
1064_16B	1602	0.43	0.10	0.45 ± 0.01	0.03 ± 0.01
1064_16C	1605	0.43	1.0	0.45 ± 0.01	0.12 ± 0.04

[a]   Calculated from the dry weight of *Na-mom* and a solid density of 2800 kg m^{-3}.

In a similar experiment, samples of Na-*mom* were saturated with NaCl in order to test, whether the exclusion volume is affected by the type of anion. For the experiments with 0.01 M NaCl, the results had to be corrected by trace contents of chloride, which were determined by HPAEC from the saturation tests with $NaClO_4$. Average values for the porosities are given in Tab. 5.2, the raw data can be found in Figs. A9 – A11 in Appendix A.1. These results indicate that the total water-accessible and the anion-accessible porosities are similar for an NaCl and an $NaClO_4$ electrolyte.

Tab. 5.2:   Average porosity values (± standard uncertainty) for the saturation of Na-*mom* with NaCl and NaClO$_4$ calculated from profiling after a saturation time of ~ 30 d.

Label	ρ_{bd} [kg m^{-3}]	ε [a] [–]	Saturation electrolyte	Total water porosity	Anion accessible porosity
FA24_5_Z1	1295	0.54	0.01 M NaCl	0.53 ± 0.01	0.03 ± 0.01 [b]
FA24_5_Z2	1302	0.54	0.1 M NaCl	0.53 ± 0.01	0.11 ± 0.01
FA24_5_Z10	1327	0.53	0.1 M NaClO$_4$	0.52 ± 0.01	0.11 ± 0.01
FA24_5_Z3	1302	0.54	1.0 M NaCl	0.53 ± 0.01	0.23 ± 0.02
FA24_5_Z4	1598	0.43	0.01 M NaCl	0.44 ± 0.01	(0.01 ± 0.01) [b, c]
FA24_5_Z5	1609	0.43	0.1 M NaCl	0.42 ± 0.01	0.05 ± 0.01 [b]
FA24_5_Z11	1640	0.42	0.1 M NaClO$_4$	0.43 ± 0.01	0.07 ± 0.01
FA24_5_Z6	1609	0.43	1.0 M NaCl	0.43 ± 0.01	0.13 ± 0.01
FA24_5_Z7	1870	0.33	0.01 M NaCl	0.33 ± 0.01	(0.01 ± 0.01) [b, c]
FA24_5_Z8	1895	0.32	0.1 M NaCl	0.34 ± 0.01	0.05 ± 0.02
FA24_5_Z12	1973	0.30	0.1 M NaClO$_4$	0.30 ± 0.01	0.06 ± 0.01
FA24_5_Z9	1901	0.32	1.0 M NaCl	0.33 ± 0.01	0.07 ± 0.01

[a]   Calculated from the dry weight of *Na-mom* and a solid density of 2800 kg m^{-3}.

[b]   After significant correction for blank content of chloride.

[c]   No significant specification of anion-accessible porosity possible.

In these experiments also the extracted amounts of SO$_4^{2-}$ were measured. These data were not transformed to anion-accessible porosities, because the samples were not in a chemical equilibrium with SO$_4^{2-}$ in the external solutions. The results (*cf.* Figs. A12 – A14 in Appendix A.1) were simply expressed as normalised for the amount of dry clay. The data were not evaluated quantitatively. From a qualitative point of view, two observations can be made: (i) The contents of sulfate are decreasing near the boundaries to the filters, indicating that the diffusive flux to the outer solution is very slow, and (ii) there is a trend of increasing amounts of sulfate with decreasing ionic strength in the outer solution. From these observations it is not possible to draw back on the chemical state of sulfate in the clay samples. However, they are indicating that sulfate may be retained by some anion-exchange sites. The pre-conditioning procedure of the clay by 3 times exchanging a 1 M NaCl solution is probably not suited to remove all sulfate from these sites, because bi-valent anions will be enriched during such a process when exchanging against a monovalent anion. One may also note that fairly soluble minerals like gypsum or anhydrite are expected to be completely solubilised during the pre-conditioning procedure of the clay.

5.2   Re-saturation of compacted clay samples

When performing diffusion tests on compacted samples of clay minerals, the question of saturation of the clay sample is of crucial importance because insufficient saturation may lead to a significant decrease of effective diffusion coefficients (Churakov 2013, Savoye et al. 2010). It is therefore important to verify that the clay porosity is fully saturated before tracer addition. Monitoring the uptake of water as a function of time, until a constant weight has been obtained, is a feasible method for this purpose and has been frequently applied during the first phase of the project. However, several experimentally related issues impair the accuracy of such measure-

ments. The weight increase of the diffusion cell cannot directly be measured without removing the diffusion cell from the circulation system, and on the other hand such measurements are difficult because of the large weight of the steel cell compared to the expected increase of mass. Further the various types of dead volumes of the diffusion cell such as the filter porosity and the volumes of the channels system need to be known. Measuring the weight loss of the liquid in the saturation reservoir is an alternative procedure. However, the evaluation of these results may be obstructed by uncertainties related to evaporation losses in the reservoir solutions.

We therefore performed targeted saturation tests, in which the various porosities were carefully determined using pre-calibrated filters and diffusion cells. Bentonite was compacted to bulk-dry densities of 1300 and 1900 kg m^{-3}, and saturated with 0.3 M NaClO$_4$ as a representative electrolyte solution for the diffusion experiments. The solid density of the clay sample (ρ_s, kg m^{-3}) is determined according to:

$$\rho_s = \frac{m_s}{V_{cell} - V_{up}}$$

(5.1)

where m_s is the dry mass (kg) of clay (corrected for residual water content), V_{cell} the cylindrical void space (m^3) for the clay sample in the diffusion cell and V_{up} the volume (m^3) of liquid taken up during the re-saturation of the clay. The latter volume was measured gravimetrically after dismantling the cell and immediately measuring the wet clay weight (m_{wet}, kg) as a function of delay time between dismantling and weighting. It was verified that potential changes in the weight by uptake of water from or loss to the atmosphere was insignificant for the first measurements. The measured weight of liquid ($m_{\text{up}} = m_{\text{wet}} - m_s$, kg) was converted to V_{up} using an estimated average density (ρ_{av}, kg m^{-3}) of the various types of liquid in the bentonite. Note that it is a commonly used assumption that interlayer has a similar density as water and that this type of pore fluid dominates the composition of the entire pore solution at bulk-dry densities of $\sim$ 1900 kg m^{-3}. For the bulk-dry densities of $\sim$ 1300 kg m^{-3} it was assumed that $\sim$ 30 % of the total porosity was filled with the electrolyte solution (0.3 M NaClO$_4$, density 1022 kg m^{-3}) and that the remaining porosity consisted of water (Van Loon et al. 2007). ρ_s was calculated thus as:

$$\rho_s = \frac{m_s \rho_{av}}{V_{cell} \rho_{av} - \left(m_{wet} - m_s\right)}$$

(5.2)

An overview of the results is given in Tab. 5.3. In view of the uncertainties involved in the cell dimensions, the results cannot be clearly differentiated from those obtained from ordinary pycnometer tests ($\rho_s = 2812 \pm 70$ kg m^{-3}), in which the solid density was determined from disperse suspensions. One may thus conclude that the samples in the diffusion cells were fully saturated within the ranges of uncertainty of the measurements. This conclusion is in agreement with the conclusions drawn for the accessible porosity from the through-diffusion experiments with HTO (*cf.* section 3.1).

In the course of these measurements the filters were dried to constant weight after dismantling of the diffusion cells in order to compare the final dry weight (after correction for the weight of NaClO$_4$ from the electrolyte solution in the filter pores) with the initial weight. The difference allows estimating roughly the amount of clay entering the filter pores during the re-saturation. The discrepancies found ranged around approximately 30 mg of dry clay. Although it is not possible to derive an accurate volume of porosity filled with clay – owing to ignorance of the bulk-dry density of the clay in the filter pores – on may conclude that only a small fraction of the porosity of the filter pores may be filled with clay. Similar conclusions could also be drawn from re-saturation experiments with Na-*mom* (data not shown).

Tab. 5.3:   Determination of ρ_s in samples of compacted Volclay bentonite.

Sample name	m_s [g]	m_{wet} [g]	V_{cell} [cm^3]	ρ_{av} [kg m^{-3}]	ρ_s [kg m^{-3}]
13_P1	7.003	9.952	5.306	1007	2945
13_P2	6.849	9.726	5.253	1007	2859
19_P1	10.170	11.842	5.326	1000	2784
19_P2	10.008	11.695	5.238	1000	2819

5.3   Hydraulic tests

The hydraulic conductivity is an important property, which may affect the quality of the results of through-diffusion tests in which circulating fluids are used to control the concentration boundary conditions at the interface between filter (and clay) and solution. Although hydraulic heads resulting from differences in height position of the reservoir flasks were avoided and circulation loops at the reservoir and at the target boundary had the same dimensions and were operated using the same peristaltic pump axis, it cannot be avoided that small differences in pressure may occur at the two boundaries. Possible reasons may be differences in the elasticity of the peristaltic tubings or small differences in the bottleneck positions of the circulating system, which both may lead to different back-pressures acting on the clay sample and thus to an advective flux. It is clear that the potential advective mass transfer must be negligible compared to diffusive mass fluxes for a reliable determination of diffusion coefficients. An assessment of this ratio is given by the Peclet number (*Pe*) which can be calculated for the setup of a through-diffusion experiment as follows:

$$Pe = \frac{K_f \frac{\Delta h}{\Delta x} c}{D_e \frac{\Delta c}{\Delta x}} = \frac{K_f \Delta h}{D_e}$$

(5.3)

K_f is the Darcy hydraulic conductivity (m s^{-1}), Δh the hydraulic head (m), *c* the concentration of the diffusing species in the source reservoir and Δc the concentration difference in a steady-state situation between the source and the target reservoir. Because the latter concentration can be approximated by zero, Δc and *c* are almost equal and cancel from the equation. From rising pipe tests, it was observed that the pressure oscillations at a pump rate of 0.1 cm^3 min^{-1} were of the order of ~ 1 mm in hydraulic head. For the purpose of a conservative examination it is assumed that Δh is 0.01 m at maximum and that *Pe* is required to be less than 0.01, meaning that the advective solute flux through the sample has to be less than 100 times the diffusive flux. Using these numbers, a critical relationship between K_f and D_e is given by:

$$\frac{K_f}{D_e} \leq 1 [m^{-1}]$$

(5.4)

No systematic measurements of K_f values were carried out in the frame of the present study, because such measurements are demanding in the range of the low values expected for the clay materials studied here. Instead we relied on literature values (Karnland et al. 2006), where K_f

values for montmorillonites and bentonites are compiled as a function of bulk-dry density and salinity in the contacting solution. For Na-montmorillonites with ρ_{bd} values larger than or equal as 1300 kg m^{-3}, no advective interferences are conceivable for HTO and cations, because D_e values are larger than 2×10^{-11} m s^{-1} throughout. With K_f values less than 5×10^{-14} m s^{-1}, the respective Pe values are less than 0.0005. For the large majority of anion measurements, also no advective disturbances are expected. The lowest D_e value measured in the present work was of the order of 10^{-14} m^2 s^{-1}. Only in such a case a minor bias may have occurred. The situation may become potentially critical for bentonites with ρ_{bd} values of the order of 1300 kg m^{-3}, where K_f values may be of the order of 10^{-12} m s^{-1} at high salinities. The measurement of anion diffusion may be affected by advective effects in such cases. For the measurement of D_e values of HTO and cations, no problems were expected since these D_e values were larger than $\sim 10^{-11}$ m^2 s^{-1}, throughout.

5.4   Batch sorption tests of $^{85}Sr^{2+}$ on dispersed Na-*mom*

A few very simple batch sorption tests were carried out in which a weighted amount of Na-*mom* (conditioned using the same procedures as for the diffusion experiments) was equilibrated with a NaClO$_4$ solution containing a known amount of $^{85}Sr^{2+}$ tracer. The concentration of NaClO$_4$ varied between 0.1 and 1.0 M and a constant solid : liquid ratio (~ 20 g dm^{-3}) was used throughout. Two replicate samples were measured after a contact time of 1 d and another two replicate samples after a contact time of 7 d. R_d values were calculated from the $^{85}Sr^{2+}$ activity measured after centrifugation of the samples for 30 min. at 100'000 g according to:

$$R_d = \frac{A^0 - A'}{A'} \cdot \frac{V}{m}$$

(5.5)

where A is the $^{85}Sr^{2+}$ activity per g of solution sample (decay corrected, Bq g^{-1}), V the solution volume [m^3] and m the dry mass of clay [kg]. The index 0 denotes the measurement before addition of clay and the index ' the measurements after centrifugation. No significant differences were found in the R_d values obtained from the two contact times (1 and 7 d). For this reason, all measurements carried out for a single concentration of NaClO$_4$ were averaged. A comparison of R_d values calculated from the α values obtained in the diffusion measurements with those from the batch sorption measurements is shown in Fig. 5.1.
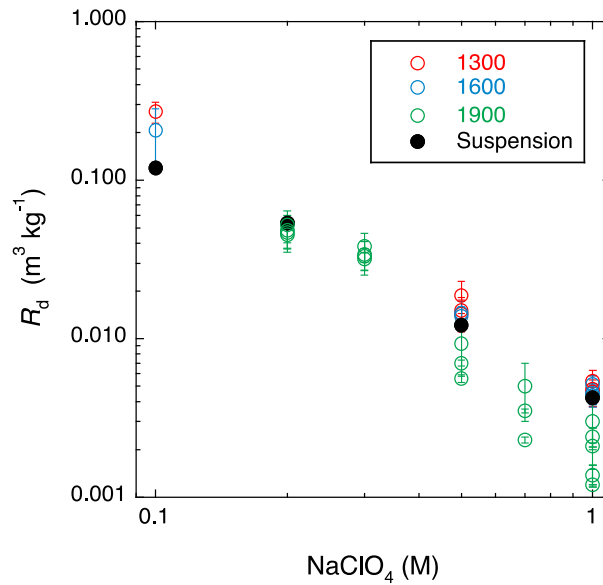
Fig. 5.1:   Comparison between R_d values measured in diffusion experiments (open symbols) with R_d values measured in dilute suspensions (closed symbols).

The different colours refer to different bulk-dry densities used in the diffusion experiments (given in the legend as kg m^{-3}).

A fairly good agreement between the results from the diffusion experiments and those from the batch sorption experiments can be noted. The data indicate that the compaction of Na-*mom* may have a slight influence for ρ_{bd} values larger or equal than 1900 kg m^{-3} with a trend of decreasing R_d value with increasing ρ_{bd}. This is an opposite trend to that observed for Cs$^+$ (Van Loon & Glaus 2008), *cf.* also section 5.5 on experiments with Cs$^+$. The trend observed here may be explained tentatively with the stronger hydration enthalpy of Sr^{2+} compared to Na$^+$, reflected by the tendency of Sr^{2+} to form rather two hydration spheres instead of one (Ohtaki & Radnai 1993). This behaviour may result in a dependence of the selectivity for the exchange of Na$^+$ for Sr^{2+} as a function of ρ_{bd}. The influence on R_d values is, however, much weaker than for the exchange of Na$^+$ for Cs$^+$. Some discrepancies are also observed for the lowest concentration of NaClO$_4$. These are most probably related to the mentioned uncertainties of determining best-fit parameter values at conditions, under which the diffusivity of the clay samples is high compared to those of the confining filters. This is increasingly the case with decreasing concentration of NaClO$_4$.

5.5   Sorption measurements of ^{134}Cs$^+$ on compacted Na-*mom* samples

Because of the uncertainties in the interpretation of the through-diffusion experiments described previously (*cf.* section 3.4.2), the sorption of Cs$^+$ was measured using compacted samples of Na-*mom*. The same procedures were applied as for the published sorption experiments with compacted Volclay bentonite samples (Van Loon & Glaus 2008): Samples of Na-*mom* compacted to bulk-dry densities between 1300 and 1900 kg m^{-3} in diffusion cells (*SFDC*'s) were contacted with solutions containing background electrolyte concentrations between 0.1 and 1.0 M NaClO$_4$ and ^{134}Cs$^+$ at activities of ~ 1100 Bq cm^{-3}. The solid:liquid ratio was identical for all experiments (10 g dm^{-3}) resulting in samples with different clay thicknesses (varying between 2.0 and 3.3 mm).

Because the diffusion experiments with $^{134}Cs^+$ were carried out using different background concentrations of stable Cs^+, part of the sorption experiments was carried out using $^{134}Cs^+$ tracer and another part of the experiments in the presence of added stable CsCl. The concentration of the latter was measured using HPCEC. For the latter measurement the sample solutions were diluted to a target concentration of 0.05 M Na^+ in order to avoid excessive matrix effects due to the presence of Na^+. The initial concentrations of Cs^+ in these experiments were adjusted according to the different dilution factors, otherwise the dynamic range of the measurements would have been too large. For this reason, the initial concentrations for the sorption experiments varied by a maximum factor of 5 between the different series. It can reasonably be assumed that this variation did not have a significant effect on the resulting R_d values because resulting equilibrium concentrations were between 0.01 and 0.3 mM. According to the sorption isotherm shown in Fig. 3.7, R_d values are relatively insensitive to changes of the background concentration of Cs^+. The concentrations of Cs^+ and $^{134}Cs^+$ in the contacting solutions were monitored by regularly taking aliquot samples until they remained virtually constant.

Fig. 5.2 shows the evolution of Cs concentration and $^{134}Cs^+$ activity, respectively for all experiments. The curves were influenced by temperature effects as these cells could not be put in the thermostated oven. With a single exception (2100/0.5) all experiments reached a well-defined equilibrium state from which R_d values and selectivity coefficients (K_c) were calculated according to the following definition (Van Loon & Glaus 2008):

$$K_c = \frac{[X\text{-}Cs][Na^+]}{[X\text{-}Na][Cs^+]}$$

(5.6)

where X denote the cation exchange sites and brackets denote molar concentrations (used instead of activities for simplicity). In the experiments with stable Cs^+, the Na^+ equilibrium concentrations were calculated from the sum of the initial concentration and the amount of Na^+ released assuming a 1:1 stoichiometric exchange. Additionally, a water evaporation rate of 28 µl d^{-1} was introduced in order to adequately take into account volume changes occurring across the long observation times. A cation exchange capacity of 0.84 eq kg^{-1} was used to calculate the fractional occupancies of the X sites.
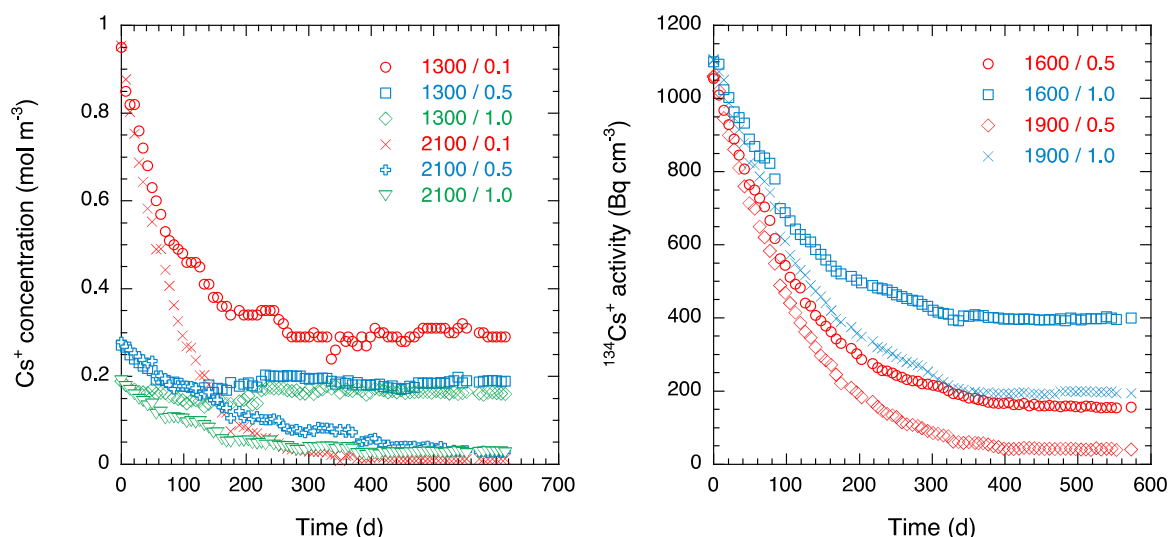
Fig. 5.2:   Evolution of the reservoir concentration of Cs as a function of time at the conditions given in the legend (bulk-dry density in kg m^{-3} / molar NaClO$_4$ concentration).

The left-hand plot shows the results measured using stable Cs-133 and the righ-hand plot those with Cs-134 tracer.

The experimental conditions and the results are summarised in Tab. 5.4. As can be seen from this table, R_d and K_c values increase strongly with increasing bulk-dry density, which is in agreement with the observations made for Volclay bentonite (Van Loon & Glaus 2008). The comparison of R_d values measured in sorption and diffusion shows a fairly good agreement. It may be assumed that the uncertainties specified in both techniques may correctly reflect the statistical uncertainties involved, but rather underestimate the true uncertainties, which are also influenced by non-statistical sources.

Tab. 5.4:   Results of the sorption measurements of Cs^+ on compacted Na-*mom* samples (experiment TON.1068).

Label	ρ_{bd} [kg m^{-3}]	ε [–]	NaClO$_4$ [M]	Isotope	Initial ^{133}Cs [mol m^{-3}]	R_d [m^3 kg^{-1}]	K_c [–]	R_d [m^3 kg^{-1}] from diffusion
1.3 A	1306	0.534	0.1 M	Cs-133	0.95	0.25 ± 0.05	34 ± 7	
1.3 B	1301	0.535	0.5 M	Cs-133	0.27	0.055 ± 0.015	39 ± 11	0.035 (Tab. 3.10)
1.3 C	1300	0.536	1.0 M	Cs-133	0.19	0.020 ± 0.010	28 ± 14	
1.6 A	1604	0.427	0.5 M	Cs-134	1.6×10^{-7}	0.61 ± 0.05	364 ± 30	0.42 (Tab. 3.10)
1.6 B	1609	0.425	1.0 M	Cs-134	1.7×10^{-7}	0.19 ± 0.01	221 ± 12	0.21 (Tab. 3.10) 0.27 (Tab. 3.14)
1.9 A	1902	0.321	0.5 M	Cs-134	1.7×10^{-7}	2.6 ± 0.2	1572 ± 121	
1.9 B	1905	0.320	1.0 M	Cs-134	1.7×10^{-7}	0.47 ± 0.02	563 ± 24	1.0 (Tab. 3.14)
2.1 A	2109	0.247	0.1 M	Cs-133	0.95	9.0 ± 0.6	1332 ± 89	
2.1 B	2102	0.249	0.5 M	Cs-133	0.28	> 0.9	> 610	
2.1 C	2102	0.249	1.0 M	Cs-133	0.19	0.63 ± 0.12	821 ± 156	

6   Discussion

The following discussion focuses on an integrative treatment of the diffusion results obtained for the different elements in the present work. When looking at the literature (e.g. Jakob et al. in *prep.*), a large variety of different interpretation of diffusion data on different levels of detail can be found. The following discussion does not aim at a basic re-invention of diffusion models. The purpose is on the one hand to underpin the data homogeneity, which is not a matter of course in view of the broad variety of experimental conditions, and on the other hand to interpret the data with simple models requiring a minimum of background information. The applicability of the results in performance assessment is a primary concern of the following sections.

The following aspects are in the foreground:

- Interpretation of the observed salinity effects

- Comparison with sorption data observed in disperse batch suspensions

6.1   The "Gimmi – Kosakowski" scheme

In the following the results will be discussed in the frame of the parallel-flux model proposed by Gimmi & Kosakowski (2011). The observed tracer flux is assumed to be the sum of two individual fluxes, viz. the flux in the aqueous phase and the flux of surface-associated species. As outlined in the latter work, two types of surfaces may be distinguished for smectites, viz. inner and outer surfaces. From a structural point of view, these may be identical. They differ, however, in the type of the adjacent porosity (González Sánchez et al. 2008b). The pore water adjacent to the inner surfaces is structurally confined by the repetitive sequence of TOT layers (TOT being the acronym for the smectite mineral structure composed of an octahedral sheet sandwiched between two tetrahedral sheets). It is also denoted to as interlayer water and, depending on the bulk-dry density and chemical composition of the external solution, it may expand to different extents in the direction perpendicular to the clay mineral layers. The spatial extent of the outer surfaces, on the contrary, is defined by the particle form of the TOT stacks and is rather irregularly structured compared to the interlayer water. From an electrochemical point of view, one may also distinguish these two types of surfaces in the type of surface potentials. The outer surfaces exhibit the typical zeta-potential, characterised by an exponential potential decrease with increasing distance from the surface, while the surface potentials of the inner surfaces are rather overlapping. Different models exist in the literature to describe the formation of zones near the surface with enriched contents of cations (such as the so-called diffuse double layer) used to neutralise the fixed negative surface charges. The electrochemical characteristics of the two types of surface potentials may be increasingly equal with increasing bulk-dry density (Miller et al. 2010). However, no established procedure can be found in the literature to describe such effects.

The Gimmi – Kosakowski scheme does not discriminate whether the cationic surface species are present in the diffuse double layer near the charged particle surfaces or in the interlayers (where these double layers may overlap). The driving forces for diffusion are the concentration gradients in the respective phases. For simplicity – and for the experimental inaccessibility of the respective information – the species concentrations are calculated on the basis of total pore volume instead of separate volumes for free aqueous phase and the 'surface phase'. More detailed models rely for example on the Donnan approach for a simple allocation of different types of porosities (Appelo et al. 2010, Tournassat & Appelo 2011).

In its simplest form, the scheme of Gimmi & Kosakowski (2011) relates a normalised effective diffusion coefficient (D_{erw}, [-]) with the sorption distribution capacity (κ, [-]) and the relative surface mobility, μ_s ($\mu_s = D_s^0/D_w$, with D_s^0 being an intrinsic surface diffusion coefficient on a flat surface) according to the following equation:

$$D_{erw} \approx 1 + \kappa\mu_s$$

(6.1)

D_{erw} is a dimensionless diffusion coefficient that reflects the enhancement of diffusive rates relative to diffusion in pore water. Assuming that the tortuosity and porosity values are the same for the test tracer and the uncharged water tracer (HTO), D_{erw} can be expressed as the ratio of D_e values for the test tracer and HTO, corrected for the respective diffusivities in bulk water (D_w, $m^2\ s^{-1}$) according to:

$$D_{erw} = \frac{D_e D_w^{HTO}}{D_w D_e^{HTO}}$$

(6.2)

κ is a dimensionless sorption distribution coefficient defined according to

$$\kappa = R_d \frac{\rho_{bd}}{\varepsilon}$$

(6.3)

κ equals the ratio of amounts (n, mol) of surface species (associated with the solid phase) to species in the aqueous phase, which can be demonstrated by replacing the right-hand terms of Eq. (6.3) by their definitions:

$$\kappa = \frac{n_s V_{aq}}{n_{aq} m_s} \frac{m_s V_{tot}}{V_{tot} V_{aq}} = \frac{n_s}{n_{aq}}$$

(6.4)

The subscript s in Eq. (6.4) denotes the solid phase and aq the bulk water phase; V_{aq} is the volume of total pore water and V_{tot} the total clay volume.

D_{erw} values larger than 1 represent a situation in which D_e values for a given cationic element are larger than can be expected from the relative ratio of the diffusion coefficients in water of the respective element and the uncharged water tracer. In view of Eq. (6.1), the enhancement of diffusive rates is not only the result of the equilibrium distribution of a given diffusing species between the solid and the aqueous phase, but also of its ratio of mobilities (diffusion coefficients) in both phases.

The unknown parameters κ and μ_s may be derived from the typical information of a diffusion experiment (viz. D_e and α), provided that the speciation of the element studied is relatively simple, which is the case for many elements investigated in the present work (such as Na^+ for example). It is rather straightforward to set κ as a known parameter based on the measured α (and thus from R_d, *cf.* Eq (1.3)) and to derive μ_s from the measured D_e values (*cf.* Eq. (6.1)). However, if an element forms different surface species, Eq. (6.1) has to be expanded (Gimmi & Kosakowski 2011) to the following form, in which the index i denotes the different surface species:

$$D_{erw} \approx 1 + \sum_i \kappa_i \mu_{s(i)}$$

(6.5)

A typical case for the application of Eq. (6.5) may be found in the diffusion of Cs$^+$ in illite. Cs$^+$ may form different surface species (Poinssot et al. 1999). According to the different chemical type of bonding, different individual μ_s values can be expected for these surface species. In such cases the determination of κ and μ_s from D_e and α is inherently associated with ambiguity.

Eq. (6.1) is closely related to the description of the enhancement of diffusive rates by surface species in the electrical double layer (EDL) of charged clays (Appelo & Wersin 2007, Appelo et al. 2010, Glaus et al. 2015a), which has been described for example by the following equation:

$$D_e = \frac{\varepsilon}{G}\left(f_{free} + f_{DL}\frac{c_{DL}}{c}q_\eta\right)D_w$$

(6.6)

This model is based on two parallel fluxes occurring in the separate volumes of the EDL and the free pore water, characterised by the respective fractional volumes (f). q_η is the ratio of viscosities of free water and EDL water, a factor which may be introduced to account for different molecular mobilities of the diffusing species in these different types of water. G is a tortuosity factor relating the pore diffusion coefficient (D_p) of the uncharged water tracer with its bulk diffusion coefficient. G can thus be related with the effective diffusion coefficient of HTO according to the following equation:

$$G = \frac{D_w^{HTO}}{D_p^{HTO}} = \frac{D_w^{HTO}\varepsilon}{D_e^{HTO}}$$

(6.7)

Combination of Eqs. (6.2), (6.6) and (6.7) yields:

$$D_{erw} = f_{free} + f_{DL}\frac{c_{DL}}{c}q_\eta$$

(6.8)

The close similarity between Eq. (6.1) and Eq. (6.8) can be recognised when bearing in mind that the concentration gradients are related to the total porosity volume in the Gimmi – Kosakowski scheme. The factors μ_s and q_η are thus equivalent. This underlines that both approaches (the Gimmi – Kosakowski scheme and the EDL approach) are based on merely the same fundamental process. Only the nomenclature and the normalisation of volumes are treated differently.

6.2   Cation data

A compilation of the present cation diffusion data within the scope of the Gimmi – Kosakowski scheme is shown in Figs. 6.1 to 6.3. Note that native measurements of D_e values for HTO were used for the calculation of D_{erw} values wherever available. The motivation of a double-logarithmic representation is simply given by a better visibility of the individual data at low κ ranges. There is no physical background for it. Rather the curved lines may be somewhat misleading in view of the linear character of Eq. (6.1).

In these plots the data are grouped according to the different types of clays and to the different bulk-dry densities. No distinction into the different concentrations of the background electrolyte was made. As can be seen from the data homogeneity, this parameter didn't have a primary influence on the potential formation of data groups. A more detailed discussion of the dependence of R_d values on the concentration of the background electrolyte solution is provided in section 6.4. Fit curves were obtained from fitting the data to Eq. (6.1). A comparison with the fit curves given in Gimmi & Kosakowski (2011) is also shown. These literature data comprise a much broader scope, including data measured in soils and intact clay rocks. Note that κ for the Volclay data has been calculated based on the partial montmorillonite densities.
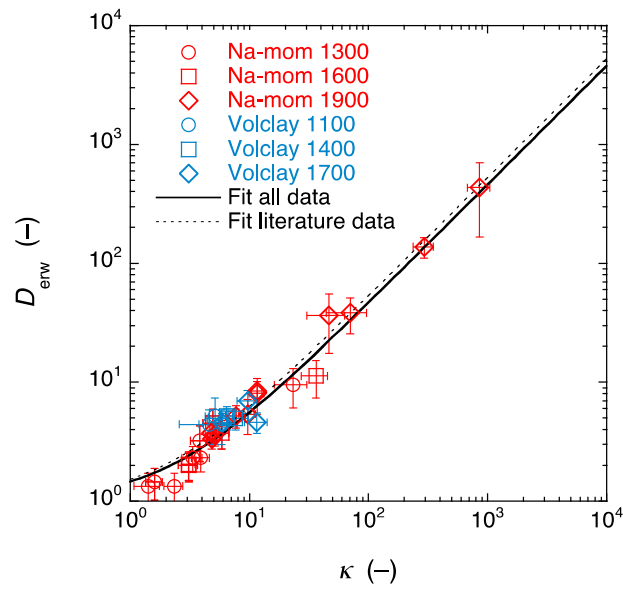
Fig. 6.1:   Representation of the diffusion data for $^{22}Na^+$ in the Gimmi – Kosakowski scheme, *cf.* Eq. (6.1) (Gimmi & Kosakowski 2011).

All κ values were calculated from the rock capacity factors obtained from diffusion. The legends indicate the bulk-dry density [kg m^{-3}]. The solid fit curve was obtained from the present measurements, the dashed line is from the data used in Gimmi & Kosakowski (2011).
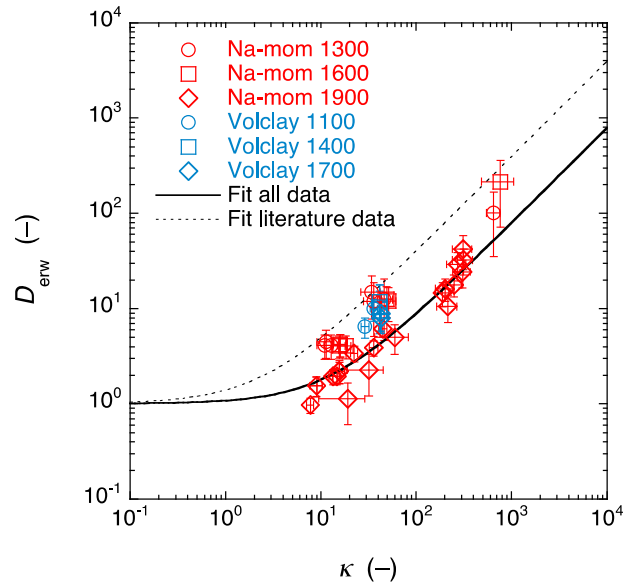
Fig. 6.2:   Representation of the diffusion data for $^{85}Sr^{2+}$ in the Gimmi – Kosakowski scheme, *cf.* Eq. (6.1) (Gimmi & Kosakowski 2011).

All κ values were calculated from the rock capacity factors obtained from diffusion. The legends indicate the bulk-dry density [kg m^{-3}]. The solid fit curve was obtained from the present measurements, the dashed line is from the data used in Gimmi & Kosakowski (2011).
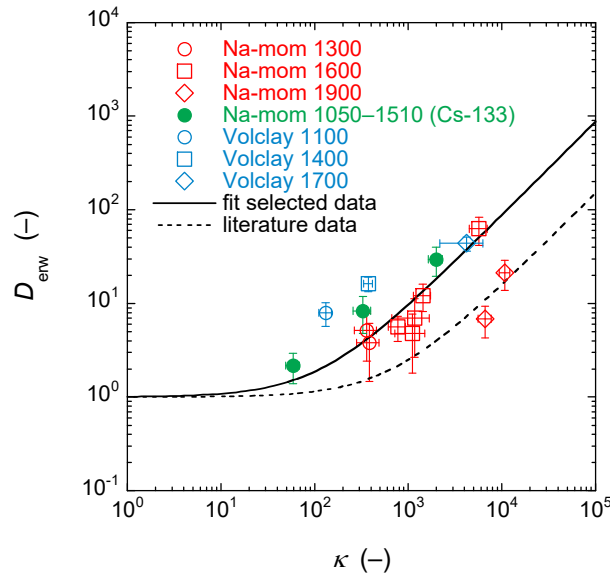
Fig. 6.3:   Representation of the diffusion data for $^{134}Cs^+$ in the Gimmi – Kosakowski scheme, *cf.* Eq. (6.1) (Gimmi & Kosakowski 2011).

All κ values were calculated from the rock capacity factors obtained from diffusion. The legends indicate the bulk-dry density [kg m^{-3}]; Cs-133 denotes the addition of stable Cs$^+$. The solid fit curve was obtained from the present measurements excluding those at 1900 kg m^{-3}, the dashed line is from the data used in Gimmi & Kosakowski (2011).

All plots show a rather homogeneous picture, whereby the homogeneity decreases gradually when going from $^{22}Na^+$ to $^{85}Sr^{2+}$ and to $^{134}Cs^+$. If the data were perfectly grouped according to the fit curve, this could be interpreted in the sense that a single type of interaction determines the formation of mobile surface species and that they exhibit a constant surface mobility across all conditions tested. The plots demonstrate the applicability of the parallel flux model described by Eq. (6.1) within a very broad range of conditions. Indirectly, they also show the validity of the various experimental techniques used in the present work to measure diffusive properties even under rather difficult conditions, such as very large diffusivities in the clay sample compared to the diffusivities in the confining filters. However, the Gimmi – Kosakowski scheme does not provide process-related information on the underlying sorbing mechanisms. Following the reasoning given in Glaus et al. (2007), R_d values are predominantly influenced by the concentration of the background solution and by the charge of the diffusing cation, indicating that the cation exchange reaction is the main influencing process determining R_d.

The formation of subgroups in Figs. 6.1 to 6.3 may be discussed in the context of variation of surface mobilities of the diffusing elements. The measurement of R_d values for Cs$^+$ has shown unequivocally an impact of bulk-dry density on sorption and suggests that structural and/or energetic differences exist between the formation of Cs$^+$ surface species at the different conditions. This has been shown to be the case for the sorption of $^{134}Cs^+$ on montmorillonite (*cf.* Tab. 5.4) and on Volclay bentonite (Van Loon & Glaus 2008). Similar effects were presumed to be effective in the case of $^{85}Sr^{2+}$ sorption (*cf.* section 5.4), however with different signs. One may hypothesise that these different surface species may have different surface mobilities. The data homogeneity generally shows that such effects may cover less than an order of magnitude in D_{erw} vs κ. A slight trend for a decreasing surface mobility with increasing bulk-dry density may be seen in the Sr^{2+} data in Fig. 6.2. The Cs$^+$ data exhibit only a weak dependency on bulk-dry density for ρ_{bd} values less than ~ 1700 kg m^{-3}. For this reason, these data were used as a single group for parameter

fitting. The surface mobility of Cs species in the cation exchange sites in that range of bulk-dry density is thus almost the same, irrespective of whether these are bound to the true montmorillo-nite cation exchange sites or to the cation exchange sites ascribed to illite impurities (*cf.* Fig. 3.7). Only at very large bulk-dry densities of the order of 1900 kg m^{-3}, a significant effect on the surface mobility can be noted in the experimental data. At such large bulk-dry densities a transition from the trilayer to a bilayer structure of the interlayer water was postulated (Holmboe et al. 2012, Kozaki et al. 1998). The observation that moderate effects in the surface mobility of Cs^{+} are observed in the experimental data (*cf.* Fig. 6.3), while these are almost absent in the ^{22}Na^{+} data (*cf.* Fig. 6.1) are in agreement with the results of molecular simulations (Kosakowski et al. 2008) for the respective range of experimental conditions.

The decrease of R_d values of ^{85}Sr^{2+} on montmorillonite with increasing bulk-dry density (*cf.* Fig. 6.2) is in agreement with its higher tendency to form a hydration sphere compared to Na^{+} (Ohtaki & Radnai 1993), which has been discussed in the scope of the results of the batch sorption measurements (*cf.* Fig. 5.1). One may hypothesise that the molecular mobility of such a highly hydrated cation decreases with decreasing interlayer distances.

For all these reasons the exact position of the fit curves will depend to some degree on the potential formation of subgroups in the data. Accordingly, the fit curves obtained from the ^{22}Na^{+} data are in excellent agreement with those of the literature compilation (Gimmi & Kosakowski 2011). The agreement of the fit curves for ^{85}Sr^{2+} and ^{134}Cs^{+} is clearly worse, however the obtained fit para-meter values are yet within the same order of magnitude.

6.3   Anion data

The description of the reduced anion-accessible porosity in smectite depends on the conceptual approach taken for the description of different types of porosity. The simplest approach proposed by Birgersson & Karnland (2009) assumes the existence of a single type of porosity in which the concentration of anions is given according to a Donnan equilibrium with the external solution. Other model concepts (Tournassat & Appelo 2011, Van Loon et al. 2007) assume a different behaviour of anions in the porosities near the outer and inner surfaces. While anions are excluded from the latter, they are distributed according to a Donnan equilibrium in the former porosities. They are further present at the same concentrations as in the external solution in porosities having the properties of bulk water. Both approaches may be used to describe the effect of anion exclu-sion for ionic strengths in the external solution up to ~1 M. For higher ionic strengths significant differences may be noted for both models (Birgersson & Karnland 2009).

The Gimmi – Kosakowski scheme can analogously be applied to anions, if the depletion of the charged pore space is described by a negative sorption distribution coefficient. This approach has been frequently applied to characterise the anion-(in)accessible volumes near clay surfaces (Schofield 1947). Reduced accessible porosities for anions have been frequently observed in diffusion experiments with negatively charged elements in smectites (Van Loon et al. 2007). The difference between the total porosity and the measured capacity factor can formally be used to calculate a R_d value according to the definition of α:

$$R_d = \frac{\alpha - \varepsilon_{tot}}{\rho_{bd}}$$

(6.9)

Combining Eq. (6.3) with Eq. (6.9) yields:

$$\kappa = \frac{\alpha - \varepsilon_{tot}}{\varepsilon_{tot}}$$

(6.10)

an equation that can be directly used to calculate κ from the available experimental information.

A compilation of the anion data is shown in Fig. 6.4. In contrast to the cation data, a semi-logarithmic representation of the axis has to be chosen for the present data because of the negative κ values.
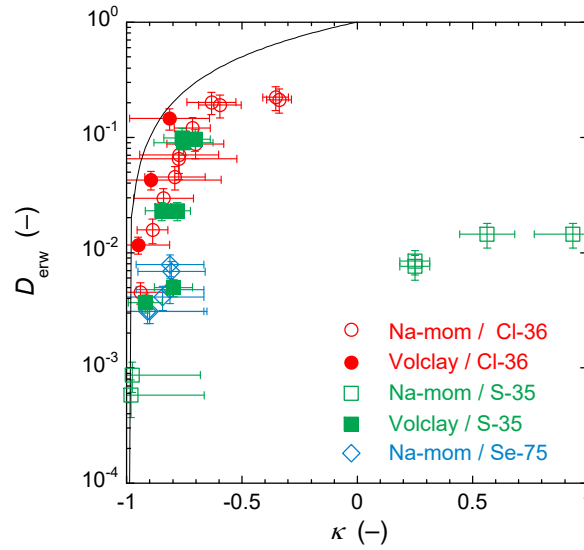
Fig. 6.4:   Representation of the anion diffusion data in the Gimmi – Kosakowski scheme, *cf.* Eq. (6.1) (Gimmi & Kosakowski 2011).

All κ values were calculated from the rock capacity factors obtained from diffusion. The solid line represents the bounding case for $\mu_s = 1$.

If no interaction between the anion and the clay surface takes place, α equals the accessible porosity. Because the latter quantity is smaller than ε_{tot}, κ is negative for anions in such cases. As already explained in section 3.5.1 the positive κ values for most of the $^{35}SO_4^{2-}$ diffusion data for Na-*mom* can most probably be explained by an isotopic exchange reaction of this tracer with stable SO_4^{2-} contained in an unidentified mineral phase in Na-*mom*. The other data follow rather the bounding case using $\mu_s = 1$, whereby the measured D_{erw} are rather clearly less than the predicted values, which can partly be explained by the lower D_w values for SO_4^{2-} and SeO_4^{2-} compared to water. The detailed structure of the data may probably also be influenced by the formation of ion pairs of the bi-valent anions with alkaline earth cations. Ion pair formation has an effect on the net charge of the tracers, which in turn impacts their distribution between the different types of clay porosity. The differences in pore water composition in the experiments with Volclay bentonite and Na-*mom* may thus be a reason for the different diffusive behaviour of the bi-valent anions in these clays. However, no attempt has been undertaken to take such effects into quantitative modelling of the data.

6.4 Comparison of sorption results in compacted versus dispersed clay samples

The agreement between sorption data obtained from disperse clay systems with those obtained from diffusion experiments using compacted clay samples depends on the cation studied. R_d values in a homoionic Na clay for the exchange of the mono-valent Na^+ cation (A) for a cation (B) with charge z can be calculated from the selectivity coefficients ($_A^B K_c$, [-]), the cation exchange capacity (CEC, [eq kg^{-1}]) and the molar Na^+ concentration in solution [Na^+] according to Bradbury & Baeyens (1994):

$$R_d = \frac{_A^B K_c CEC \gamma_B}{z[Na^+]^z \gamma_A^z}$$

(6.11)

where γ are the activity coefficients (–) of cations A and B and z the charge of B. After rearranging Eq. (6.11) and transforming to a logarithmic form, the following equation is obtained that can also be used to extract $_A^B K_c$ from the experimental data:

$$\log\left(R_d \frac{\gamma_A^z}{\gamma_B} \right) = \log\left(\frac{_A^B K_c CEC}{z} \right) - z\log\left([Na^+] \right)$$

(6.12)

Note that R_d has to be used on a dm^3 kg^{-1} scale in order to be compatible with the definition of activity coefficients which is based on a mol dm^{-3} scale.

Fig. 6.5 shows the sorption results obtained from the diffusion experiments in a logarithmic representation according to Eq. (6.12). The activity coefficients were calculated using the Davies equation (Grenthe et al. 1997), which may not be the best choice for ionic strengths larger than 0.5. However, for the present purpose, the bias introduced thereby is irrelevant. The CEC was set to 0.83 eq kg^{-1} (own unpublished measurements).
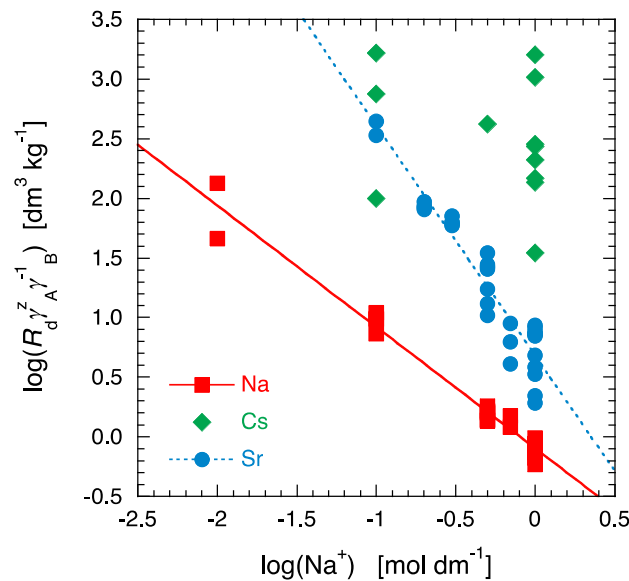
Fig. 6.5:   Logarithmic representation of the R_d values taken from diffusion results according to Eq. (6.12).

Obviously, the Na^+ and Sr^{2+} data are well correlated with the concentration of the background electrolyte, while no correlation is present in the Cs^+ data. The reason for the latter circumstance is the strong dependency of Cs^+ sorption on bulk-dry density (*cf.* Tab. 5.4), which is also visible to a certain extent in the Sr^{2+} data. The best-fit parameter values obtained by regression of the absolute (Eq. (6.11)) and logarithmic (Eq. (6.12)) values are given in Tab. 6.1.

Tab. 6.1:   Best-fit parameter values derived from regression (*cf.* Eq. (6.12)) of the data shown in Figs. 6.1 and 6.2. *q* is the minuend of the right-hand side of Eq. (6.12).

Cation	Regression of logarithmic values			Regression of absolute values	
	z	q	$^B_A K_c$	z	$^B_A K_c$
Na^+	1.02 ± 0.03	-0.098 ± 0.02	0.96 ± 0.2	0.99 ± 0.24	1.1 ± 0.9
Sr^{2+}	1.93 ± 0.11	0.68 ± 0.05	11.5 ± 0.7	1.91 ± 0.09	10.9 ± 1.6

In agreement with our previous findings (Glaus et al. 2007), the values of the slopes in Fig. 6.5 agree well with the charges of Na^+ and Sr^{2+}. Furthermore, the selectivity of the exchange of the stable isotope $^{23}Na^+$ for a $^{22}Na^+$ cation agrees perfectly with the theoretical value of unity. In the case of Sr^{2+} it has already been shown (*cf.* Fig. 5.1), that the R_d values derived from diffusion experiments using compacted clay samples agree fairly well with those from sorption experiments using disperse clay suspensions with a certain bias noted for the highest bulk-dry densities. One may further note that the selectivity of ~ 11 is larger than a literature value of 2.6 (Bradbury & Baeyens 2003), which has been derived from Ca^{2+} exchange data in disperse systems. The evaluation of selectivity from the sorption data shown in Fig. 5.1 obtained from disperse systems also yields values larger than this estimate, whereby one has to note that the slope (charge) is clearly less than 2 (~ 1.5).

Summarising one may assert that the agreement of sorption data in compacted clays with those obtained from disperse systems is perfect for Na^+ and rather acceptable for Sr^{2+}, while a noticeable disagreement can be noted for Cs^+. Similar conclusions were drawn for Na^+ and Sr^{2+} in a comparative study using Opalinus Clay (Van Loon et al. 2005).

6.5   Conclusions and implications for the selection of diffusion coefficients for radionuclides in performance assessment

Summarising it can be concluded that the entire set of diffusion data exhibits self-consistency to a large degree and wide conformity with literature data. This has been tested using a broad and relevant range of parameter values for bulk-dry density and concentration of the background electrolyte. Some issues, which appear not conform with Fickian diffusion (e.g. the effects of bulk-dry density on the phase distribution equilibria of cations and the related effects on diffusive fluxes, *cf.* sections 3.4.1 and 3.4.2), can be regarded as rather being of scientific interest than of having a significant impact on the overall conclusions. The conclusions are thus applicable for the specific conditions of the Swiss concept of a bentonite backfill or buffer in a deep-geological repository for radioactive waste. Wherever heterogeneity in the data or the formation of subgroups was observed, a process-based explanation for this behaviour can be given. The parameter dependence on the composition of the external background electrolyte solution and the homogeneous data clustering underpin the hypothesis that surface species in the cation exchange sites (or the presence of cationic species in the EDL, *cf.* Eq. (6.6) in an electrostatic view) need to be treated formally as mobile species for transport modelling. The volumetric enrichment of these species

compared to the true aqueous phase species accounts for the capacity of the clay for such species. Accordingly, a delayed breakthrough is observed compared to a simple uncharged water tracer. The same implications can be put forward for transport modelling as in previous literature work on the diffusive behaviour of Sr^{2+} and selected bivalent transition element cations (Glaus et al. 2015a). These can be regarded as complementary to those already stated in the Introduction (section 1.1):

- Diffusion of cationic species in compacted charged clays and clay minerals cannot be viewed as a physical transport process of aqueous phase species only.

- The potential influence of mobile surface species on diffusive fluxes needs to be taken into account by knowledge of their equilibrium distribution and by an appropriate assessment of their mobility.

- The traditional procedure of deriving effective diffusion coefficients from measurements of an uncharged water tracer (HTO for example) may underestimate the migration distances of cationic species significantly depending on the prevailing chemical conditions.

The present report suggests that these conclusions are valid for all types of cations bound to argillaceous materials via a cationic exchange mechanism. In terms of applications in the context of disposal of radioactive waste, Cs^+, Ba^{2+} and Ra^{2+} are of particular interest. The extent of the potential bias between the traditional pore diffusion model (which only takes into account the mobility of bulk aqueous phase species) and a modified transport model for surface species will, however, depend on the chemical conditions of the respective pore waters. For a base scenario involving stagnant pore waters with a seawater composition, such effects are expected to be less than for scenarios in which fresh water displaces the stagnant pore water for example.

The estimation of diffusion coefficients may also comprise other influencing factors than those outlined above, depending on the conditions encountered for a specific case. It has to be kept in mind that diffusive fluxes are the result of electrochemical potential gradients and thus mainly based on gradients of ion activities and electric potentials (Appelo & Wersin 2007). The experimental setup chosen in this work excludes the formation of such potentials. In view of the rather broad variation of the concentrations of the background electrolyte, we may also conclude that effects related to activity coefficients are of rather subordinate role for the present data. Otherwise a larger heterogeneity of the data would be expected. Note that in related work we extended the range of background electrolyte concentrations to values as low as 0.01 M without notifying significant deviations from the Gimmi – Kosakowski scheme (Glaus et al. 2015a and b).

The application of the present results in performance assessment is rather straightforward. κ values may be derived from available sorption data bases or other sources of information (e.g. Eq. (6.11)), and the relevant information on diffusion can be derived from combining these with adequate values for μ_s in Eq. (6.1). Such information is readily available for cations. For anions the situation is less straightforward because the accessible porosity under the specific geochemical conditions needs to be known in order to calculate κ (*cf.* Eq. 6.10). Two possibilities are available for that purpose. Either the accessible porosity for anions is calculated using a conceptual approach, such as the Donnan exclusion model (Appelo et al. 2010, Karnland et al. 2011, Tournassat & Appelo 2011), or it is assessed using empiric relationships such as given for bentonite at a variety of bulk-dry densities and background electrolyte concentrations (Van Loon et al. 2007).

The choice of appropriate μ_s values depends on the degree of conservativity associated. Although the data compilation of Gimmi & Kosakowski (2011) indicates a noticeable variation in μ_s values for different types of metallic elements, it is recommended here to choose rather upper values for

μ_s for all types of elements. Our recent experiments using transition metal ions (Glaus et al. 2015a) indicated that μ_s is of the same order of magnitude for transition metal cations as for Sr^{2+} as an example. The discrepancy of this recent observation with the data presented by Gimmi & Kosakowski (2011) can simply be explained by the different assumptions taken for the number of mobile species. A detailed discussion is, however, outside the scope of the present report.

The procedure outlined here is thus by large in agreement with the procedure recently proposed by Van Loon (2014), in which Eq. (6.1) is basically applied to estimate effective diffusion coefficients. The relevant information on geometry factors (*cf.* Eq. (6.2)) is obtained using a so-called cementation factor (*m*), which was taken from literature data for the diffusion of HTO, according to Archie's law (Archie 1942) applied for diffusive mass transfer:

$$D_e^{HTO} = A\ \varepsilon^m \tag{6.13}$$

The second adjustable parameter in Eq. (6.13), A, is often equalled to the D_w value of water. In such a case Eq. (6.13) may be combined with Eq. (1.2) to obtain:

$$\varepsilon^m = \varepsilon\ \frac{\delta}{\tau^2} \tag{6.14}$$

or:

$$\varepsilon^{m-1} = \frac{\delta}{\tau^2} \tag{6.15}$$

Knowledge on m gives thus access to the geometry factor. The exact choice of the adjustable parameters, however, depends largely on the source data as is shown in Fig. 6.6a. The position of potential fit curves for different clay minerals may vary by approximately one order of magnitude (Glaus et al. 2010). The determination A and m for Na-*mom* in the latter work was mainly governed by the position of the chloride data and not the HTO data. For the HTO data only a very restricted range of porosity values was available. For that reason, the chloride and HTO data were pooled for curve fitting (whereby the accessible chloride porosity was used for ε in Eq. (6.13)). The same can be stated for the other fit curves. They are largely based on anion diffusion data because this allows for a considerable extension of the parameter space.

In view of the diffusion data measured for HTO in the present work the range of porosities can now be extended. It can even be extended to larger ranges when including also data measured recently in a PhD work (Bestel 2014). As can be seen from Fig. 6.6b, the pooled HTO diffusion data do not match either of the existing fit curves. Applying a simple Archie relation would in principle be feasible but leads to an inconsistent description of the pooled HTO and anion diffusion data at high porosity values. For this reason, we propose to extend Archie's relation similarly to an extended form proposed in Van Loon (2014):

$$D_e^{HTO} = A_1\ \varepsilon^{m_1} + A_2\ \varepsilon^{m_2} \tag{6.16}$$

In order to be compatible with the existing anion diffusion data in Na-*mom*, A_1 and m_1 are set to literature values (Glaus et al. 2010), while A_2 and m_2 are left as adjustable parameters. Tab. 6.2 gives the full set of parameter values obtained from the blue fit curve shown in Fig. 6.6b.
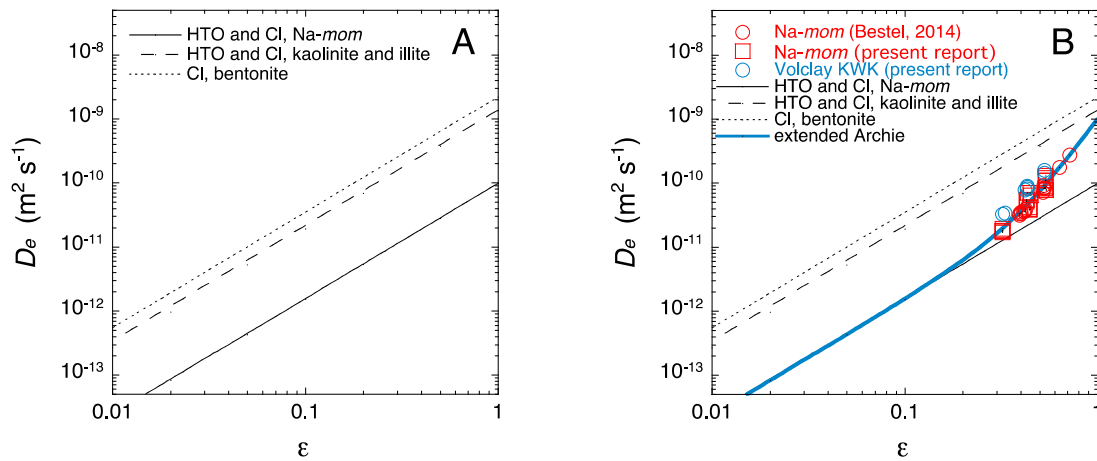
Fig. 6.6:   Fit curves proposed in the literature to describe the dependence of D_e values on the porosity.

Van Loon et al. (2007) for the bentonite data, Glaus et al. (2010) for the other data plot A). Overview of HTO diffusion data in Na-*mom* (including those measured by Bestel 2014) and Volclay KWK in the present work (plot B) together with an additional fit curve (blue line) obtained by fitting these data to the extended Archie relation (*cf.* Eq. (6.13)).

Tab. 6.2:   Best-fit parameter values for the HTO diffusion data in Na-*mom* using the extended Archie relation (*cf.* Eq. (6.13)).

Species	A_1	m_1	A_2	m_2
HTO	9.8×10^{-11}	1.8	9.0×10^{-10}	4.3

The combination of Eq. (6.1) and Eq. (6.16) yields thus:

$$D_e \approx \left(A_1 \varepsilon^{m_1} + A_2 \varepsilon^{m_2} \right)\left(1 + \kappa \mu_s \right) \tag{6.17}$$

Note that this equation assumes that the D_e/D_e^{HTO} factor is of the order of 1. The equation takes into account the various effects of clay compaction and porosity structure, as well as the specific interaction of the diffusing species with the clay surface resulting in enhanced or attenuated concentration gradients according to the type of charge of the diffusing species.

The application of Eq. (6.17) is restricted to situations that are consistent with the basic outline of its derivation, which is the parallel diffusive flux of an aqueous phase and a surface species related by a chemical equilibrium reaction. This may apply to the diffusion of trace species irrespective of whether these are radionuclides or other ionic components in the clay pore water. A tricky situation may arise if the species under consideration is also the main species on the surface. An example would be the diffusion of Na^+ ions in a homoionic Na-montmorillonite. In such a case the surface might be taken into account as a pathway for diffusion, however, the resulting cation fluxes are negligible because there is no substantial concentration gradient for Na^+. The resulting changes in solution concentration of Na^+ are thus also negligible. One may also note that the exchange of a Na^+ cation on the surface against a Na^+ cation in solution does not lead to any changes in the respective concentrations. Such a reaction does not lead to mass transfer from a macroscopic point of view. The $\kappa \mu_s$ term in Eq. (6.17) can therefore be regarded as futile for such a case and approximated by zero.

The advantage in the use of Eq. (6.17) is that mass transfer in clay can simply be calculated from the chemical gradients of aqueous phase species treating the chemical coupling as a sort of black box process. The evident drawback is that the effective diffusion coefficients are no longer constants, but quantities depending on chemical factors such as pH and ionic strength. Which of the advantages or disadvantages prevail, depends on the specific situation of the application. No generic statement can be made. However, it is important that the proposed procedures are applied in an adequate and pertinent manner with respect to the specific problem.

6.6 General conclusions on 'surface-diffusion effects'

As outlined in the Introduction (section 1.2), the concept of surface diffusion has been a subject of controversy in the literature. The present work cannot discriminate between the various feasible explanations for the "enhanced cation diffusion" in an absolute sense, too. The reason is that the two key parameters involved in a model description of surface diffusion, (i) the amount of mobile cationic species at the clay surface and (ii) the mobility of these surface cations cannot be quantified independently by the present experiments.

The value of the present work lies rather in yielding a consistent set of experimental data measured across broad ranges of conditions (salinity of the background electrolyte, bulk-dry density of the clay sample), demonstrating that the concept of surface diffusion is at least a viable approach explaining the observed phenomena across parameter ranges relevant for the conditions encountered in realistic bentonite backfill or buffers.

Surface diffusion is more than a side effect possibly observed under exotic conditions. Evidences from recent experiments further showed that surface diffusion might also be a relevant transport process for transition metals (Glaus et al. 2015a). A robust assessment of the mobility of cations in charged clay media needs therefore to take this process into account and estimate its potential contribution to the overall migration process.

7   References

Aldaba, D., Glaus, M.A., Leupin, O., Van Loon, L.R., Vidal, M. & Rigol, A. (2014): Suitability of various materials for porous filters in diffusion experiments. Radiochim. Acta 102, 723-730.

Aldaba, D., Glaus, M.A., Van Loon, L.R., Rigol, A. & Vidal, M. (2017): Diffusion of radiosulphate and radiocaesium in kaolinite clay (KGA-2): Testing the applicability of the pore water diffusion model. Applied Geochemistry 86, 84-91.

Altmann, S., Tournassat, C., Goutelard, F., Parneix, J.-C., Gimmi, T. & Maes, N. (2012): Diffusion-driven transport in clayrock formations. Appl. Geochem. 27, 463-478.

Appelo, C.A.J. & Wersin, P. (2007): Multicomponent diffusion modeling in clay systems with application to the diffusion of tritium, iodide, and sodium in Opalinus Clay. Environ. Sci. Technol. 41, 5002–5007.

Appelo, C.A.J., Van Loon, L.R. & Wersin, P. (2010): Multicomponent diffusion of a suite of tracers (HTO, Cl, Br, I, Na, Sr, Cs) in a single sample of Opalinus Clay. Geochim. Cosmochim. Acta 74, 1201–1219.

Archie, G.E. (1942): The electrical resistivity log as an aid in determining some reservoir characteristics. Trans. AIME 146, 54-62.

Bergaya, F., Theng, B.K.G. & Lagaly, G. (2006): Handbook of clay science. Elsevier, Amsterdam, The Netherlands.

Bestel, M. (2014): Water-montmorillonite systems: neutron scattering and tracer through-diffusion studies. Diss. University of Bern, Switzerland.

Bestel, M., Frick, S., Glaus, M.A., Gimmi, T., Van Loon, L.R. & Diamond, L.W. (*in prep.*): Combined tracer through-diffusion of HTO and ^{22}Na through Na-montmorillonite with different bulk dry densities. *Submitted to Appl. Geochem.*

Birgersson, M. & Karnland, O. (2009): Ion equilibrium between montmorillonite interlayer space and an external solution – consequences for diffusional transport. Geochim. Cosmochim. Acta 73, 1908-1923.

Bourg, I.C., Bourg, A.C.M. & Sposito, G. (2003): Modeling diffusion and adsorption in compacted bentonite: a critical review. J. Contam. Hydrol. 61, 293-302.

Bourg, I.C., Sposito, G. & Bourg, A.C.M. (2006): Tracer diffusion in compacted, water-saturated bentonite. Clays Clay Miner. 54, 363-374.

Bourg, I.C., Sposito, G. & Bourg, A.C.M. (2007): Modeling cation diffusion in compacted water-saturated sodium bentonite at low ionic strength. Environ. Sci. Technol. 41, 8118-8122.

Boving, T.B. & Grathwohl, P. (2001): Tracer diffusion coefficients in sedimentary rocks: correlation to porosity and hydraulic conductivity. J. Contam. Hydrol. 53, 85-100.

Bradbury, M.H. & Baeyens, B. (1994): Sorption by cation exchange: incorporation of a cation exchange model into geochemical computer codes. PSI Bericht 94-07, Paul Scherrer Institut, Villigen, Switzerland. Also published as Nagra Tech. Report NTB 94-11.

Bradbury, M.H. & Baeyens, B. (2003): Near field sorption data bases for compacted MX-80 bentonite for performance assessment of a high-level radioactive waste repository in Opalinus Clay host rock. PSI Bericht 03-07, Paul Scherrer Institut, Villigen, Switzerland. Also published as Nagra Tech. Report NTB 02-18.

Churakov, S.V. & Gimmi, T. (2011): Up-scaling of molecular diffusion coefficients in clays: a two-step approach. J. Phys. Chem. C 115, 6703-6714.

Churakov, S.V. (2013): Mobility of Na and Cs on montmorillonite surface under partially saturated conditions. Environ. Sci. Technol. 47, 9816-9823.

Conca, J.L., Apted, M. & Arthur, R. (1993): Aqueous diffusion in repository and backfill environments. Mater. Res. Soc. Symp. Proc. 294, 395-402.

Gimmi, T. & Kosakowski, G. (2011): How mobile are sorbed cations in clays and clay rocks? Environ. Sci. Technol. 45, 1443-1449.

Gimmi, T., Leupin, O.X., Eikenberg, J., Glaus, M.A., Van Loon, L.R., Waber, H.N., Wersin, P., Wang, H.A.O., Grolimund, D., Borca, C.N., Dewonck, S. & Wittebroodt, C. (2014): Anisotropic diffusion at the field scale in a 4-year multi-tracer diffusion and retention experiment – I: Insights from the experimental data. Geochim. Cosmochim. Acta 125, 373-393.

Glaus, M.A., Baeyens, B., Bradbury, M.H., Jakob, A., Van Loon, L.R. & Yaroshchuk, A. (2007): Diffusion of ^{22}Na and ^{85}Sr in montmorillonite: Evidence of interlayer diffusion being the dominant pathway at high compaction. Environ. Sci. Technol. 41, 478-485.

Glaus, M.A., Rossé, R., Van Loon, L.R. & Yaroshchuk, A.E. (2008): Tracer diffusion in sintered stainless steel filters: Measurement of effective diffusion coefficients and implications for diffusion studies with compacted clays. Clays Clay Miner. 56, 677-685.

Glaus, M.A., Frick, S., Rossé, R. & Van Loon, L.R. (2010): Comparative study of tracer diffusion of HTO, ^{22}Na$^+$ and ^{36}Cl$^-$ in compacted kaolinite, illite and montmorillonite. Geochim. Cosmochim. Acta 74, 1999-2010.

Glaus, M.A., Frick, S., Rossé, R. & Van Loon, L.R. (2011): Consistent interpretation of the results of through-, out-diffusion and tracer profile analysis for trace anion diffusion in compacted montmorillonite. J. Contam. Hydrol. 123, 1-10.

Glaus, M.A., Birgersson, M., Karnland, O. & Van Loon, L.R. (2013): Seeming steady-state uphill diffusion of Na-22(+) in compacted montmorillonite. Environ. Sci. Technol. 47, 11522-11527.

Glaus, M.A., Aertsens, M., Appelo, C.A.J., Kupcik, T., Maes, N., Van Laer, L. & Van Loon, L.R. (2015a): Cation diffusion in the electrical double layer enhances the mass transfer rates for Sr^{2+}, Co^{2+} and Zn^{2+} in compacted illite. Geochim. Cosmochim. Acta 165, 376-388.

Glaus, M.A., Aertsens, M., Maes, N., Van Laer, L. & Van Loon, L.R. (2015b): Treatment of boundary conditions in through-diffusion: A case study of ^{85}Sr^{2+} diffusion in compacted illite. J. Contam. Hydrol. 177-178, 239-248.

González Sánchez, F., Jurányi, F., Gimmi, T., Van Loon, L.R., Unruh, T. & Diamond, L.W. (2008a): Translational diffusion of water and its depenence on temperature in charged and uncharged clays: A neutron scattering study. J. Chem. Phys. 129, 174706.

González Sánchez, F., Van Loon, L.R., Gimmi, T., Jakob, A., Glaus, M.A. & Diamond, L.W. (2008b): Self-diffusion of water and its dependence on temperature and ionic strength in highly compacted montmorillonite, illite and kaolinite. Appl. Geochem. 23, 3840-3851.

Grenthe, I., Plyasunov, A.V. & Spahiu, K. (1997): Estimation of medium effects on thermo-dynamic data. *In:* Grenthe, I. & Puigdomenèch, I. (eds.): Modelling in aquatic chemistry. OECD's Nuclear Energy Agency, Paris, France, 325-426.

Hedstrom, M. & Karnland, O. (2012): Donnan equilibrium in Na-montmorillonite from a molecu-lar dynamics perspective. Geochim. Cosmochim. Acta 77, 266-274.

Holmboe, M., Wold, S. & Jonsson, M. (2012): Porosity investigation of compacted bentonite using XRD profile modeling. J. Contam. Hydrol. 128, 19-32.

Jakob, A., Baeyens, B., Gimmi, T., Glaus, M.A., Pfingsten, W. & Van Loon, L.R. (*in prep.*): Solute diffusion in argillaceous rocks and their constituent clay minerals. Nagra Tech. Report NTB 12-02.

Jensen, D.J. & Radke, C.J. (1988): Caesium and strontium diffusion through sodium montmorillo-nite at elevated temperature. European Journal of Soil Science 39, 53-64.

Jougnot, D., Revil, A. & Leroy, P. (2009): Diffusion of ionic tracers in the Callovo-Oxfordian clay-rock using the Donnan equilibrium model and the formation factor. Geochim. Cosmo-chim. Acta 73, 2712-2726.

Karnland, O., Olsson, S. & Nilsson, U. (2006): Mineralogy and sealing properties of various bentonites and smectite-rich clay materials. SKB Technical Report TR-06-30. SKB, Stockholm, Sweden.

Karnland, O., Birgersson, M. & Hedstrom, M. (2011): Selectivity coefficient for Ca/Na ion exchange in highly compacted bentonite. Phys. Chem. Earth 36, 1554-1558.

Kosakowski, G., Churakov, S.V. & Thoenen, T. (2008): Diffusion of Na and Cs in montmorillo-nite. Clays Clay Miner. 56, 190-206.

Kozaki, T., Fujishima, A., Sato, S. & Ohashi, H. (1998): Self-diffusion of sodium ions in com-pacted montmorillonite. Nucl. Technol. 121, 63-69.

Malikova, N., Dubois, E., Marry, V., Rotenberg, B. & Turq, P. (2010): Dynamics in clays – com-bining neutron scattering and microscopic simulations. Z. Phys. Chem. 224, 153-181.

Malusis, M.A., Shackelford, C.D. & Maneval, J.E. (2012): Critical review of coupled flux formu-lations for clay membranes based on nonequilibrium thermodynamics. J. Contam. Hydrol. 138, 40-59.

Melkior, T., Yahiaoui, S., Thoby, D., Motellier, S. & Bartès, V. (2007): Diffusion coefficients of alkaline cations in Bure mudrock. Phys. Chem. Earth 32, 453-462.

Melkior, T., Gaucher, E.C., Brouard, C., Yahiaoui, S., Thoby, D., Clinard, C., Ferrage, E., Guyonnet, D., Tournassat, C. & Coelho, D. (2009): Na$^+$ and HTO diffusion in compacted bentonite: Effect of surface chemistry and related texture. J. Hydrol. 370, 9-20.

Miller, A.W., Rodriguez, D.R. & Honeyman, B.D. (2010): Upscaling sorption/desorption processes in reactive transport models to describe metal/radionuclide transport: a critical review. Environ. Sci. Technol. 44, 7996-8007.

Miller, A.W. & Wang, Y. (2012): Radionuclide interaction with clays in dilute and heavily compacted systems: A critical review. Environ. Sci. Technol. 46, 1981-1994.

Molera, M. & Eriksen, T. (2002): Diffusion of ^{22}Na$^+$, ^{85}Sr^{2+}, ^{134}Cs$^+$ and ^{57}Co^{2+} in bentonite clay compacted to different densities: experiments and modeling. Radiochim. Acta 90, 753-760.

Muurinen, A., Rantanen, J. & Penttilä-Hiltunen, P. (1986): Diffusion mechanisms of strontium, cesium and cobalt in compacted sodium bentonite. Mater. Res. Soc. Symp. Proc. 50, 617-624.

Nagra (2002): Project Opalinus Clay: Safety report – Demonstration of disposal feasibility for spent fuel, vitrified high-level waste and long-lived intermediate-level waste (Entsorgungsnachweis). Nagra Tech. Report NTB 02-05.

Norrish, K. (1954): The swelling of montmorillonite. Discuss. Faraday Soc. 18, 120-134.

Ochs, M., Lothenbach, B., Wanner, H., Sato, H. & Yui, M. (2001): An integrated sorption–diffusion model for the calculation of consistent distribution and diffusion coefficients in compacted bentonite. J. Contam. Hydrol. 47, 283-296.

Ohtaki, H. & Radnai, T. (1993): Structure and dynamics of hydrated ions. Chem. Rev. 93, 1157–1204.

Poinssot, C., Baeyens, B. & Bradbury, M.H. (1999): Experimental and modelling studies of caesium sorption on illite. Geochim. Cosmochim. Acta 63, 3217-3227.

Salles, F., Douillard, J.-M., Bildstein, O., El Ghazi, S., Prelot, B., Zajac, J. & Van Damme, H. (2015): Diffusion of interlayer cations in swelling clays as a function of water content: case of montmorillonites saturated with alkali cations. J. Phys. Chem. C 119, 10370-10378.

Sato, H. & Suzuki, S. (2003): Fundamental study on the effect of an orientation of clay particles on diffusion pathway in compacted bentonite. Appl. Clay Sci. 23, 51-60.

Savoye, S., Page, J., Puente, C., Imbert, C. & Coelho, D. (2010): New experimental approach for studying diffusion through an intact and unsaturated medium: A case study with Callovo-Oxfordian argillite. Environ. Sci. Technol. 44, 3698-3704.

Schofield, K. (1947): Calculation of surface areas from measurements of negative sorption. Nature 160, 408-410.

Shackelford, C.D. (1991): Laboratory diffusion testing for waste disposal – a review. J. Contam. Hydrol. 7, 177-217.

Shackelford, C.D. & Moore, S.M. (2013): Fickian diffusion of radionuclides for engineered containment barriers: Diffusion coefficients, porosities, and complicating issues. Eng. Geol. 152, 133-147.

Tachi, Y. & Yotsuji, K. (2014): Diffusion and sorption of Cs^+, Na^+, I^- and HTO in compacted sodium montmorillonite as a function of porewater salinity: Integrated sorption and diffusion model. Geochim. Cosmochim. Acta 132, 75-93.

Tournassat, C. & Appelo, C.A.J. (2011): Modelling approaches for anion-exclusion in compacted Na-bentonite. Geochim. Cosmochim. Acta 75, 3698-3710.

van Brakel, J. & Heertjes, P.M. (1974): Analysis of diffusion in macroporous media in terms of a porosity, a tortuosity and a constrictivity factor. Int. J. Heat Mass Tran. 17, 1093-1103.

Van Loon, L.R. (2014): Effective diffusion coefficients and porosity values for argillaceous rocks and bentonite: Measured and estimated values for the provisional safety analyses for SGT-E2. Nagra Technical Report NTB 12-03.

Van Loon, L.R. & Glaus, M.A. (2008): Mechanical compaction of smectite clays increases ion exchange selectivity for cesium. Environ. Sci. Technol. 42, 1600-1604.

Van Loon, L.R. & Jakob, A. (2005): Evidence for a second transport porosity for the diffusion of tritiated water (HTO) in a sedimentary rock (Opalinus Clay - OPA): application of through- and out-diffusion techniques. Transport Porous Med. 61, 193-214.

Van Loon, L.R. & Soler, J.M. (2003): Diffusion of HTO, $^{36}Cl^-$, $^{125}I^-$ and $^{22}Na^+$ in Opalinus Clay: Effect of confining pressure, sample orientation, sample depth and temperature. PSI Bericht 04-03, Paul Scherrer Institut, Villigen, Switzerland. Also published as Nagra Tech. Report NTB 03-07.

Van Loon, L.R., Soler, J.M. & Bradbury, M.H. (2003a): Diffusion of HTO, $^{36}Cl^-$ and $^{125}I^-$ in Opalinus Clay samples from Mont Terri. Effect of confining pressure. J. Contam. Hydrol. 61, 73-83.

Van Loon, L.R., Soler, J.M., Jakob, A. & Bradbury, M.H. (2003b): Effect of confining pressure on the diffusion of HTO, $^{36}Cl^-$ and $^{125}I^-$ in a layered argillaceous rock (Opalinus Clay): diffusion perpendicular to the fabric. Appl. Geochem. 18, 1653-1662.

Van Loon, L.R., Baeyens, B. & Bradbury, M.H. (2005): Diffusion and retention of sodium and strontium in Opalinus clay: comparison of sorption data from diffusion and batch sorption measurements, and geochemical calculations. Appl. Geochem. 20, 2351-2363.

Van Loon, L.R., Glaus, M.A. & Müller, W. (2007): Anion exclusion effects in compacted bentonites: Towards a better understanding of anion diffusion. Appl. Geochem. 22, 2536-2552.

van Schaik, J.C., Kemper, W.D. & Olsen, S.R. (1966): Contribution of adsorbed cations to diffusion in clay-water systems. Soil Sci. Soc. Am. Proc. 30, 17-22.

Yaroshchuk, A., Glaus, M.A. & Van Loon, L.R. (2007): Studies of electrochemical properties of compacted clays by concentration potential method. J. Colloid Interface Sci. 309, 262-271.

Yaroshchuk, A.E., Glaus, M.A. & Van Loon, L.R. (2008): Diffusion through confined media at variable concentrations in reservoirs. J. Membr. Sci. 319, 133-140.

A   Appendix: Experimental data for Montmorillonite

A.1   Diffusion of HTO
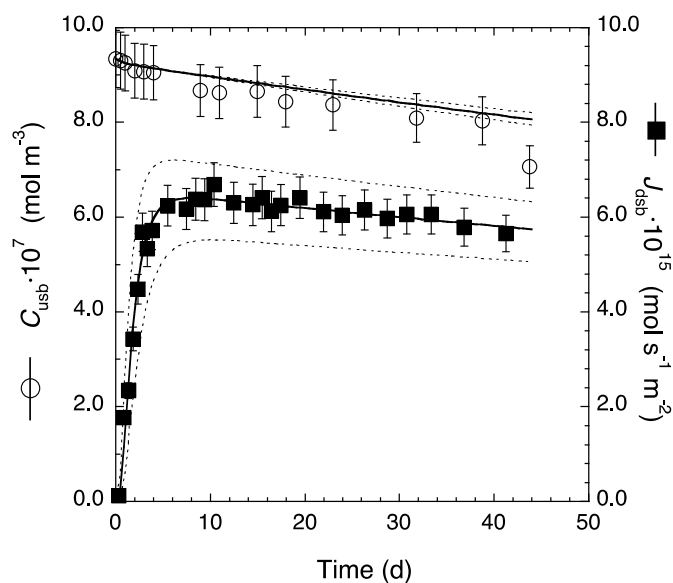
Fig. A1:   Flux at the zero-concentration boundary and reservoir concentration of HTO through-diffusion in Na-*mom* at ρ_{bd} = 1297 kg m^{-3} and 0.01 M NaClO$_4$ external salt concentration (experiment 1064_13A, *cf.* Tab. 3.1).
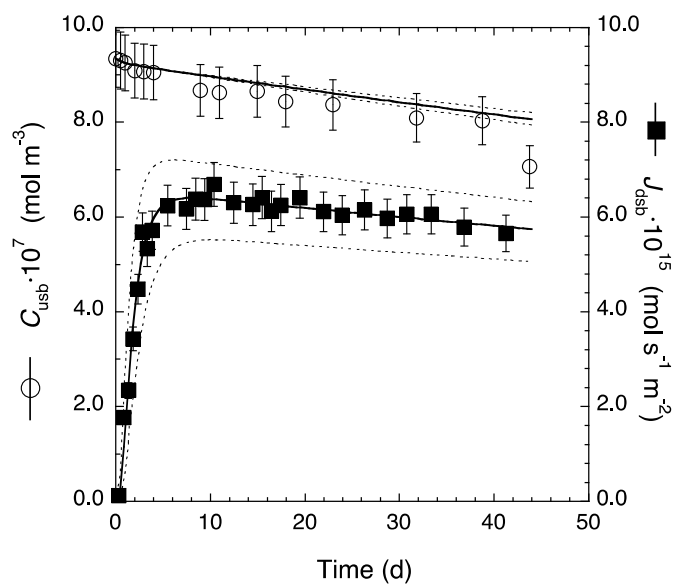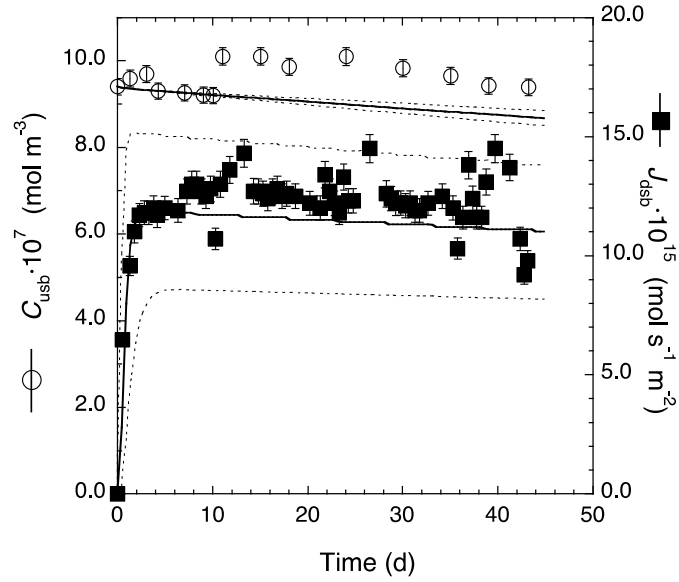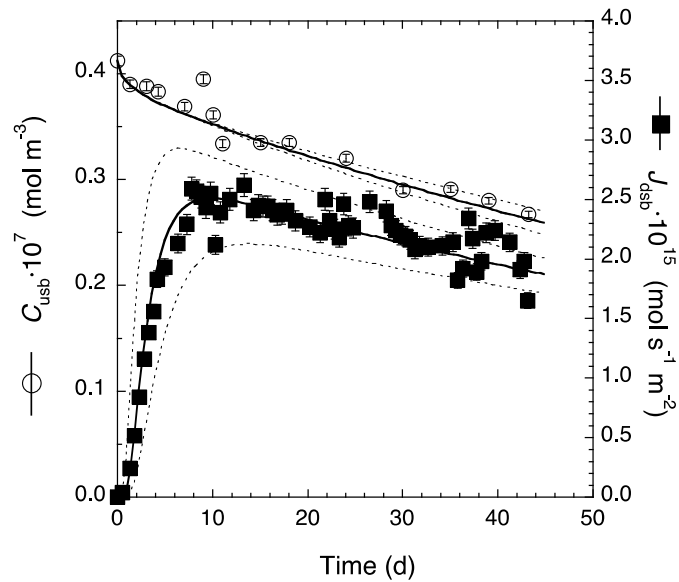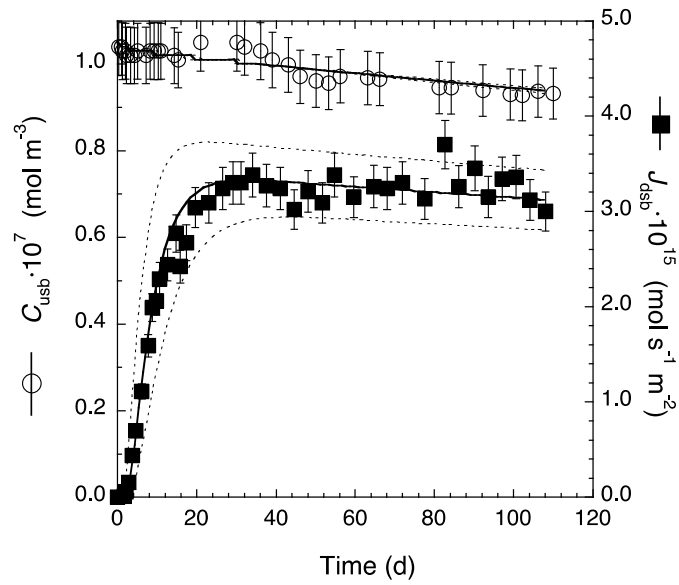

Fig. A2:   Flux at the zero-concentration boundary and reservoir concentration of HTO through-diffusion in Na-*mom* at ρ_{bd} = 1301 kg m^{-3} and 0.1 M NaClO$_4$ external salt concentration (experiment 1064_13B, *cf.* Tab. 3.1).
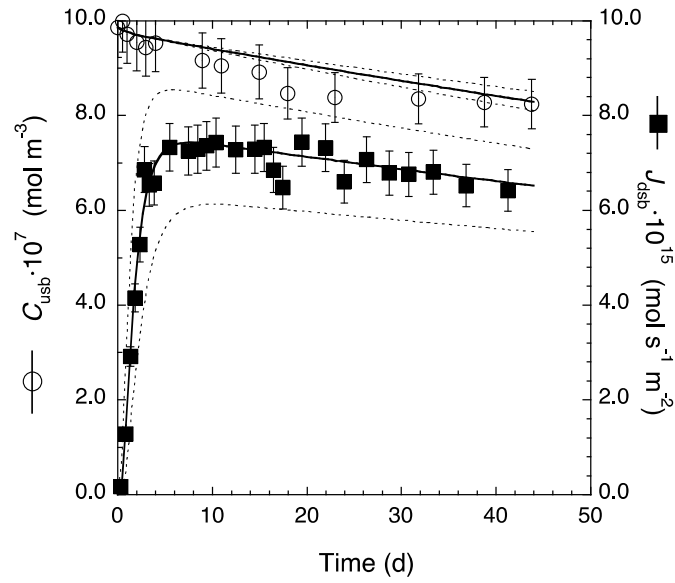
Fig. A3:   Flux at the zero-concentration boundary and reservoir concentration of HTO through-diffusion in Na-*mom* at ρ_{bd} = 1299 kg m^{-3} and 1.0 M NaClO$_4$ external salt concentration (experiment 1064_13C, *cf.* Tab. 3.1).
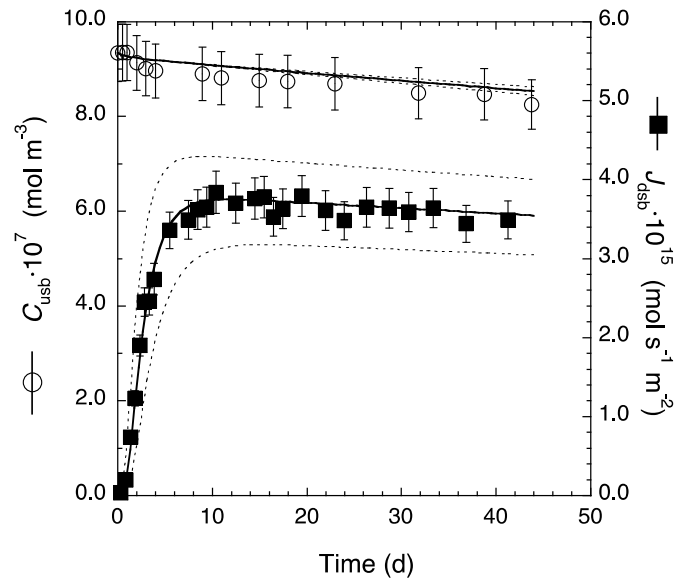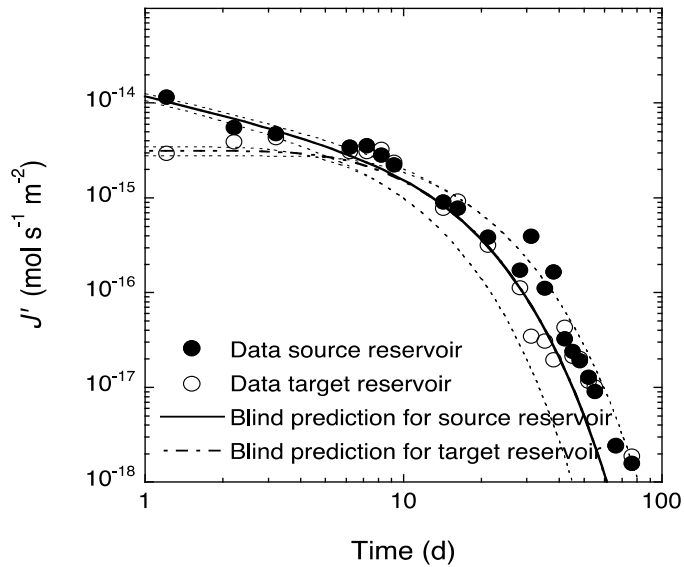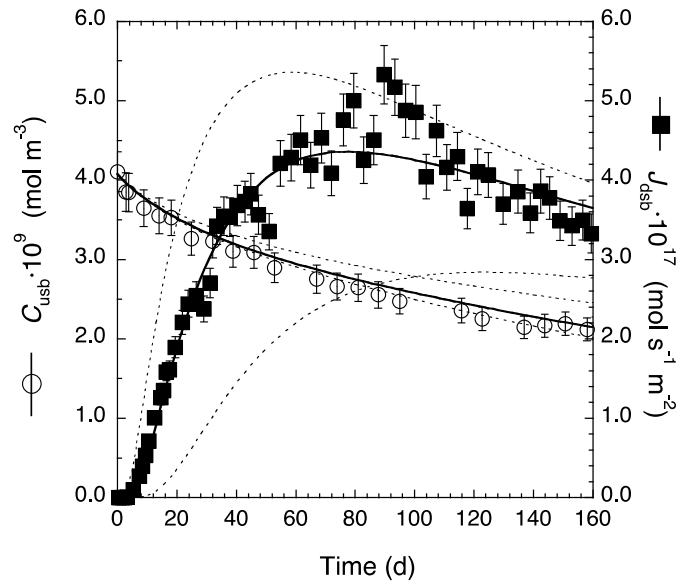

Fig. A4:   Flux at the zero-concentration boundary and reservoir concentration of HTO through-diffusion in Na-*mom* at ρ_{bd} = 1608 kg m^{-3} and 0.01 M NaClO$_4$ external salt concentration (experiment 1064_16A, *cf.* Tab. 3.1).
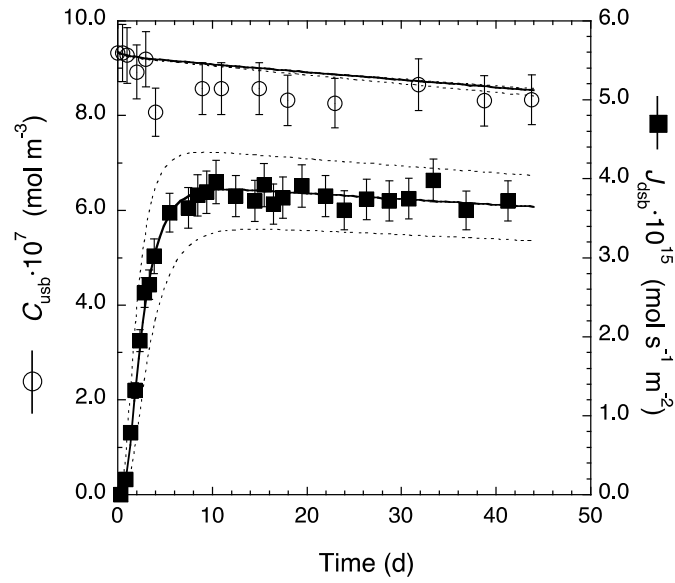
Fig. A5:   Flux at the zero-concentration boundary and reservoir concentration of HTO through-diffusion in Na-*mom* at ρ_{bd} = 1602 kg m^{-3} and 0.1 M NaClO$_4$ external salt concentration (experiment 1064_16B, *cf.* Tab. 3.1).
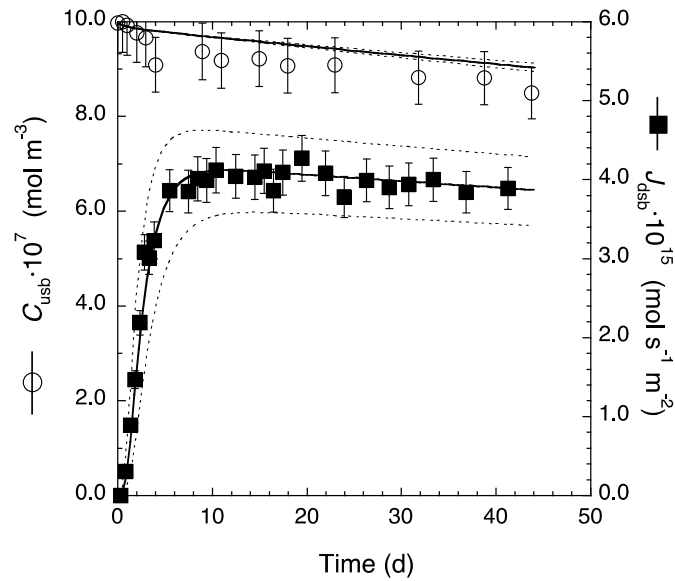
Fig. A6:   Flux at the zero-concentration boundary and reservoir concentration of HTO through-diffusion in Na-*mom* at ρ_{bd} = 1605 kg m^{-3} and 1.0 M NaClO$_4$ external salt concentration (experiment 1064_16C, *cf.* Tab. 3.1).
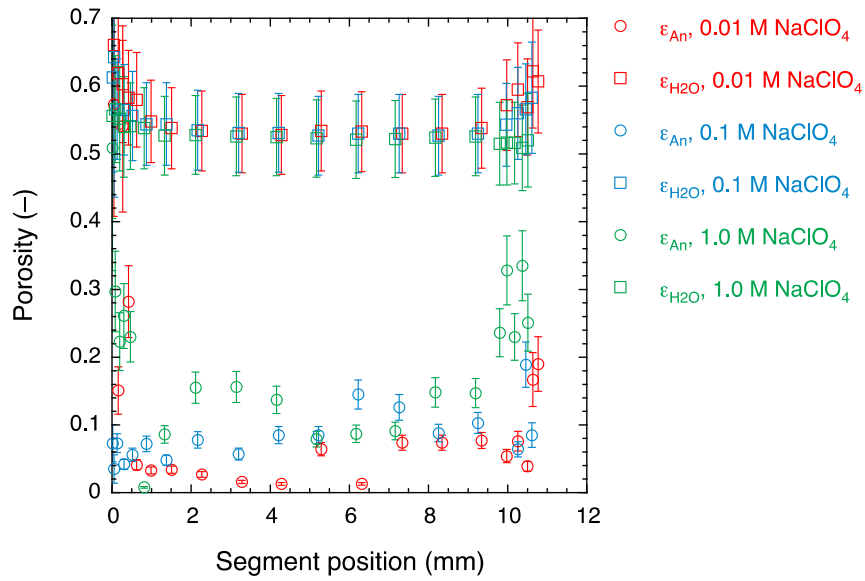
Fig. A7:   Profiles of anion-accessible porosity (ε_{An}, procedure from Glaus et al. 2011) and total water porosity (ε_{H2O}, from loss of water) from clay plugs (ρ_{bd} 1300 kg m^{-3}) of experiment 1064_13A, B and C sectioned after through-diffusion (average values: *cf.* Tab. 5.1).
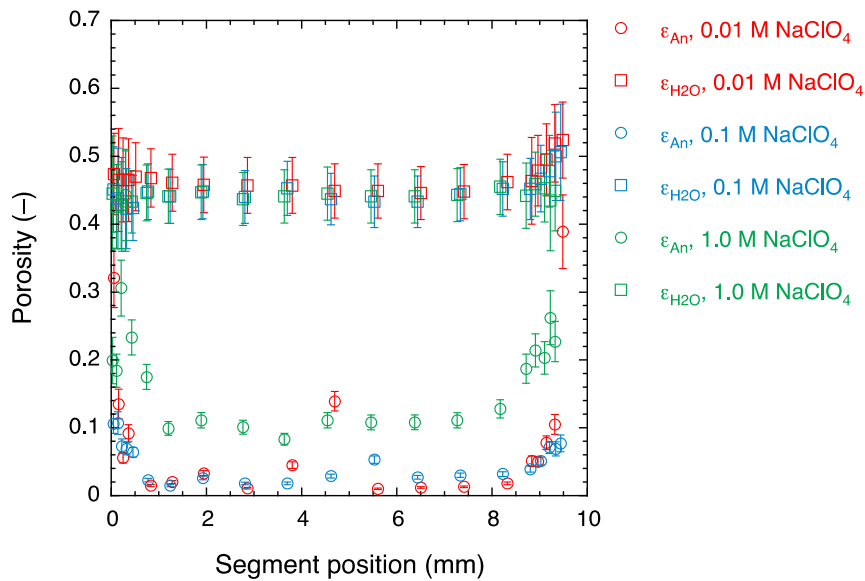
Fig. A8:   Profiles of anion-accessible porosity (ε_{An}, procedure from Glaus et al. 2011) and total water porosity (ε_{H2O}, from loss of water) from clay plugs (ρ_{bd} ~ 1600 kg m^{-3}) of experiment 1064_16A, B and C sectioned after through-diffusion (average values: *cf.* Tab. 5.1).
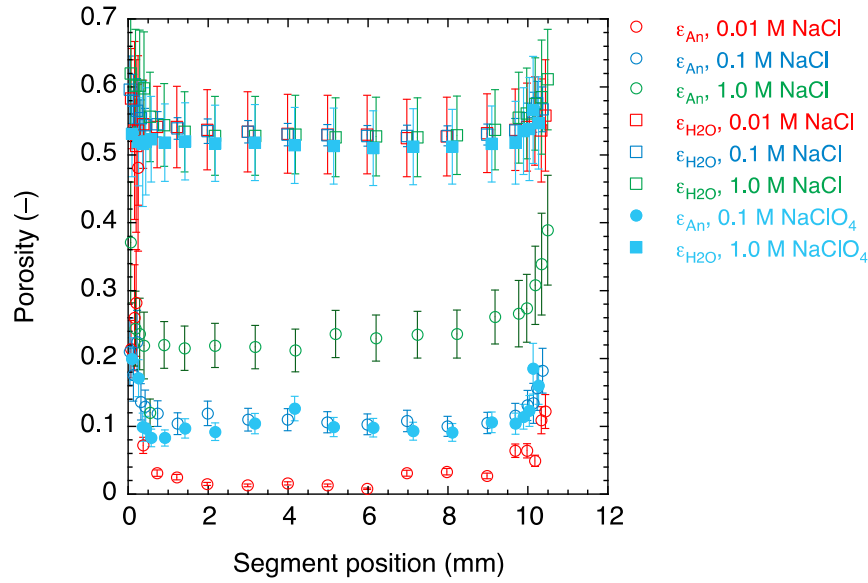
Fig. A9:   Profiles of anion-accessible porosity (ε_{An}, procedure from Glaus et al. 2011) and total water porosity (ε_{H2O}, from loss of water) from clay plugs (ρ_{bd} 1300 kg m^{-3}) measured after saturation with the electrolytes indicated for $\sim$ 30 d (average values: *cf.* Tab. 5.2).

Fig. A10:   Profiles of anion-accessible porosity (ε_{An}, procedure from Glaus et al. 2011) and total water porosity (ε_{H2O}, from loss of water) from clay plugs ($\rho_{bd} \sim$ 1600 kg m^{-3}) measured after saturation with the electrolytes indicated for $\sim$ 30 d (average values: *cf.* Tab. 5.2).
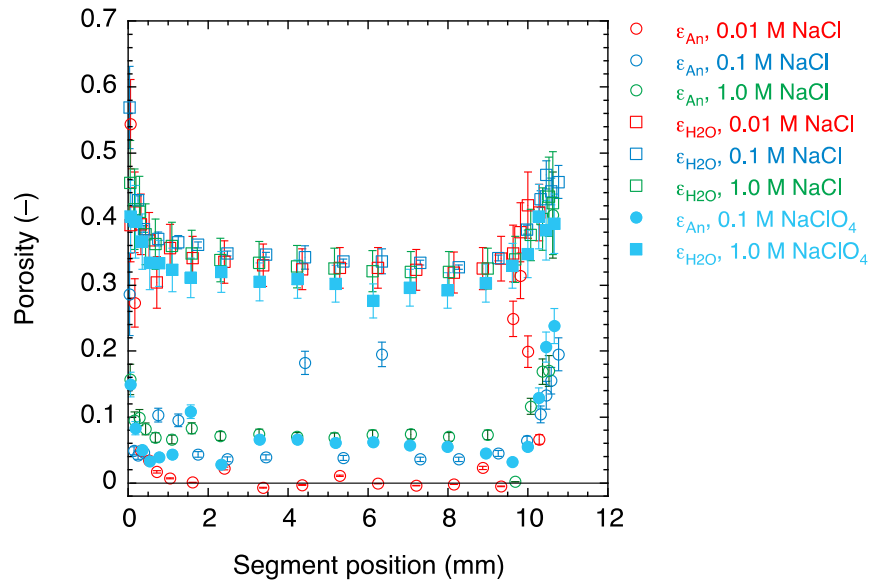
Fig. A11:   Profiles of anion-accessible porosity (ε_{An}, procedure from Glaus et al. 2011) and total water porosity (ε_{H2O}, from loss of water) from clay plugs ($\rho_{bd} \sim 1900$ kg m^{-3}) measured after saturation with the electrolytes indicated for ~ 30 d (average values: *cf.* Tab. 5.2).
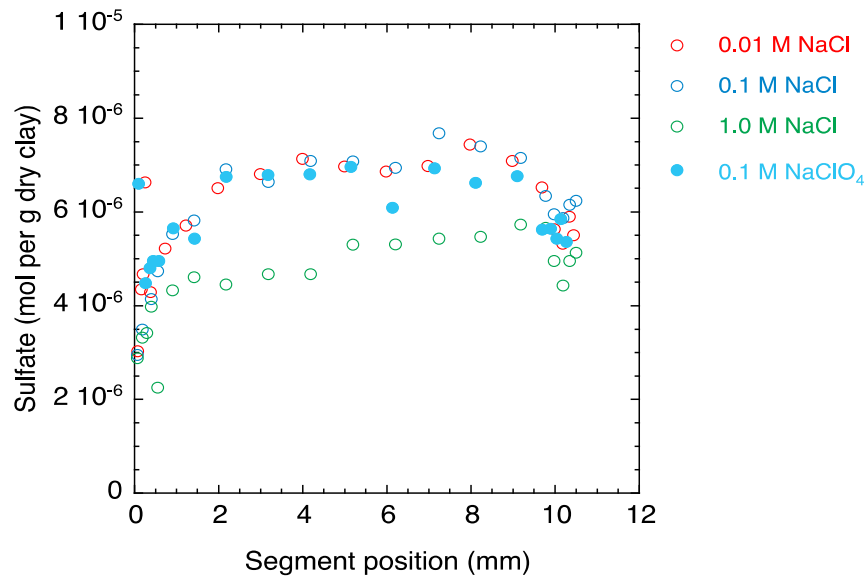
Fig. A12:   Sulfate extracted from clay plugs ($\rho_{bd} \sim 1300$ kg m^{-3}) measured after saturation with the electrolytes indicated for ~ 30 d.
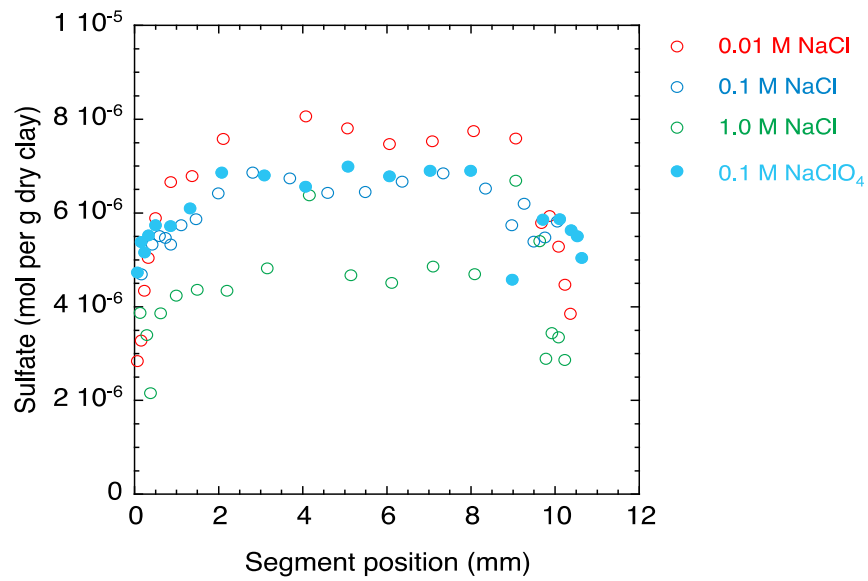
Fig. A13:   Sulfate extracted from clay plugs ($\rho_{bd} \sim 1600$ kg m^{-3}) measured after saturation with the electrolytes indicated for ~ 30 d.
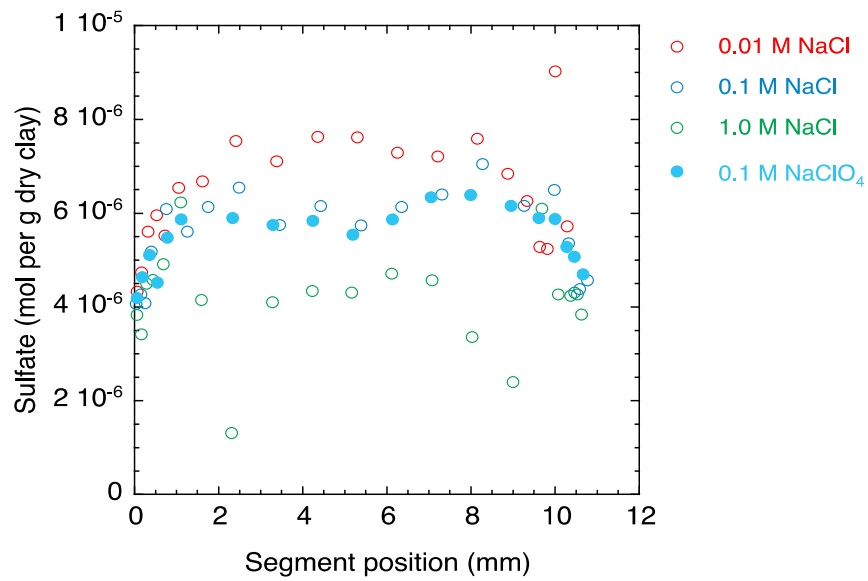
Fig. A14:   Sulfate extracted from clay plugs ($\rho_{bd} \sim 1900$ kg m^{-3}) measured after saturation with the electrolytes indicated for ~ 30 d.

A.2 Combined through-diffusion of ^{22}Na$^+$ and HTO (0.5 and 1.0 M NaClO$_4$)
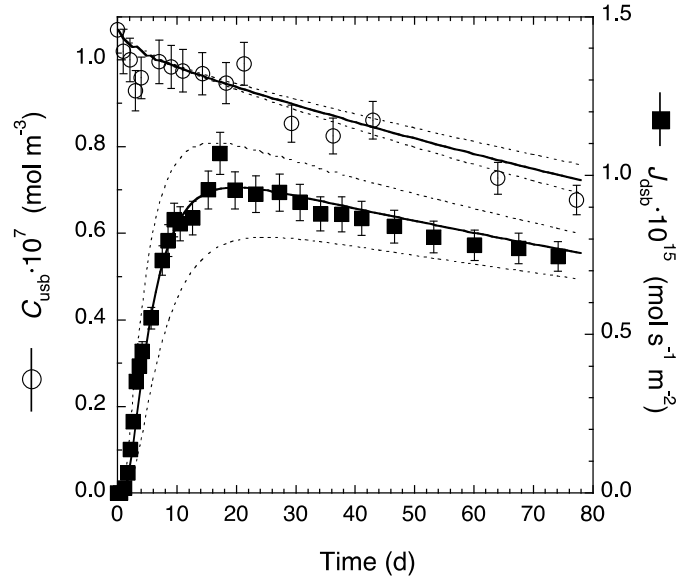
Fig. A15a: Flux at the zero-concentration boundary and reservoir concentration of ^{22}Na$^+$ through-diffusion in Na-*mom* at ρ_{bd} = 1295 kg m^{-3} and 0.5 M NaClO$_4$ external salt concentration (experiment 1055_1A, *cf.* Tab. 3.2).
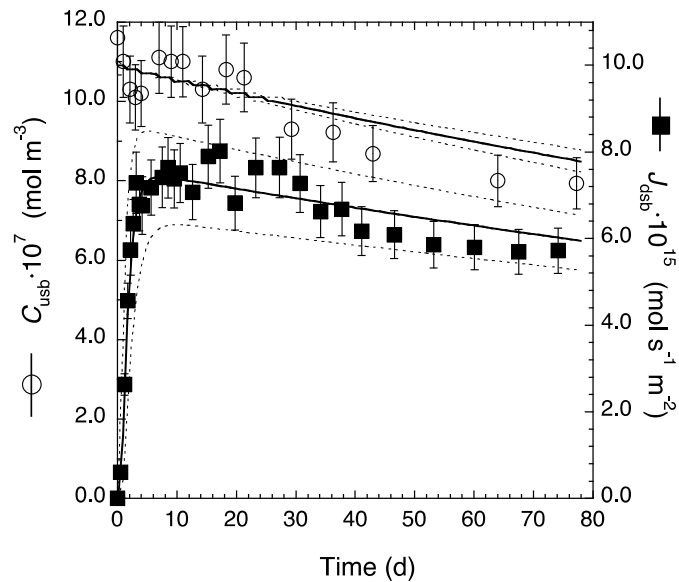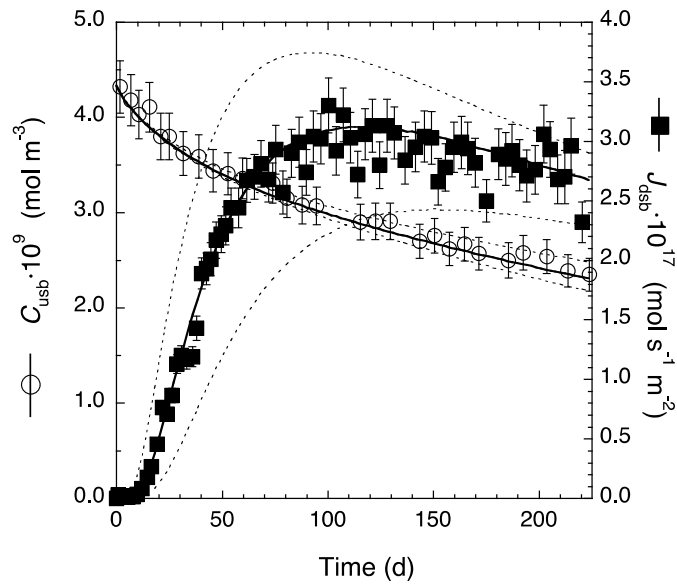

Fig. A15b: Flux at the zero-concentration boundary and reservoir concentration of HTO through-diffusion in Na-*mom* at ρ_{bd} = 1295 kg m^{-3} and 0.5 M NaClO$_4$ external salt concentration (experiment 1055_1A, *cf.* Tab. 3.2).
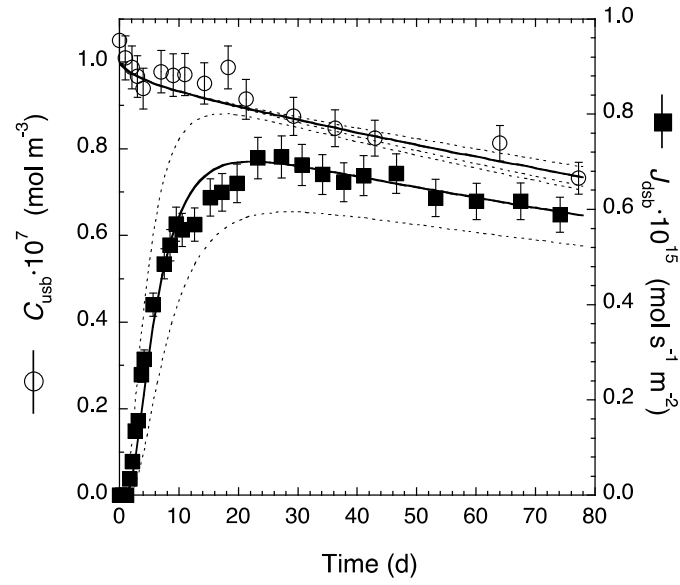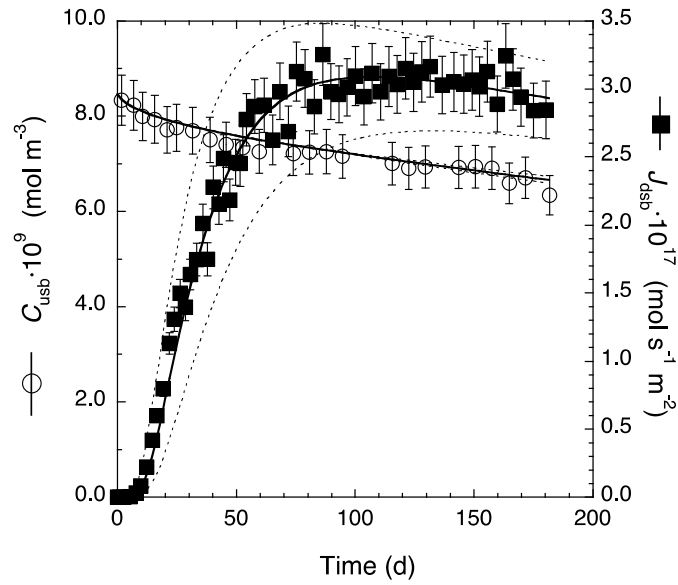
Fig. A16a: Flux at the zero-concentration boundary and reservoir concentration of ^{22}Na$^+$ through-diffusion in Na-*mom* at ρ_{bd} = 1305 kg m^{-3} and 0.5 M NaClO$_4$ external salt concentration (experiment 1055_1B, *cf.* Tab. 3.2).
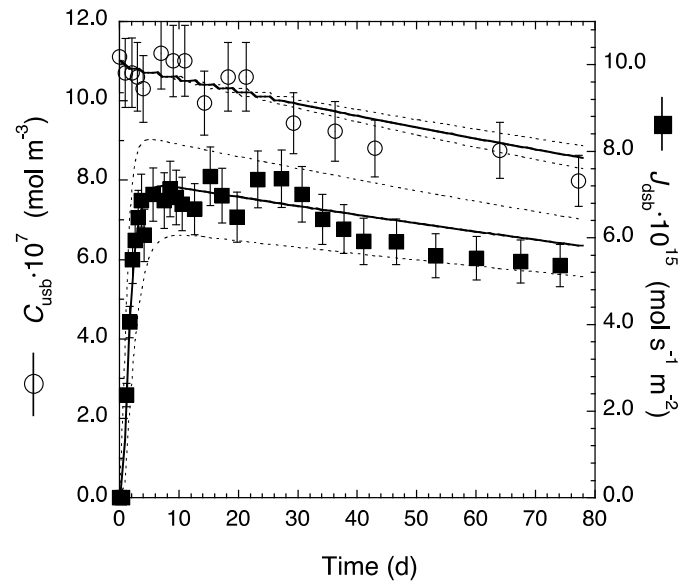
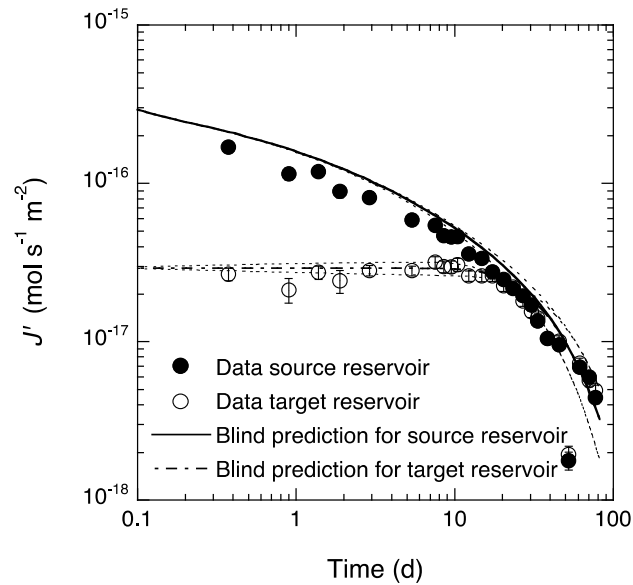Fig. A16b: Flux at the zero-concentration boundary and reservoir concentration of HTO through-diffusion in Na-*mom* at ρ_{bd} = 1305 kg m^{-3} and 0.5 M NaClO$_4$ external salt concentration (experiment 1055_1B, *cf.* Tab. 3.2).
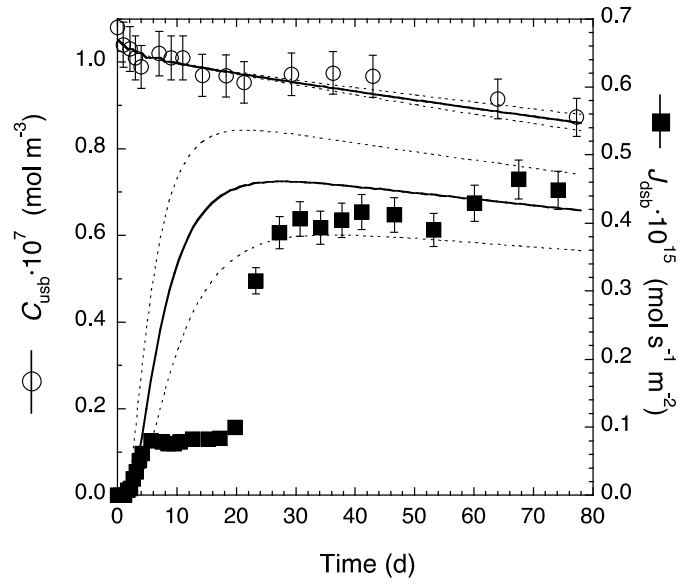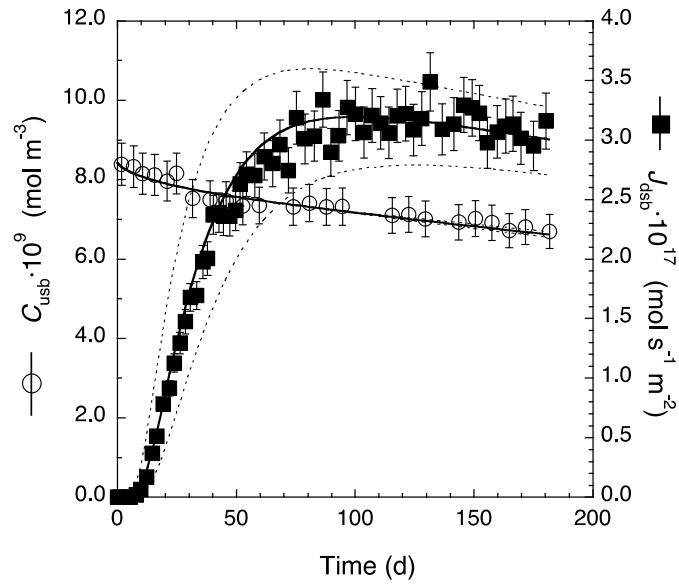
Fig. A17a: Flux at the zero-concentration boundary and reservoir concentration of ^{22}Na$^+$ through-diffusion in Na-*mom* at ρ_{bd} = 1293 kg m^{-3} and 1.0 M NaClO$_4$ external salt concentration (experiment 1055_2A, *cf.* Tab. 3.2).
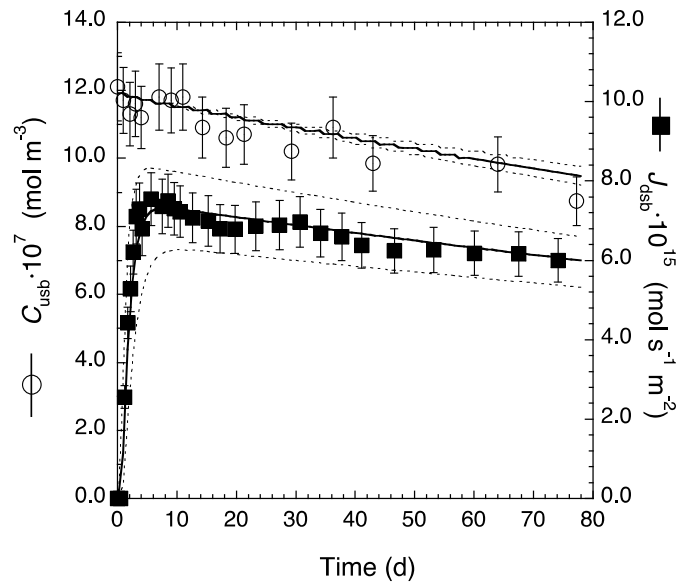
Fig. A17b: Flux at the zero-concentration boundary and reservoir concentration of HTO through-diffusion in Na-*mom* at ρ_{bd} = 1293 kg m^{-3} and 1.0 M NaClO$_4$ external salt concentration (experiment 1055_2A, *cf.* Tab. 3.2).
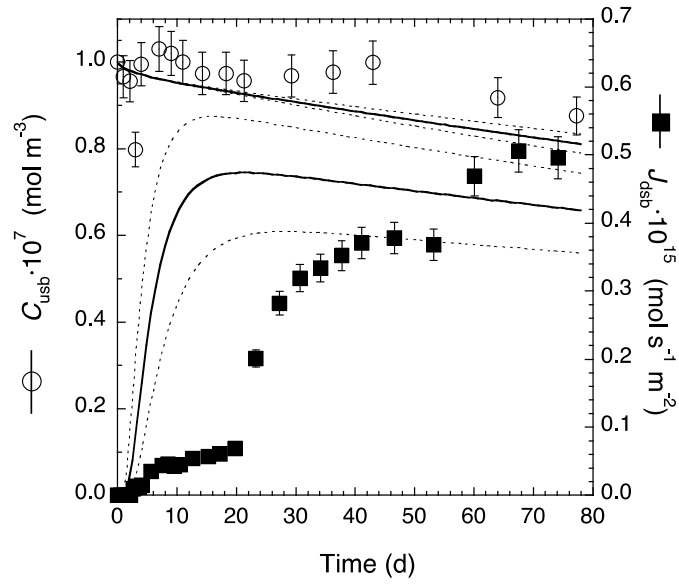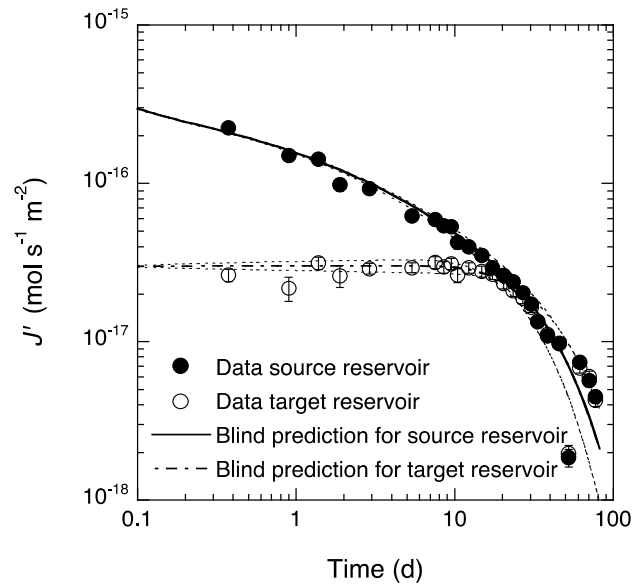
Fig. A18a: Flux at the zero-concentration boundary and reservoir concentration of $^{22}Na^+$ through-diffusion in Na-*mom* at $\rho_{bd} = 1287$ kg m^{-3} and 1.0 M NaClO$_4$ external salt concentration (experiment 1055_2B, *cf.* Tab. 3.2).
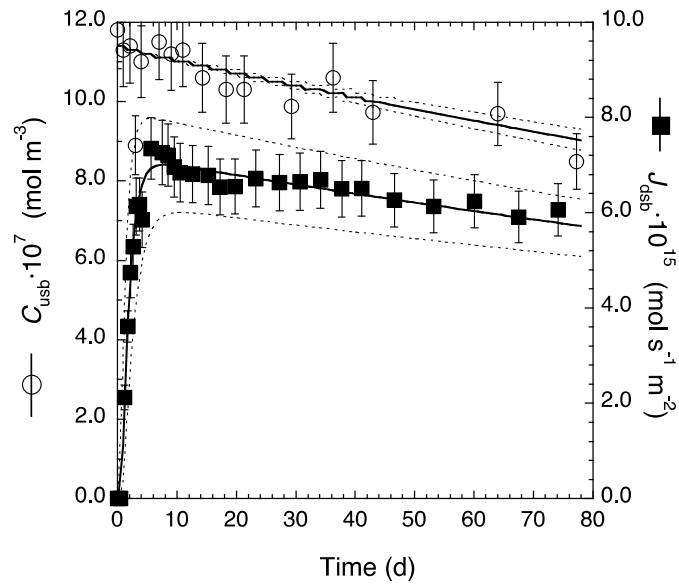
Fig. A18b: Flux at the zero-concentration boundary and reservoir concentration of HTO through-diffusion in Na-*mom* at $\rho_{bd} = 1287$ kg m^{-3} and 1.0 M NaClO$_4$ external salt concentration (experiment 1055_2B, *cf.* Tab. 3.2).
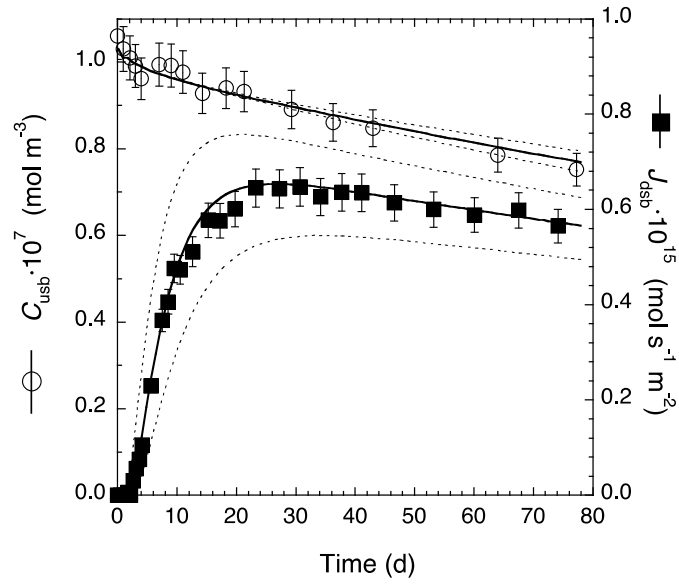
Fig. A19a: Flux at the zero-concentration boundary and reservoir concentration of $^{22}Na^+$ through-diffusion in Na-*mom* at $\rho_{bd} = 1558$ kg m^{-3} and 0.5 M NaClO$_4$ external salt concentration (experiment 1055_3A, *cf.* Tab. 3.2).
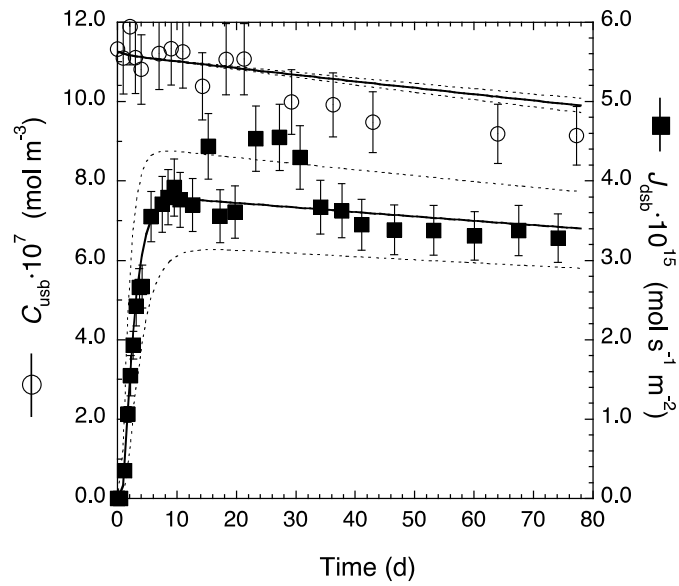
Fig. A19b: Flux at the zero-concentration boundary and reservoir concentration of HTO through-diffusion in Na-*mom* at $\rho_{bd} = 1558$ kg m^{-3} and 0.5 M NaClO$_4$ external salt concentration (experiment 1055_3A, *cf.* Tab. 3.2).
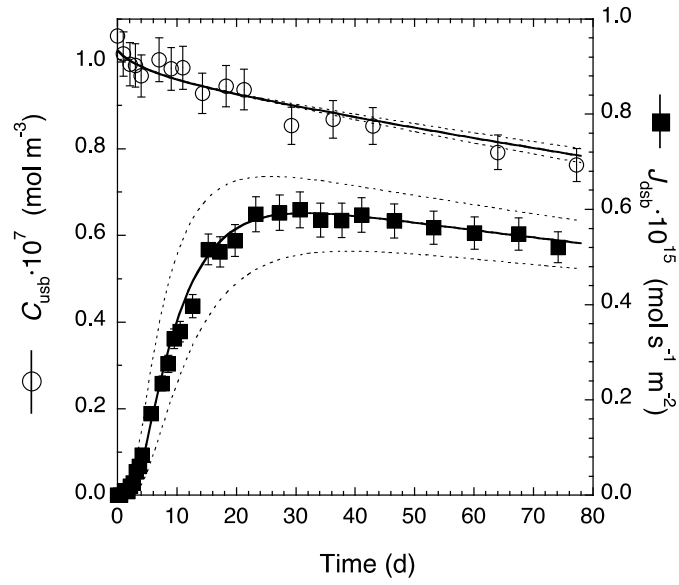
Fig. A20a: Flux at the zero-concentration boundary and reservoir concentration of $^{22}Na^+$ through-diffusion in Na-*mom* at ρ_{bd} = 1560 kg m^{-3} and 0.5 M NaClO$_4$ external salt concentration (experiment 1055_3B, *cf.* Tab. 3.2).
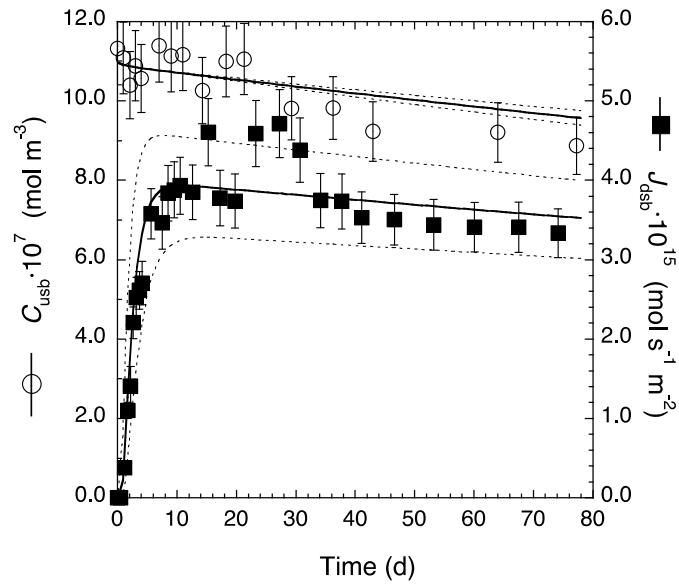
Fig. A20b: Flux at the zero-concentration boundary and reservoir concentration of HTO through-diffusion in Na-*mom* at ρ_{bd} = 1560 kg m^{-3} and 0.5 M NaClO$_4$ external salt concentration (experiment 1055_3B, *cf.* Tab. 3.2).
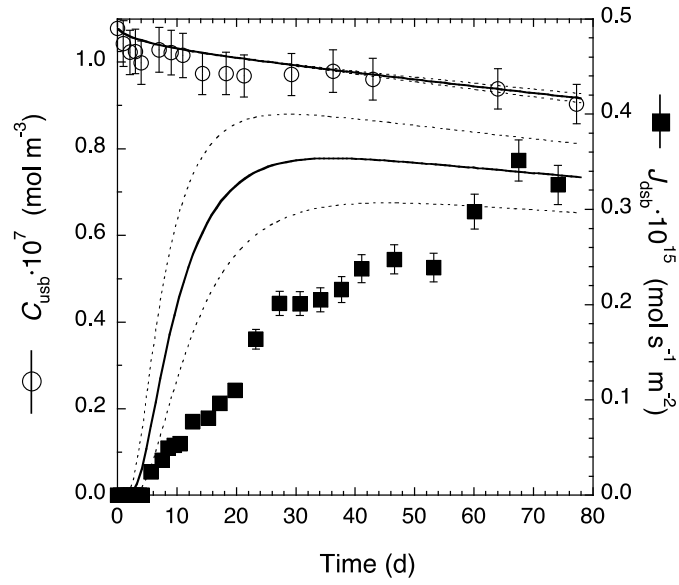
Fig. A21a: Flux at the zero-concentration boundary and reservoir concentration of $^{22}Na^+$ through-diffusion in Na-*mom* at ρ_{bd} = 1565 kg m^{-3} and 1.0 M NaClO$_4$ external salt concentration (experiment 1055_4A, *cf.* Tab. 3.2).
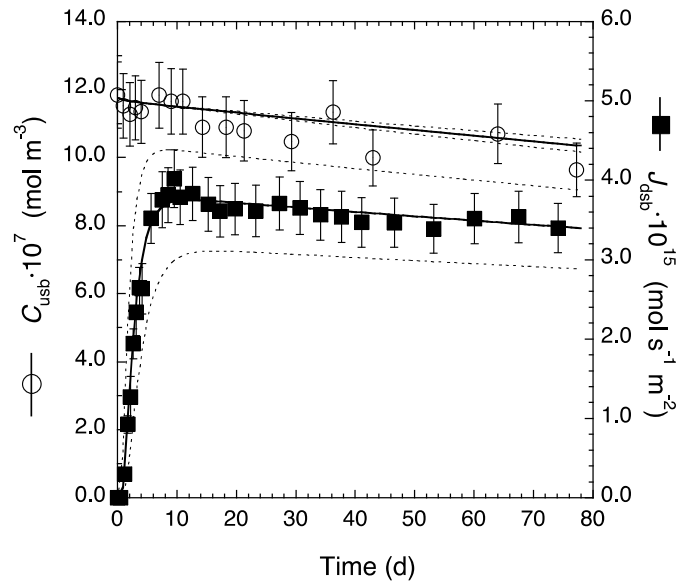
Fig. A21b: Flux at the zero-concentration boundary and reservoir concentration of HTO through-diffusion in Na-*mom* at ρ_{bd} = 1565 kg m^{-3} and 1.0 M NaClO$_4$ external salt concentration (experiment 1055_4A, *cf.* Tab. 3.2).
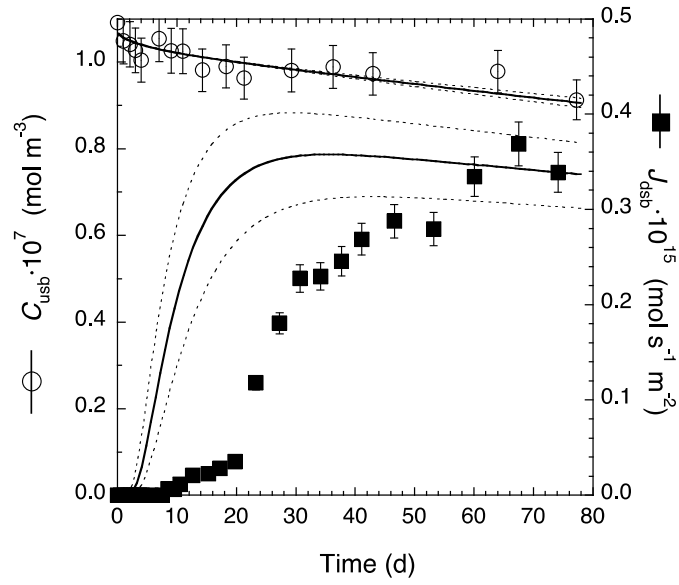
Fig. A22a: Flux at the zero-concentration boundary and reservoir concentration of $^{22}Na^+$ through-diffusion in Na-*mom* at ρ_{bd} = 1562 kg m^{-3} and 1.0 M NaClO$_4$ external salt concentration (experiment 1055_4B, *cf.* Tab. 3.2).
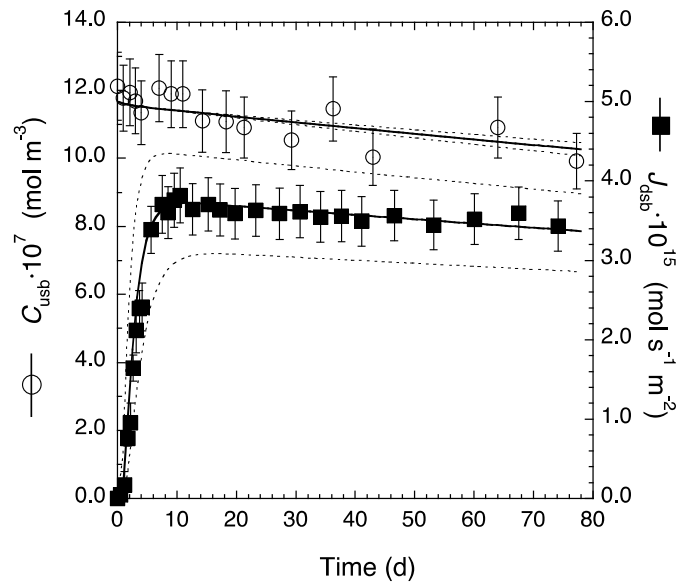
Fig. A22b: Flux at the zero-concentration boundary and reservoir concentration of HTO through-diffusion in Na-*mom* at ρ_{bd} = 1562 kg m^{-3} and 1.0 M NaClO$_4$ external salt concentration (experiment 1055_4B, *cf.* Tab. 3.2).

A.3   Combined out-diffusion of ^{22}Na$^+$ and HTO (0.5 and 1.0 M NaClO$_4$)
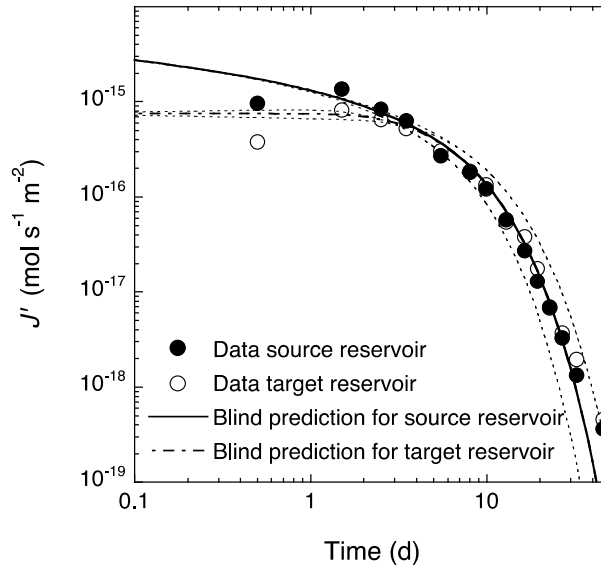
Fig. A23a: Out-diffusion of ^{22}Na$^+$ from Na-*mom* at ρ_{bd} = 1295 kg m^{-3} and 0.5 M NaClO$_4$ external salt concentration (experiment 1055_1A, *cf.* Tab. 3.3).

The fit curves were obtained using the parameters from through-diffusion.
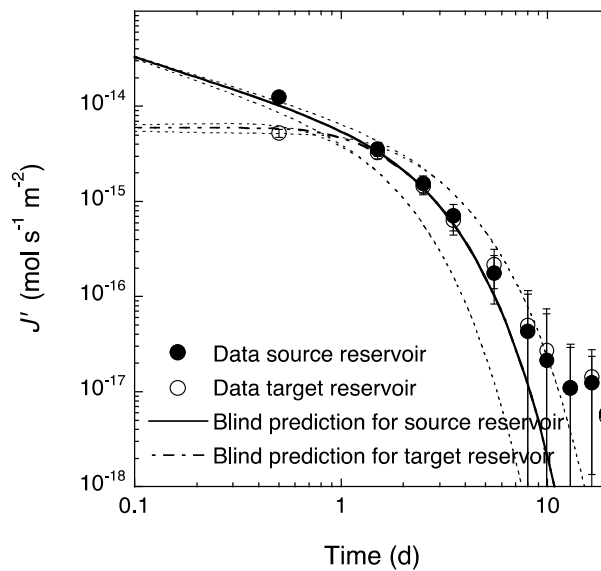
Fig. A23b: Out-diffusion of HTO from Na-*mom* at ρ_{bd} = 1295 kg m^{-3} and 0.5 M NaClO$_4$ external salt concentration (experiment 1055_1A, *cf.* Tab. 3.3).

The fit curves were obtained using the parameters from through-diffusion.
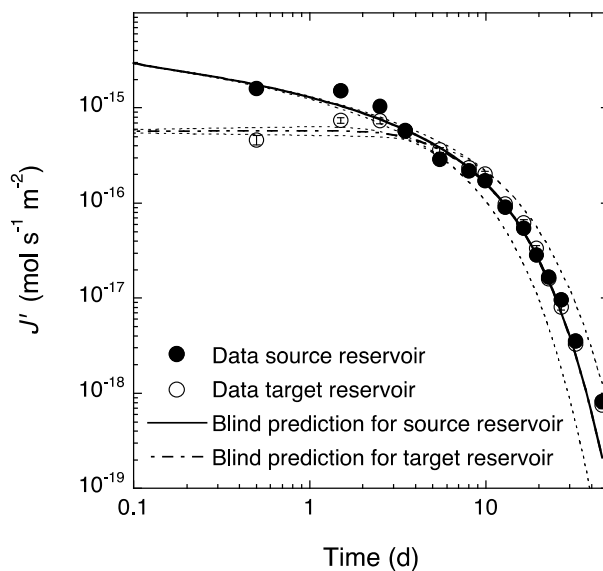
Fig. A24a: Out-diffusion of $^{22}Na^+$ from Na-*mom* at ρ_{bd} = 1305 kg m^{-3} and 0.5 M NaClO$_4$ external salt concentration (experiment 1055_1B, *cf.* Tab. 3.3).

The α value was slightly adapted to obtain a better fit.
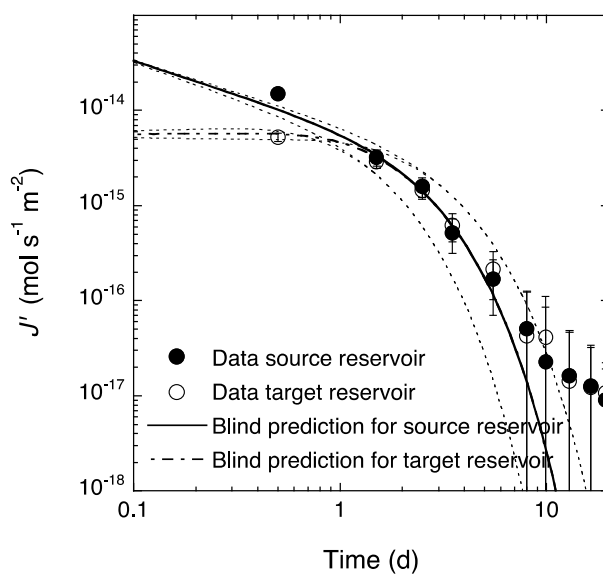
Fig. A24b: Out-diffusion of HTO from Na-*mom* at ρ_{bd} = 1305 kg m^{-3} and 0.5 M NaClO$_4$ external salt concentration (experiment 1055_1B, *cf.* Tab. 3.3).

The fit curves were obtained using the parameters from through-diffusion.
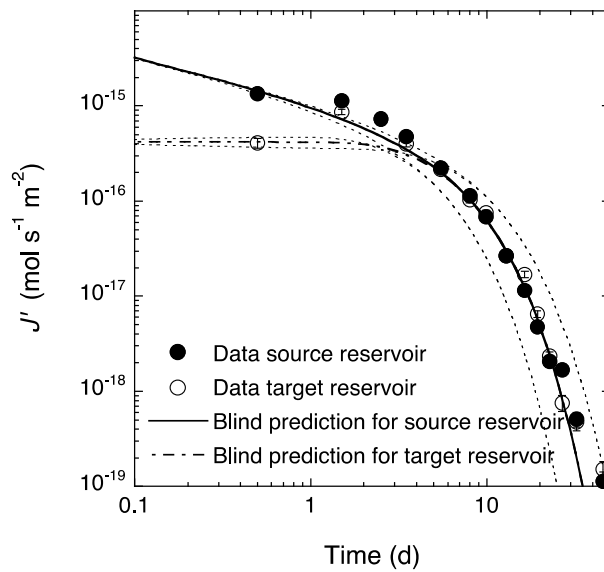
Fig. A25a: Out-diffusion of $^{22}Na^+$ from Na-*mom* at ρ_{bd} = 1293 kg m^{-3} and 1.0 M NaClO$_4$ external salt concentration (experiment 1055_2A, *cf.* Tab. 3.3).

The α value was slightly adapted to obtain a better fit.
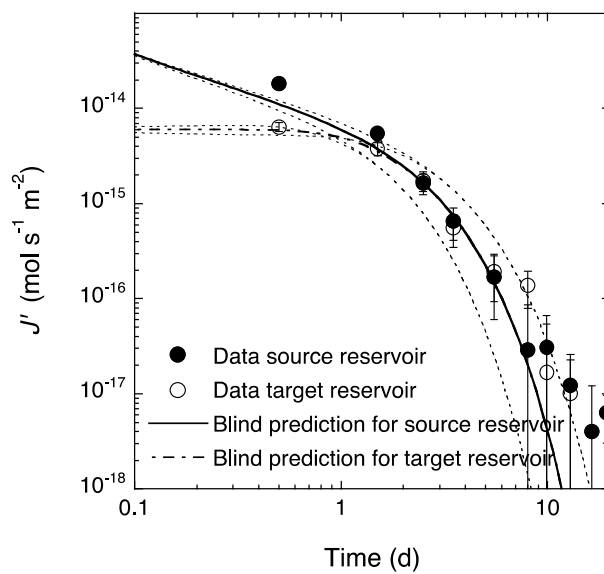
Fig. A25b: Out-diffusion of HTO from Na-*mom* at ρ_{bd} = 1293 kg m^{-3} and 1.0 M NaClO$_4$ external salt concentration (experiment 1055_2A, *cf.* Tab. 3.3).

The fit curves were obtained using the parameters from through-diffusion.
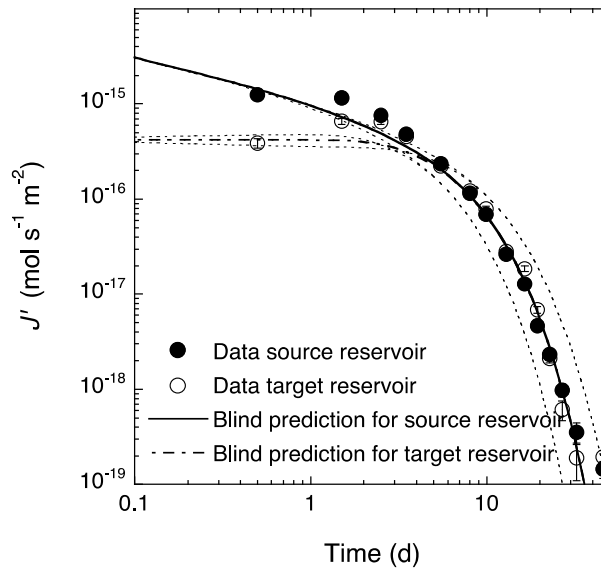
Fig. A26a: Out-diffusion of $^{22}Na^+$ from Na-*mom* at ρ_{bd} = 1287 kg m^{-3} and 1.0 M NaClO$_4$ external salt concentration (experiment 1055_2B, *cf.* Tab. 3.3).

The α value was slightly adapted to obtain a better fit.
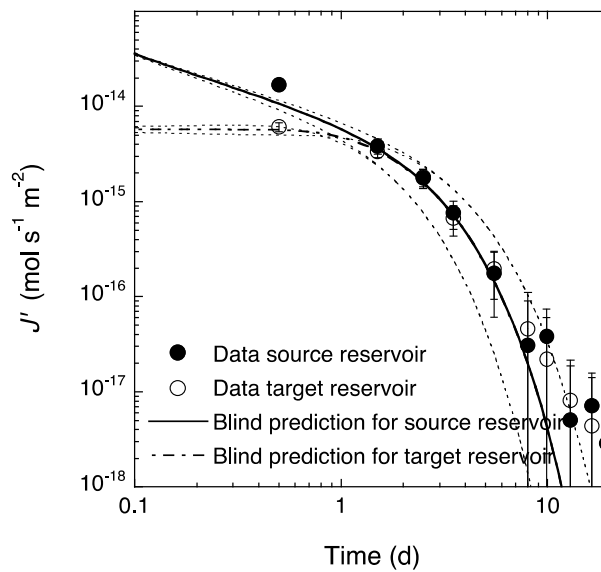
Fig. A26b: Out-diffusion of HTO from Na-*mom* at ρ_{bd} = 1287 kg m^{-3} and 1.0 M NaClO$_4$ external salt concentration (experiment 1055_2B, *cf.* Tab. 3.3).

The fit curves were obtained using the parameters from through-diffusion.
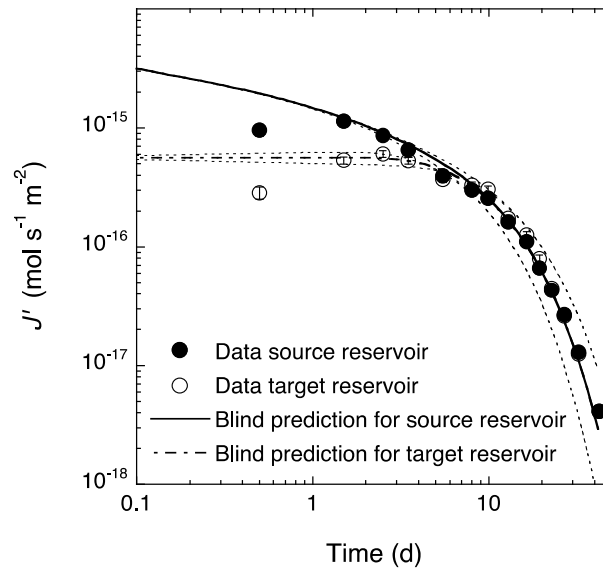
Fig. A27a: Out-diffusion of ^{22}Na$^+$ from Na-*mom* at ρ_{bd} = 1558 kg m^{-3} and 0.5 M NaClO$_4$ external salt concentration (experiment 1055_3A, *cf.* Tab. 3.3).

The α value was slightly adapted to obtain a better fit.
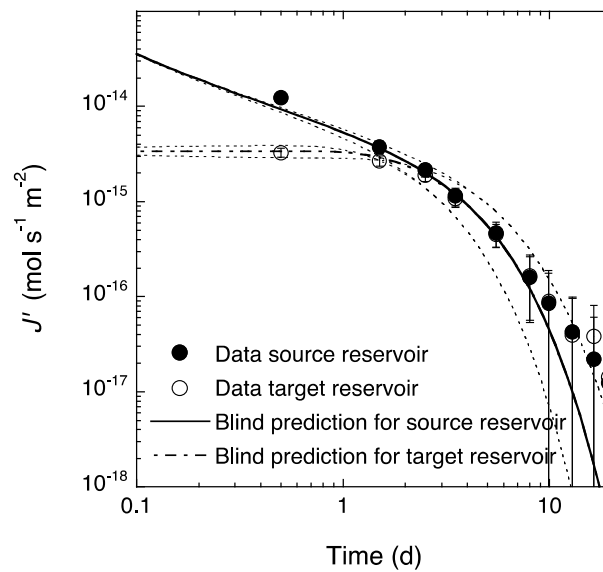
Fig. A27b: Out-diffusion of HTO from Na-*mom* at ρ_{bd} = 1558 kg m^{-3} and 0.5 M NaClO$_4$ external salt concentration (experiment 1055_3A, *cf.* Tab. 3.3).

The α value was slightly adapted to obtain a better fit.
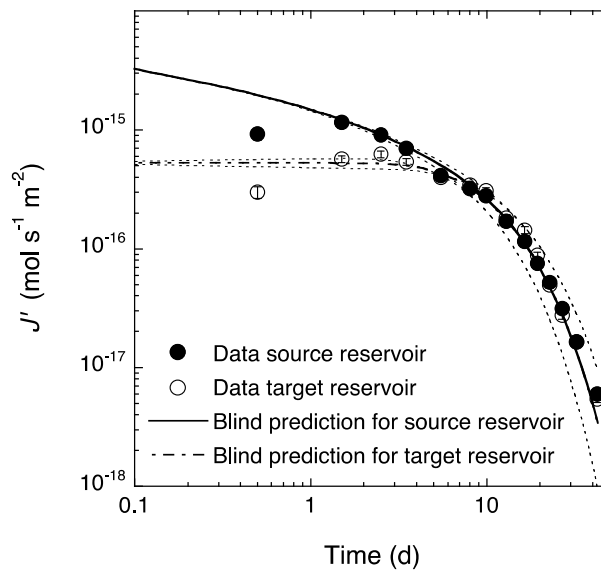
Fig. A28a: Out-diffusion of $^{22}Na^+$ from Na-*mom* at ρ_{bd} = 1560 kg m^{-3} and 0.5 M NaClO$_4$ external salt concentration (experiment 1055_3B, *cf.* Tab. 3.3).

The α value was slightly adapted to obtain a better fit.
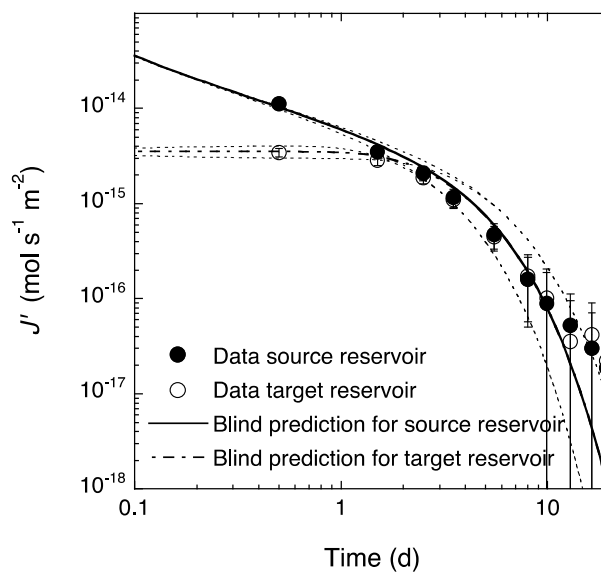
Fig. A28b: Out-diffusion of HTO from Na-*mom* at ρ_{bd} = 1560 kg m^{-3} and 0.5 M NaClO$_4$ external salt concentration (experiment 1055_3B, *cf.* Tab. 3.3).

The α value was slightly adapted to obtain a better fit.
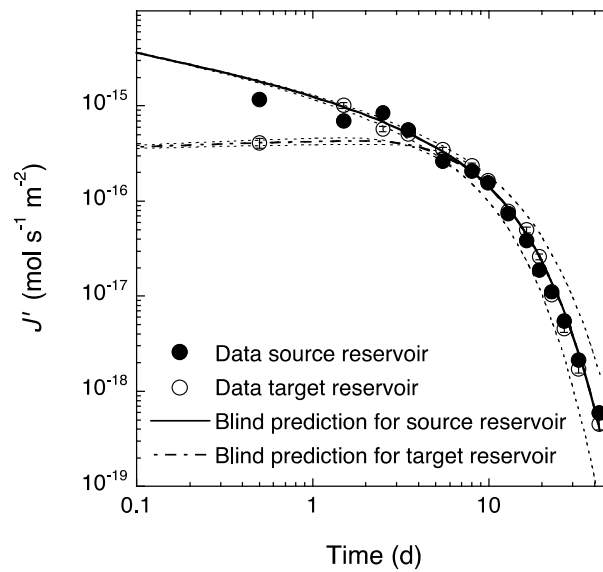
Fig. A29a: Out-diffusion of $^{22}Na^+$ from Na-*mom* at ρ_{bd} = 1565 kg m^{-3} and 1.0 M NaClO$_4$ external salt concentration (experiment 1055_4A, *cf.* Tab. 3.3).

The D_e value was slightly adapted to obtain a better fit.
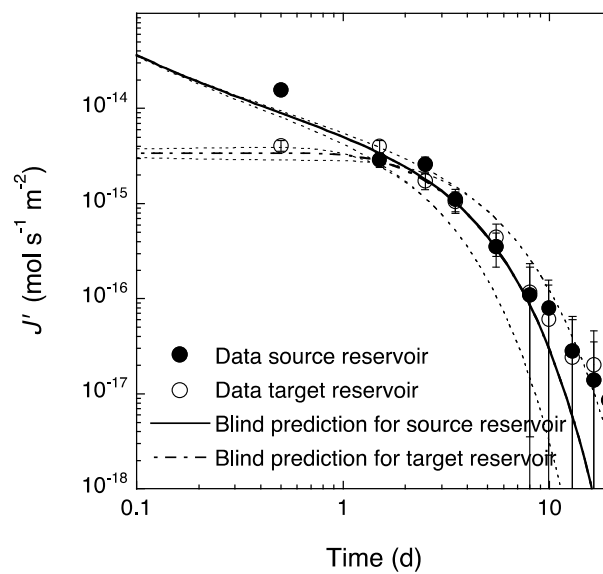
Fig. A29b: Out-diffusion of HTO from Na-*mom* at ρ_{bd} = 1565 kg m^{-3} and 1.0 M NaClO$_4$ external salt concentration (experiment 1055_4A, *cf.* Tab. 3.3).

The fit curves were obtained using the parameters from through-diffusion.
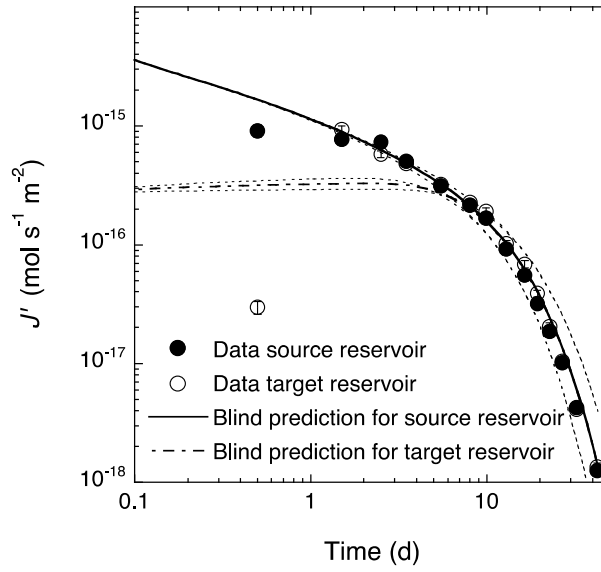
Fig. A30a: Out-diffusion of ^{22}Na$^+$ from Na-*mom* at ρ_{bd} = 1562 kg m^{-3} and 1.0 M NaClO$_4$ external salt concentration (experiment 1055_4B, *cf.* Tab. 3.3).

The fit curves were obtained using the parameters from through-diffusion.
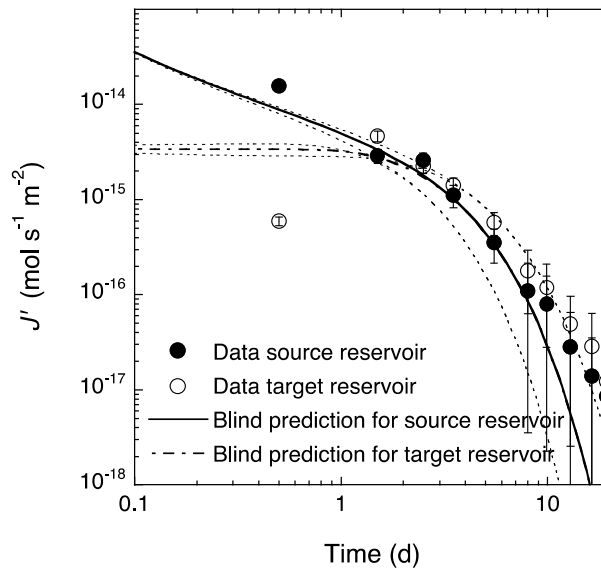
Fig. A30b: Out-diffusion of HTO from Na-*mom* at ρ_{bd} = 1562 kg m^{-3} and 1.0 M NaClO$_4$ external salt concentration (experiment 1055_4B, *cf.* Tab. 3.3).

The fit curves were obtained using the parameters from through-diffusion.

A.4   Combined through- and out-diffusion of $^{22}Na^+$ and HTO (0.1 M NaClO$_4$)

Fig. A31a: Flux at the zero-concentration boundary and reservoir concentration of HTO through-diffusion in Na-*mom* at ρ_{bd} = 1297 kg m^{-3} and 0.1 M NaClO$_4$ external salt concentration (experiment 1058 1A, *cf.* Tab. 3.4).

Fig. A31b: Flux at the zero-concentration boundary and reservoir concentration of $^{22}Na^+$ through-diffusion in Na-*mom* at ρ_{bd} = 1297 kg m^{-3} and 0.1 M NaClO$_4$ external salt concentration (experiment 1058 1A, *cf.* Tab. 3.4).

Fig. A32a: Flux at the zero-concentration boundary and reservoir concentration of $^{22}Na^+$ through-diffusion in Na-*mom* at ρ_{bd} = 1597 kg m^{-3} and 0.1 M NaClO$_4$ external salt concentration (experiment 1047#3_2, *cf.* Tab. 3.4).

Fig. A32b: Out-diffusion of $^{22}Na^+$ from Na-*mom* at ρ_{bd} = 1597 kg m^{-3} and 0.1 M NaClO$_4$ external salt concentration (experiment 1047#3_2, *cf.* Tab. 3.4).

The fit curves were obtained using the parameters from through-diffusion.

A.5   Through- and out-diffusion of $^{85}Sr^{2+}$ (0.5 and 1.0 M NaClO₄)

Fig. A33a: Flux at the zero-concentration boundary and reservoir concentration of $^{85}Sr^{2+}$ through-diffusion in Na-*mom* at ρ_{bd} = 1295 kg m⁻³ and 0.5 M NaClO₄ external salt concentration (experiment 1055_1A, *cf.* Tab. 3.5).
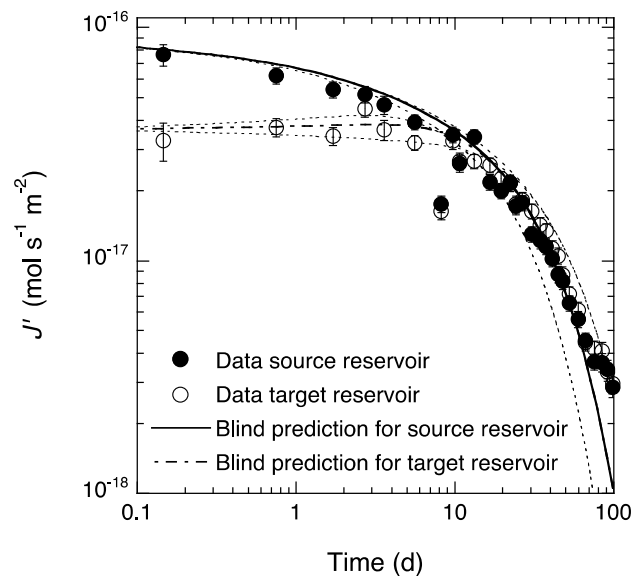
Fig. A33b: Out-diffusion of $^{85}Sr^{2+}$ from Na-*mom* at ρ_{bd} = 1295 kg m⁻³ and 0.5 M NaClO₄ external salt concentration (experiment 1055_1A, *cf.* Tab. 3.5.

The fit curves were obtained using slightly changed parameter values compared to through-diffusion (*cf.* Tab. 3.5).
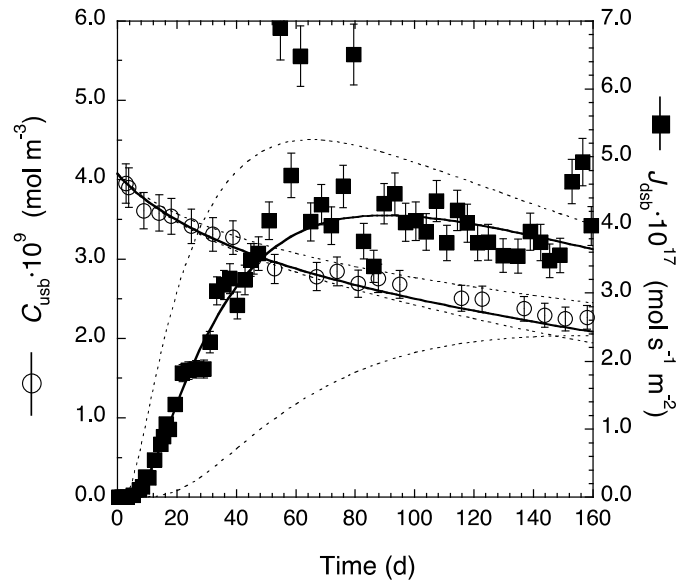
Fig. A34:   Flux at the zero-concentration boundary and reservoir concentration of $^{85}Sr^{2+}$ through-diffusion in Na-*mom* at ρ_{bd} = 1305 kg m^{-3} and 0.5 M NaClO$_4$ external salt concentration (experiment 1055_1B, *cf.* Tab. 3.5).
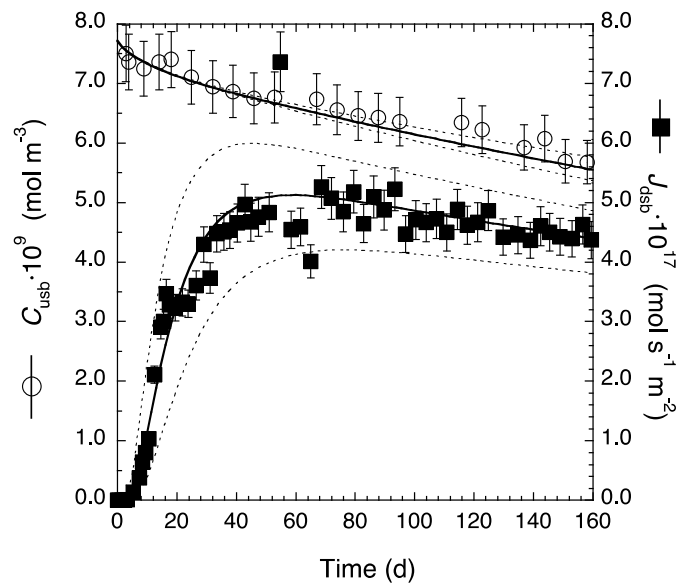
Fig. A35a:　Flux at the zero-concentration boundary and reservoir concentration of $^{85}Sr^{2+}$ through-diffusion in Na-*mom* at ρ_{bd} = 1295 kg m^{-3} and 1.0 M NaClO$_4$ external salt concentration (experiment 1055_2A, *cf.* Tab. 3.5).
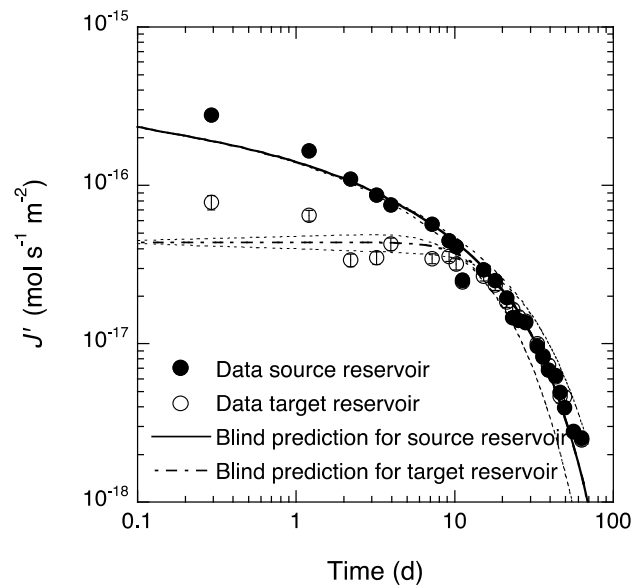
Fig. A35b:　Out-diffusion of $^{85}Sr^{2+}$ from Na-*mom* at ρ_{bd} = 1295 kg m^{-3} and 1.0 M NaClO$_4$ external salt concentration (experiment 1055_2A, *cf.* Tab. 3.5).

The fit curves were obtained using slightly changed parameter values compared to through-diffusion (*cf.* Tab. 3.5).
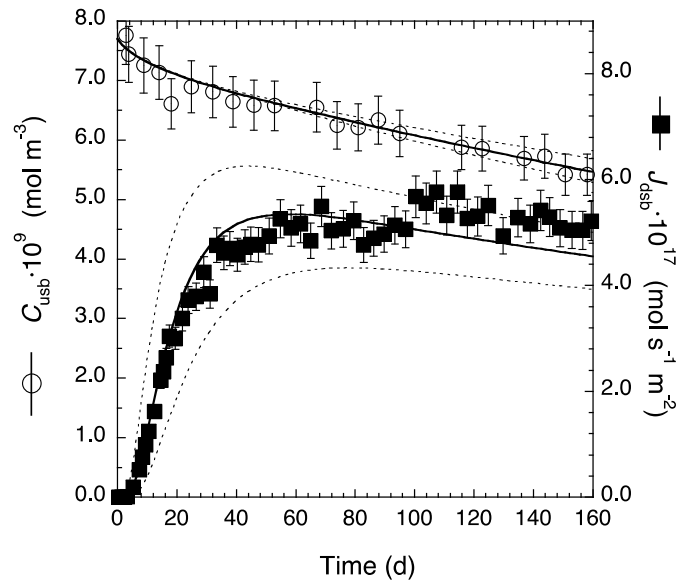
Fig. A36a: Flux at the zero-concentration boundary and reservoir concentration of $^{85}Sr^{2+}$ through-diffusion in Na-*mom* at ρ_{bd} = 1297 kg m^{-3} and 1.0 M NaClO$_4$ external salt concentration (experiment 1055_2B, *cf.* Tab. 3.5).
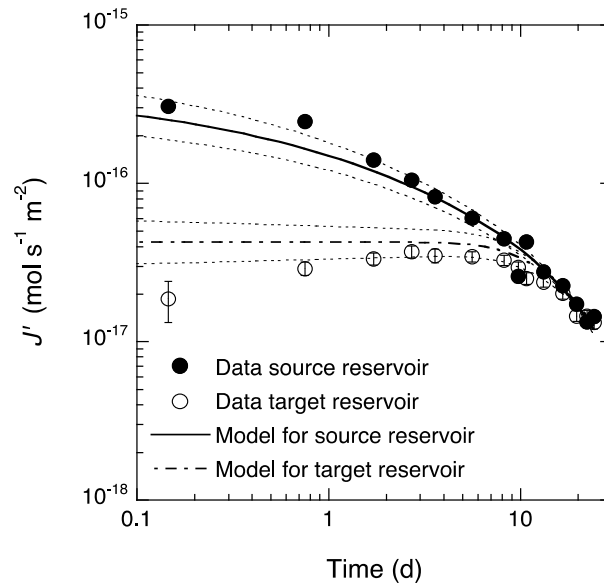
Fig. A36b: Out-diffusion of $^{85}Sr^{2+}$ from Na-*mom* at ρ_{bd} = 1297 kg m^{-3} and 1.0 M NaClO$_4$ external salt concentration (experiment 1055_2B, *cf.* Tab. 3.5).

The fit curves were obtained from simultaneously fitting the through- and the out-diffusion data (*cf.* Tab. 3.5).
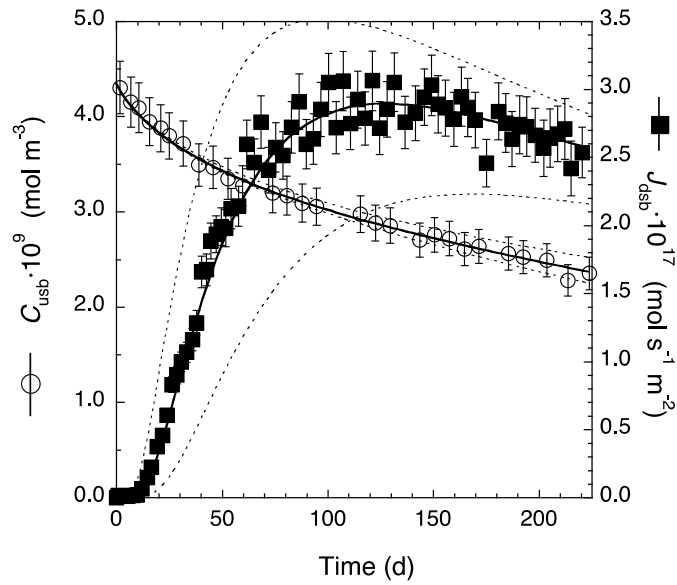
Fig. A37: Flux at the zero-concentration boundary and reservoir concentration of $^{85}Sr^{2+}$ through-diffusion in Na-*mom* at ρ_{bd} = 1583 kg m^{-3} and 0.5 M NaClO$_4$ external salt concentration (experiment 1055_3A, *cf.* Tab. 3.5).

Fig. A38: Flux at the zero-concentration boundary and reservoir concentration of $^{85}Sr^{2+}$ through-diffusion in Na-*mom* at ρ_{bd} = 1587 kg m^{-3} and 0.5 M NaClO$_4$ external salt concentration (experiment 1055_3B, *cf.* Tab. 3.5).

Fig. A39a: Flux at the zero-concentration boundary and reservoir concentration of $^{85}Sr^{2+}$ through-diffusion in Na-*mom* at ρ_{bd} = 1587 kg m^{-3} and 1.0 M NaClO$_4$ external salt concentration (experiment 1055_4A, *cf.* Tab. 3.5).

Fig. A39b: Out-diffusion of $^{85}Sr^{2+}$ from Na-*mom* at ρ_{bd} = 1587 kg m^{-3} and 1.0 M NaClO$_4$ external salt concentration (experiment 1055_4A, *cf.* Tab. 3.5).

The fit curves were obtained using slightly changed parameter values compared to through-diffusion (*cf.* Tab. 3.5).

Fig. A40a: Flux at the zero-concentration boundary and reservoir concentration of $^{85}Sr^{2+}$ through-diffusion in Na-*mom* at ρ_{bd} = 1586 kg m^{-3} and 1.0 M NaClO$_4$ external salt concentration (experiment 1055_4B, *cf.* Tab. 3.5).

Fig. A40b: Out-diffusion of $^{85}Sr^{2+}$ from Na-*mom* at ρ_{bd} = 1586 kg m^{-3} and 1.0 M NaClO$_4$ external salt concentration (experiment 1055_4B, *cf.* Tab. 3.5).

The fit curves were obtained using slightly changed parameter values compared to through-diffusion (*cf.* Tab. 3.5).

A.6 ^{134}Cs in-diffusion
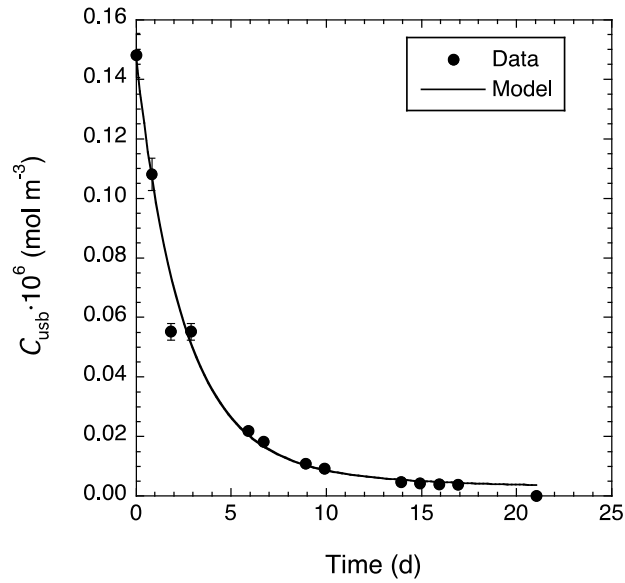
Fig. A41a: Reservoir concentration of ^{134}Cs$^+$ in-diffusion in Na-*mom* at $\rho_{bd} = 1550$ kg m^{-3} and 0.1 M NaClO$_4$ external salt concentration (experiment 1061_16A, *cf.* Tab. 3.10) with no added ^{133}Cs.
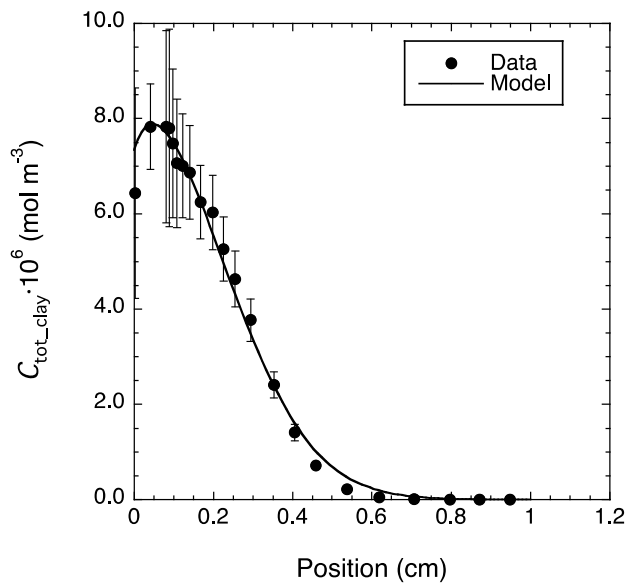
Fig. A41b: Profile data after 21 d of in-diffusion of ^{134}Cs$^+$ in Na-*mom* at $\rho_{bd} = 1550$ kg m^{-3} and 0.1 M NaClO$_4$ external salt concentration (experiment 1061_16A, *cf.* Tab. 3.10) with no added ^{133}Cs.
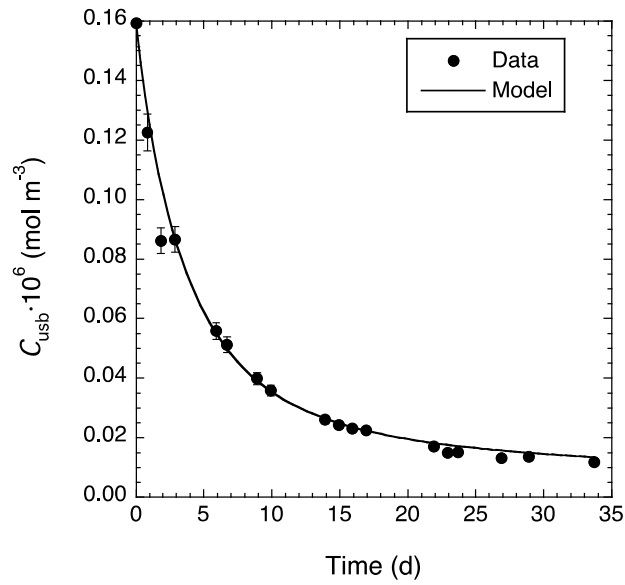
Fig. A42a: Reservoir concentration of $^{134}Cs^+$ in-diffusion in Na-*mom* at ρ_{bd} = 1540 kg m^{-3} and 0.5 M NaClO$_4$ external salt concentration (experiment 1061_16B, *cf.* Tab. 3.10) with no added ^{133}Cs.
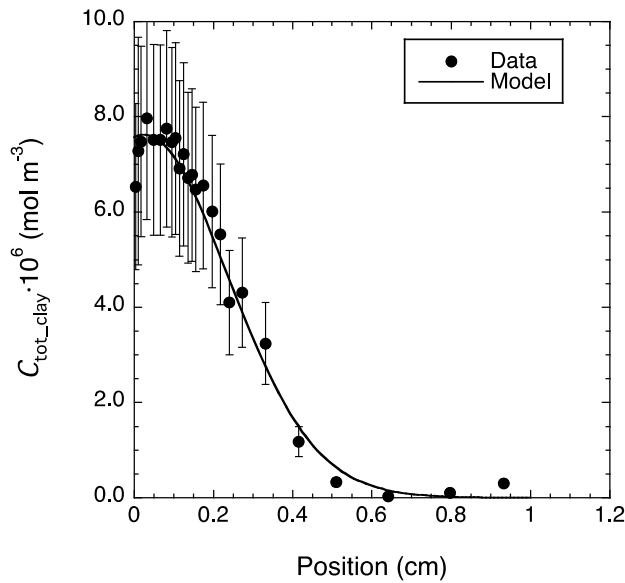
Fig. A42b: Profile data after 34 d of in-diffusion of $^{134}Cs^+$ in Na-*mom* at ρ_{bd} = 1540 kg m^{-3} and 0.5 M NaClO$_4$ external salt concentration (experiment 1061_16B, *cf.* Tab. 3.10) with no added ^{133}Cs.
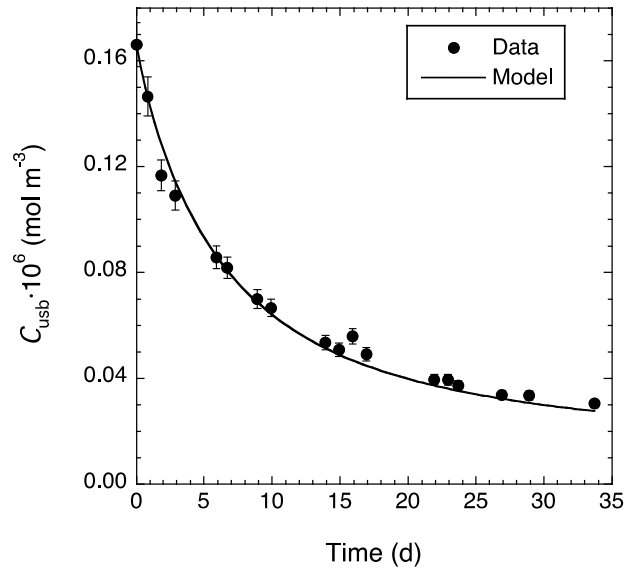
Fig. A43a: Reservoir concentration of $^{134}Cs^+$ in-diffusion in Na-*mom* at ρ_{bd} = 1590 kg m^{-3} and 1.0 M NaClO$_4$ external salt concentration (experiment 1061_16C, *cf.* Tab. 3.10) with no added ^{133}Cs.
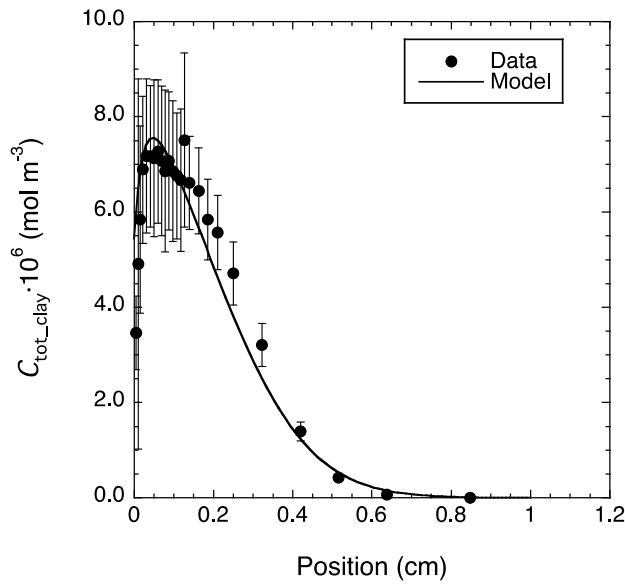
Fig. A43b: Profile data after 34 d of in-diffusion of $^{134}Cs^+$ in Na-*mom* at ρ_{bd} = 1590 kg m^{-3} and 1.0 M NaClO$_4$ external salt concentration (experiment 1061_16C, *cf.* Tab. 3.10) with no added ^{133}Cs.
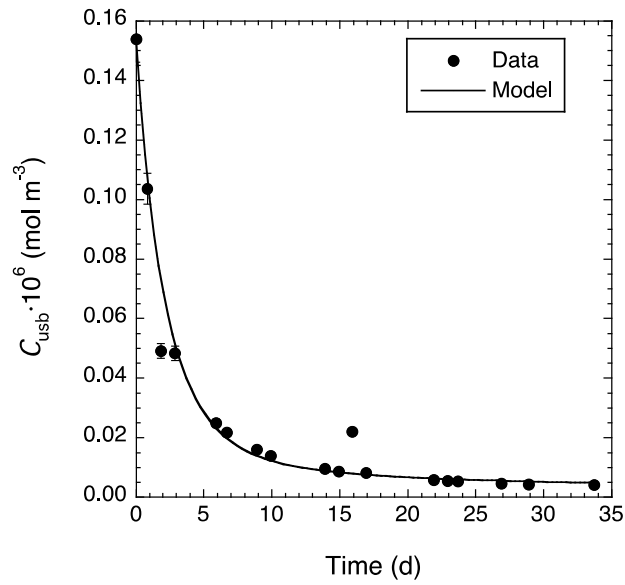
Fig. A44a: Reservoir concentration of ^{134}Cs$^+$ in-diffusion in Na-*mom* at ρ_{bd} = 1360 kg m^{-3} and 0.1 M NaClO$_4$ external salt concentration (experiment 1061_1B, *cf.* Tab. 3.10) and 0.01 mM added ^{133}Cs.
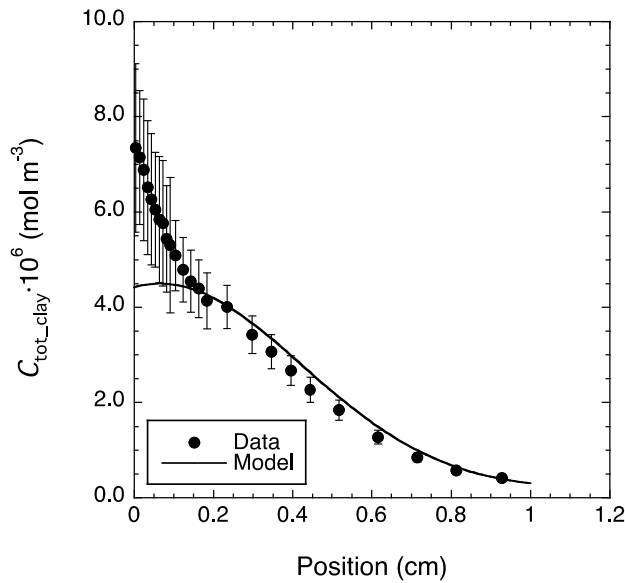

Fig. A44b: Profile data after 34 d of in-diffusion of ^{134}Cs$^+$ in Na-*mom* at ρ_{bd} = 1360 kg m^{-3} and 0.1 M NaClO$_4$ external salt concentration (experiment 1061_1B, *cf.* Tab. 3.10) and 0.01 mM added ^{133}Cs.
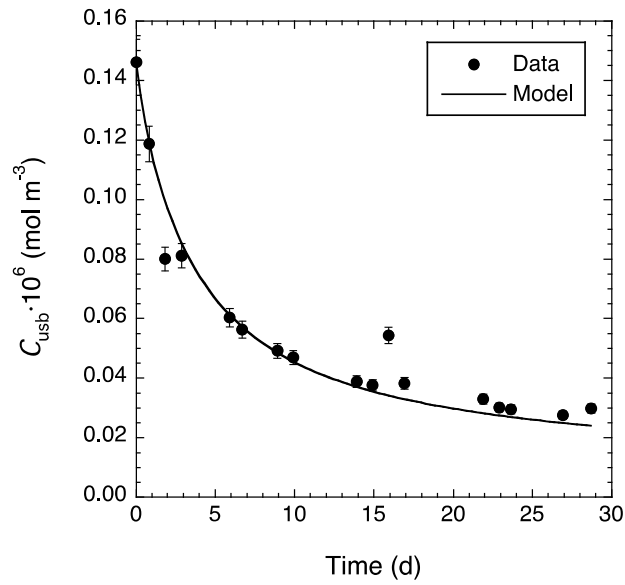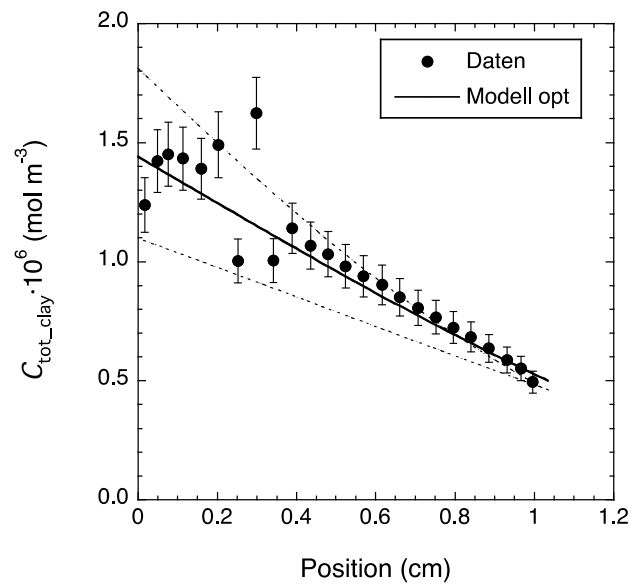
Fig. A45a: Reservoir concentration of [134]Cs^{+} in-diffusion in Na-*mom* at ρ_{bd} = 1510 kg m^{-3} and 0.1 M NaClO$_4$ external salt concentration (experiment 1061_2B, *cf.* Tab. 3.10) and 10 mM added [133]Cs.
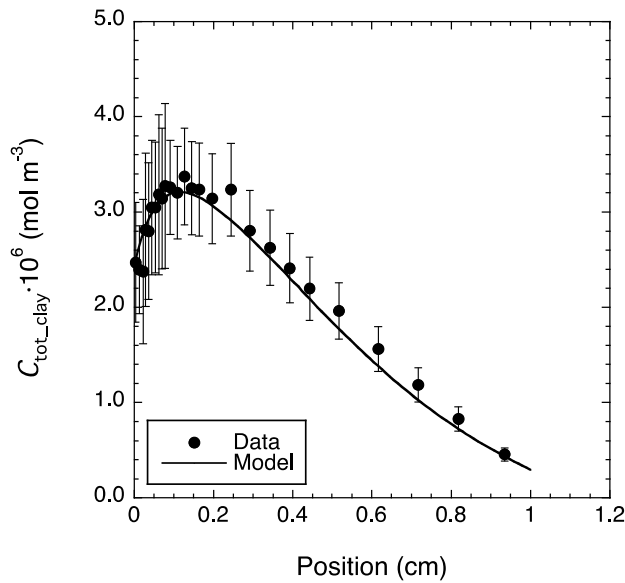
Fig. A45b: Profile data after 29 d of in-diffusion of [134]Cs^{+} in Na-*mom* at ρ_{bd} = 1510 kg m^{-3} and 0.1 M NaClO$_4$ external salt concentration (experiment 1061_2B, *cf.* Tab. 3.10) and 10 mM added [133]Cs.
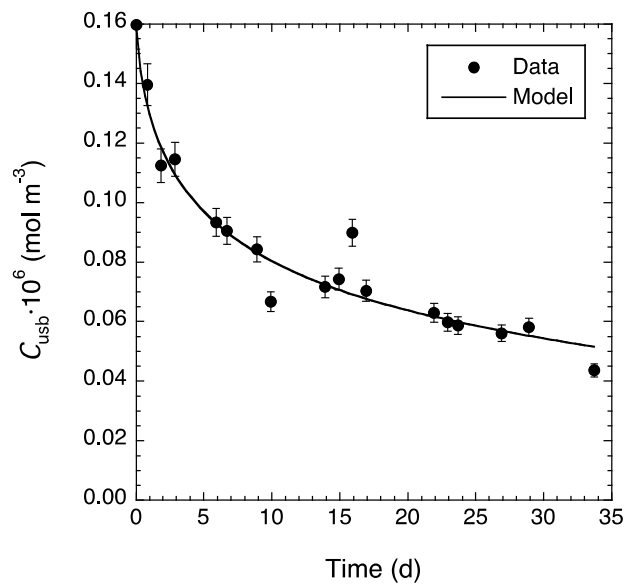
Fig. A46a: Reservoir concentration of $^{134}Cs^+$ in-diffusion in Na-*mom* at ρ_{bd} = 1050 kg m^{-3} and 1.0 M NaClO$_4$ external salt concentration (experiment 1061_1C, *cf.* Tab. 3.10) and 0.1 mM added ^{133}Cs.
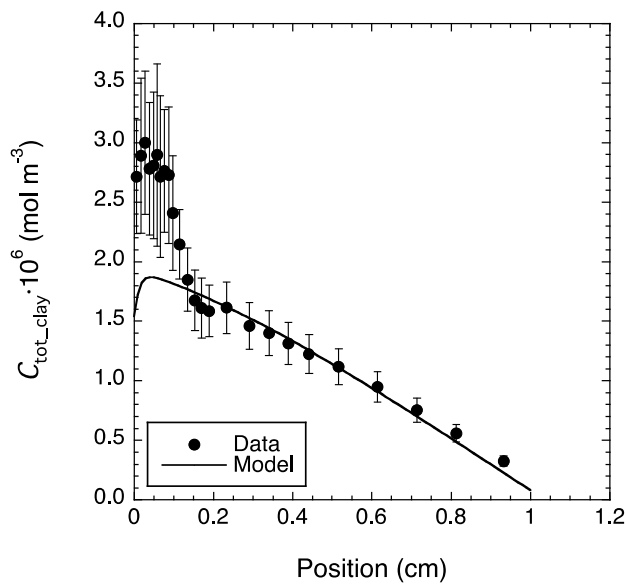

Fig. A46b: Profile data after 34 d of in-diffusion of $^{134}Cs^+$ in Na-*mom* at ρ_{bd} = 1050 kg m^{-3} and 1.0 M NaClO$_4$ external salt concentration (experiment 1061_1C, *cf.* Tab. 3.10) and 0.1 mM added ^{133}Cs.

A.7 Combined diffusion of HTO and ^{36}Cl$^-$ (0.5 and 1.0 M NaClO$_4$)
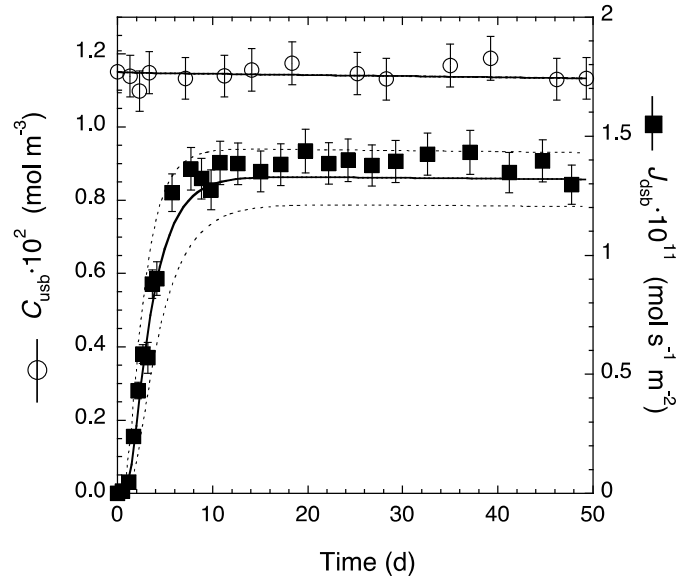
Fig. A47a: Upstream concentration and downstream flux of ^{36}Cl$^-$ in through-diffusion of HTO and ^{36}Cl$^-$ in Na-*mom* at ρ_{bd} = 1308 kg m^{-3} and 0.5 M NaClO$_4$ background electrolyte (experiment 1045_1A, *cf.* Tab. 3.11).
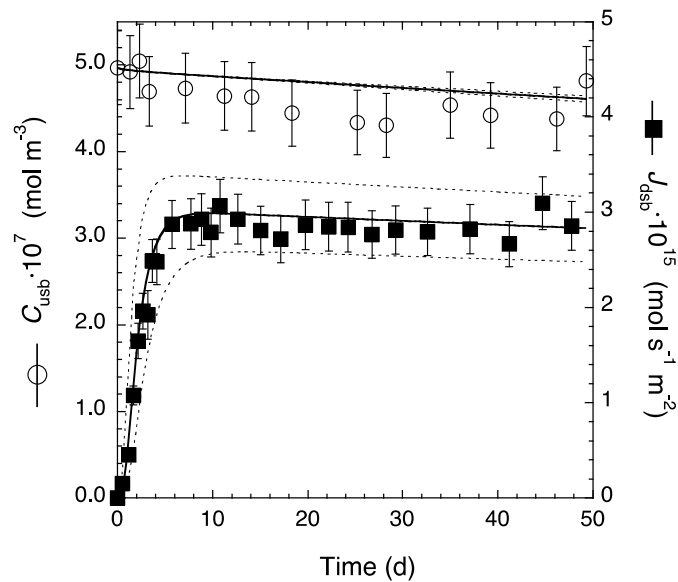
Fig. A47b: Upstream concentration and downstream flux of HTO in through-diffusion of HTO and ^{36}Cl$^-$ in Na-*mom* at ρ_{bd} = 1308 kg m^{-3} and 0.5 M NaClO$_4$ background electrolyte (experiment 1045_1A, *cf.* Tab. 3.11).
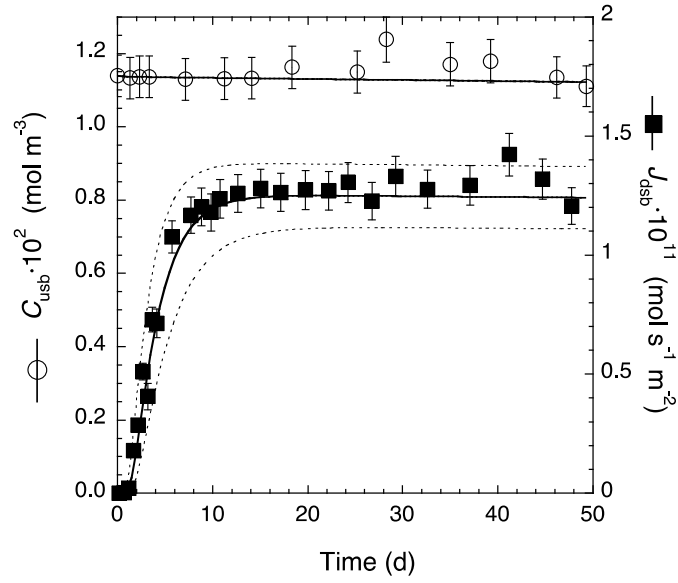
Fig. A48a: Upstream concentration and downstream flux of $^{36}Cl^-$ in through-diffusion of HTO and $^{36}Cl^-$ in Na-*mom* at $\rho_{bd} = 1304$ kg m^{-3} and 0.5 M NaClO$_4$ background electrolyte (experiment 1045_1B, *cf.* Tab. 3.11).
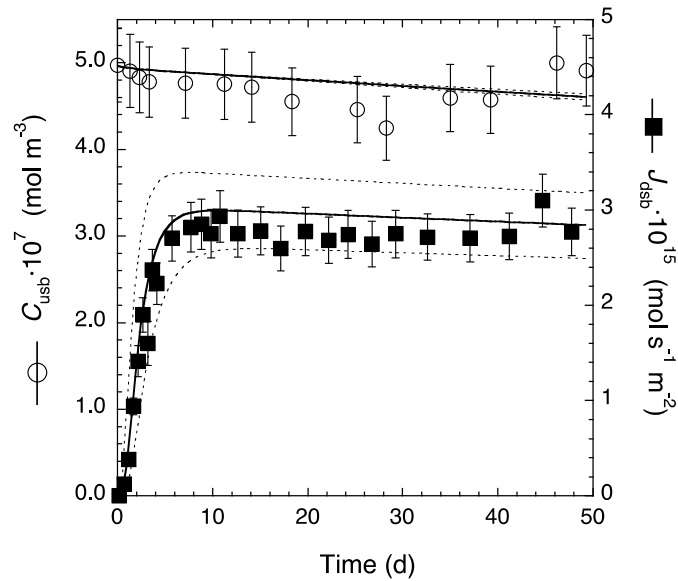
Fig. A48b: Upstream concentration and downstream flux of HTO in through-diffusion of HTO and $^{36}Cl^-$ in Na-*mom* at $\rho_{bd} = 1304$ kg m^{-3} and 0.5 M NaClO$_4$ background electrolyte (experiment 1045_1B, *cf.* Tab. 3.11).
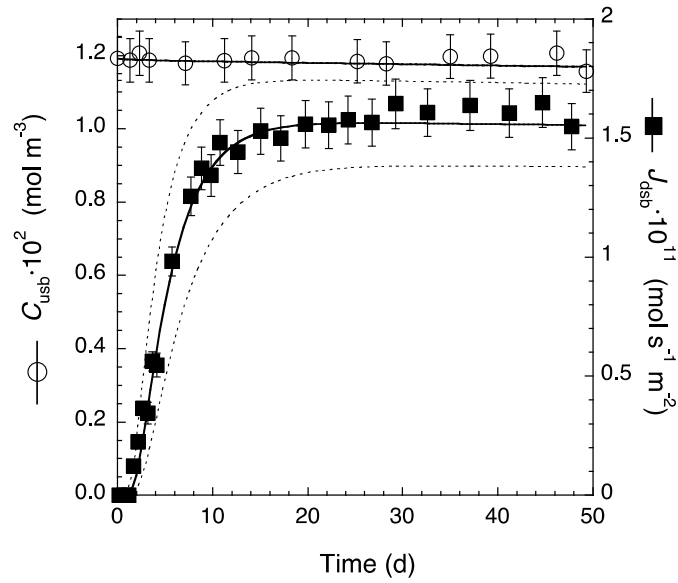
Fig. A49a: Upstream concentration and downstream flux of $^{36}Cl^-$ in through-diffusion of HTO and $^{36}Cl^-$ in Na-*mom* at ρ_{bd} = 1282 kg m^{-3} and 1.0 M NaClO$_4$ background electrolyte (experiment 1045_2A, *cf.* Tab. 3.11).
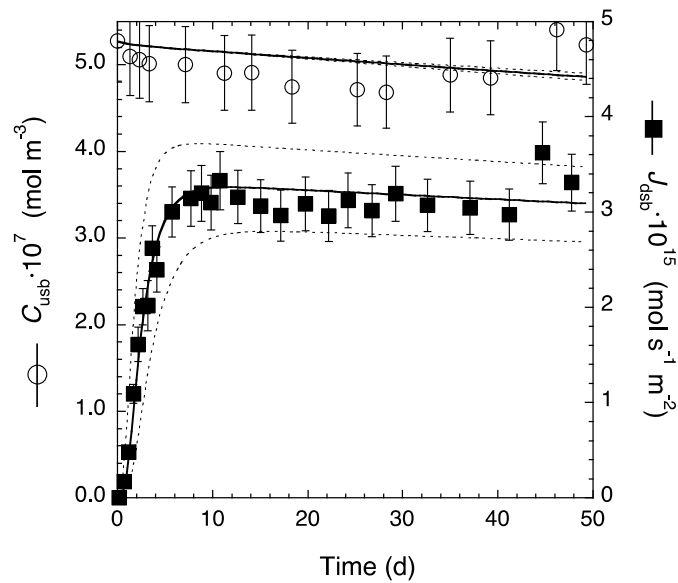
Fig. A49b: Upstream concentration and downstream flux of HTO in through-diffusion of HTO and $^{36}Cl^-$ in Na-*mom* at ρ_{bd} = 1282 kg m^{-3} and 1.0 M NaClO$_4$ background electrolyte (experiment 1045_2A, *cf.* Tab. 3.11).
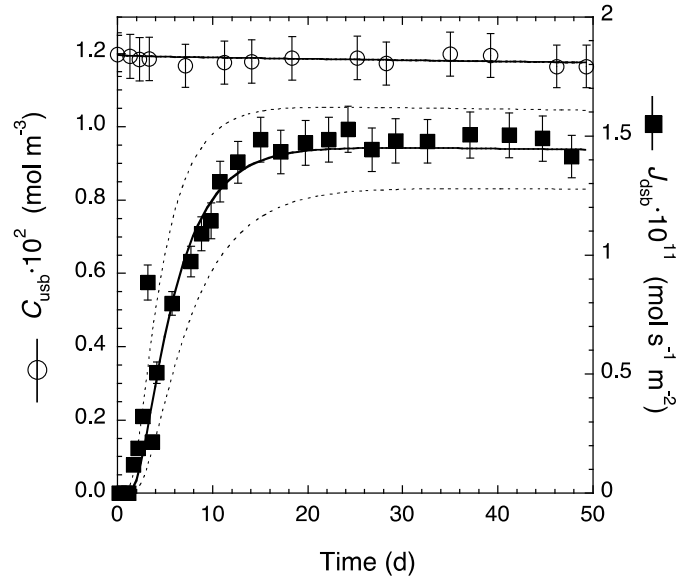
Fig. A50a: Upstream concentration and downstream flux of $^{36}Cl^-$ in through-diffusion of HTO and $^{36}Cl^-$ in Na-*mom* at $\rho_{bd} = 1317$ kg m^{-3} and 1.0 M NaClO$_4$ background electrolyte (experiment 1045_2B, *cf.* Tab. 3.11).
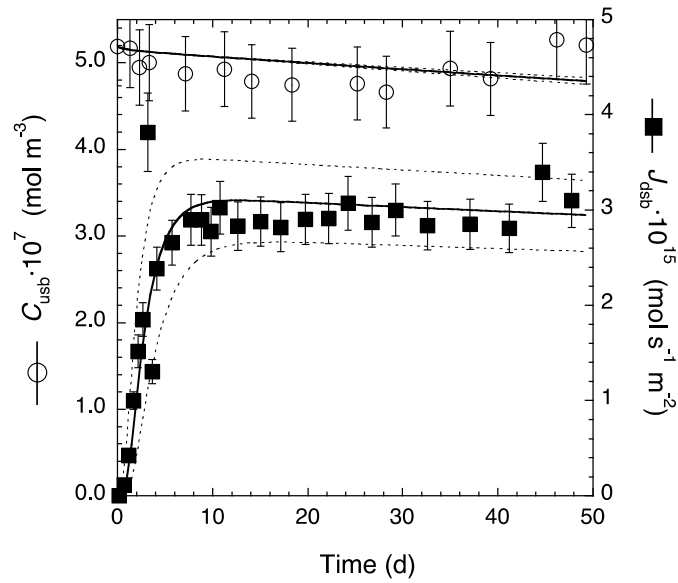
Fig. A50b: Upstream concentration and downstream flux of HTO in through-diffusion of HTO and $^{36}Cl^-$ in Na-*mom* at $\rho_{bd} = 1317$ kg m^{-3} and 1.0 M NaClO$_4$ background electrolyte (experiment 1045_2B, *cf.* Tab. 3.11).
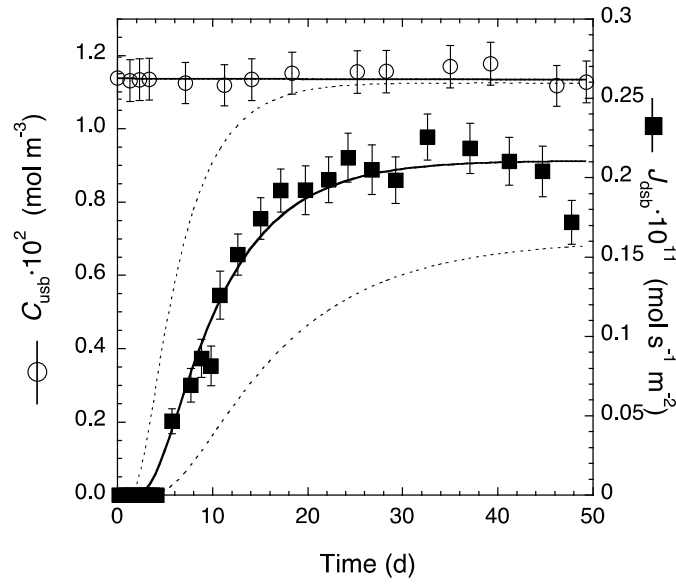
Fig. A51a: Upstream concentration and downstream flux of $^{36}Cl^-$ in through-diffusion of HTO and $^{36}Cl^-$ in Na-*mom* at $\rho_{bd} = 1623$ kg m^{-3} and 0.5 M NaClO$_4$ background electrolyte (experiment 1045_3A, *cf.* Tab. 3.11).
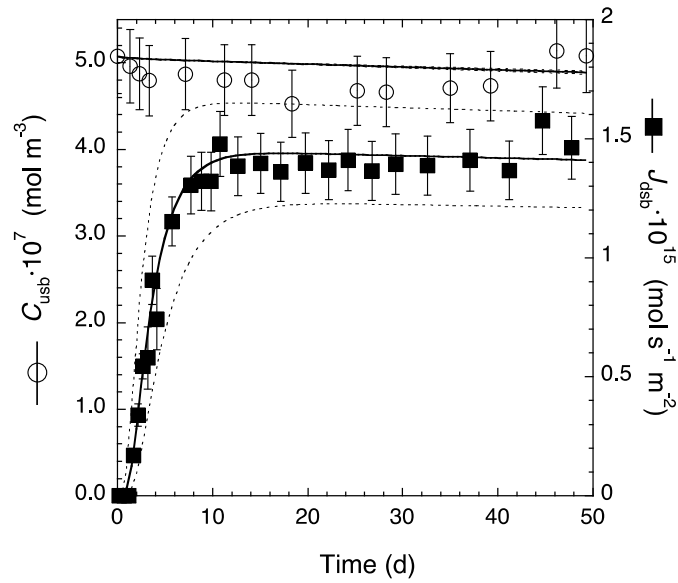
Fig. A51b: Upstream concentration and downstream flux of HTO in through-diffusion of HTO and $^{36}Cl^-$ in Na-*mom* at $\rho_{bd} = 1623$ kg m^{-3} and 0.5 M NaClO$_4$ background electrolyte (experiment 1045_3A, *cf.* Tab. 3.11).
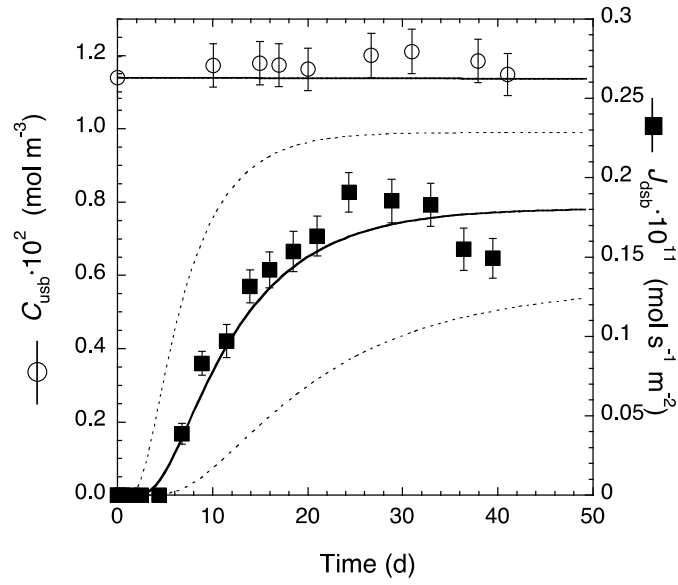
Fig. A52a: Upstream concentration and downstream flux of ^{36}Cl$^-$ in through-diffusion of HTO and ^{36}Cl$^-$ in Na-*mom* at ρ_{bd} = 1623 kg m^{-3} and 0.5 M NaClO$_4$ background electrolyte (experiment 1045_3B, *cf.* Tab. 3.11).
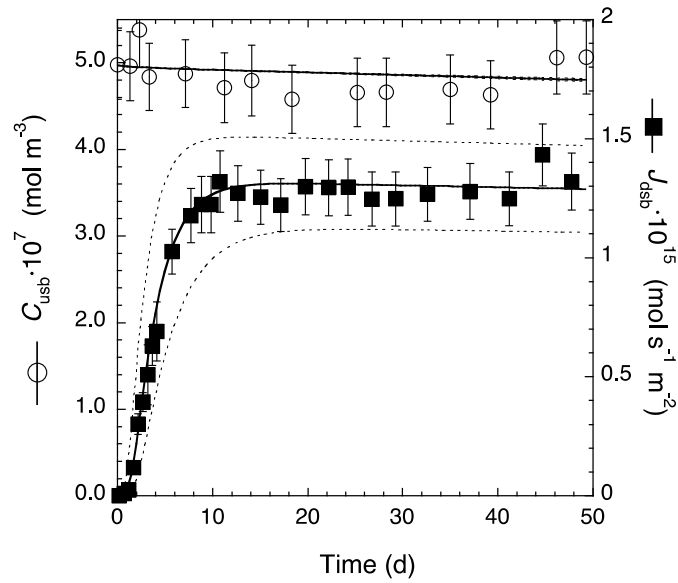
Fig. A52b: Upstream concentration and downstream flux of HTO in through-diffusion of HTO and ^{36}Cl$^-$ in Na-*mom* at ρ_{bd} = 1623 kg m^{-3} and 0.5 M NaClO$_4$ background electrolyte (experiment 1045_3B, *cf.* Tab. 3.11).
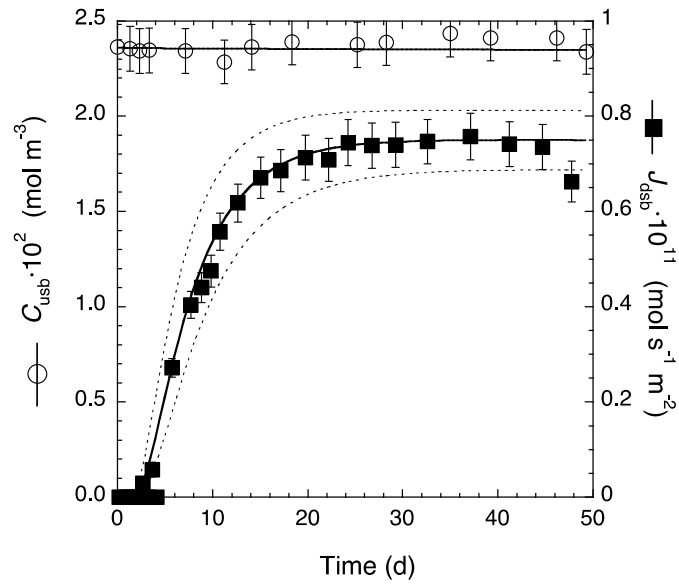
Fig. A53a: Upstream concentration and downstream flux of $^{36}Cl^-$ in through-diffusion of HTO and $^{36}Cl^-$ in Na-*mom* at $\rho_{bd} = 1622$ kg m^{-3} and 1.0 M NaClO$_4$ background electrolyte (experiment 1045_4A, *cf.* Tab. 3.11).
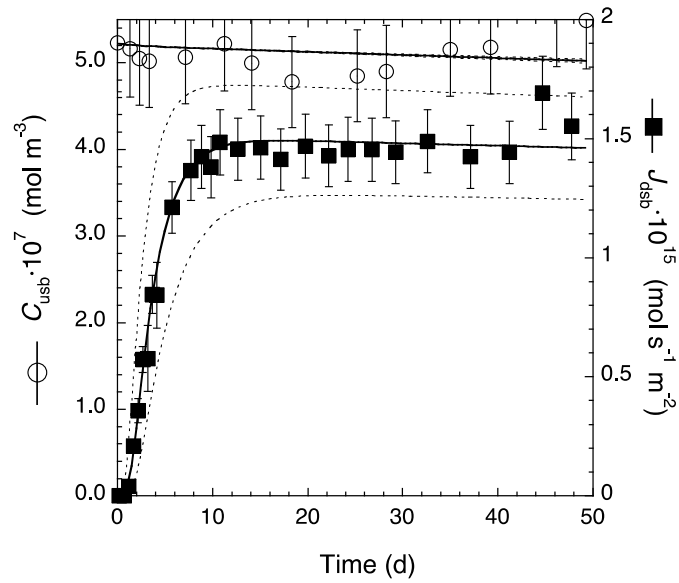
Fig. A53b: Upstream concentration and downstream flux of HTO in through-diffusion of HTO and $^{36}Cl^-$ in Na-*mom* at $\rho_{bd} = 1622$ kg m^{-3} and 1.0 M NaClO$_4$ background electrolyte (experiment 1045_4A, *cf.* Tab. 3.11).
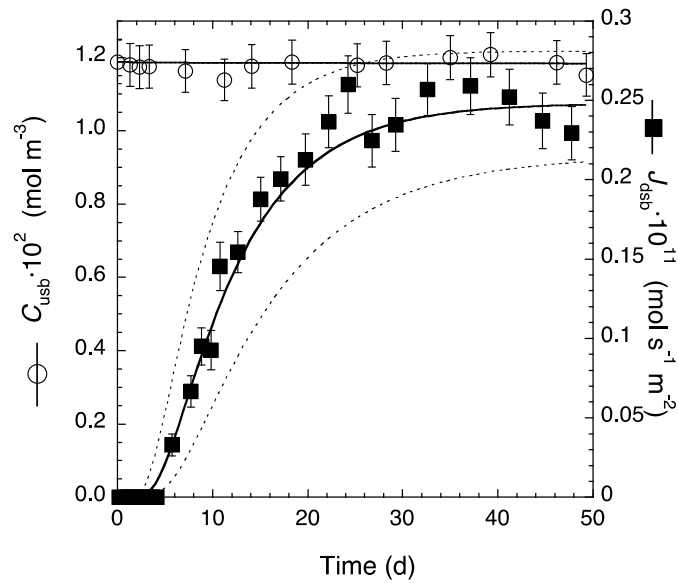
Fig. A54a: Upstream concentration and downstream flux of ^{36}Cl$^-$ in through-diffusion of HTO and ^{36}Cl$^-$ in Na-*mom* at ρ_{bd} = 1623 kg m^{-3} and 1.0 M NaClO$_4$ background electrolyte (experiment 1045_4B, *cf.* Tab. 3.11).
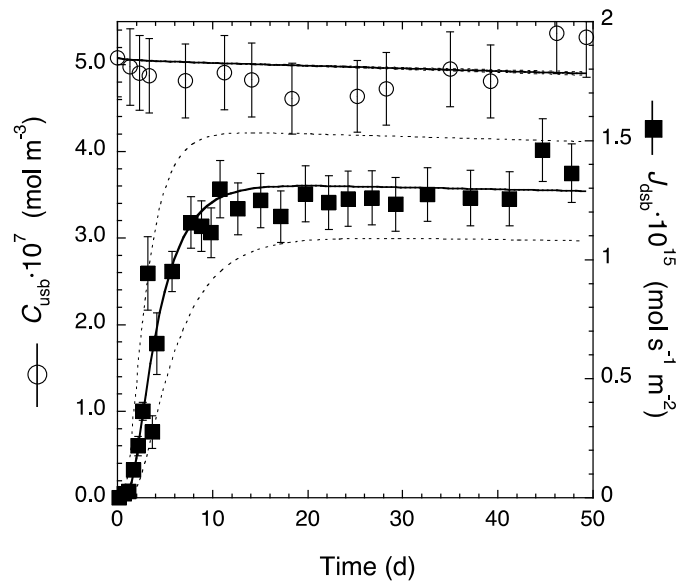
Fig. A54b: Upstream concentration and downstream flux of HTO in through-diffusion of HTO and ^{36}Cl$^-$ in Na-*mom* at ρ_{bd} = 1623 kg m^{-3} and 1.0 M NaClO$_4$ background electrolyte (experiment 1045_4B, *cf.* Tab. 3.11).

A.8 ^{85}Sr special test
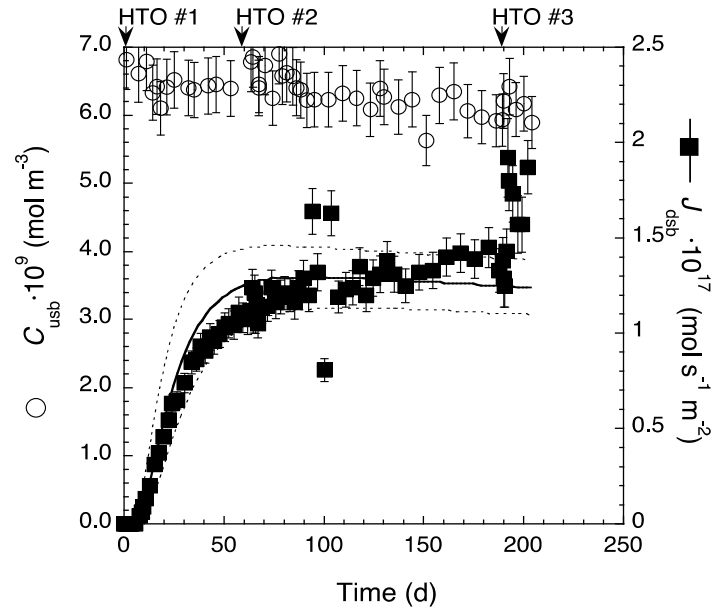
Fig. A55a: Flux at the zero-concentration boundary and reservoir concentration of ^{85}Sr^{2+} in simultaneous diffusion of HTO and ^{85}Sr^{2+} through Na-*mom* at $\rho_{bd} = 1956$ kg m^{-3} and 1.0 M NaClO$_4$ external salt concentration (experiment 1027_5A, *cf.* Tab. 3.12).

The starting times for HTO diffusion (*cf.* Fig. 55b) are indicated by arrows.
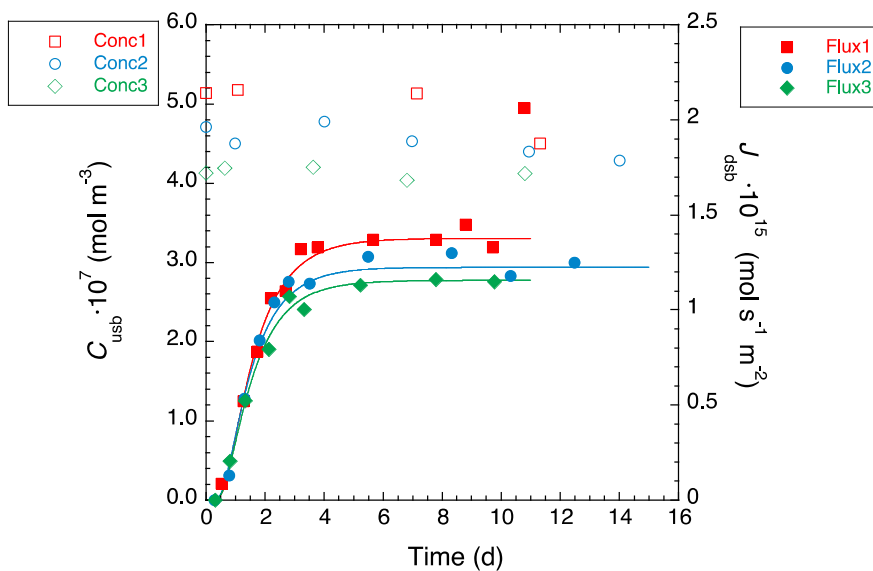
Fig. A55b: HTO diffusion data measured in three experiments (HTO #1, HTO #2, HTO #3) during the diffusion of ^{85}Sr^{2+} shown in Fig. 55a.

The time scale is thus relative to each of the HTO diffusion experiments.
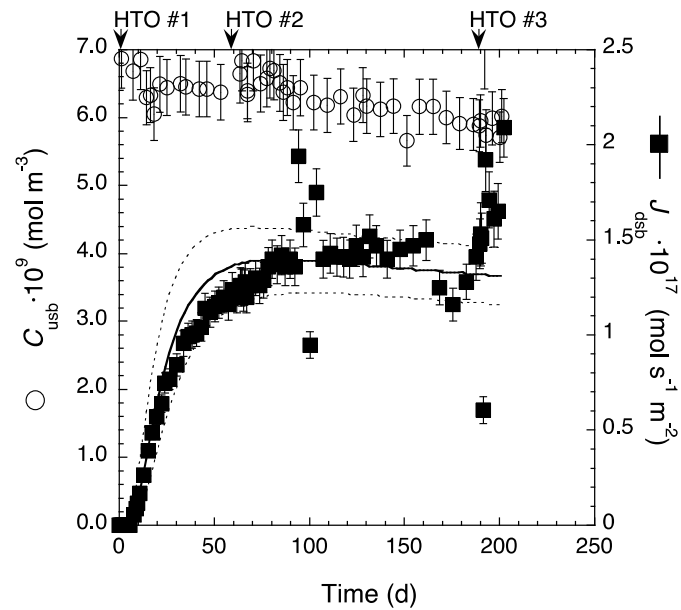
Fig. A56a: Flux at the zero-concentration boundary and reservoir concentration of $^{85}Sr^{2+}$ in simultaneous diffusion of HTO and $^{85}Sr^{2+}$ through Na-*mom* at $\rho_{bd} = 1950$ kg m^{-3} and 1.0 M NaClO$_4$ external salt concentration (experiment 1027_5B, *cf.* Tab. 3.12).

The starting times for HTO diffusion (*cf.* Fig. 56b) are indicated by arrows.
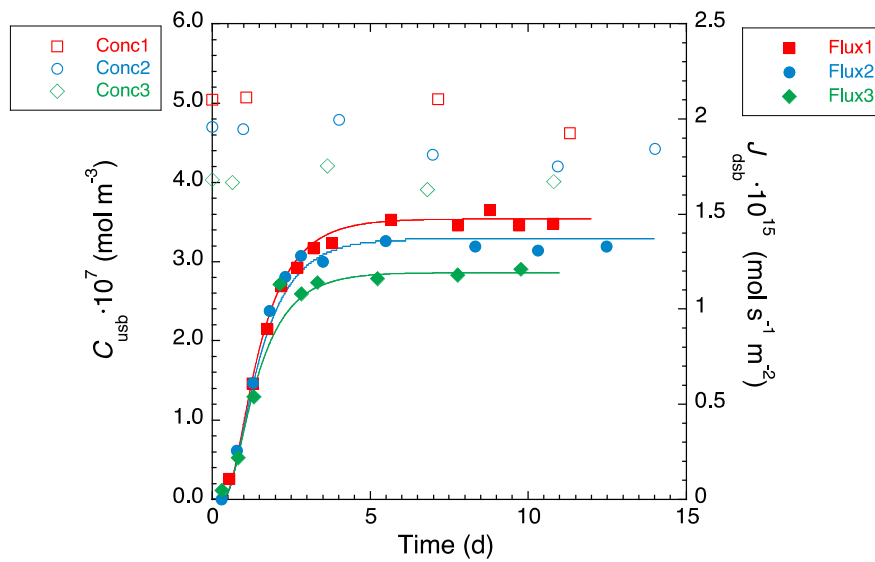
Fig. A56b: HTO diffusion data measured in three experiments (HTO #1, HTO #2, HTO #3) during the diffusion of $^{85}Sr^{2+}$ shown in Fig. 56a.

The time scale is thus relative to each of the HTO diffusion experiments.
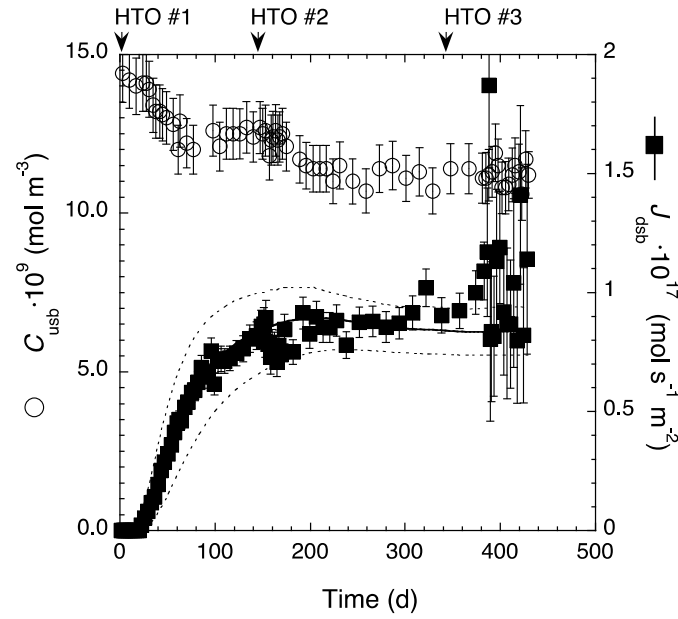
Fig. A57a: Flux at the zero-concentration boundary and reservoir concentration of $^{85}Sr^{2+}$ in simultaneous diffusion of HTO and $^{85}Sr^{2+}$ through Na-*mom* at ρ_{bd} = 1962 kg m^{-3} and 1.0 M NaClO$_4$ external salt concentration (experiment 1027_10C, *cf.* Tab. 3.12).

The starting times for HTO diffusion (*cf.* Fig. 57b) are indicated by arrows.
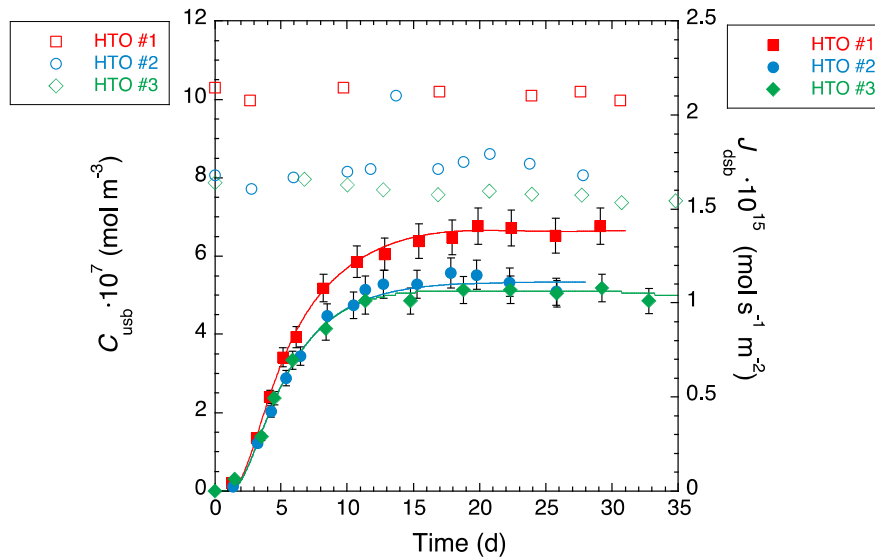
Fig. A57b: HTO diffusion data measured in three experiments (HTO #1, HTO #2, HTO #3) during the diffusion of $^{85}Sr^{2+}$ shown in Fig. 57a.

The time scale is thus relative to each of the HTO diffusion experiments.
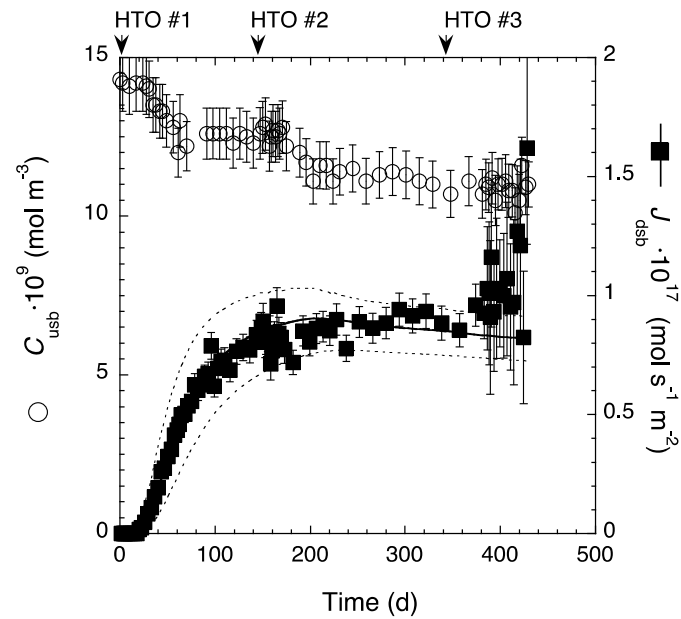
Fig. A58a: Flux at the zero-concentration boundary and reservoir concentration of $^{85}Sr^{2+}$ in simultaneous diffusion of HTO and $^{85}Sr^{2+}$ through Na-*mom* at $\rho_{bd} = 1958$ kg m^{-3} and 1.0 M NaClO$_4$ external salt concentration (experiment 1027_10D, *cf.* Tab. 3.12).

The starting times for HTO diffusion (*cf.* Fig. 58b) are indicated by arrows.
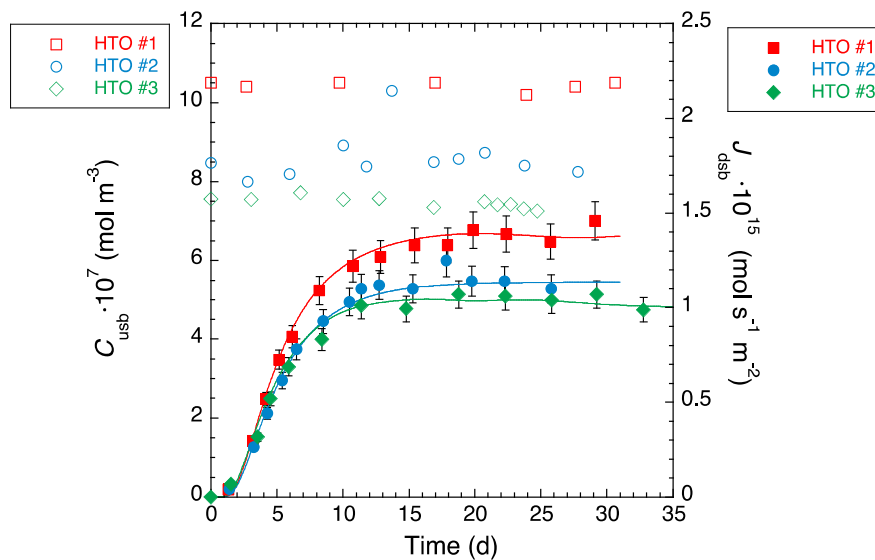
Fig. A58b: HTO diffusion data measured in three experiments (HTO #1, HTO #2, HTO #3) during the diffusion of $^{85}Sr^{2+}$ shown in Fig. 58a.

The time scale is thus relative to each of the HTO diffusion experiments.
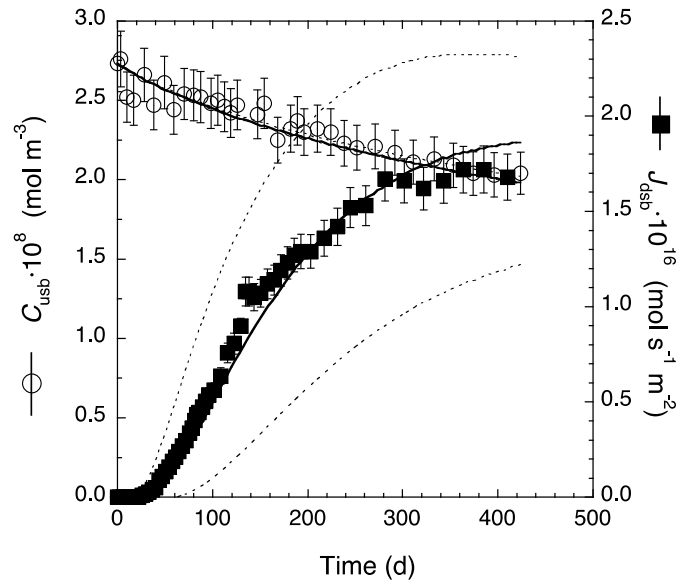
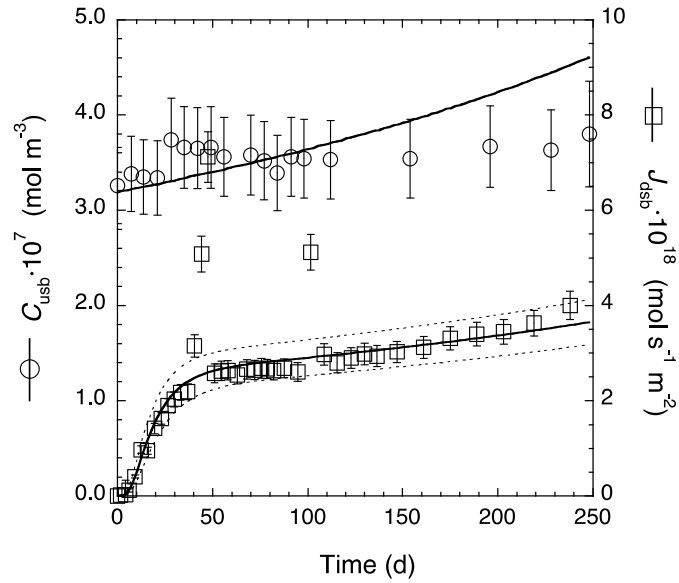Fig. A59a: Flux at the zero-concentration boundary and reservoir concentration of $^{85}Sr^{2+}$ through-diffusion in Na-*mom* at ρ_{bd} = 1900 kg m^{-3} and 0.2 M NaClO$_4$ external salt concentration (experiment 1023_10A, *cf.* Tab. 3.13).
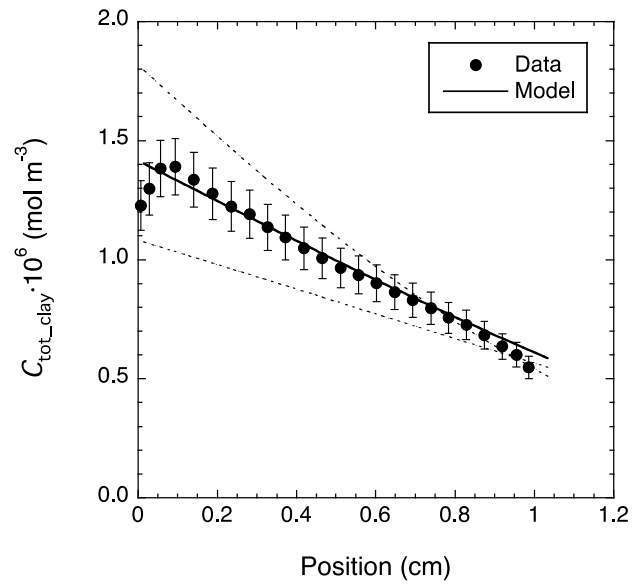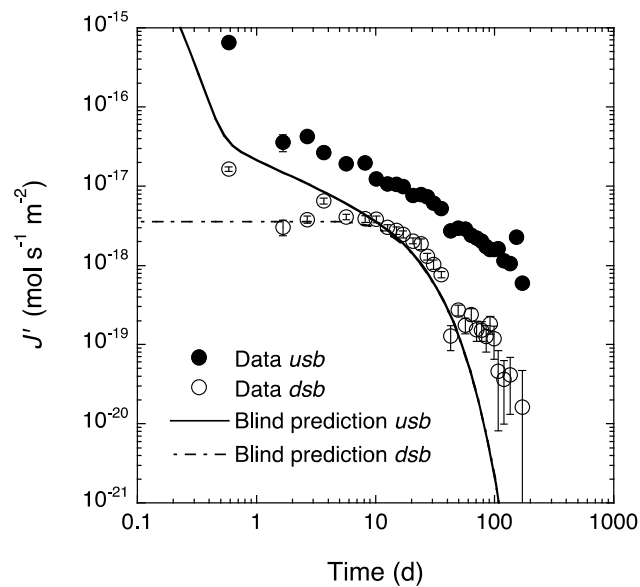

Fig. A59b: Tracer profile data of experiment 1023 10A.
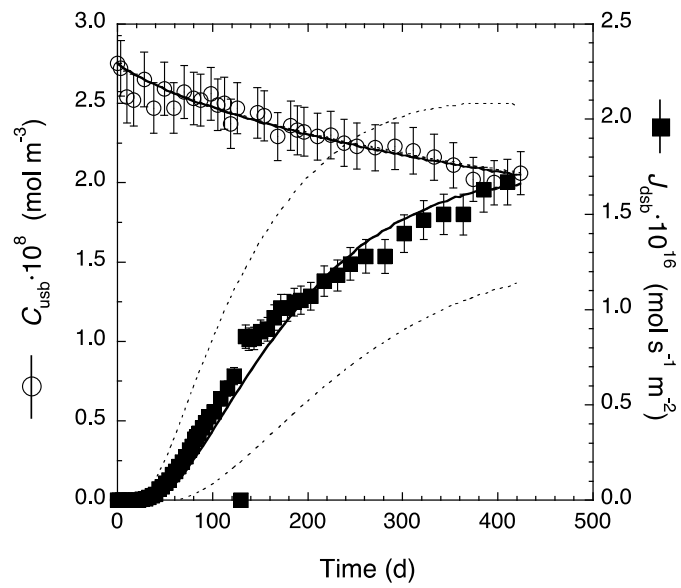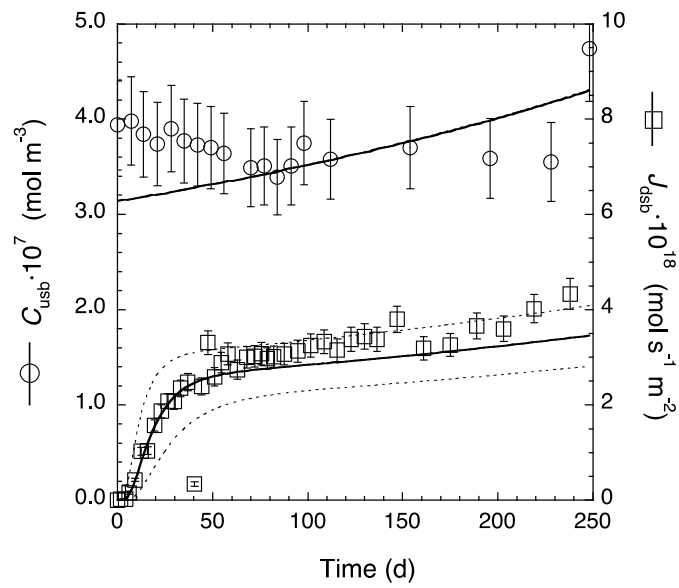
Fig. A60a: Flux at the zero-concentration boundary and reservoir concentration of $^{85}Sr^{2+}$ through-diffusion in Na-*mom* at ρ_{bd} = 1956 kg m^{-3} and 0.2 M NaClO$_4$ external salt concentration (experiment 1023_10B, *cf.* Tab. 3.13).

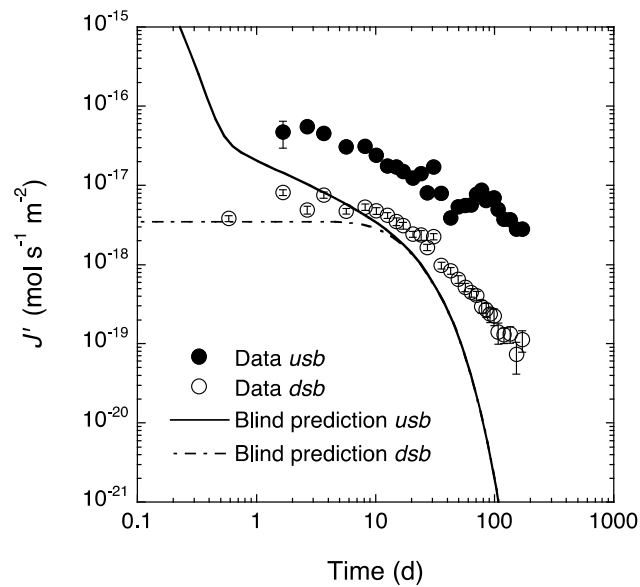Fig. A60b: Tracer profile data of experiment 1023 10B.
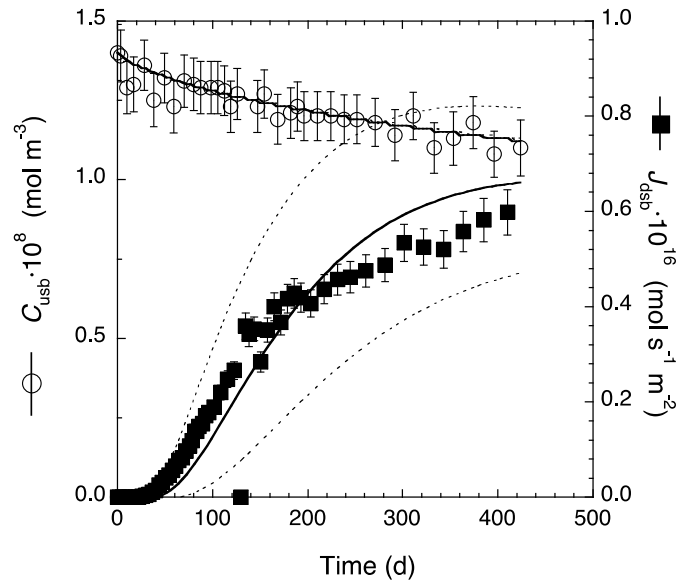
Fig. A61a: Flux at the zero-concentration boundary and reservoir concentration of $^{85}Sr^{2+}$ through-diffusion in Na-*mom* at ρ_{bd} = 1895 kg m^{-3} and 0.3 M NaClO$_4$ external salt concentration (experiment 1023_10C, *cf.* Tab. 3.13).
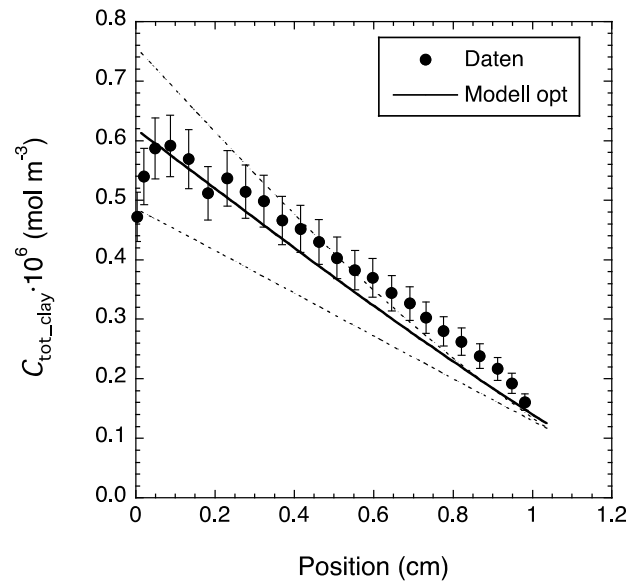
Fig. A61b: Tracer profile data of experiment 1023 10C.
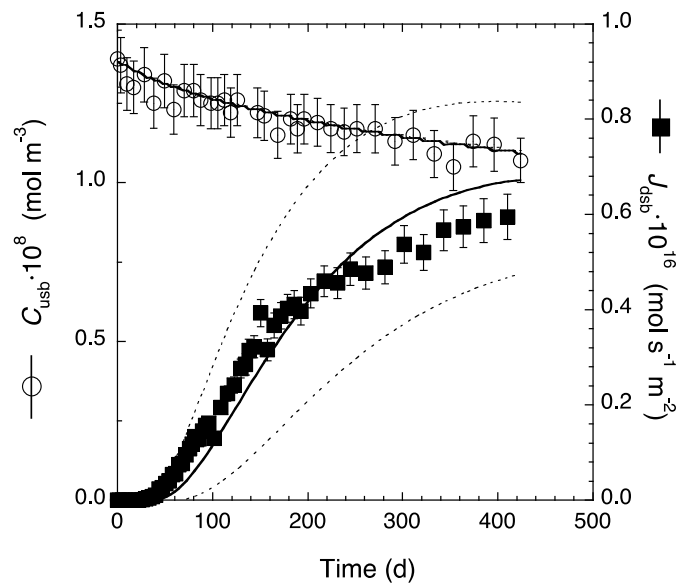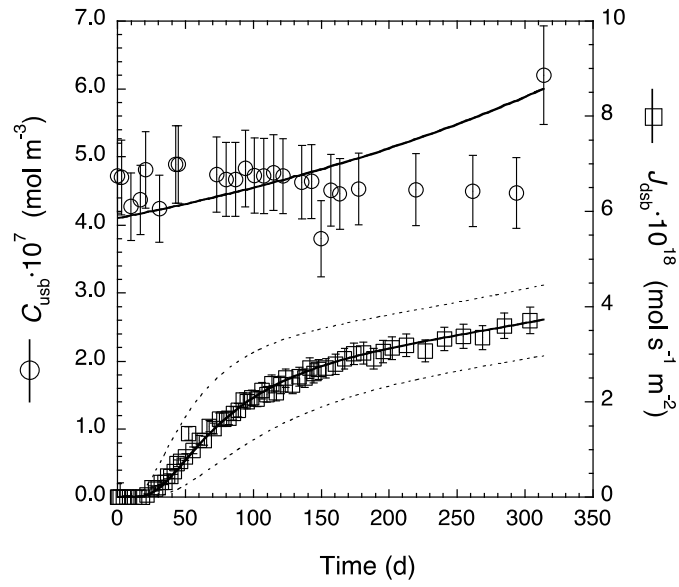
Fig. A62a: Flux at the zero-concentration boundary and reservoir concentration of $^{85}Sr^{2+}$ through-diffusion in Na-*mom* at ρ_{bd} = 1952 kg m^{-3} and 0.3 M NaClO$_4$ external salt concentration (experiment 1023_10D, *cf.* Tab. 3.13).
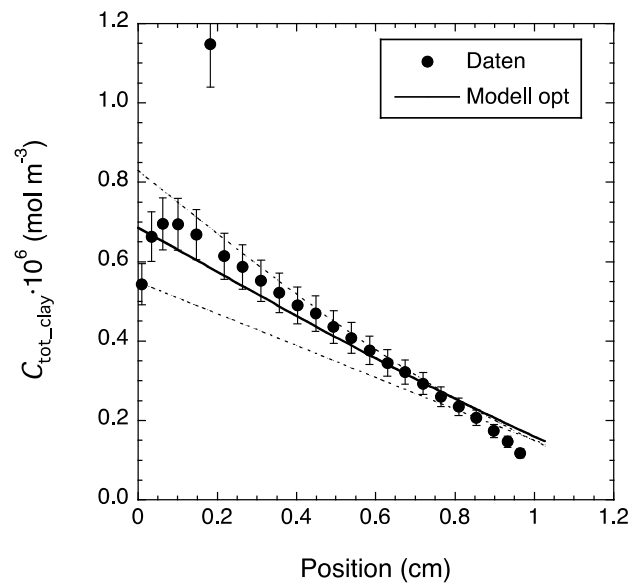
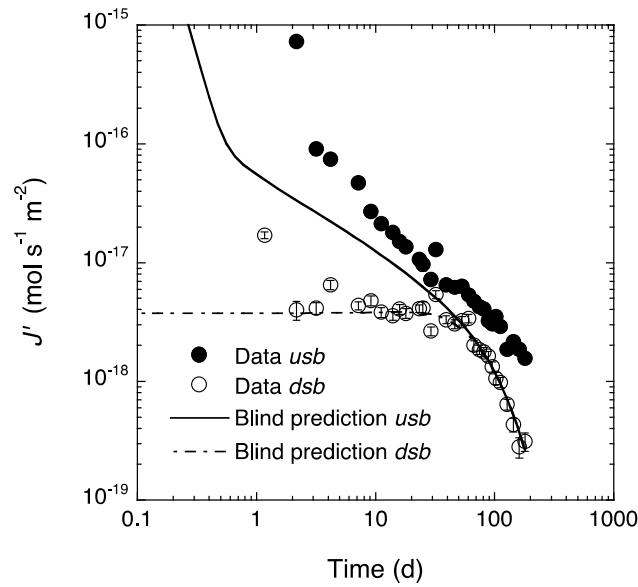Fig. A62b: Tracer profile data of experiment 1023 10D.

A.9   Diffusion tests of $^{134}Cs^+$ in thin clay samples
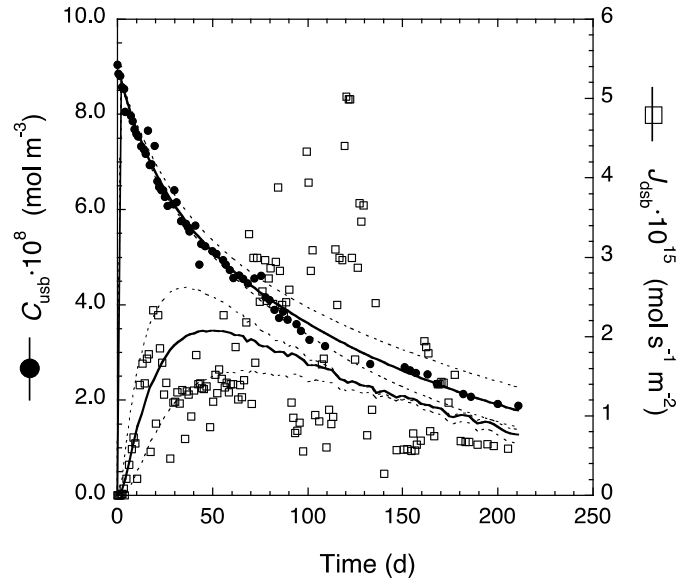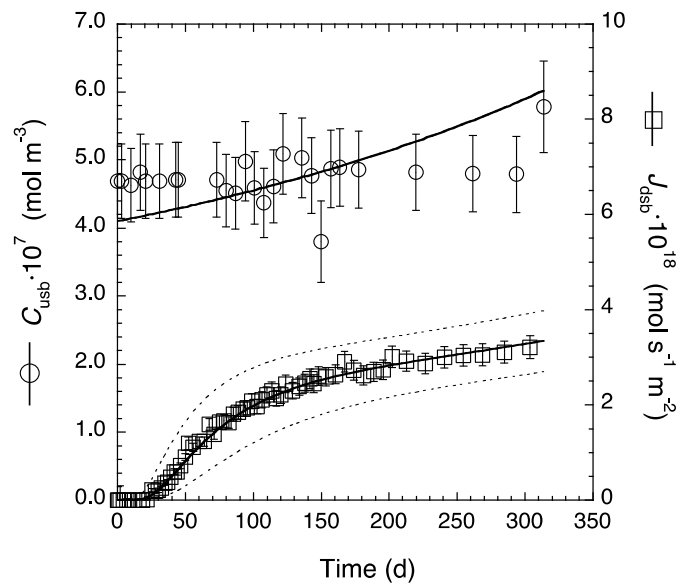

Fig. A63a: Flux at the zero-concentration boundary and reservoir concentration of $^{134}Cs^+$ in hrough-diffusion in Na-*mom* at ρ_{bd} = 1365 kg m^{-3} and 1.0 M NaClO$_4$ external salt concentration (experiment 1034_13C, *cf.* Tab. 3.14).
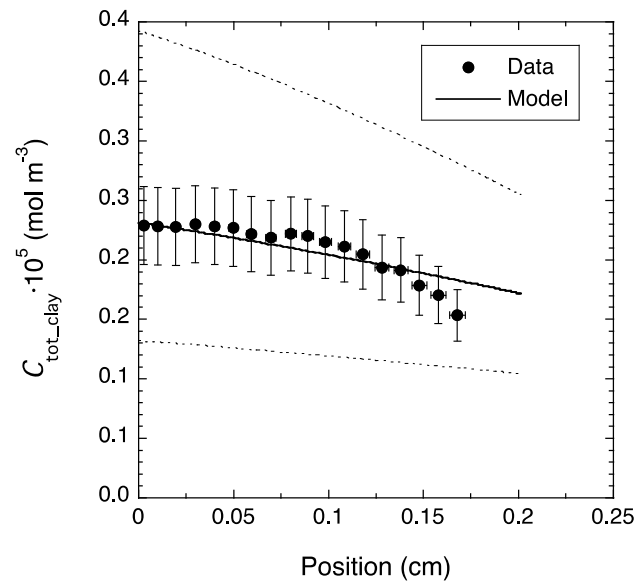
Fig. A63b: Tracer profile data of experiment 1034_13C measured at the end of through-diffusion.
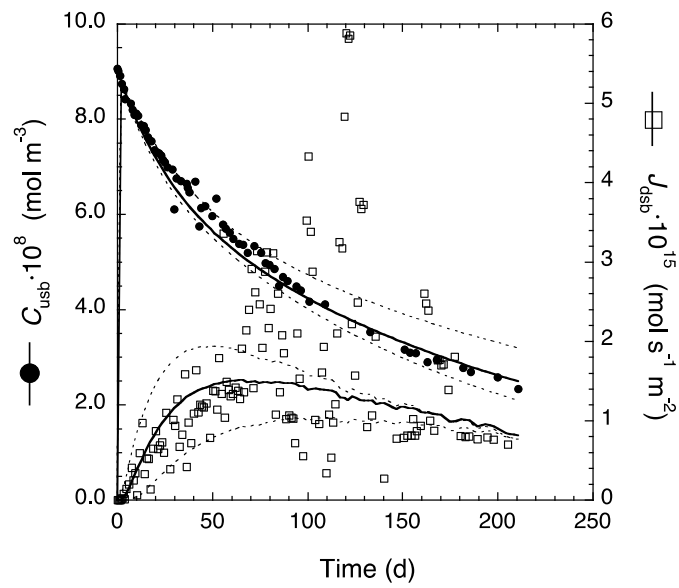
Fig. A64a: Flux at the zero-concentration boundary and reservoir concentration of $^{134}Cs^+$ in through-diffusion in Na-*mom* at ρ_{bd} = 1355 kg m^{-3} and 1.0 M NaClO$_4$ external salt concentration (experiment 1034_13D, *cf.* Tab. 3.14).
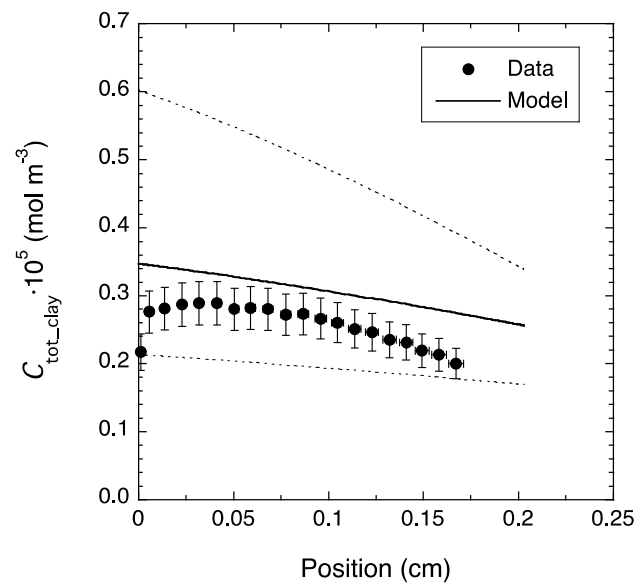
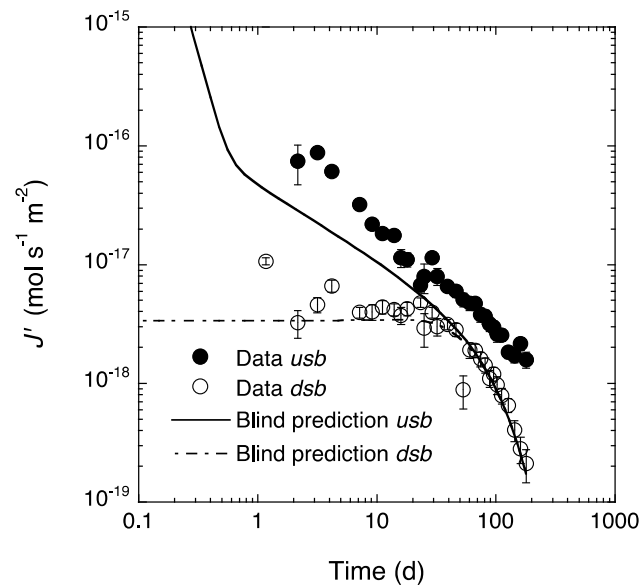Fig. A64b: Tracer profile data of experiment 1034_13D measured at the end of through-diffusion.
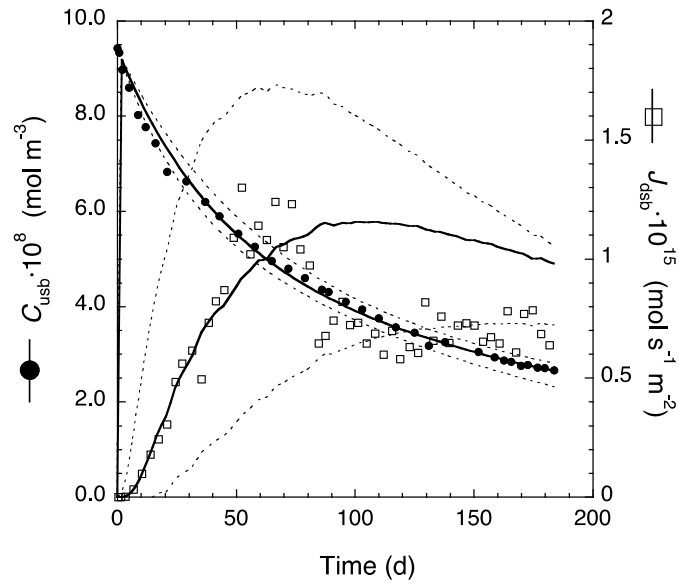
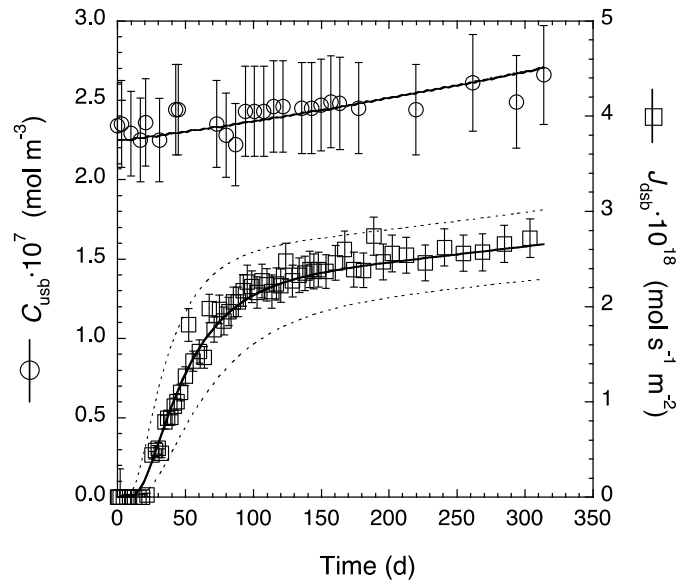Fig. A65a: Flux at the zero-concentration boundary and reservoir concentration of ^{134}Cs$^+$ in through-diffusion in Na-*mom* at ρ_{bd} = 1667 kg m^{-3} and 1.0 M NaClO$_4$ external salt concentration (experiment 1034_16A, *cf.* Tab. 3.14).
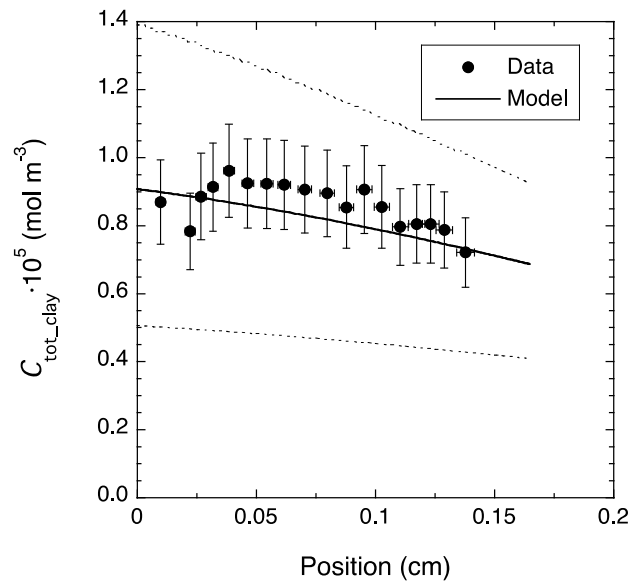
Fig. A65b: Tracer profile data of experiment 1034_16A measured at the end of through-diffusion.
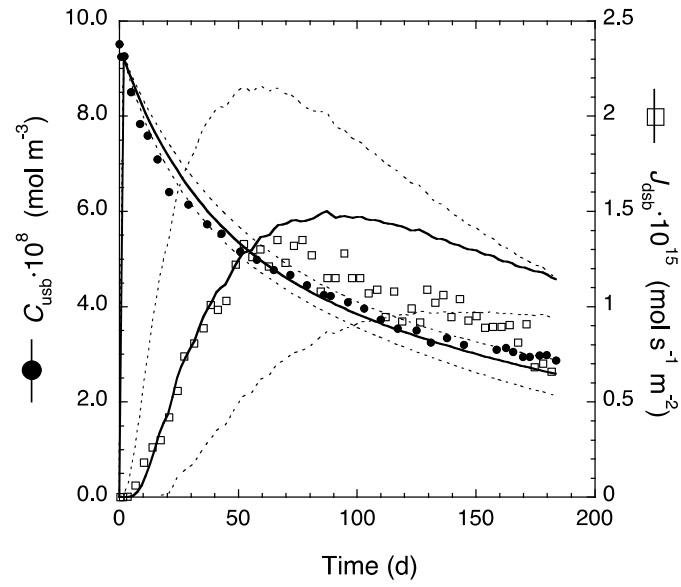
Fig. A66a: Flux at the zero-concentration boundary and reservoir concentration of $^{134}Cs^+$ in through-diffusion in Na-*mom* at ρ_{bd} = 1657 kg m^{-3} and 1.0 M NaClO$_4$ external salt concentration (experiment 1034_16B, *cf.* Tab. 14).
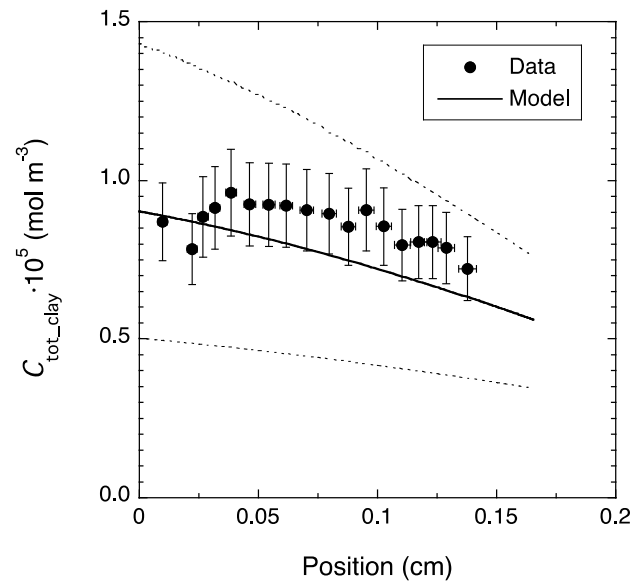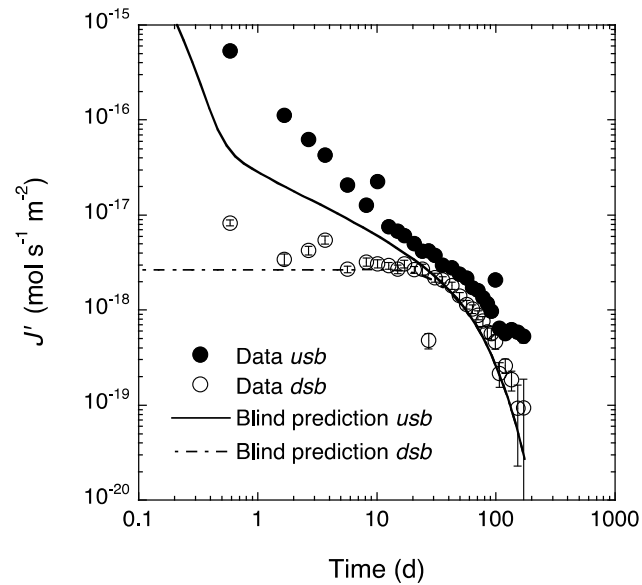

Fig. A66b: Tracer profile data of experiment 1034_16B measured at the end of through-diffusion.
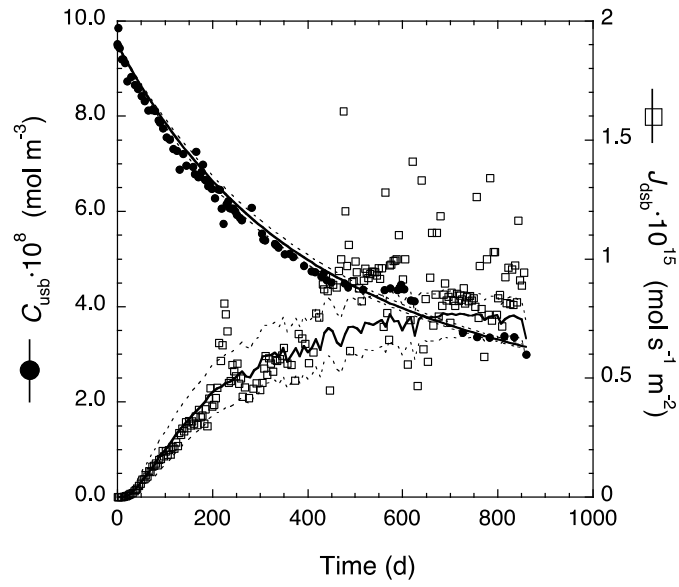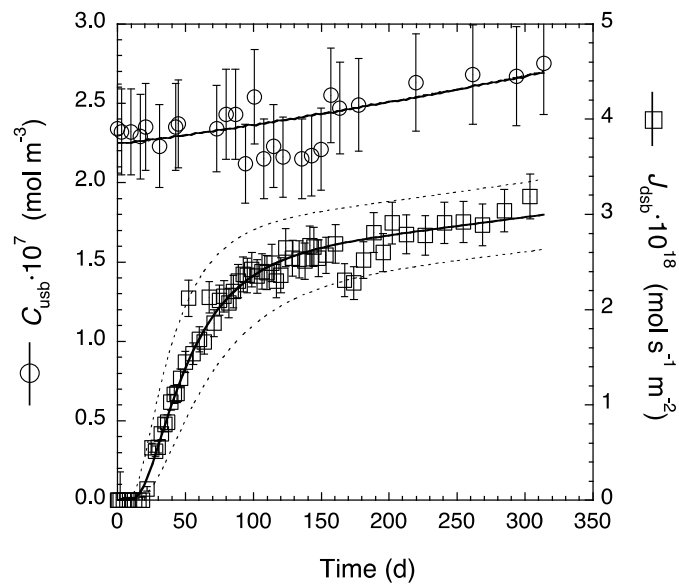
Fig. A67a: Flux at the zero-concentration boundary and reservoir concentration of $^{134}Cs^+$ in through-diffusion in Na-*mom* at $\rho_{bd} = 1978$ kg m^{-3} and 1.0 M NaClO$_4$ external salt concentration (experiment 1034_19A, *cf.* Tab. 3.14).
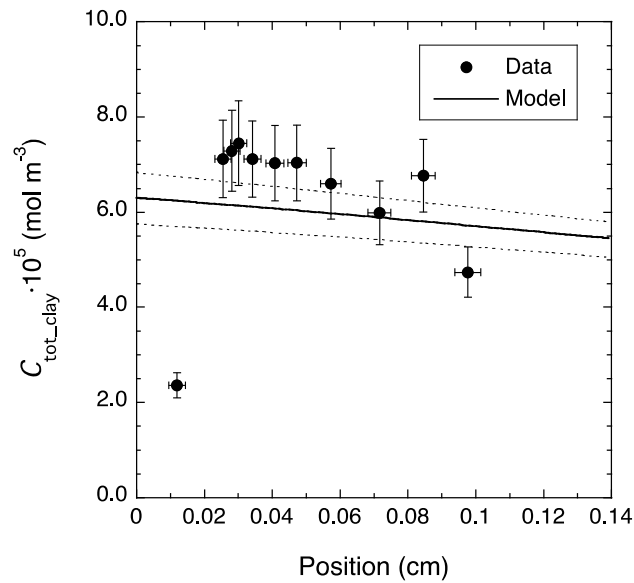
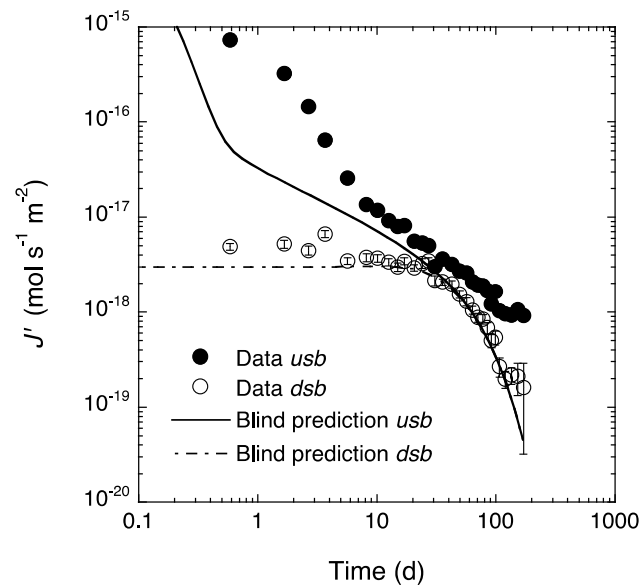Fig. A67b: Tracer profile data of experiment 1034_19A measured at the end of through-diffusion.
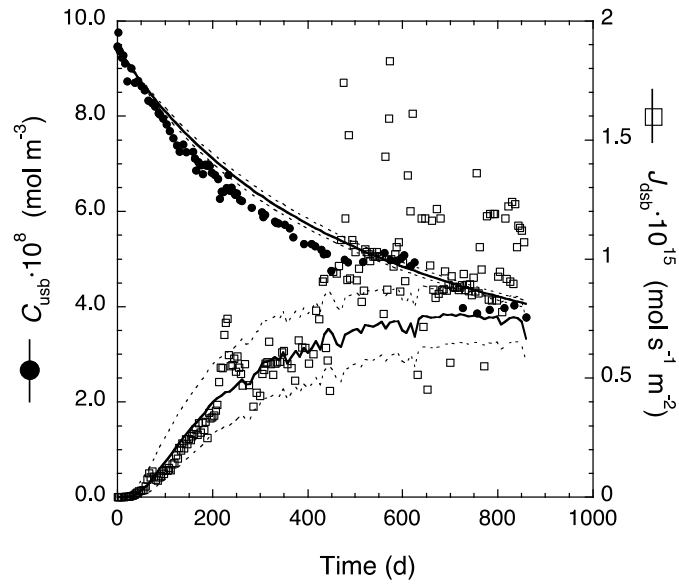
Fig. A68a: Flux at the zero-concentration boundary and reservoir concentration of $^{134}Cs^+$ in through-diffusion in Na-*mom* at ρ_{bd} = 1949 kg m^{-3} and 1.0 M NaClO$_4$ external salt concentration (experiment 1034_19B, *cf.* Tab. 3.14).
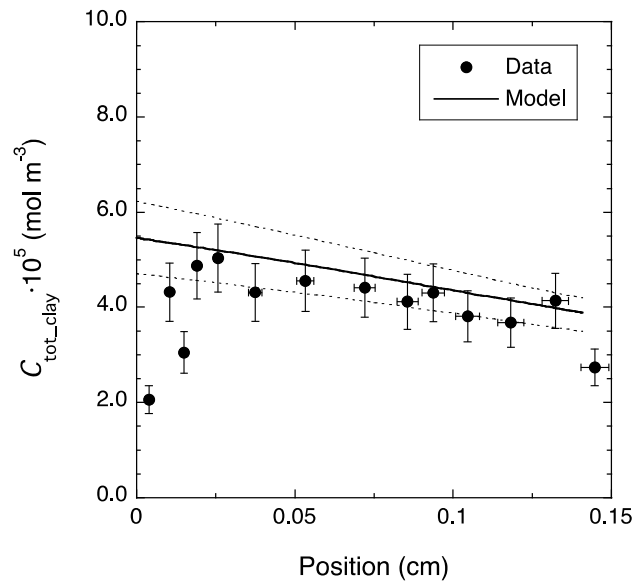
Fig. A68b: Tracer profile data of experiment 1034_19B measured at the end of through-diffusion.

A.10   Through- and out-diffusion of $^{35}SO_4{}^{2-}$
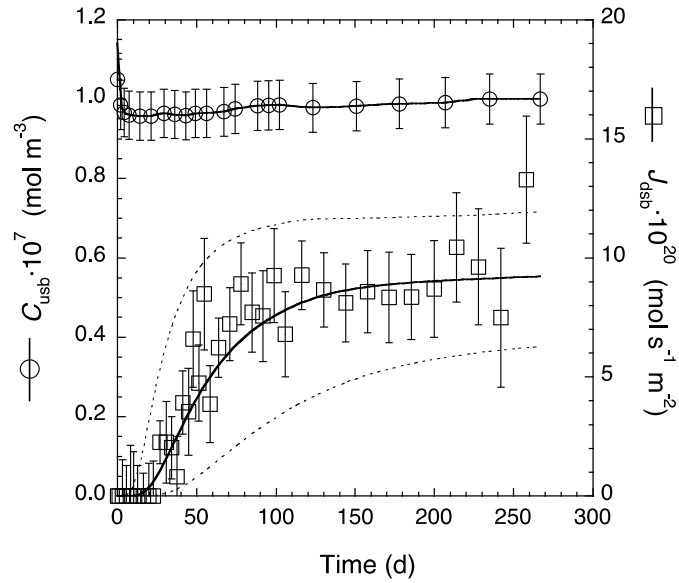
Fig. A69a: Flux at the zero-concentration boundary and reservoir concentration of $^{35}SO_4{}^{2-}$ in through-diffusion in Na-*mom* at ρ_{bd} = 1942 kg m^{-3} and 0.1 M NaClO$_4$ external salt concentration (experiment 1032_1A, *cf.* Tab. 3.15).
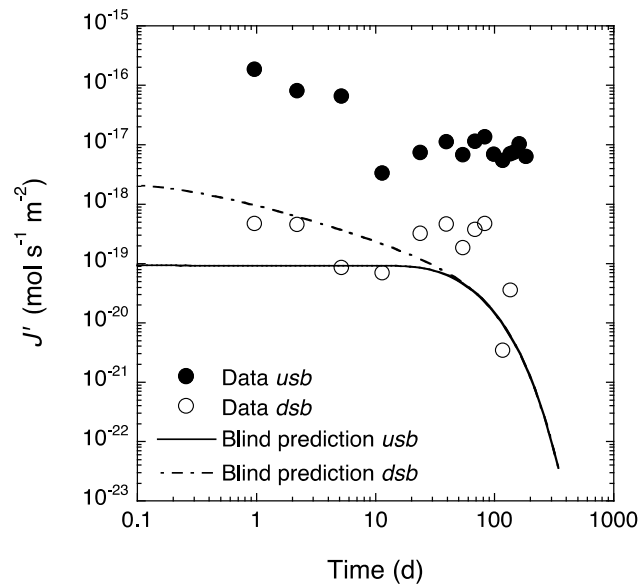
Fig. A69b: Out-diffusion data of experiment 1032_1A measured after through-diffusion.

The fit curves were obtained using the parameters from through-diffusion.
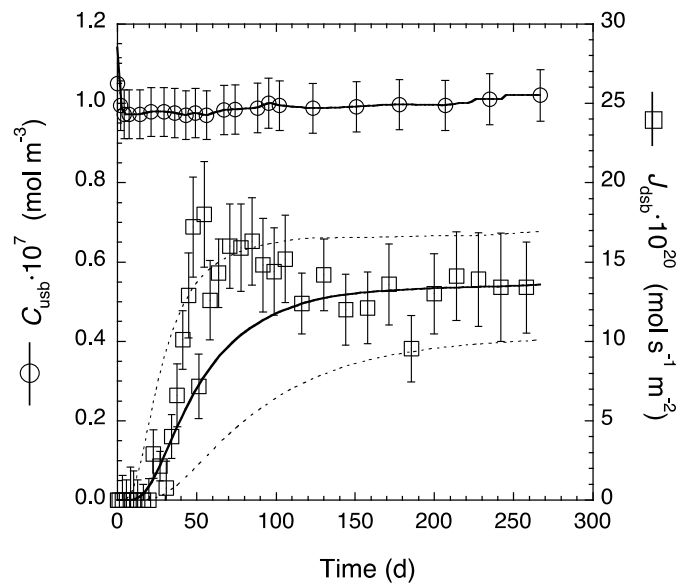
Fig. A70a: Flux at the zero-concentration boundary and reservoir concentration of $^{35}SO_4^{2-}$ in through-diffusion in Na-*mom* at ρ_{bd} = 1954 kg m^{-3} and 0.1 M NaClO$_4$ external salt concentration (experiment 1032_1B, *cf.* Tab. 3.15).
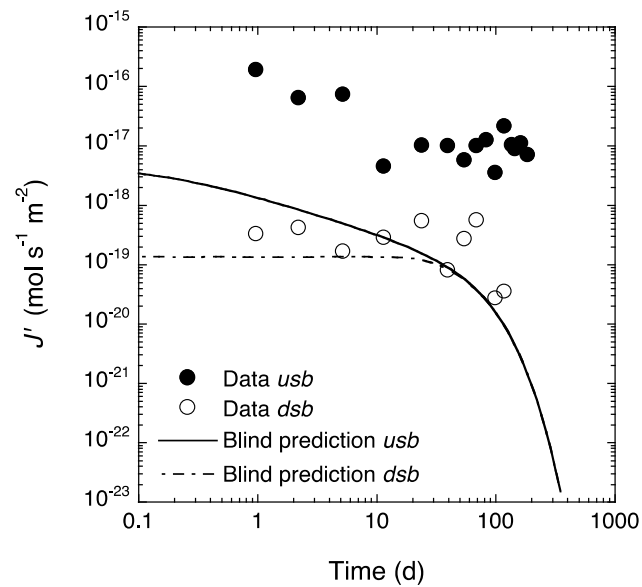
Fig. A70b: Tracer profile data of experiment 1032_1B measured at the end of through-diffusion.
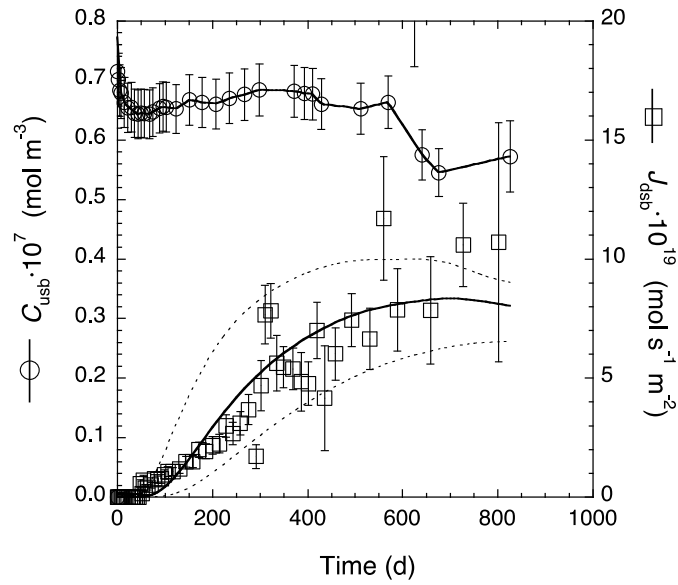
Fig. A71:   Flux at the zero-concentration boundary and reservoir concentration of $^{35}SO_4^{2-}$ in through-diffusion in Na-*mom* at ρ_{bd} = 1945 kg m^{-3} and 0.5 M NaClO$_4$ external salt concentration (experiment 1032_2A, *cf.* Tab. 3.15).
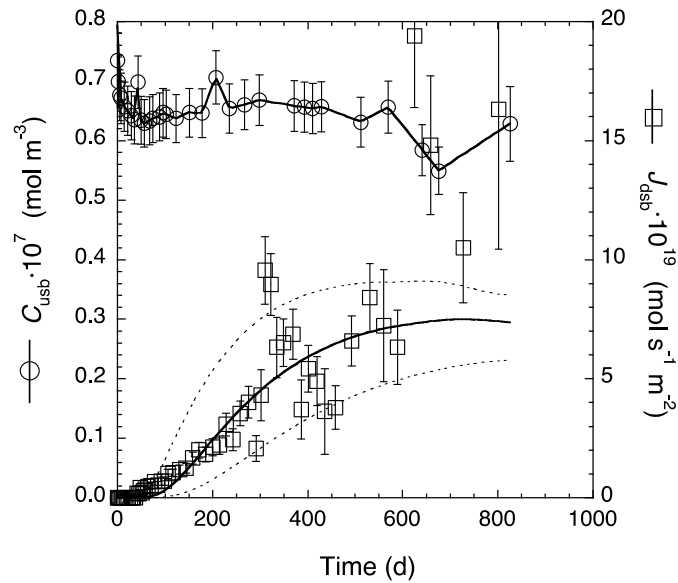
Fig. A72:   Flux at the zero-concentration boundary and reservoir concentration of $^{35}SO_4^{2-}$ in through-diffusion in Na-*mom* at ρ_{bd} = 1951 kg m^{-3} and 0.5 M NaClO$_4$ external salt concentration (experiment 1032_2B, *cf.* Tab. 3.15).
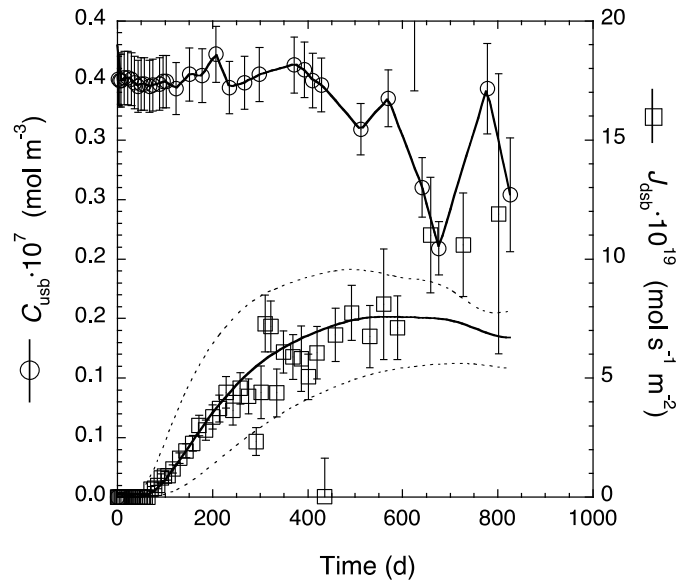
Fig. A73:   Flux at the zero-concentration boundary and reservoir concentration of $^{35}SO_4^{2-}$ in through-diffusion in Na-*mom* at ρ_{bd} = 1962 kg m^{-3} and 1.0 M NaClO$_4$ external salt concentration (experiment 1032_3A, *cf.* Tab. 3.15).
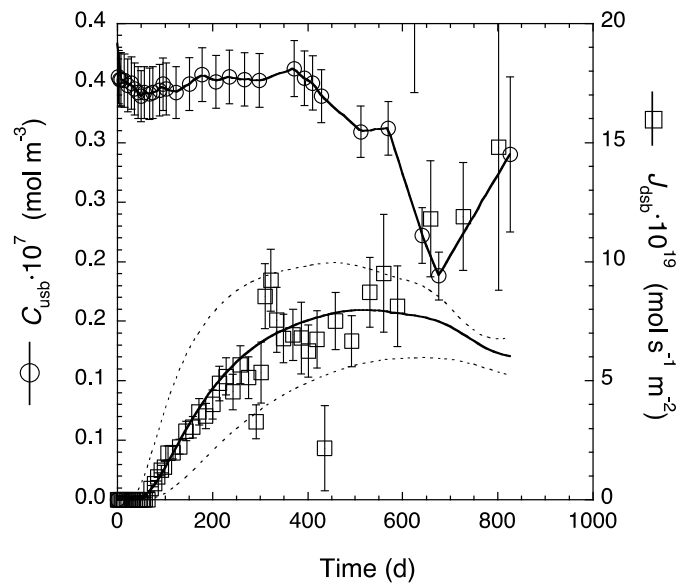
Fig. A74:   Flux at the zero-concentration boundary and reservoir concentration of $^{35}SO_4^{2-}$ in through-diffusion in Na-*mom* at ρ_{bd} = 1950 kg m^{-3} and 1.0 M NaClO$_4$ external salt concentration (experiment 1032_3B, *cf.* Tab. 3.15).

A.11   Through- and out-diffusion of $^{75}SeO_4^{2-}$

Fig. A75a: Flux at the zero-concentration boundary and reservoir concentration of $^{75}SeO_4^{2-}$ in through-diffusion in Na-*mom* at $\rho_{bd} = 1994$ kg m^{-3} and 0.1 M NaClO$_4$ external salt concentration (experiment 1059_1A, *cf.* Tab. 3.16).

Fig. A75b: Out-diffusion data of experiment 1059_1A measured after through-diffusion.

The fit curves were obtained using the parameters from through-diffusion.

Fig. A76a: Flux at the zero-concentration boundary and reservoir concentration of $^{75}SeO_4^{2-}$ in through-diffusion in Na-*mom* at ρ_{bd} = 1989 kg m^{-3} and 0.1 M NaClO$_4$ external salt concentration (experiment 1059_1B, *cf.* Tab. 3.16).

Fig. A76b: Tracer profile data of experiment 1059_1B measured at the end of through-diffusion. The fit curves were obtained using the parameters from through-diffusion.

Fig. A77a: Flux at the zero-concentration boundary and reservoir concentration of $^{75}SeO_4^{2-}$ in through-diffusion in Na-*mom* at ρ_{bd} = 1945 kg m^{-3} and 0.5 M NaClO$_4$ external salt concentration (experiment 1059_2A, *cf.* Tab. 3.16).

Fig. A77b: Tracer profile data of experiment 1059_2A measured at the end of through-diffusion. The fit curves were obtained using the parameters from through-diffusion.

Fig. A78a: Flux at the zero-concentration boundary and reservoir concentration of $^{75}SeO_4^{2-}$ in through-diffusion in Na-*mom* at ρ_{bd} = 1951 kg m^{-3} and 0.5 M NaClO$_4$ external salt concentration (experiment 1059_2B, *cf.* Tab. 3.16).

Fig. A78b: Tracer profile data of experiment 1059_2B measured at the end of through-diffusion. The fit curves were obtained using the parameters from through-diffusion.

Fig. A79a: Flux at the zero-concentration boundary and reservoir concentration of $^{75}SeO_4^{2-}$ in through-diffusion in Na-*mom* at ρ_{bd} = 1962 kg m^{-3} and 1.0 M NaClO$_4$ external salt concentration (experiment 1059_3A, *cf.* Tab. 3.16).

Fig. A79b: Tracer profile data of experiment 1059_3A measured at the end of through-diffusion. The fit curves were obtained using the parameters from through-diffusion.

Fig. A80a: Flux at the zero-concentration boundary and reservoir concentration of $^{75}SeO_4^{2-}$ in through-diffusion in Na-*mom* at $\rho_{bd} = 1950$ kg m^{-3} and 1.0 M NaClO$_4$ external salt concentration (experiment 1059_3B, *cf.* Tab. 3.16).

Fig. A80b: Tracer profile data of experiment 1059_3B measured at the end of through-diffusion. The fit curves were obtained using the parameters from through-diffusion.

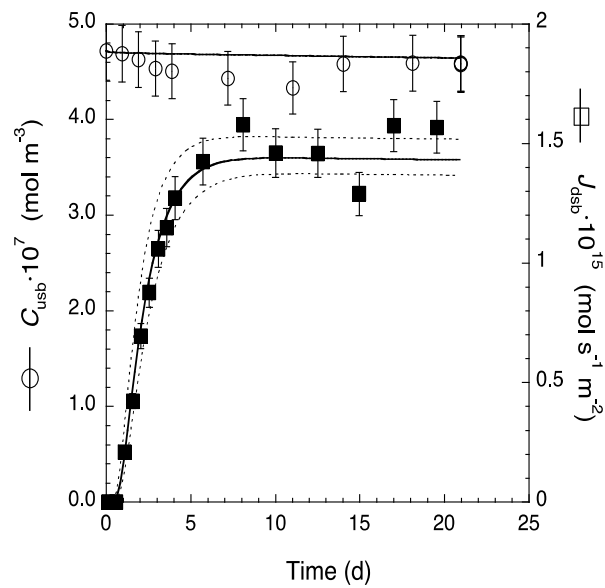# B   Appendix: Experimental data for Bentonite

B.1   Diffusion of HTO
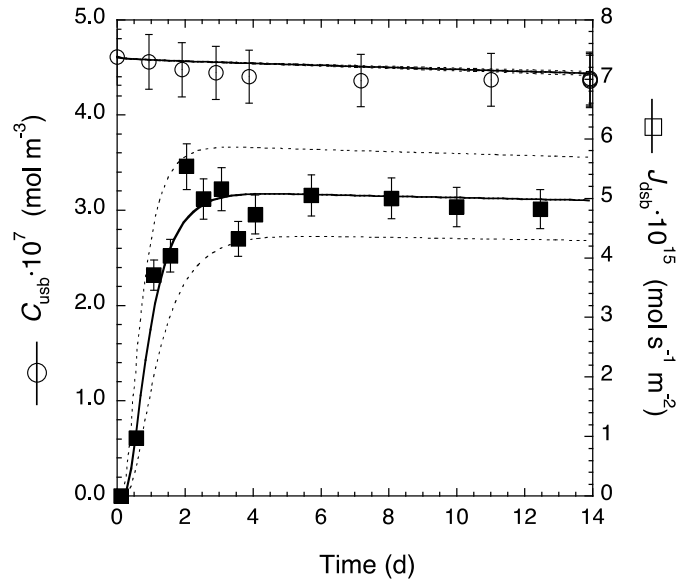
Fig. B1a: Flux at the zero-concentration boundary and reservoir concentration of HTO through-diffusion in Volclay at ρ_{bd} = 1306 kg m^{-3} and BPW1300 as the background electrolyte solution (experiment 12001BEN_13A, *cf.* Tab. 4.1).
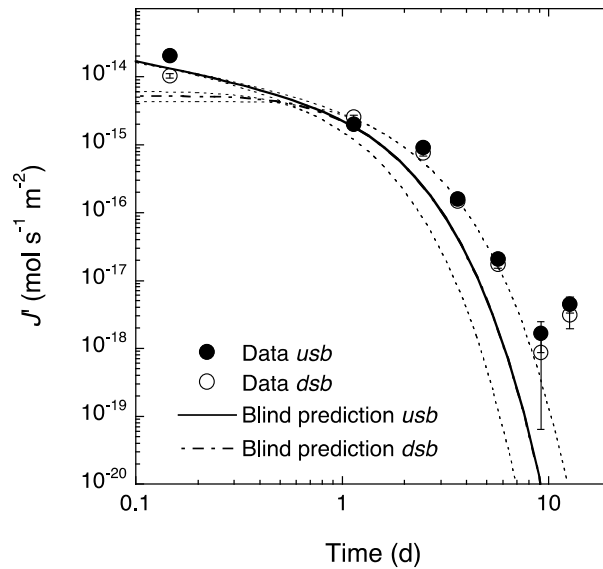
Fig. B1b: Out-diffusion of HTO from Volclay at ρ_{bd} = 1306 kg m^{-3} and BPW1300 as the background electrolyte solution (experiment 12001BEN_13A, *cf.* Tab. 4.1).

The fit curves were obtained by using the best-fit parameter values from through-diffusion.
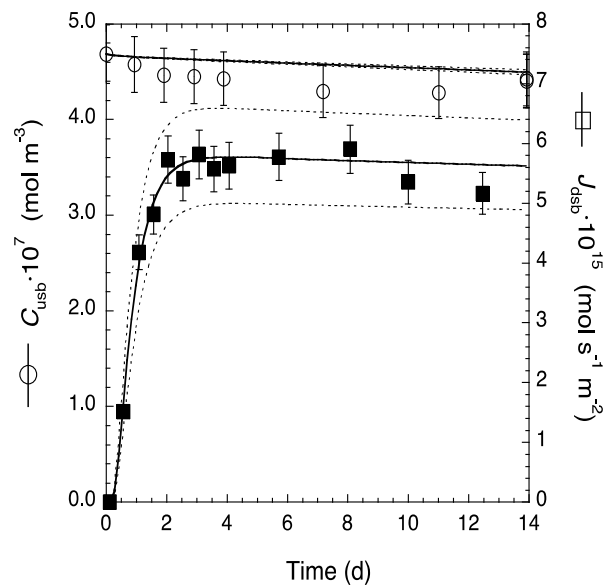
Fig. B2a: Flux at the zero-concentration boundary and reservoir concentration of HTO through-diffusion in Volclay at ρ_{bd} = 1320 kg m^{-3} and 0.3 M NaClO$_4$ as the background electrolyte solution (experiment 12001BEN_13B, *cf.* Tab. 4.1).
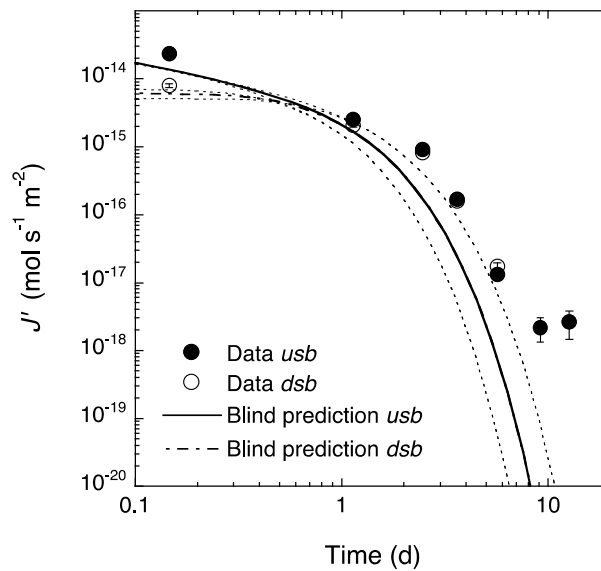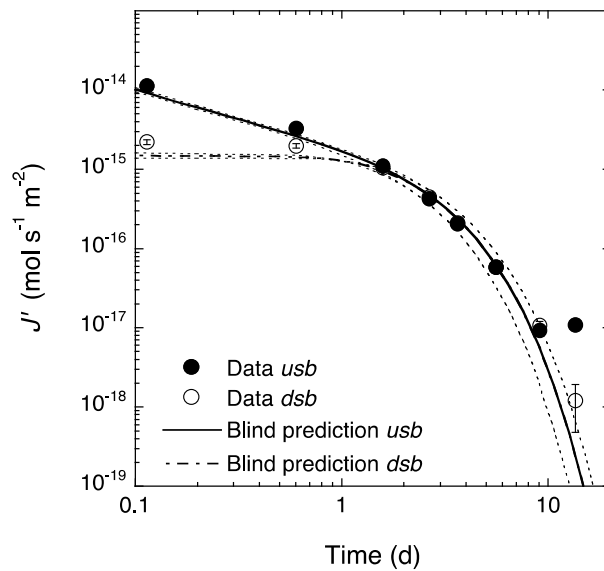

Fig. B2b: Out-diffusion of HTO from Volclay at ρ_{bd} = 1320 kg m^{-3} and 0.3 M NaClO$_4$ as the background electrolyte solution (experiment 12001BEN_13B, *cf.* Tab. 4.1).

The fit curves were obtained by using the best-fit parameter values from through-diffusion.
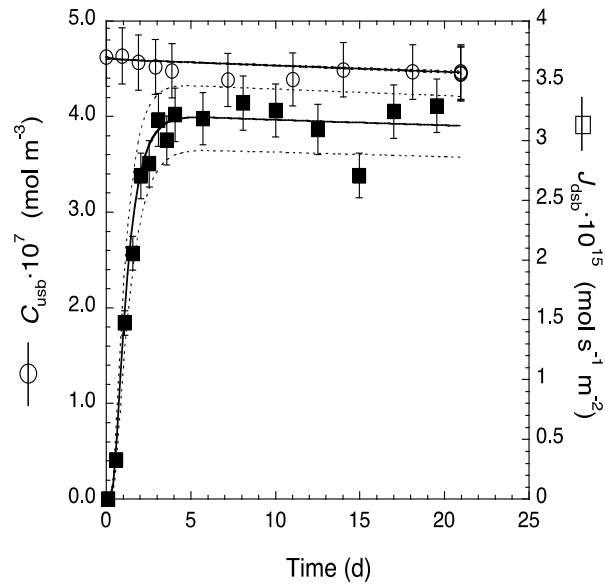
Fig. B3a: Flux at the zero-concentration boundary and reservoir concentration of HTO through-diffusion in Volclay at $\rho_{bd} = 1598$ kg m^{-3} and BPW1600 as the background electrolyte solution (experiment 12001BEN_16A, *cf.* Tab. 4.1).
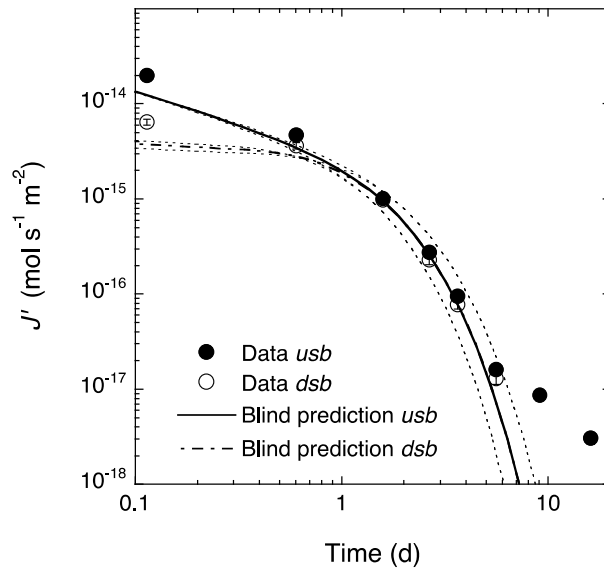

Fig. B3b: Out-diffusion of HTO from Volclay at $\rho_{bd} = 1598$ kg m^{-3} and BPW1600 as the background electrolyte solution (experiment 12001BEN_16A, *cf.* Tab. 4.1).

The fit curves were obtained by using the best-fit parameter values from through-diffusion.
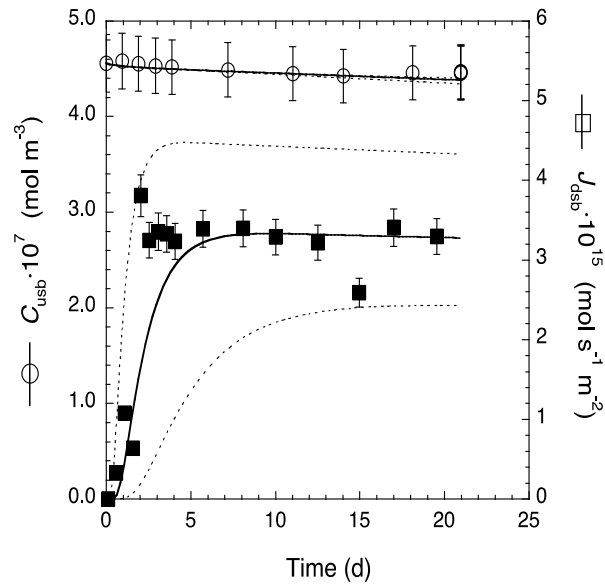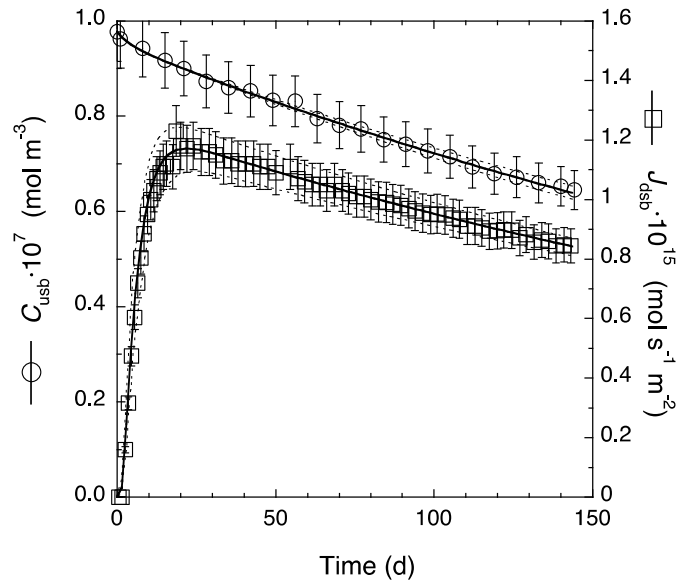
Fig. B4a: Flux at the zero-concentration boundary and reservoir concentration of HTO through-diffusion in Volclay at ρ_{bd} = 1603 kg m^{-3} and 0.01 M NaClO$_4$ as the background electrolyte solution (experiment 12001BEN_16B, *cf.* Tab. 4.1).
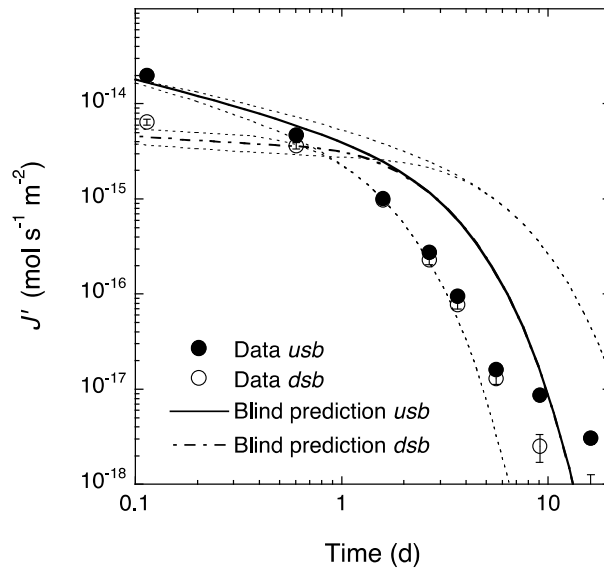
Fig. B4b: Out-diffusion of HTO from Volclay at ρ_{bd} = 1603 kg m^{-3} and 0.01 M NaClO$_4$ as the background electrolyte solution (experiment 12001BEN_16B, *cf.* Tab. 4.1).

The fit curves were obtained by using the best-fit parameter values from through-diffusion.
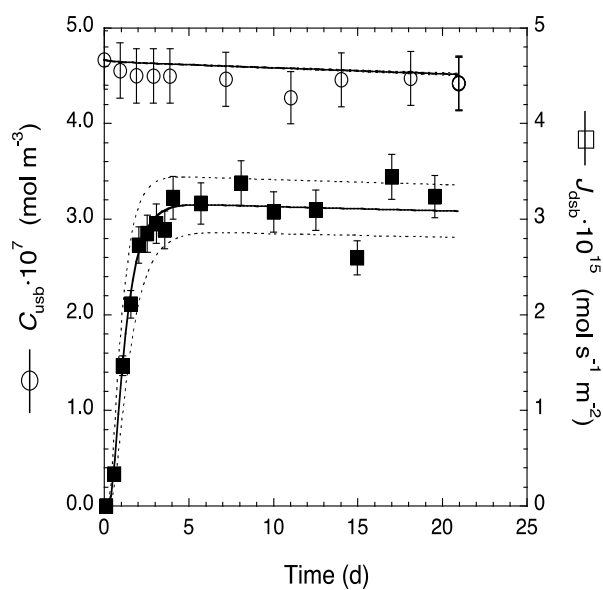
Fig. B5a: Flux at the zero-concentration boundary and reservoir concentration of HTO through-diffusion in Volclay at ρ_{bd} = 1613 kg m^{-3} and 0.3 M NaClO$_4$ as the background electrolyte solution (experiment 12001BEN_16C, *cf.* Tab. 4.1).
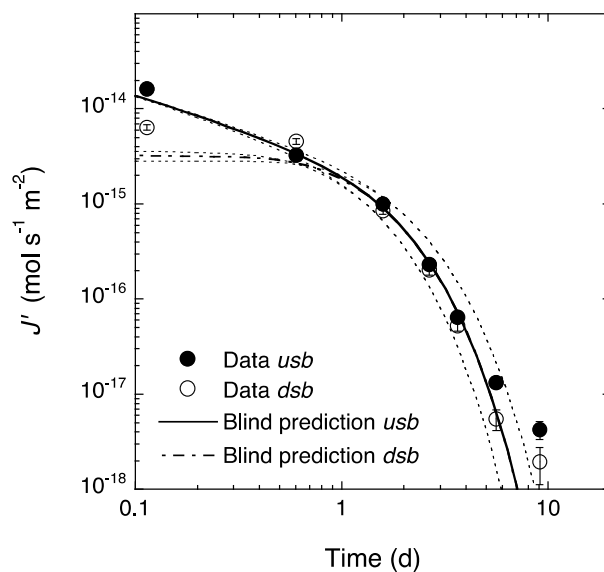

Fig. B5b: Out-diffusion of HTO from Volclay at ρ_{bd} = 1613 kg m^{-3} and 0.3 M NaClO$_4$ as the background electrolyte solution (experiment 12001BEN_16C, *cf.* Tab. 4.1).

The fit curves were obtained by using the best-fit parameter values from through-diffusion.
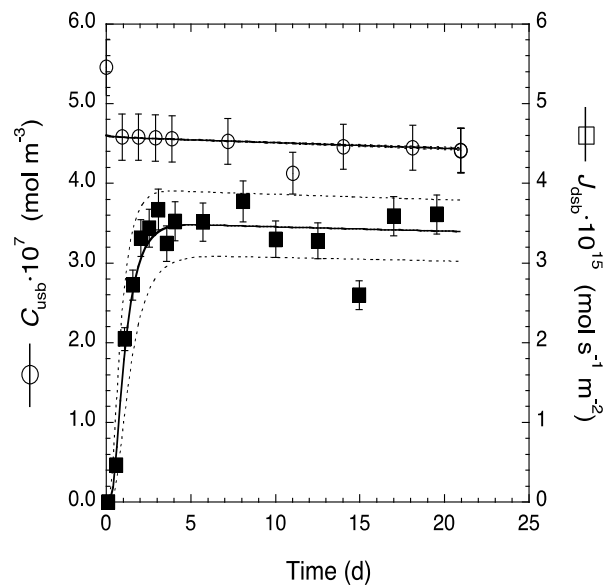
Fig. B6a: Flux at the zero-concentration boundary and reservoir concentration of HTO through-diffusion in Volclay at ρ_{bd} = 1602 kg m^{-3} and 1.0 M NaClO$_4$ as the background electrolyte solution (experiment 12001BEN_16D, *cf.* Tab. 4.1).
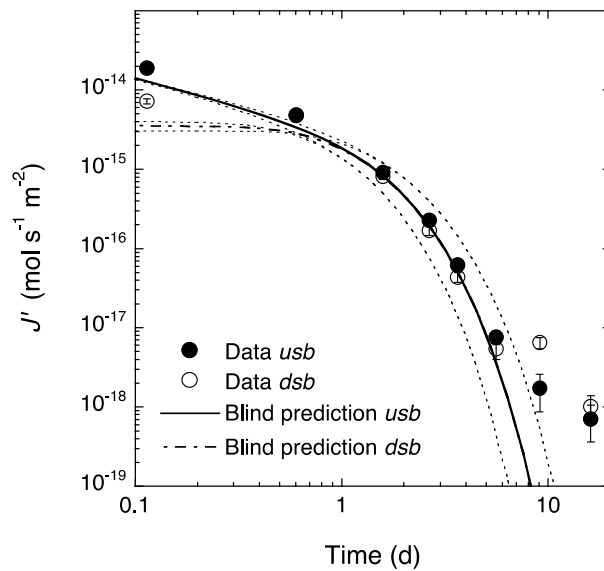

Fig. B6b: Out-diffusion of HTO from Volclay at ρ_{bd} = 1602 kg m^{-3} and 1.0 M NaClO$_4$ as the background electrolyte solution (experiment 12001BEN_16D, *cf.* Tab. 4.1).

The fit curves were obtained by using the best-fit parameter values from through-diffusion.
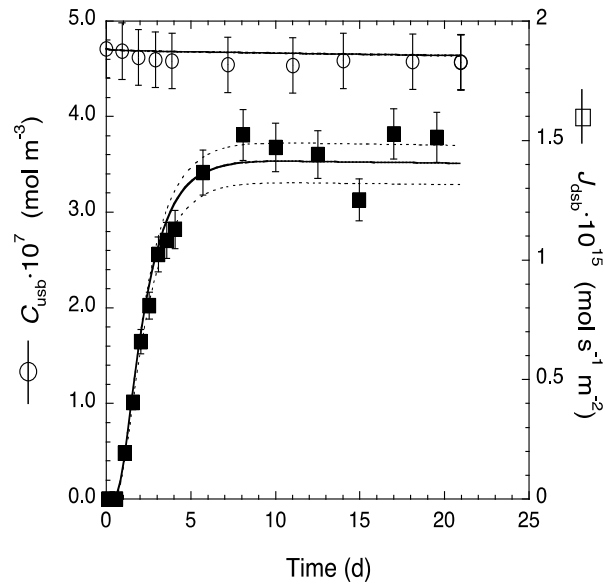
Fig. B7a: Flux at the zero-concentration boundary and reservoir concentration of HTO through-diffusion in Volclay at $\rho_{bd} = 1911$ kg m^{-3} and BPW1900 as the background electrolyte solution (experiment 12001BEN_19A, *cf.* Tab. 4.1).
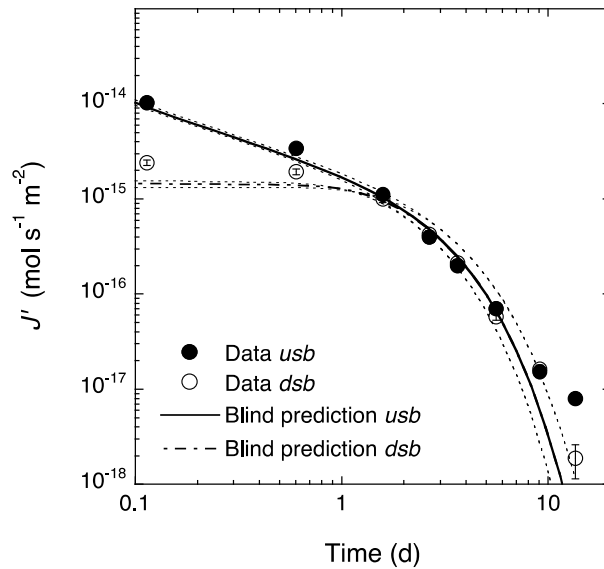
Fig. B7b: Out-diffusion of HTO from Volclay at $\rho_{bd} = 1911$ kg m^{-3} and BPW1900 as the background electrolyte solution (experiment 12001BEN_19A, *cf.* Tab. 4.1).

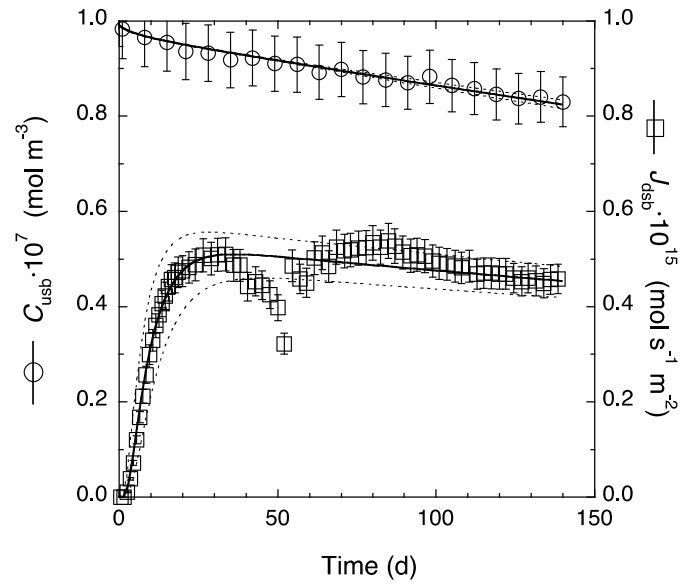The fit curves were obtained by using the best-fit parameter values from through-diffusion.

Fig. B8a:　Flux at the zero-concentration boundary and reservoir concentration of HTO through-diffusion in Volclay at ρ_{bd} = 1886 kg m^{-3} and 0.3 M NaClO$_4$ as the background electrolyte solution (experiment 12001BEN_19B, *cf.* Tab. 4.1).

Fig. B8b:　Out-diffusion of HTO from Volclay at ρ_{bd} = 1886 kg m^{-3} and 0.3 M NaClO$_4$ as the background electrolyte solution (experiment 12001BEN_19B, *cf.* Tab. 4.1).

The fit curves were obtained by using the best-fit parameter values from through-diffusion.

B.2   Through- and out-diffusion of ^{22}Na$^+$
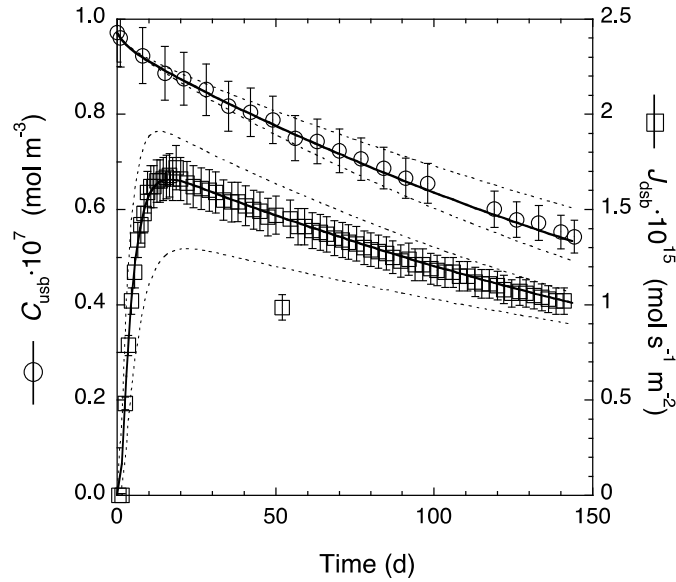
Fig. B9a: Flux at the zero-concentration boundary and reservoir concentration of ^{22}Na$^+$ in through-diffusion in Volclay at ρ_{bd} = 1301 kg m^{-3} and BPW1300 as the background electrolyte (BEN1004_Na13A, *cf.* Tab. 4.2).
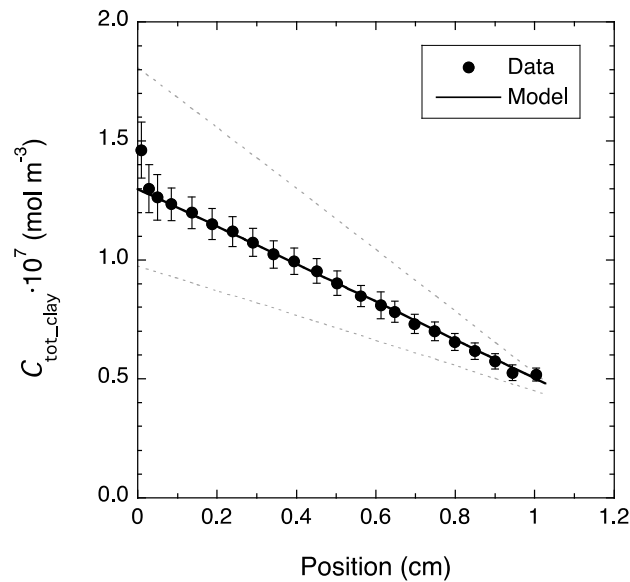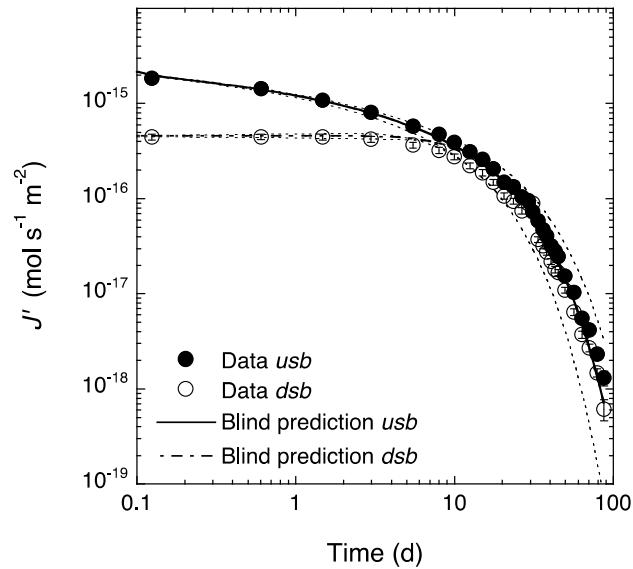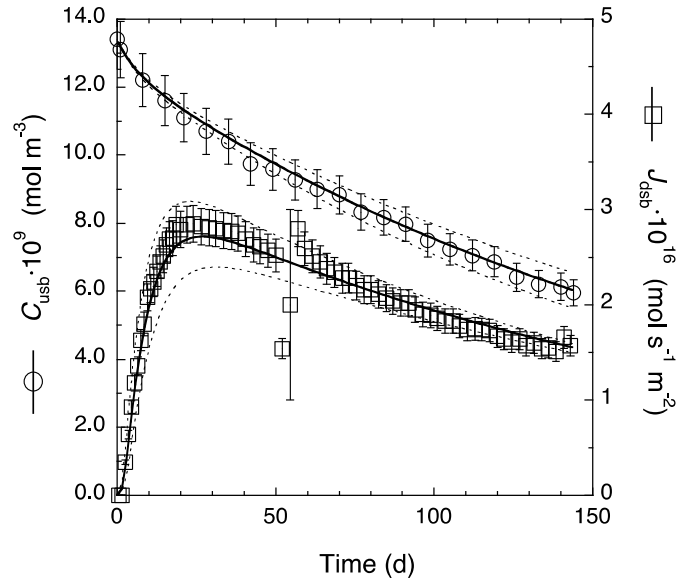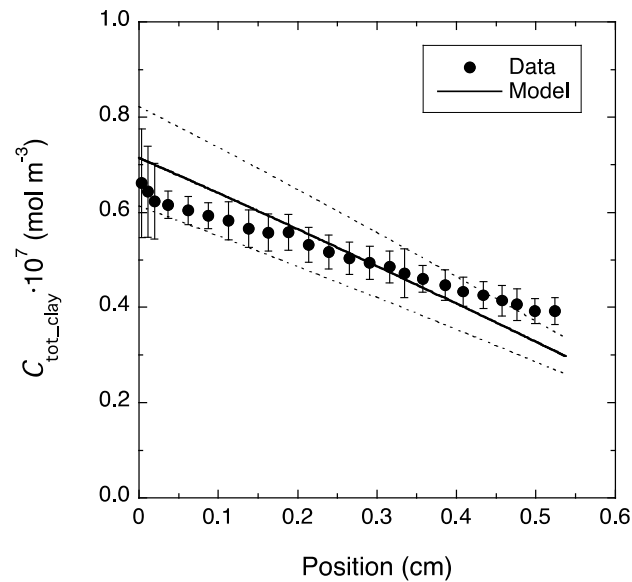

Fig. B9b: Tracer profile data of experiment BEN1004_Na 13A measured at the end of through-diffusion.

The fit curve was obtained by using the best-fit parameter values from through-diffusion.
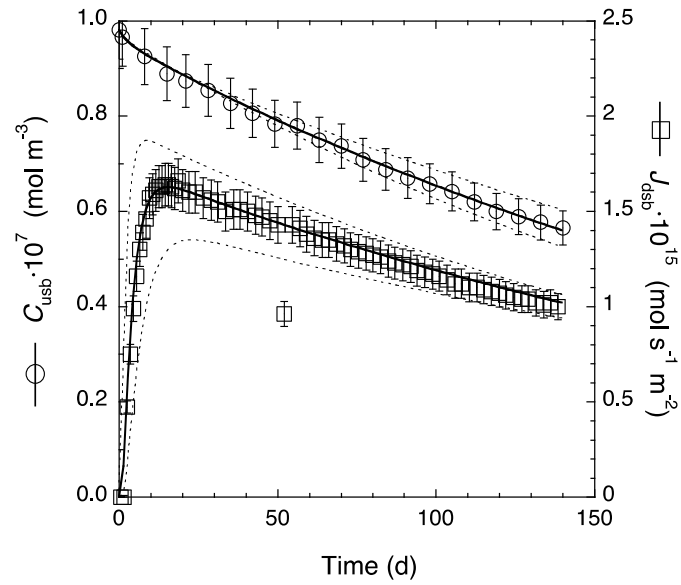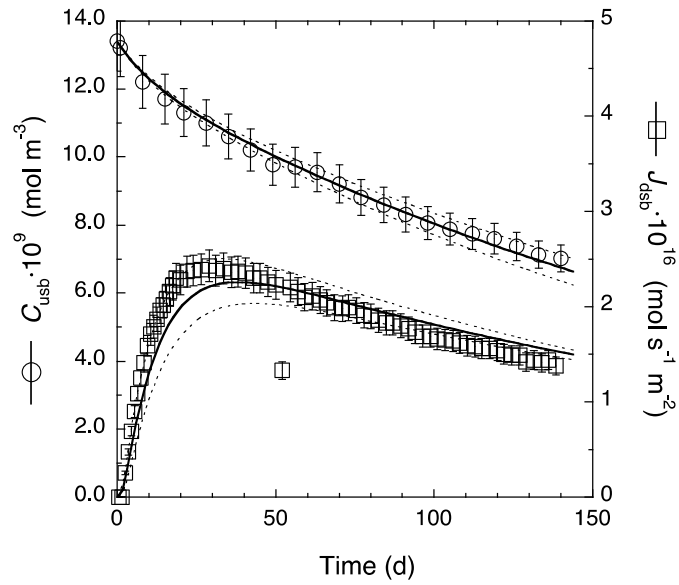
Fig. B10a: Flux at the zero-concentration boundary and reservoir concentration of ^{22}Na$^+$ in through-diffusion in Volclay at $\rho_{bd} = 1302$ kg m^{-3} and BPW1300 as the background electrolyte (experiment BEN1004_Na13B, *cf.* Tab. 4.2).
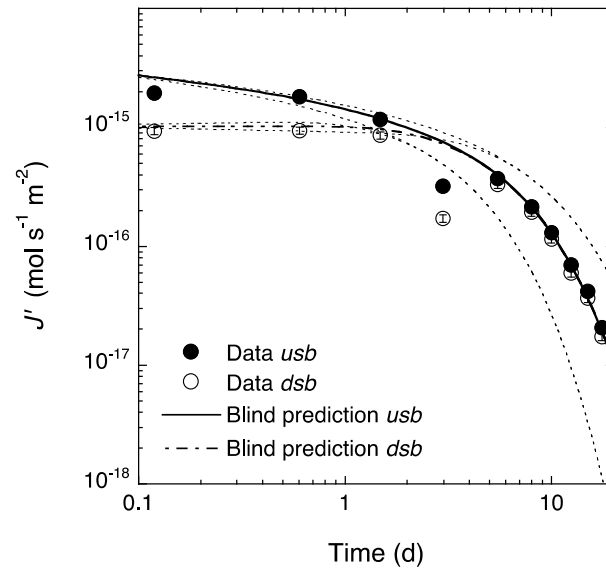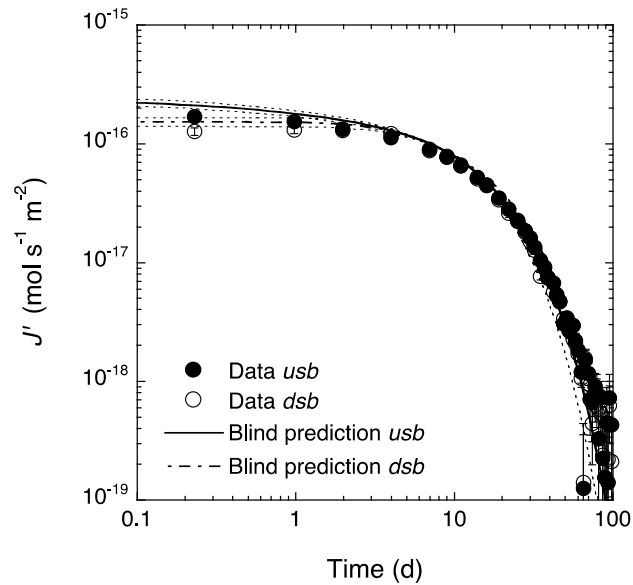

Fig. B10b: Out-diffusion data of experiment BEN1004_Na13B measured after through-diffusion.

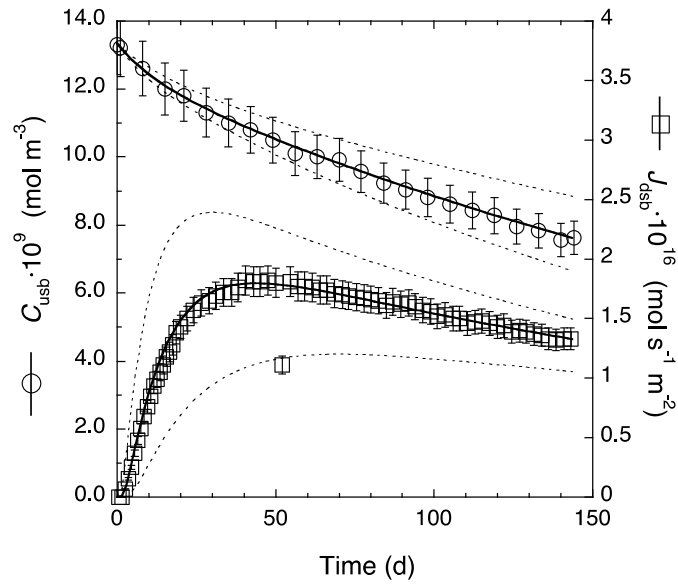The best-fit parameter values were slightly adapted (*cf.* Tab. 4.2) for the fit curves.

Fig. B11a: Flux at the zero-concentration boundary and reservoir concentration of $^{22}Na^+$ in through-diffusion in Volclay at ρ_{bd} = 1595 kg m^{-3} and BPW1600 as the background electrolyte (BEN1004_Na16A, *cf.* Tab. 4.2).
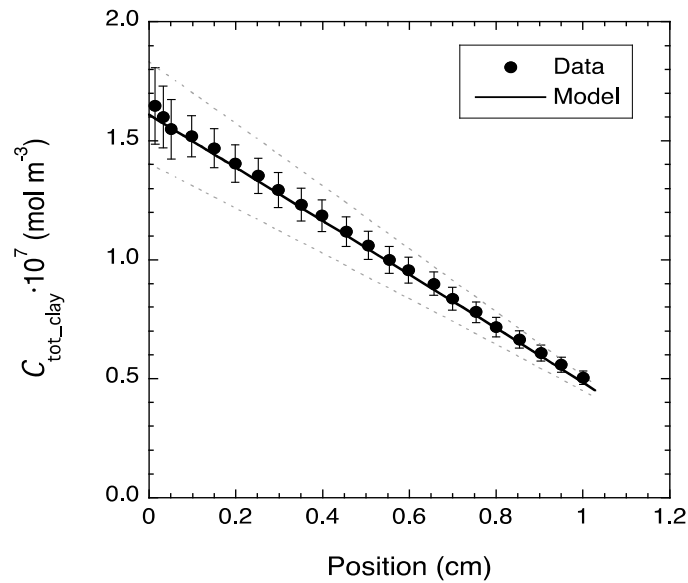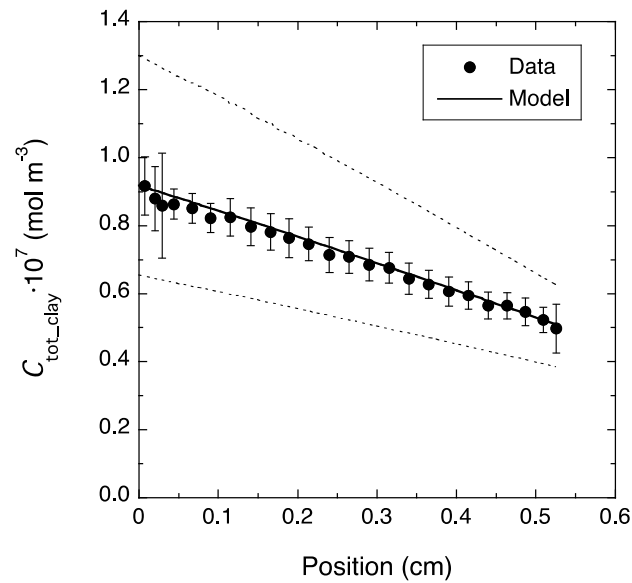

Fig. B11b: Tracer profile data of experiment BEN1004_Na16A measured at the end of through-diffusion.

The fit curve was obtained by using the best-fit parameter values from through-diffusion.
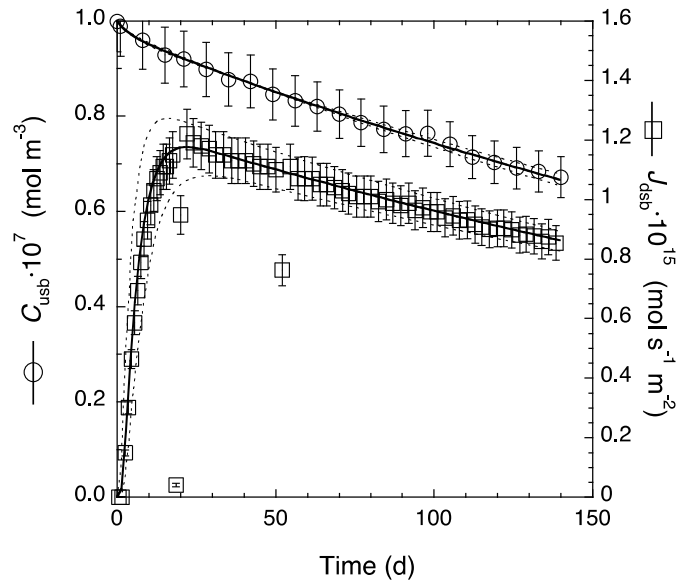
Fig. B12a: Flux at the zero-concentration boundary and reservoir concentration of $^{22}Na^+$ in through-diffusion in Volclay at $\rho_{bd} = 1600$ kg m^{-3} and BPW1600 as the background electrolyte (BEN1004_Na16B, *cf.* Tab. 4.2).
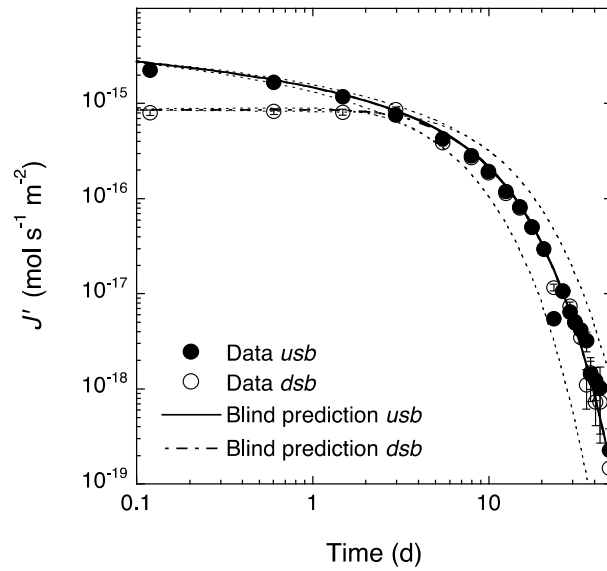
Fig. B12b: Out-diffusion data of experiment BEN1004_Na16B measured after through-diffusion.

The best-fit parameter values were slightly adapted (*cf.* Tab. 4.2) for the fit curves.
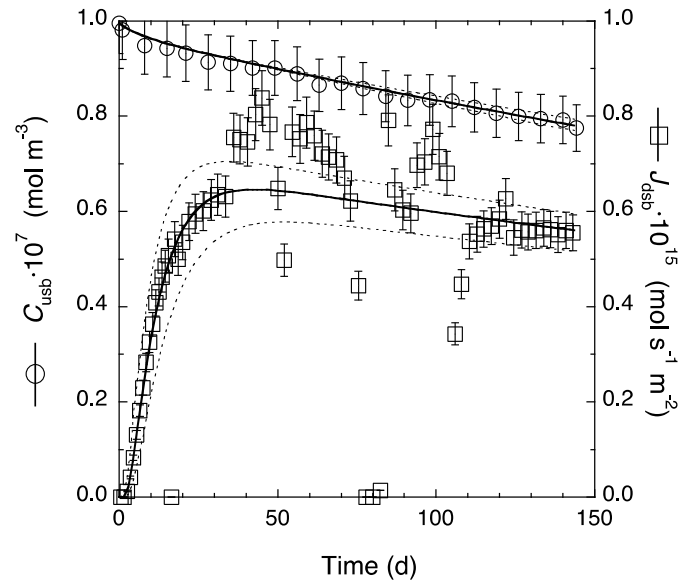
Fig. B13a: Flux at the zero-concentration boundary and reservoir concentration of $^{22}Na^+$ in through-diffusion in Volclay at $\rho_{bd} = 1905$ kg m^{-3} and BPW1900 as the background electrolyte (BEN1004_Na19A, *cf.* Tab. 4.2).
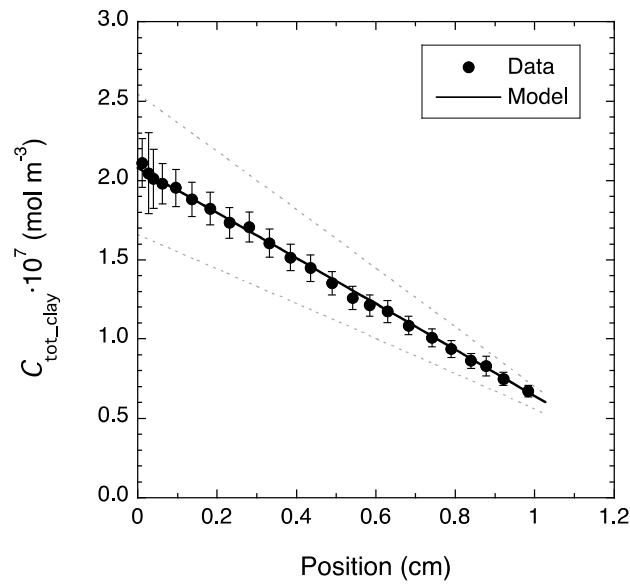
Fig. B13b: Tracer profile data of experiment BEN1004_Na19A measured at the end of through-diffusion.

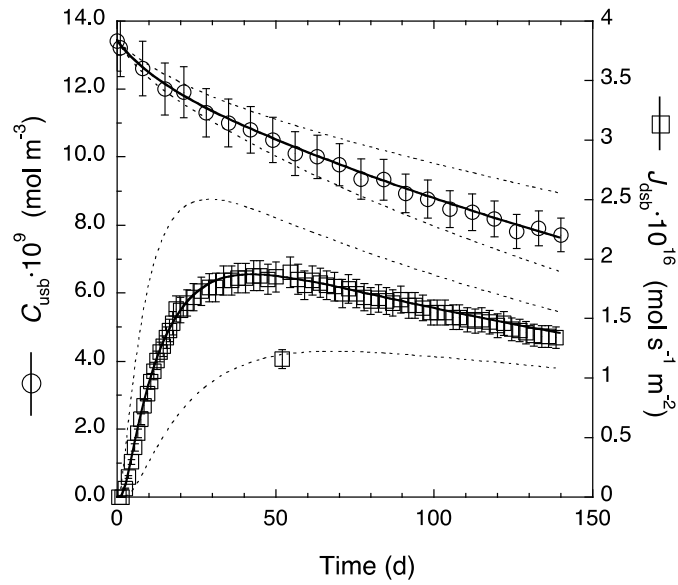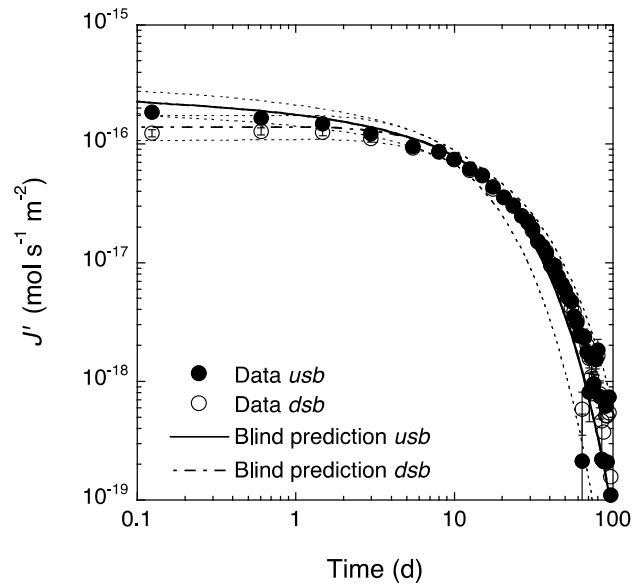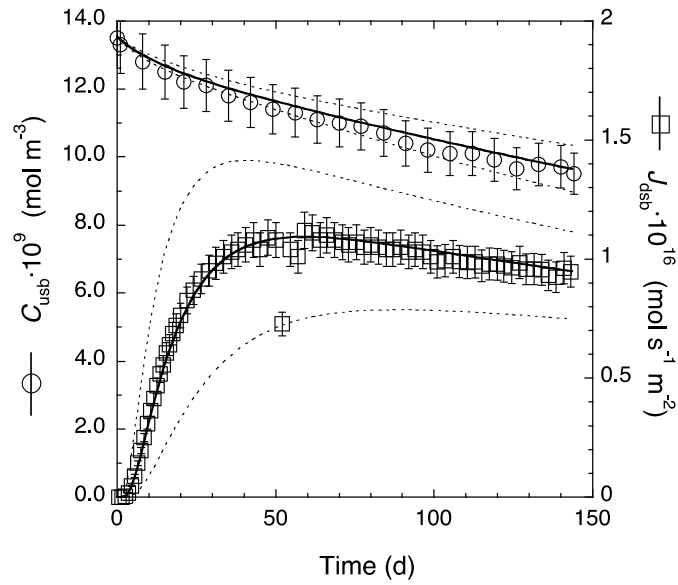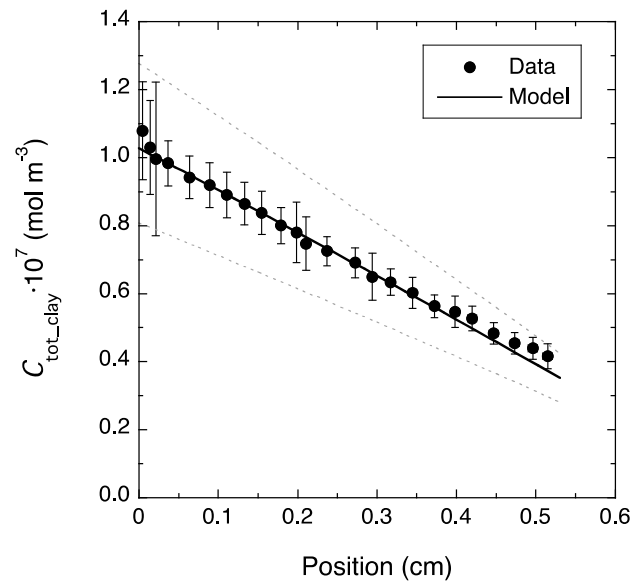The fit curve was obtained by using the best-fit parameter values from through-diffusion.

Fig. B14a: Flux at the zero-concentration boundary and reservoir concentration of $^{22}Na^+$ in through-diffusion in Volclay at $\rho_{bd} = 1904$ kg m^{-3} and BPW1900 as the background electrolyte (BEN1004_Na19B, *cf.* Tab. 4.2).

Fig. B14b: Out-diffusion data of experiment BEN1004_Na19B measured after through-diffusion.

The best-fit parameter values were slightly adapted (*cf.* Tab. 4.2) for the fit curves.
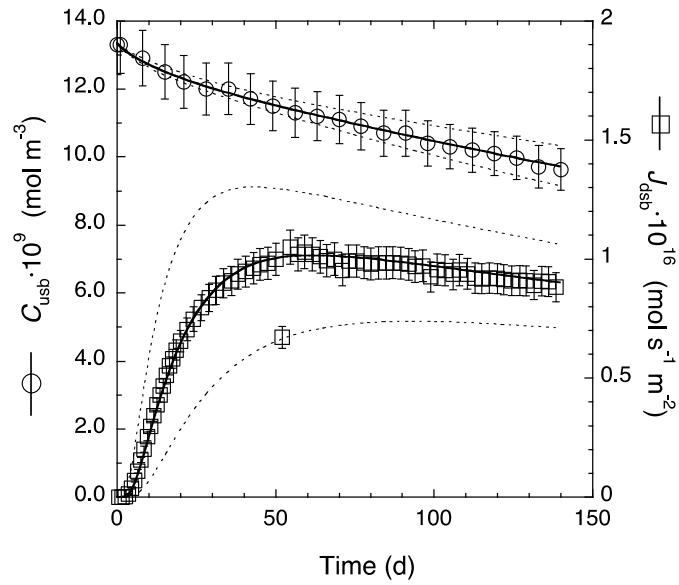
B.3 Through- and out-diffusion of ^{85}Sr^{2+}

Fig. B15a: Flux at the zero-concentration boundary and reservoir concentration of ^{85}Sr^{2+} in through-diffusion in Volclay at $\rho_{bd} = 1295$ kg m^{-3} and BPW1300 as the background electrolyte (BEN1004_Sr13A, *cf.* Tab. 4.3).

Fig. B15b: Tracer profile data of experiment BEN1004_Sr13A measured at the end of through-diffusion.

The fit curve was obtained from a simultaneous fitting of the reservoir, flux and profile data.

Fig. B16a: Flux at the zero-concentration boundary and reservoir concentration of $^{85}Sr^{2+}$ in through-diffusion in Volclay at ρ_{bd} = 1310 kg m^{-3} and BPW1300 as the background electrolyte (BEN1004_Sr13B, *cf.* Tab. 4.3).

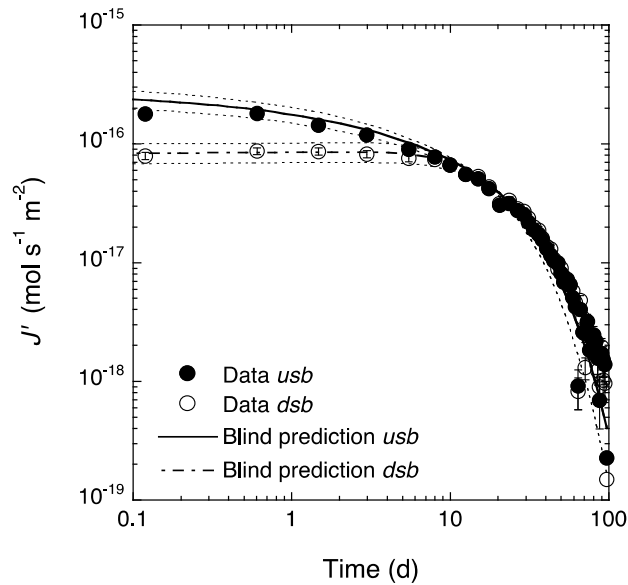Fig. B16b: Out-diffusion data of experiment BEN1004_Sr13B measured after through-diffusion.

The fit curve was obtained from a simultaneous fitting of the reservoir concentrations, the through-diffusion and out-diffusion fluxes.
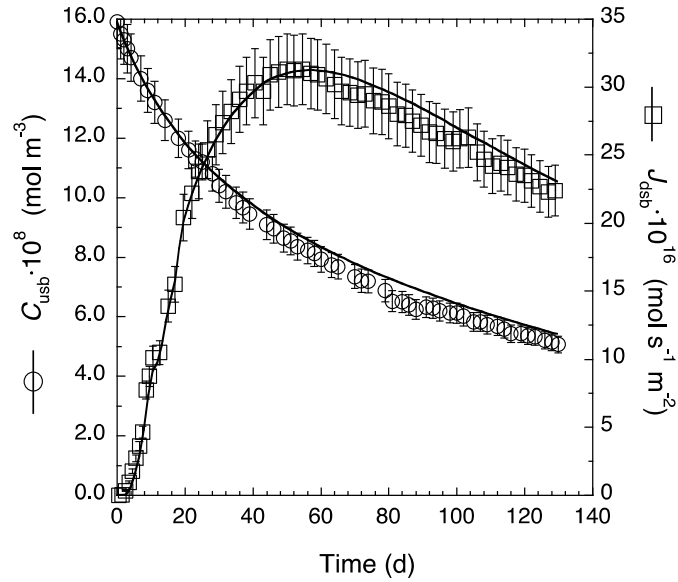
Fig. B17a: Flux at the zero-concentration boundary and reservoir concentration of $^{85}Sr^{2+}$ in through-diffusion in Volclay at ρ_{bd} = 1619 kg m^{-3} and BPW1600 as the background electrolyte (BEN1004_Sr16A, *cf.* Tab. 4.3).
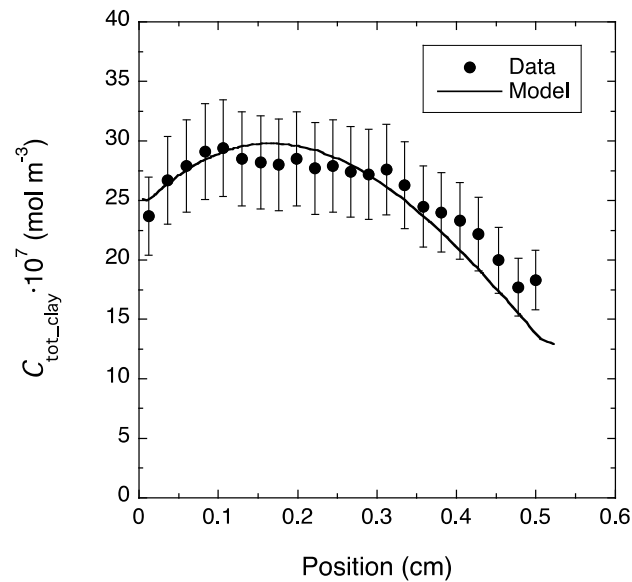

Fig. B17b: Tracer profile data of experiment BEN1004_Sr16A measured at the end of through-diffusion.

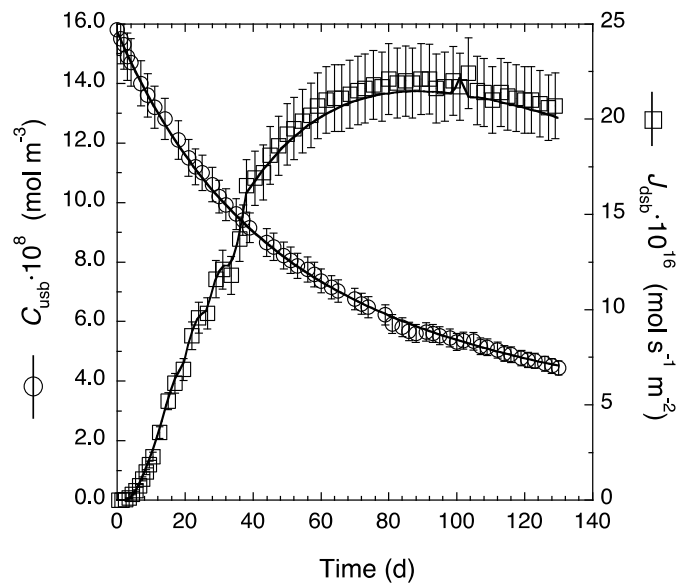The fit curve was obtained by using the best-fit parameter values from through-diffusion.

Fig. B18a: Flux at the zero-concentration boundary and reservoir concentration of $^{85}Sr^{2+}$ in through-diffusion in Volclay at ρ_{bd} = 1611 kg m^{-3} and BPW1600 as the background electrolyte (BEN1004_Sr16B, *cf.* Tab. 4.3).

Fig. B18b: Out-diffusion data of experiment BEN1004_Sr16B measured after through-diffusion.

The fit curve was obtained by using the best-fit parameter values from through-diffusion.

Fig. B19a: Flux at the zero-concentration boundary and reservoir concentration of $^{85}Sr^{2+}$ in through-diffusion in Volclay at ρ_{bd} = 1896 kg m^{-3} and BPW1900 as the background electrolyte (BEN1004_Sr19A, *cf.* Tab. 4.3).
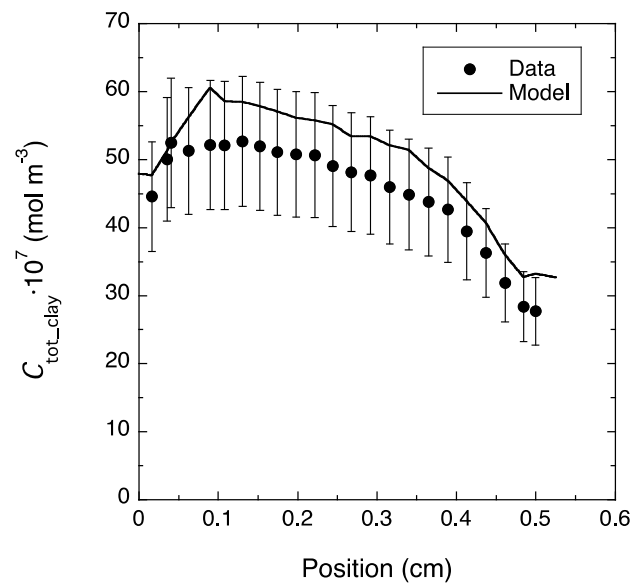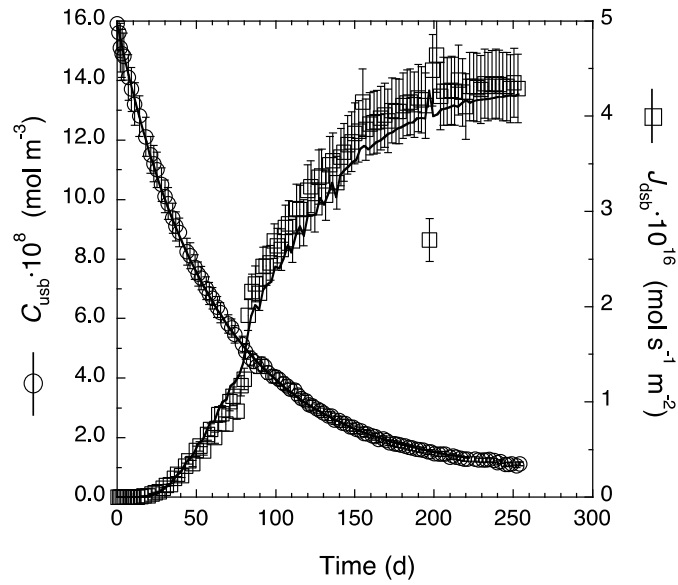

Fig. B19b: Tracer profile data of experiment BEN1004_Sr19A measured at the end of through-diffusion.

The fit curve was obtained by using the best-fit parameter values from through-diffusion.

Fig. B20a: Flux at the zero-concentration boundary and reservoir concentration of $^{85}Sr^{2+}$ in through-diffusion in Volclay at $\rho_{bd} = 1902$ kg m^{-3} and BPW1900 as the background electrolyte (BEN1004_Sr19B, *cf.* Tab. 4.3).

Fig. B20b: Out-diffusion data of experiment BEN1004_Sr19B measured after through-diffusion.

The fit curve was obtained by using the best-fit parameter values from through-diffusion.

B.4   Through-diffusion of $^{134}Cs^+$

Fig. B21a: Flux at the zero-concentration boundary and reservoir concentration of $^{134}Cs^+$ in through-diffusion in Volclay at $\rho_{bd} = 1310$ kg m^{-3} and BPW1300 as the background electrolyte (BEN1006_Cs13B, *cf.* Tab. 4.4).
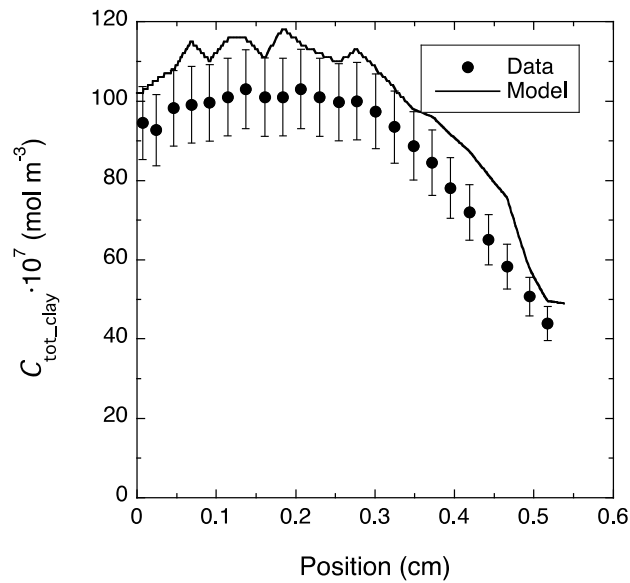

Fig. B21b: Tracer profile data of experiment BEN1006_Cs13B measured at the end of through-diffusion.

The fit curve was obtained from a simultaneous fitting of the reservoir, flux and profile data.

Fig. B22a: Flux at the zero-concentration boundary and reservoir concentration of $^{134}Cs^+$ in through-diffusion in Volclay at $\rho_{bd} = 1611$ kg m^{-3} and BPW1600 as the background electrolyte (BEN1006_Cs16B, *cf.* Tab. 4.4).

Fig. B22b: Tracer profile data of experiment BEN1006_Cs16B measured at the end of through-diffusion.

The fit curve was obtained from a simultaneous fitting of the reservoir, flux and profile data.

Fig. B23a: Flux at the zero-concentration boundary and reservoir concentration of $^{134}Cs^+$ in through-diffusion in Volclay at $\rho_{bd} = 1902$ kg m^{-3} and BPW1900 as the background electrolyte (BEN1006_Cs19B, *cf.* Tab. 4.4).


Fig. B23b: Tracer profile data of experiment BEN1006_Cs19B measured at the end of through-diffusion.

The fit curve was obtained from a simultaneous fitting of the reservoir, flux and profile data.

B.5 Through- and out-diffusion of $^{36}Cl^-$
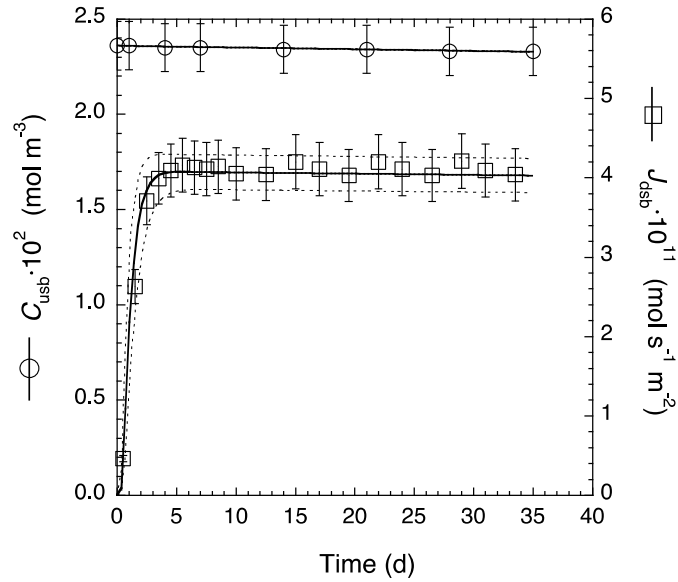
Fig. B24a: Flux at the zero-concentration boundary and reservoir concentration of $^{36}Cl^-$ in through-diffusion in Volclay at $\rho_{bd} = 1302$ kg m^{-3} and BPW1300 as the background electrolyte (BEN1006_13B, *cf.* Tab. 4.5).
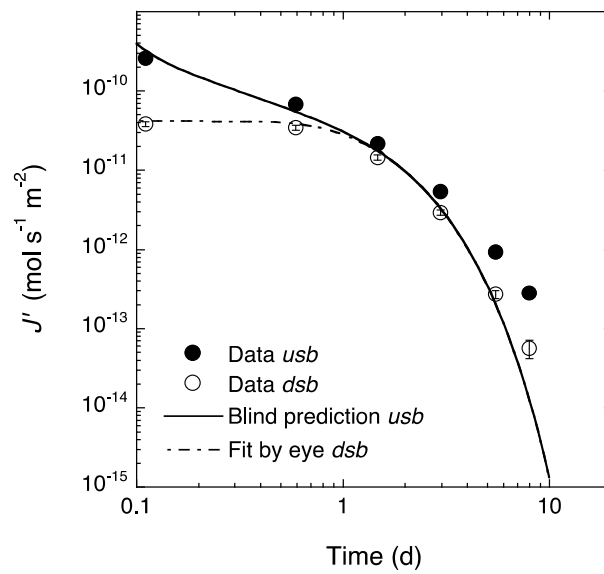
Fig. B24b: Out-diffusion data of experiment BEN1006_13B measured after through-diffusion.

The fit curve was obtained by slightly adapting the best-fit parameter values from through-diffusion.
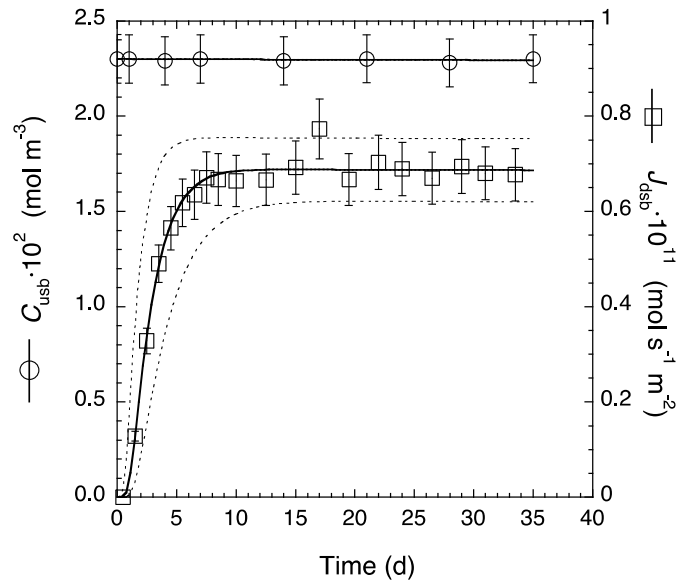
Fig. B25a: Flux at the zero-concentration boundary and reservoir concentration of $^{36}Cl^-$ in through-diffusion in Volclay at $\rho_{bd} = 1600$ kg m^{-3} and BPW1600 as the background electrolyte (BEN1006_16B, *cf.* Tab. 4.5).
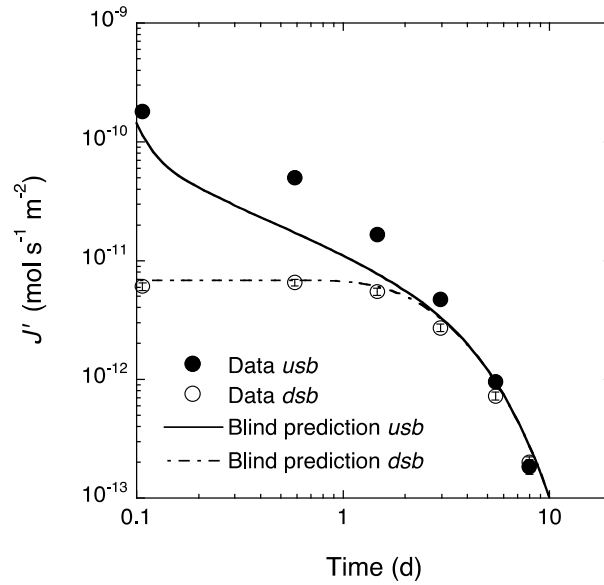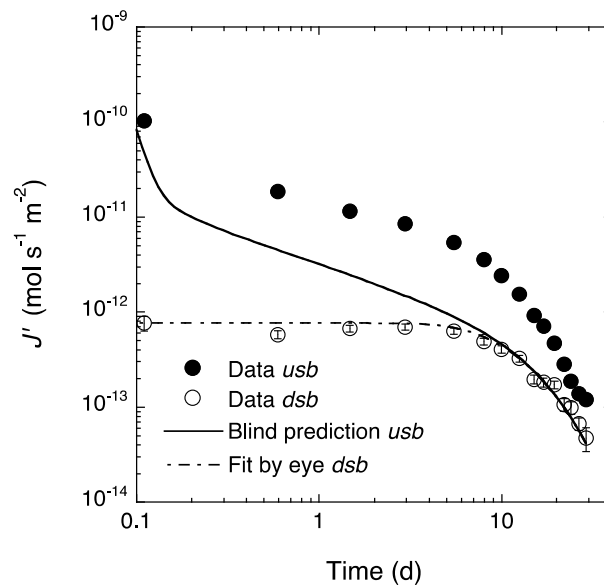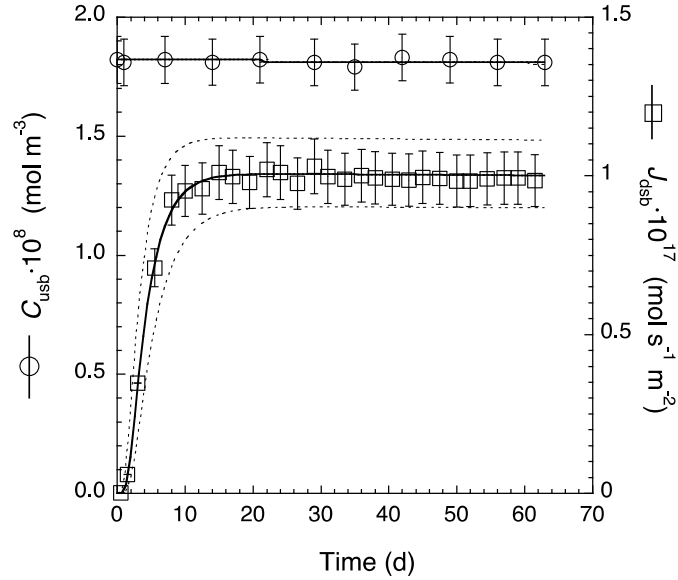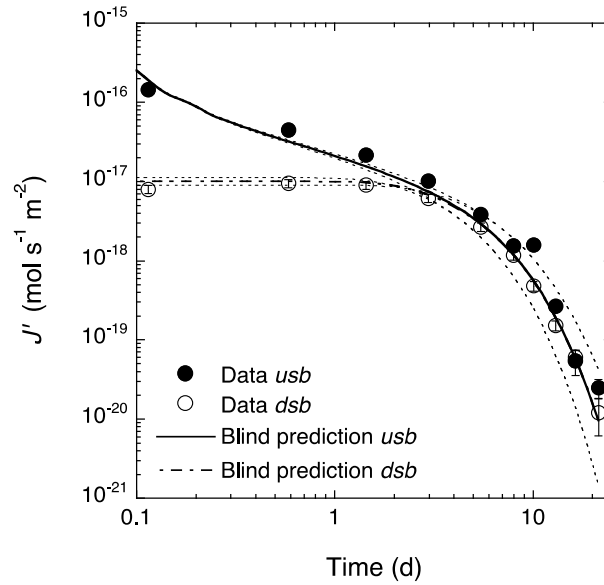

Fig. B25b: Out-diffusion data of experiment BEN1006_16B measured after through-diffusion.

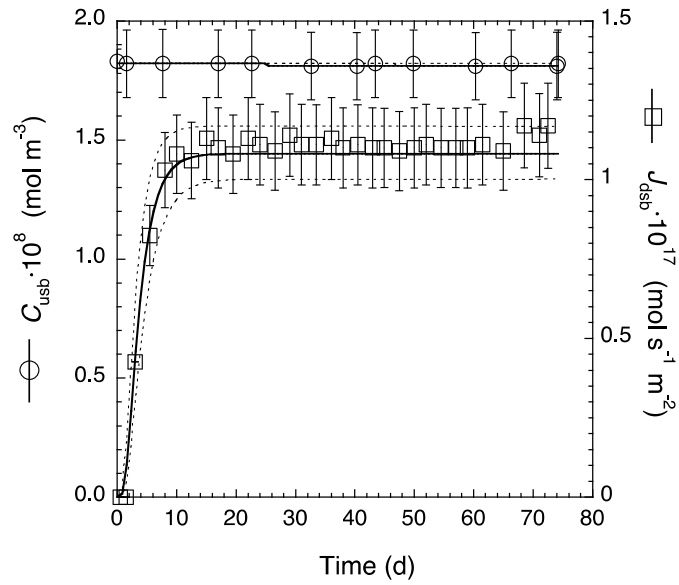The fit curve was obtained by using the best-fit parameter values from through-diffusion.
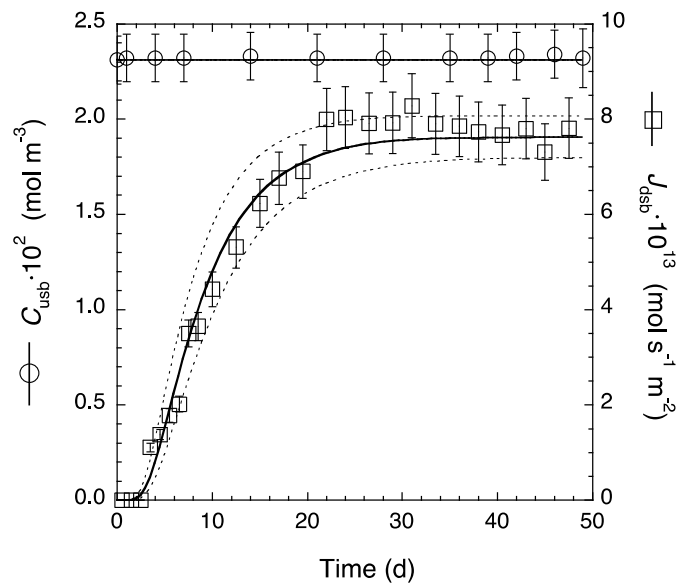
Fig. B26a: Flux at the zero-concentration boundary and reservoir concentration of ^{36}Cl$^-$ in through-diffusion in Volclay at ρ_{bd} = 1904 kg m^{-3} and BPW1900 as the background electrolyte (BEN1006_19B, *cf.* Tab. 4.5).

Fig. B26b: Out-diffusion data of experiment BEN1006_19B measured after through-diffusion.

The fit curve was obtained by using the best-fit parameter values from through-diffusion.

B.6   Through- and out-diffusion of $^{35}SO_4^{2-}$

Fig. B27a: Flux at the zero-concentration boundary and reservoir concentration of $^{35}SO_4^{2-}$ in through-diffusion in Volclay at ρ_{bd} = 1312 kg m^{-3} and BPW1300 as the background electrolyte (BEN1009_13A, *cf.* Tab. 4.6).

Fig. B27b: Out-diffusion data of experiment BEN1009_13A measured after through-diffusion.

The fit curve was obtained from a simultaneous fitting of the reservoir concentrations, the through-diffusion and out-diffusion fluxes.

Fig. B28a: Flux at the zero-concentration boundary and reservoir concentration of $^{35}SO_4^{2-}$ in through-diffusion in Volclay at ρ_{bd} = 1297 kg m^{-3} and BPW1300 as the background electrolyte (BEN1009_13B, *cf.* Tab. 4.6).
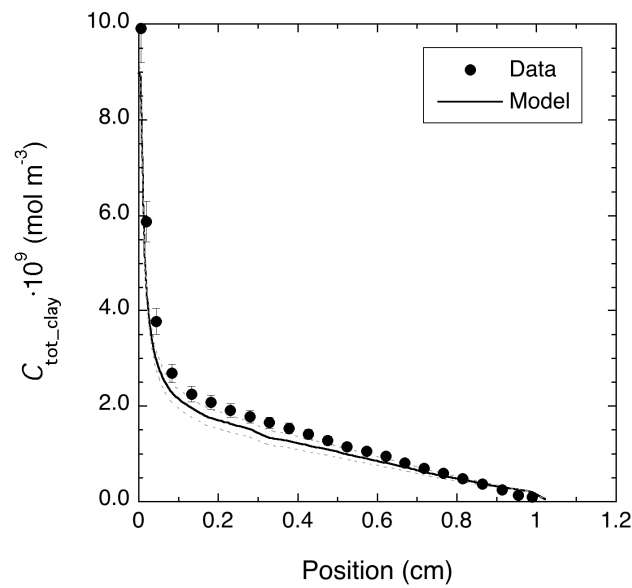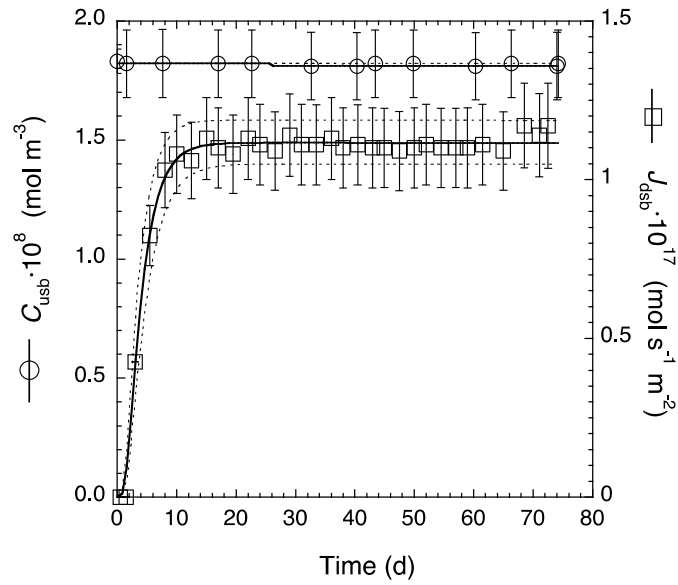
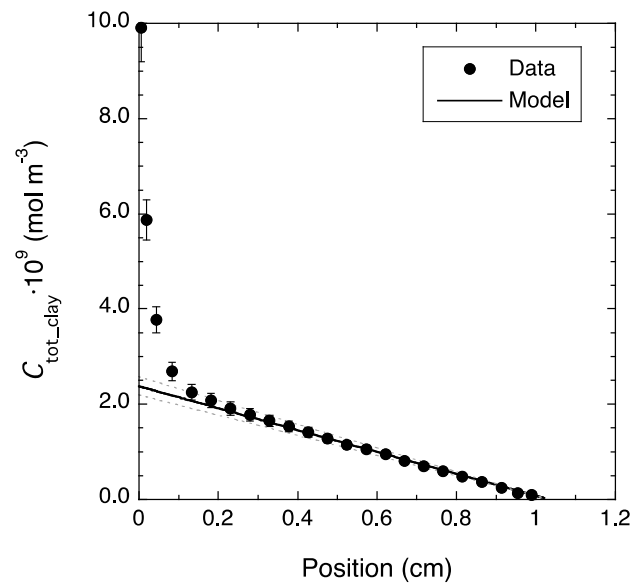A heterogeneous porosity distribution was assumed.

Fig. B28b: Tracer profile data of experiment BEN1009_13B measured at the end of through-diffusion.

The fit curve was obtained from a simultaneous fitting of the reservoir, flux and profile data taking into account porosity inhomogeneities near the clay boundaries.
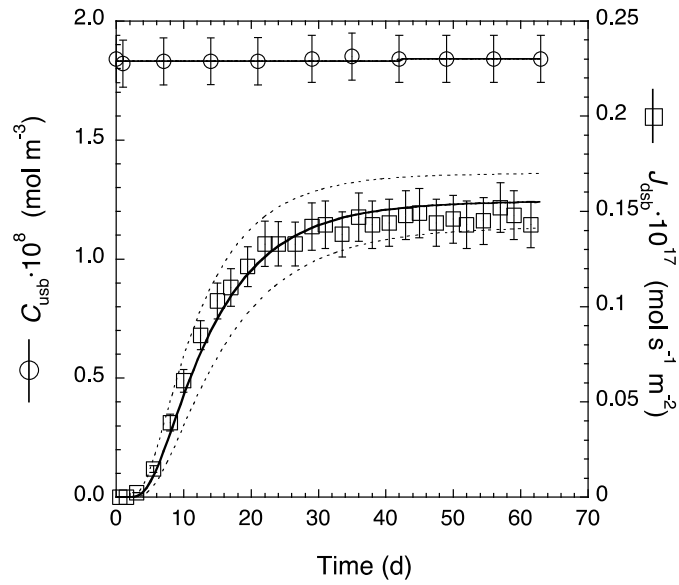
Fig. B28c: Flux at the zero-concentration boundary and reservoir concentration of $^{35}SO_4^{2-}$ in through-diffusion in Volclay at $\rho_{bd} = 1297$ kg m^{-3} and BPW1300 as the background electrolyte (BEN1009_13B, *cf.* Tab. 4.6).

A homogeneous porosity distribution was assumed.

Fig. B28d: Tracer profile data of experiment BEN1009_13B measured at the end of through-diffusion.

The fit curve was obtained from a simultaneous fitting of the reservoir, flux and profile data assuming a homogeneous distribution of porosity across the entire clay sample.

Fig. B29a: Flux at the zero-concentration boundary and reservoir concentration of $^{35}SO_4^{2-}$ in through-diffusion in Volclay at $\rho_{bd} = 1602$ kg m^{-3} and BPW1600 as the background electrolyte (BEN1009_16A, *cf.* Tab. 4.6).
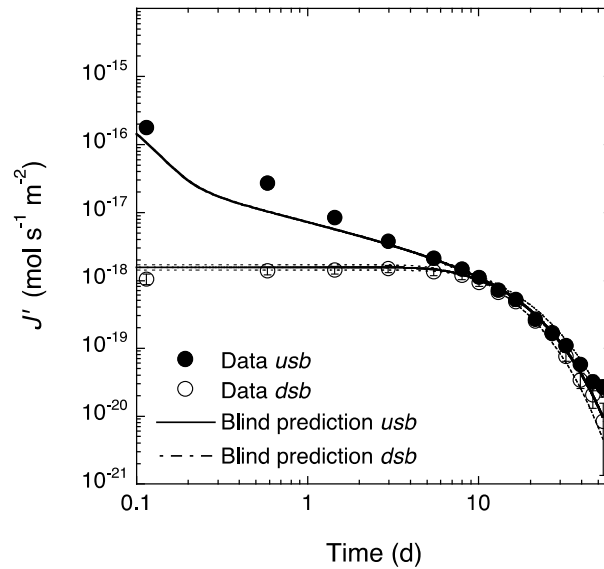

Fig. B29b: Out-diffusion data of experiment BEN1009_16A measured after through-diffusion.

The fit curve was obtained from a simultaneous fitting of the reservoir concentrations, the through-diffusion and out-diffusion fluxes.
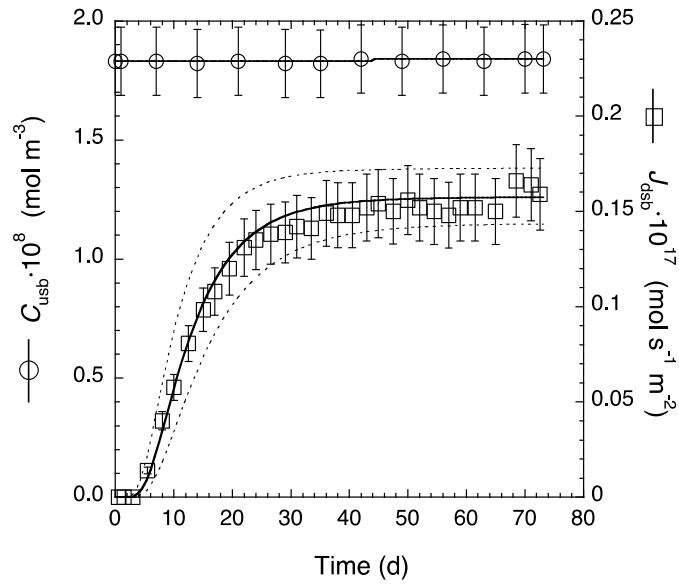
Fig. B30a: Flux at the zero-concentration boundary and reservoir concentration of $^{35}SO_4^{2-}$ in through-diffusion in Volclay at $\rho_{bd} = 1605$ kg m^{-3} and BPW1600 as the background electrolyte (BEN1009_16B, *cf.* Tab. 4.6).
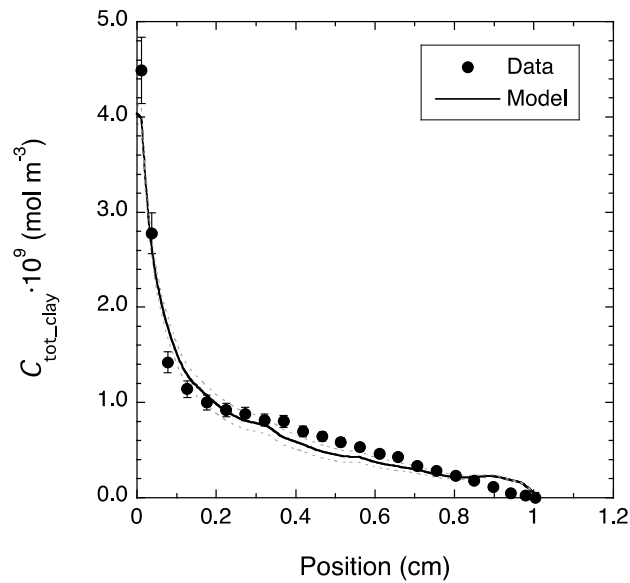

Fig. B30b: Tracer profile data of experiment BEN1009_16B measured at the end of through-diffusion.

The fit curve was obtained from a simultaneous fitting of the reservoir, flux and profile data taking into account porosity inhomogeneities near the clay boundaries.
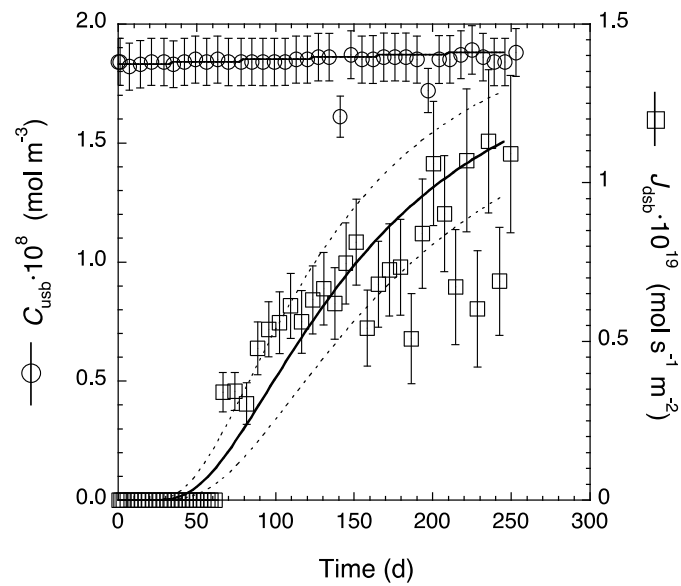
Fig. B31a: Flux at the zero-concentration boundary and reservoir concentration of $^{35}SO_4^{2-}$ in through-diffusion in Volclay at $\rho_{bd} = 1900$ kg m^{-3} and BPW1900 as the background electrolyte (BEN1009_19A, *cf.* Tab. 4.6).
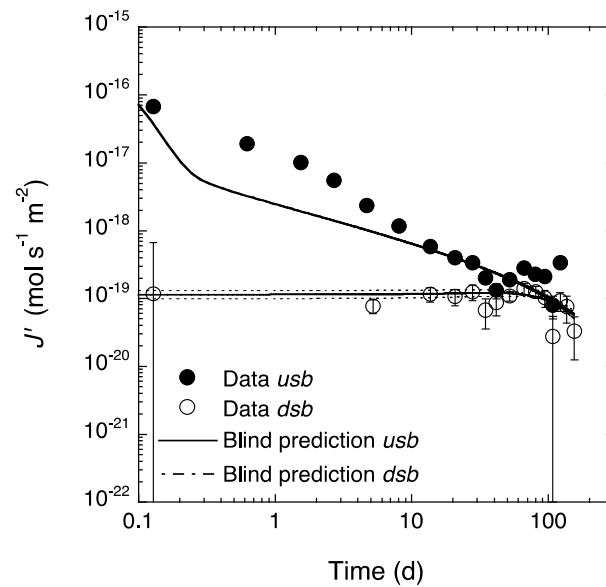

Fig. B31b: Out-diffusion data of experiment BEN1009_19A measured after through-diffusion.

The fit curve was obtained from a simultaneous fitting of the reservoir concentrations, the through-diffusion and out-diffusion fluxes.
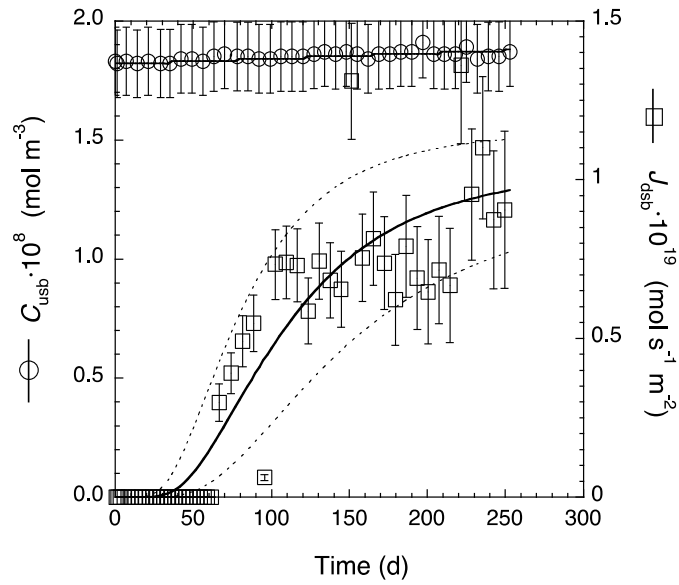
Fig. B32a: Flux at the zero-concentration boundary and reservoir concentration of $^{35}SO_4^{2-}$ in through-diffusion in Volclay at $\rho_{bd} = 1897$ kg m^{-3} and BPW1900 as the background electrolyte (BEN1009_19B, *cf.* Tab. 4.6).
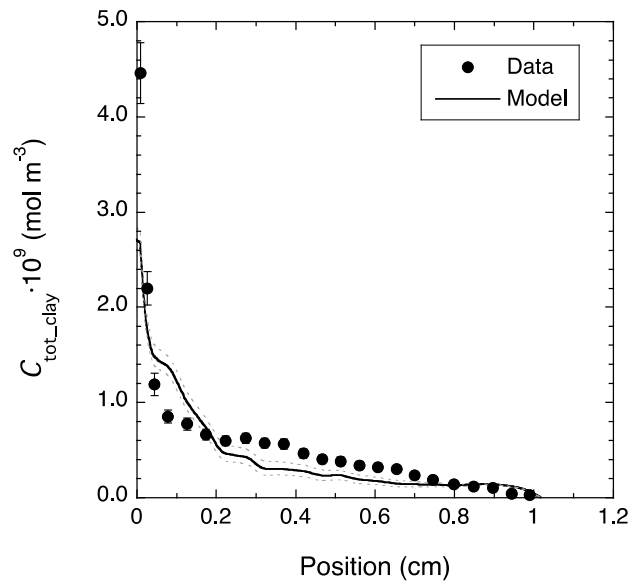

Fig. B32b: Tracer profile data of experiment BEN1009_19B measured at the end of through-diffusion.

The fit curve was obtained from a simultaneous fitting of the reservoir, flux and profile data taking into account porosity inhomogeneities near the clay boundaries.